Hydration and Ion Binding of Small Biologically Active Molecules: The Case of Neurotransmitters

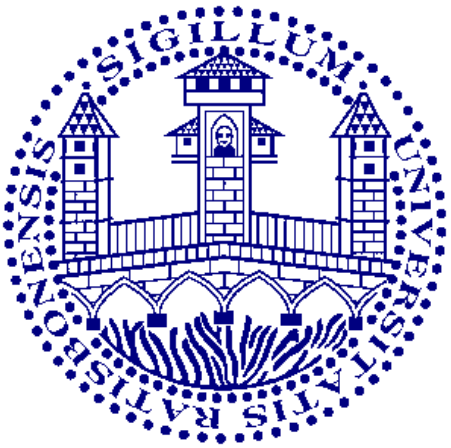

Dissertation zur Erlangung des Doktorgrades der Naturwissenschaften
(Dr. rer. nat.) der Fakultät für Chemie und Pharmazie
der Universität Regensburg

vorgelegt von
Sergej Friesen
aus Ermak (KAZ)
2019

Promotionsgesuch eingereicht am:	14.10.2019
Tag des Kolloquims:	05.12.2019
Die Arbeit wurde angeleitet von:	Apl. Prof. Dr. Richard Buchner
Prüfungsausschuss:	Apl. Prof. Dr. Richard Buchner
	Prof. Dr. Dominik Horinek
	Prof. Dr. Joachim Wegener
	Prof. Dr. Oliver Tepner (Vorsitzender)

meinen Eltern
und
Sophia

Vorwort

Diese Arbeit entstand im Zeitraum vom Oktober 2017 bis Oktober 2019 am Institut für Physikalische und Theoretische Chemie der naturwissenschaftlichen Fakultät IV – Chemie und Pharmazie – der Universität Regensburg.

Allen voran möchte ich mich beim Herrn Apl. Prof. Dr. Richard Buchner für die Erteilung des Themas bedanken. Stete Unterstützung, diverse fachliche Diskussionen und seine wertvollen Ratschläge haben maßgeblich zum Gelingen der Arbeit beigetragen. Außerdem möchte ich ihm für das Ermöglichen von mehreren Konferenzteilnahmen und dem Forschungsauftenthalt danken.

Zudem möchte ich dem Leiter des Lehrstuhls, Herrn Prof. Dr. W. Kunz für die großzügige Unterstützung danken.

Ferner geht mein Dank and die zahlreichen Kooperationspartner:

• Herrn Prof. Dr. Glenn Hefter, Murdoch University, Western Australia, für die großzügige Unterstützung und zahlreichen fachlichen Diskussionen bei seinen alljährlichen Besuchen in Regensburg. Vor allem hinsichtlich der anorganischen Salzlösungen haben seinen Ratschläge wesentlich zu meinem Verständnis auf diesem Gebiet beigetragen und die Entstehung des Kapitel 4.1 wäre ohne ihn nicht möglich gewesen.

• Frau Prof. Dr. Marija Bešter-Rogač, University of Ljubljana, Ljubljana, Slowenien, für das Bereitstellen der Leitfähigkeitsdaten von verdünnten Acetylcholinchlorid und Carbachol Lösungen. Außerdem möchte ich mich für den zwar kurzen aber sehr interessanten Aufenthalt an ihrem Lehrstuhl bedanken.

• Frau Prof. Dr. Marina V. Fedotoca, Russian Academy of Sciences, G.A. Krestov Institute of Solution Chemistry, Ivanovo, Russland, für die fruchtbare Zusammenarbeit und die RISM Kalkulationen. Zudem möchte ich sie für die wertvollen Diskussionen auf den zahlreichen Konferenzen danken.

• Dem Verband der Chemischem Industrie e.V., Stiftung Stipendien-Fonds, für die Gewährung eines Doktorandenstipendiums.

Ohne diese Kooperationen und Zuwendungen wären große Teile dieser Arbeit niemals möglich gewesen.

Allen Mitarbeitern und Kollegen des Lehrstuhls danke ich für die freundschaftliche Atmosphäre und Hilfsbereitschaft. Dabei richtet sich mein besonderer Dank an die (ehemaligen) Mitarbeiter des AK Buchner, M. Sc. Andreas Nazet und Dr. Nicolas Moreno, für die freundschaftliche Aufnahme in die Arbeitsgruppe, die Einweisung in die Messinstrumente und ihre zahlreichen Tipps, welche entscheidend zum Gelingen dieser Arbeit beigetragen haben. Ein ganz besonderer Dank geht an M. Sc. Andreas Nazet für die langjährige Zusammenarbeit und die Einführung in die Welt der dielektrischen Spektroskopie. Die freundschaftliche Arbeitsatmosphäre und seine stete Diskussionsbereitschaft über fachliche (oder auch nicht-fachliche) Themen waren für mich eine große Bereicherung.

Ebenso bedanke ich mich ganz herzlich bei den internationalen Gästen Dr. Iwona Płowaś-Korus, Dr. Vera Agieienko, Dr. Keiichi Yanase und Dr. Ziga Medoš, mit denen ich in der Zeit der Entstehung dieser Arbeit zusammen arbeiten durfte.

Ganz besonders möchte ich auch meiner Familie und meiner Freundin Sophia danken, die mich jederzeit unterstützt haben.

Für die mentale Unterstützung am Arbeitsplatz möchte ich mich herzlich bei allen Teilnehmern der Kaffeerunde bedanken, welche für einen angenehmen Ausgleich gesorgt haben und deren tägliche Diskussionen mich zweifelsohne in meinem Leben bereichert haben.

Zu guter Letzt möchte ich allen Mitarbeitern der Werkstätten der Universität Regensburg für die schnelle und gewissenhafte Erledigung der Aufträge bedanken.

Contents

Constants, Symbols and Acronyms

Constants

Elementary charge	e_0	$= 1.60217739 \cdot 10^{-19}\,\mathrm{C}$
Permittivity of free space	ε_0	$= 8.854187816 \cdot 10^{-12}\,\mathrm{C^2 J^{-1} m^{-1}}$
Avogadro's constant	N_A	$= 6.0221367 \cdot 10^{23}\,\mathrm{mol^{-1}}$
Speed of light	c	$= 2.99792458 \cdot 10^{8}\,\mathrm{m\,s^{-1}}$
Boltzmann's constant	k_B	$= 1.380658 \cdot 10^{-23}\,\mathrm{J\,K^{-1}}$
Gas constant	R	$= 8.3144598\,\mathrm{J\,K^{-1} mol^{-1}}$
Permeability of free space	μ_0	$= 4\pi \cdot 10^{-7}\,\mathrm{J^2 s^2 C^{-2} m^{-1}}$
Planck's constant	h	$= 6.6260755 \cdot 10^{-34}\,\mathrm{J\,s}$

Symbols

α	polarizability ($\mathrm{C\,m^2\,V^{-1}}$)	$\vec{E}$	electrical field strength ($\mathrm{V\,m^{-1}}$)
$\vec{D}$	dielectric displacement ($\mathrm{C\,m^{-2}}$)	$\vec{H}$	magnetic field strength ($\mathrm{A\,m^{-1}}$)
$\vec{P}$	polarization ($\mathrm{C\,m^{-2}}$)	$\vec{j}$	electric current density ($\mathrm{A\,m^{-2}}$)
$\hat{\gamma}$	complex propagation coefficient ($\mathrm{m^{-1}}$)	$\hat{k}$	complex wave number ($\mathrm{m^{-1}}$)
λ_m	medium wavelength (m)	$\hat{\varepsilon}$	complex permittivity
ε'	real part of $\hat{\varepsilon}$	ε''	imaginary part of $\hat{\varepsilon}$
μ	dipole moment (C m)	$\hat{\eta}$	generalized complex permittivity
α_m	absorption coefficient ($\mathrm{Np\ m^{-1}}$)	β	phase constant ($\mathrm{m^{-1}}$)
ε	$\lim_{\nu \to 0} (\varepsilon')$	ε_∞	$\lim_{\nu \to \infty} (\varepsilon')$
T	temperature (K)	τ	relaxation time (s)
t	time (s)	κ	electrical conductivity ($\mathrm{S\,m^{-1}}$)
ν	frequency (Hz)	ω	angular frequency ($\mathrm{s^{-1}}$)
ρ	density ($\mathrm{kg\,m^{-3}}$)	c	molarity ($\mathrm{mol\ dm^{-3}}$)
m	mass (kg)	η	dynamic viscosity (Pa s)
ϑ	temperature (°C)	b	molality ($\mathrm{mol\ kg^{-1}}$)
I	ionic strength ($\mathrm{mol\,L^{-1}}$)	Λ	molar conductivity ($\mathrm{S\,m^2\,mol^{-1}}$)

Acronyms

MW	microwave	IR	infrared
DR(S)	dielectric relaxation (spectroscopy)	MD	molecular dynamics
TDR	time domain reflectometry	IB	irrational bonding
IFM	interferometer	VNA	vector network analyzer
H_2O	water	EP	electrode polarization
D	Debye	CC	Cole-Cole
CD	Cole-Davidson	HN	Havriliak-Negami
UV	ultraviolet	DFT	density functional theory
EJM	extended jump model	NMR	nuclear magnetic resonance
OKE	optical Kerr effect spectroscopy	PCM	polarizable continuum model
RISM	reference interaction site model	PDF	pair distribution function
SDF	spatial distribution function	DMA	dimethylacetamide
FA	formamide	PC	propylene carbonate
DFT	density functional theory	IC	ion-cloud
IP	ion pair	HO	Hubbard and Onsager
SKA	Sega, Kantorovich and Arnold	CIP	contact ion pair
SIP	solvent-shared ion pair	2SIP	solvent-separated ion pair

Motivation

General Aspects

Water is ubiquitous. Water is the most common liquid on our planet and it is essential for life to exist. It constitutes $\sim 50 - 70\,\%$ of the cell content, where it does not simply act as a medium but rather plays a fundamental part in all biological processes. As pointed out by Ball in his famous review on water in biological systems, it is "a substance that actively engages and interacts with biomolecules in complex, subtle, and essential ways" [1]. For instance, folding, stabilization and dynamics of proteins and hence their activity are governed by their hydration [2–6]. Further, ligand recognition and the kinetics and thermodynamics of binding in biological processes are majorly controlled by the solvation of both, the ligand and the receptor [4, 7–9].

Despite the emergence of many different techniques to study the solvation of various solutes during the last decades, fundamental rules and guidelines for the description of the hydration structure and dynamics are still lacking. On the one hand, this might originate from the fact that different techniques probe different hydration characteristics and an unified definition of "hydration water" does not exist [10]. For example, nuclear magnetic resonance [11, 12], neutron scattering [13–15] and statistical mechanical calculations [16–18] report only short-range effects at a timescale greater than the picosecond regime, while most MD simulations [19], terahertz [20, 21] and dielectric spectroscopy studies [22] investigate the (collective) dynamics and structure of the solutions, including long-range effects, at shorter picosecond/sub-picosecond timescales. However, keeping in mind that each individual technique examines different aspects of hydration by probing different solvation phenomena at different timescales, a coherent picture can sometimes still be deduced by combining the results of the individual techniques [10].

On the other hand, this lack of universal guidelines might just reflect the whole complexity of solvation and the inability of combining all the specific hydration phenomena of different classes of solutes (charged/uncharged, hydrophilic/hydrophobobic, macromolecules/small molecules) into one unified concept.

The situation is fairly odd for the hydration of larger biomolecules, *e.g.* proteins. In spite of many investigations of these systems (see Refs. [23], [10] and [1] for an overview), basic principles for understanding the solvation of these macromolecules have not really been established yet. Probably the main reason for this is that comparably few work has been done on small, biologically relevant molecules, which could serve as simplified "model"

species, and thus "it may not be possible either to generalize or to reduce the structural and dynamic aspects of hydration to simplistic rules of thumb" [1]. Amino acid solutions would certainly be appropriate candidates for such studies.

The effect of ions on aqueous systems containing biomolecules is even more baffling. Understanding and interpreting specific ion effects has concerned physical chemist for over hundred years. Franz Hofmeister was the first to study the effect of ions on the precipitation of egg white protein and he proposed a series for their respective efficiency to do so [24, 25]. Today it is known that the empirical Hofmeister effect depends on many different aspects of the present solution, *e.g.* buffer, pH or polarity of the protein surface, and the series may even be reversed if one of these factors is varied [26, 27]. These specific ion effects cannot be explained by conventional electrostatic theories (DLVO, Debye-Hückel, *etc.*). A subtle interplay between local, rather than long-range, ion-water-biomolecule interactions seems to govern the ability (or disability) of ions to bind to distinct moieties of the biomolecule [28].
About 20 years ago, Collins introduced a more sophisticated approach, which is often called the Collins's rule or "law of matching water affinities". In this concept, electrostatics and hydration effects of each individual ion are automatically taken into account. Many ion specific phenomena could successfully be explained by it [29–31]. On the other hand, this concept merely considers ion-ion interactions, which renders impossible its application to explain specific interaction of ions with uncharged entities *e.g.* in biological systems [29].
All these concepts of ions often involve the terms "structure-making" and "structure-breaking" ions [32], or the more or less equivalent appellations "kosmotrope" or "chaotrope" [33], which try to classify ions according to their influence on the H-bond network of water. Loosely speaking, structure-makers (or kosmotropes) refer to highly-solvated ions of high surface charge density and structure-breakers (or chaotropes), on the other hand, designate weakly hydrated, rather large ions. However, a clear classification of ions into the corresponding categories often depends on the applied experiment. In addition to that, there seems to be no consensus of how to properly quantify a "water-structure" experimentally, which makes this classification even more puzzling [34].

It seems that despite recent advances in the field of solute-solvent and specific ion interactions, many questions are still open and finding answers to at least some of these matters could be of crucial importance for chemistry, biochemistry and chemical engineering.
However, in order not to get hopelessly lost in its complexity, it is instructive to focus on a certain class of small (bio-)molecules. Thorough investigations of their physico-chemical behaviour in aqueous solution could infer information on the solute-solute and solvent-solvent interactions. These data, in the case of biologically relevant solutes, could shed some light on their biological activity and, on the other hand, could potentially be used for the construction of models for other solutes.

Neurotransmitters (NTs) belong to the class of small, biologically active molecules. Despite their great importance, detailed investigations of their solvation and dynamics in aqueous

solution are rather scarce. Interestingly, most studies of these systems were highly focused on the NT-conformation [35–40, 40, 41], often neglecting other significant solvent-solute and solute-solute effects, which might be equally if not even more important for their biological action.

Aim of this Study

The general aim of this thesis is the investigation of the structure and dynamics of aqueous solutions of neurotransmitters and other chemically-related, biologically relevant molecules by the means of dielectric relaxation spectroscopy (DRS) in the megahertz to gigahertz frequency range. The present study can be subdivided into three main parts:

In the first part of the experimental results, a detailed study of the complex permittivity spectra of binary neurotransmitter solutions and chemically related compounds is described. Therefore, concentration-dependent measurements are performed at 25 °C to infer information on the hydration, dynamics and ion-binding properties of the biomolecules.

For the cationic NTs acetylcholine and carbomoylcholine additional insight into the dynamical properties of the various relaxation processes will be gained by measuring the dielectric spectra over a wide range of temperatures. Further, the dielectric data of the latter systems will be accompanied by dilute-conductivity measurements and statistical mechanical calculations (1D-and 3D-RISM) to provide as detailed description as possible on the behaviour of these NTs in solution.
The proteinogenic amino-acid and neurotransmitter L-glutamate will be compared to the structurally-related amino-acid L-glutamine, while the investigation of the NT γ-aminobutyric acid and its isomer α-aminobutyric acid will reveal structural and dynamical information on the effect of changing position of the amine moiety at these biomolecules.

The second part deals with binary solutions of inorganic salts. The hydration and ion-pair formation in aqueous $MgCl_2$, $CaCl_2$ and Me_4NCl solutions is studied. The Me_4N^+ cation is of particular interest due to its special hydrophobic/hydrophobic balance and its structural relation to many biologically important compounds, while Mg^{2+} and Ca^{2+} are omnipresent in living organisms. Although these systems were extensively studied in previous works [14, 42–49], precise and systematic dielectric relaxation studies over a wide frequency range were still lacking.

In the last portion of this thesis, effects of addition of inorganic, biologically-relevant salts to biomolecule solutions will be investigated. Ion-binding effects and the impact of salts on the acetylcholine, glutamate and glutamine hydration will be studied. Possible structures of ion aggregates and their degree of association will be deduced. By varying the cations or the anions, respectively, specific ion effects can also be studied in this way. These ternary solutions represent much better the real conditions in living systems, which involve a great number of various solvated ions interacting with the bioactive solute.

A special focus of this thesis will be the interpretation of the DRS results on a microscopic level with the aid of quantum chemical calculation of various low-energy conformers of the investigated molecules. Comparisons of these results with other theoretical and experimental approaches will be drawn, with the aim to provide a coherent picture and thus to build a bridge between the different techniques.
To address all issues mentioned above, proper analysis of the DR spectra is prerequisite. Thus, new mathematical approaches for the analysis of the relaxation parameters and for the correction of the DR spectra for interfering relaxation modes were developed and utilized in this work.

Chapter 1

Theory

1.1 Interaction of Electromagnetic Fields with Dielectric Materials

1.1.1 Dielectric Polarization in Static Electric Fields

When applying a static electric field to dielectric matter, charge displacement occurs. The type of the displacement depends on kind of charges present in the system. In the case of free charges, *e.g.* (dilute) electrolyte solutions, a translational motion of positive and negative charges towards the respective electrodes can be observed. For "bound" pairs of positive and negative charge, *i.e.*, dipoles, the applied field induces a reorientation of the dipoles such that the dipole moment vectors align themselves parallel to the field, minimizing their potential energy. The two cases represent conduction through an electric current and conduction through a displacement current, respectively. Note that the latter is a transient process and occurs until the dipoles reach their new equilibrium orientation which is determined by the interplay between intermolecular interactions, the electric field and thermal energy. A system comprising both kinds of charges, free charges and permanent or induced dipoles, is often referred as "real dielectric" [50], as it most appropriately describes the situation in many real systems, *e.g.* salt solutions, ionic liquids *etc.*
Mathematically, the response of a material to an applied low-intensity* electric field, $\vec{E}$, is described by the phenomenon of polarization, $\vec{P}$. The polarization, which is defined as the macroscopic dipole moment of the system per unit volume, of an isotropic and uniform system is connected to the electric field *via*

$$\vec{P} = (\varepsilon - 1)\varepsilon_0 \vec{E} \tag{1.1}$$

In Eq. 1.1, ε_0 is the permittivity of free space and ε the relative permittivity of the sample. The factor $(\varepsilon - 1)$ is also known as the electrical susceptibility.

*For field strengths of $\sim 10^6$ V/m or higher non-linear effects become noticeable. Within the scope of this thesis the non-linear effects are unimportant and thus no further description of these effects will be pursued. The subsequent derivation of the mathematical equations refers to the linear response only.

Following the approach of Maxwell, which treats matter as continuous charge distribution, the electric field inside the material is the result of electric displacement, $\vec{D}$, which is connected to polarization by

$$\vec{D} = \varepsilon_0 \vec{E} + \vec{P} = \varepsilon_0 \varepsilon \vec{E} \tag{1.2}$$

To be able to extract information on molecular-level processes from polarization, it is convenient to split up $\vec{P}$ into two distinct contributions [51]:

$$\vec{P} = \vec{P}_\mu + \vec{P}_\alpha \tag{1.3}$$

where $\vec{P}_\mu$ is the orientational (dipolar) polarization, which can be written as

$$\vec{P}_\mu = \sum_k \rho_k \langle \vec{\mu}_k \rangle \tag{1.4}$$

and $\vec{P}_\alpha$ is the induced polarization, given by

$$\vec{P}_\alpha = \sum_k \rho_k \vec{\mu}_{k,\mathrm{ind}} = \sum_k \rho_k \alpha_k (\vec{E}_i)_k \tag{1.5}$$

In Eqs. 1.4 and 1.5, ρ_k is the number density of particles k, $\langle \vec{\mu}_k \rangle$ is the ensemble average of the permanent dipole moment, which can be obtained from Langevin theory taking into account all particle orientations, and $\vec{\mu}_{k,\mathrm{ind}}$ is the induced dipole moment. The latter can be expressed by the molecular polarizability, α_k, and the avarage local field acting upon the particle, $(\vec{E}_i)_k$. This local field does not coincide with the applied external field nor the permanent dipole moment vector $\vec{\mu}$ of the regarded species but it is a superposition of all sources of electric field at the position of the particle k minus the field due to the particle itself.

Orientational polarization, $\vec{P}_\mu$, is the result of partial alignment of a species with a permanent dipole moment against thermal motion in an applied electric field. The intermolecular interactions and the inertia of the species lead to a finite time for the establishment of full polarization. For molecular liquids the characteristic time is at the pico- to nanosecond timescale, corresponding to frequencies in the microwave region.

The induced polarization, $\vec{P}_\alpha$, itself comprises two contributions, namely the atomic polarization, resulting from the relative shift of the core positions, and the electron polarization, due to the fluctuations of the electron sheath density relative to the core. These two processes are rather fast and their characteristic frequency is located in the infrared and ultraviolet range, respectively.

Since $\vec{P}_\mu$ and $\vec{P}_\alpha$ occur at significantly different timescales, both effects can be well separated on the frequency scale and can be regarded as linearly independent. By the incorporation of the induced polarization contribution into the infinite frequency permittivity, ε_∞, one may write in the style of Eq. 1.1:

$$\vec{P}_\mu = \varepsilon_0 (\varepsilon - \varepsilon_\infty) \vec{E} \tag{1.6}$$

$$\vec{P}_\alpha = \varepsilon_0 (\varepsilon_\infty - 1) \vec{E} \tag{1.7}$$

The value of infinite frequency permittivity, ε_∞, is usually determined in the far-infrared region, at around 200 cm^{-1}, and it states the permittivity after the decay of the orientational polarization [52]. In practice, the value extrapolated to higher frequencies from the measurements in the microwave frequency range is often taken for ε_∞.

1.1.2 Dielectric Properties in Alternating Electric Fields

As can be seen above, time is an important variable when talking about polarization of material, as certain processes require characteristic periods of time to establish a certain value of polarization. Whereas the polarization is in equilibrium with the electric field in the static case, it does not necessarily have to be for the time-dependent electric fields. This so-called dynamic case can most easily be described with the help of a harmonic, *e.g.* sinusoidally, oscillating electric field, $\hat{\vec{E}}(t)$[†], with the amplitude, $\vec{E}_0$, and the angular frequency, $\omega = 2\pi\nu$:

$$\hat{\vec{E}}(t) = \vec{E}_0 \exp(\mathrm{i}\omega t) \tag{1.8}$$

If the frequency of the electric field is sufficiently low, the microscopic particles in the condensed matter will be able to follow the electric field instantaneously (quasi-static case, see above). The frequency threshold until which the quasi-static conditions apply depends strongly on type of material and the temperature, and for liquids far from their glass-transition temperature it lies typically between 1 MHz and 1 GHz [53]. Exceeding this frequency, the microscopic particles cannot follow the changes in the electric field anymore, which leads to a frequency-dependent phase delay $\delta(\omega)$ between the harmonic electric field and the dielectric displacement. Therefore one may write:

$$\hat{\vec{D}}(t) = \vec{D}_0 \exp[\mathrm{i}(\omega t - \delta(\omega))] \tag{1.9}$$

where $\vec{D}_0$ is the amplitude of the sinusoidal variation. Using the same relation between $\hat{\vec{E}}(t)$ and $\hat{\vec{D}}(t)$ as given in Eq. 1.2 for the static case, the complex, frequency dependent permittivity, $\hat{\varepsilon}(\omega)$, can be introduced:

$$\hat{\varepsilon}(\omega) = \frac{\vec{D}_0}{\varepsilon_0 \vec{E}_0} \exp[-\mathrm{i}\delta(\omega)] \tag{1.10}$$

By using the Euler's relation

$$\hat{\varepsilon}(\omega) = \varepsilon'(\omega) - \mathrm{i}\varepsilon''(\omega) \tag{1.11}$$

is finally obtained, where $\varepsilon'(\omega) = \frac{\vec{D}_0}{\varepsilon_0 \vec{E}_0}\cos[\delta(\omega)]$ and $\varepsilon''(\omega) = \frac{\vec{D}_0}{\varepsilon_0 \vec{E}_0}\sin[\delta(\omega)]$. Both quantities are interconnected through the Kramers-Kronig relation and can be converted into each

[†]Electric fields always give rise to magnetic fields and vice versa, thus the electromagnetic theory must be used. Mostly, however, it is sufficient to consider the electric field only. The ˆ symbol denotes that the quantity is expressed as a complex function.

other. For $\omega = 0$ equation 1.10 reduces to the static-case relation 1.2 with $\varepsilon'(\omega) = \varepsilon$, therefore $\varepsilon'(\omega)$ can be considered as a generalization of the dielectric constant for oscillating fields and describes the dispersive in-phase response. The dissipative out-of-phase response, $\varepsilon''(\omega)$, (with a phase shift of $\pi/2$ with respect to $\hat{\vec{E}}(t)$) determines the loss of energy in the dielectric. Consequently, $\varepsilon''(\omega)$ is called the dielectric loss.
The energy dissipated per unit of time in an ideally insulating dielectric is given by

$$\dot{W} = \frac{1}{2}\omega E_0^2 \varepsilon_o \varepsilon''(\omega) \tag{1.12}$$

However, in reality most dielectrics show a certain electrical dc conductivity contribution, κ. This leads to an electrical current density, $\hat{\vec{j}}$, which is in phase with the electric field and is given by

$$\hat{\vec{j}}(t) = \kappa \hat{\vec{E}}(t) \tag{1.13}$$

The dissipated amount of energy per unit of time by the electric current can be obtained from Joule's law

$$\dot{W} = \frac{1}{2}\kappa E_0^2 \tag{1.14}$$

From the comparison of equations 1.12 and 1.14, it becomes clear that the absorption of energy in a dielectric material is determined by the sum $\varepsilon''(\omega) + \kappa/(\varepsilon_0\omega)$. As long as κ is constant, no difficulties in separation of the effects of conduction and polarization arise. However, when it takes a certain time for the current to reach its equilibrium value, equation 1.13 has to be replaced by

$$\hat{\vec{j}}(t) = \hat{\kappa}(\omega)\hat{\vec{E}}(t) \tag{1.15}$$

where

$$\hat{\kappa}(\omega) = \kappa'(\omega) - \mathrm{i}\kappa''(\omega) \tag{1.16}$$

analogous to the complex representation of $\hat{\varepsilon}(\omega)$. The quantity κ' determines the part of the current which is in-phase with the applied field and leads to the energy absorption, while the imaginary part, κ'', gives the part of current with a phase shift of $\pi/2$ with respect to the field. The combination of dielectric displacement and the electrical current in the form of a generalized dielectric displacement (for details see [51]) leads to the introduction of the experimentally accessible generalized complex permittivity, $\hat{\eta}(\omega) = \eta'(\omega) - \mathrm{i}\eta''(\omega)$, with its real part

$$\eta'(\omega) = \varepsilon'(\omega) - \frac{\kappa''(\omega)}{\omega\varepsilon_0} \tag{1.17}$$

and the imaginary part

$$\eta''(\omega) = \varepsilon''(\omega) + \frac{\kappa'(\omega)}{\omega\varepsilon_0} \tag{1.18}$$

An univocal separation of $\hat{\varepsilon}(\omega)$ and $\hat{\kappa}(\omega)$ is impossible, as long as the molecular origin of the various contributions to $\hat{\eta}(\omega)$ is unknown. Generally, reorientations of dipoles or

charge displacements within particles must be attributed to the $\hat{\varepsilon}(\omega)$, while translational processes of charges are governed by $\hat{\kappa}(\omega)$. Some dispersion of the complex conductivity can be explained by the classical theory of Debye and Falkenhagen [54] for electrolyte solutions and is thought to be the result of ion-cloud relaxations. However, quantitative approaches for the separation of $\hat{\varepsilon}(\omega)$ and $\hat{\kappa}(\omega)$ are still lacking [55]. The inability of determining the two contributions independently particularly affects the analysis of dielectric properties of conductive systems. To circumvent this problem, the dc conductivity, $\kappa = \kappa'(0) = \hat{\kappa}(0)$, can be used to account for the frequency-independent contribution of conductivity whereas potential frequency-dependent processes are covered by $\hat{\varepsilon}(\omega)$. Thus, the complex dielectric permittivity can be calculated as

$$\varepsilon'(\omega) = \eta'(\omega) \tag{1.19}$$

$$\varepsilon''(\omega) = \eta''(\omega) - \frac{\kappa'(0)}{\omega\varepsilon_0} \tag{1.20}$$

Using this approach, ε' and ε'' can be obtained from the experimentally accessible quantities η', η'' and κ. Note that the second term on the right-hand side of Eq. 1.20 strongly increases at decreasing frequencies, thus it determines the minimum frequency down to which precise $\hat{\varepsilon}(\omega)$ spectra are available in the experiment [52].

1.1.3 Response Function of Orientational Polarization

As mentioned in Section 1.1.1, orientational polarization does not occur instantaneously but requires a certain time due to inertia and friction acting on the reorienting particles. Thus, for sufficiently high frequencies of the electric field the dipoles are not able to follow the field variation and the polarization can not attain its maximum value anymore. In this case the response function gives the relation between $\hat{\vec{E}}$ and $\hat{\vec{P}}$. To derive the response function for an isotropic and linear dielectric[‡] a thought experiment has to be considered. The thought experiment is visualized in Figure 1.1. A static electric field $\vec{E}(t) = \vec{E}_0$, causing the polarization $\vec{P}(t) = \vec{P}_0$, is switched off at $t = 0$ and a decay of the polarization can be observed. While the induced polarization is assumed to drop instantaneously, $\vec{P}_\mu(t)$ decreases monotonically with t.

[‡]In a linear dielectric the superposition principle applies *e.g.* for electric fields and the respective induced polarizations.

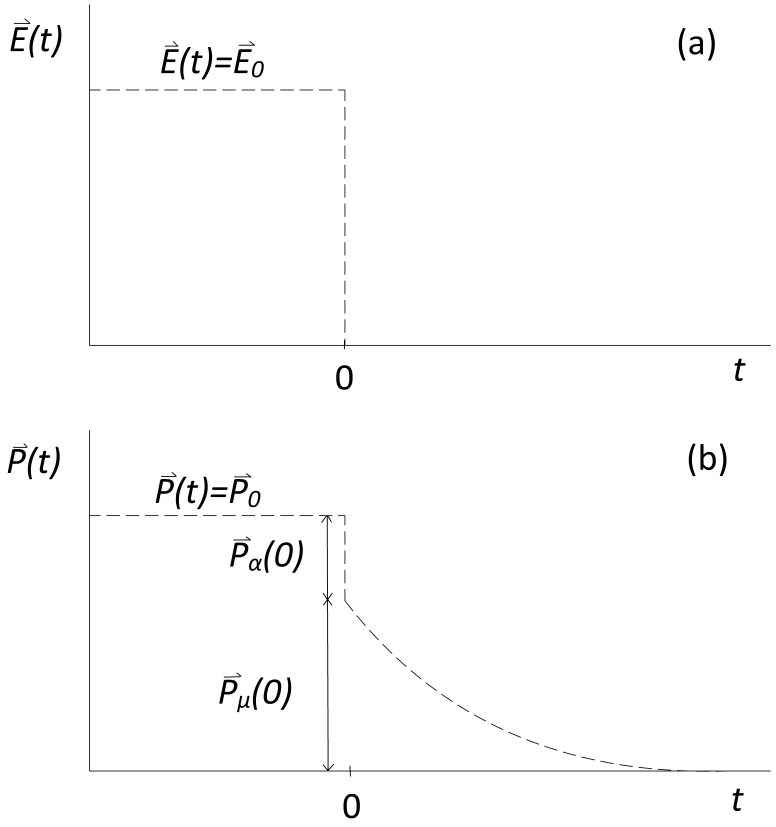

Figure 1.1: Evolution of (a) $\vec{E}(t)$, being cut off at $t = 0$, and (a) the polarization, $\vec{P}(t)$.

The time evolution of the remaining orientational polarization can be expressed as [51]

$$\hat{\vec{P}}_\mu(t) = \hat{\vec{P}}_\mu(0) \cdot F_P^{\mathrm{or}}(t) \text{ with } F_P^{\mathrm{or}}(0) = 1, F_P^{\mathrm{or}}(\infty) = 0 \tag{1.21}$$

where the step response function (time domain autocorrelation function) $F_P^{\mathrm{or}}(t)$ is defined as [52]

$$F_P^{\mathrm{or}}(t) = \frac{\left\langle \hat{\vec{P}}_\mu(0) \cdot \hat{\vec{P}}_\mu(t) \right\rangle}{\left\langle \hat{\vec{P}}_\mu(0) \cdot \hat{\vec{P}}_\mu(0) \right\rangle} \tag{1.22}$$

The step response function is directly accessible *via* time domain experiments, *e.g.* Time Domain Reflectometry (TDR) [56, 57].

However, from an experimental point of view, frequency domain experiments are of a greater interest. A time-dependent electric field can be approximated by splitting it up in an infinite number of differential square pulses. Thus, for a harmonically oscillating electrical field the orientational polarization at any time t can be written as

$$\hat{\vec{P}}_\mu(\omega, t) = \varepsilon_0(\varepsilon - \varepsilon_\infty)\hat{\vec{E}}(t) \int_0^\infty \exp(-\mathrm{i}\omega t') f_P^{\mathrm{or}}(t')dt' \tag{1.23}$$

where $f_P^{\mathrm{or}}(t')$ is the pulse response function in the time domain and is the negative time-derivative of the normalized step response function:

$$f_P^{\mathrm{or}}(t') = -\frac{\partial F_P^{\mathrm{or}}(t-t')}{\partial(t-t')} \text{ normalized according to } \int_0^\infty f_P^{\mathrm{or}}(t')dt' = 1 \tag{1.24}$$

The integral in Eq. 1.23 is the Laplace-transformed pulse response function of the orientational polarization:

$$\int_0^\infty \exp(-\mathrm{i}\omega t') f_P^{\mathrm{or}}(t')dt' = \mathcal{L}_{\mathrm{i}\omega}[f_P^{\mathrm{or}}(t')] \tag{1.25}$$

By comparing equation 1.6, modified accordingly for oscillating fields, and Eq. 1.23 the connection between the complex permittivity and the Laplace-transformed pulse response function becomes evident [51]:

$$\hat{\varepsilon}(\omega) = \varepsilon'(\omega) - \mathrm{i}\varepsilon''(\omega) = \varepsilon_\infty + (\varepsilon - \varepsilon_\infty) \cdot \mathcal{L}_{\mathrm{i}\omega}[f_P^{\mathrm{or}}(t')] = \varepsilon_\infty + (\varepsilon - \varepsilon_\infty) \cdot F(\omega) \tag{1.26}$$

Here, the pulse response function (often referred as relaxation or band-shape function), $F(\omega)$, is the representation of the autocorrelation function $F_P^{\mathrm{or}}(t)$ in the frequency domain and comprises equivalent information on the relaxation dynamics [52].

As can be seen from the model broadband dielectric spectrum in Figure 1.2, relaxation bands are rather broad due to its coupling to the surrounding medium compared to the sharp absorption peaks of the intramolecular processes in the IR or UV range. The latter processes, which are covered by $\vec{P}_\alpha$, obey the rules of quantum mechanics and give rise to resonant vibrational transitions at infrared frequencies and resonant electronic transitions in the ultraviolet range, respectively [58].

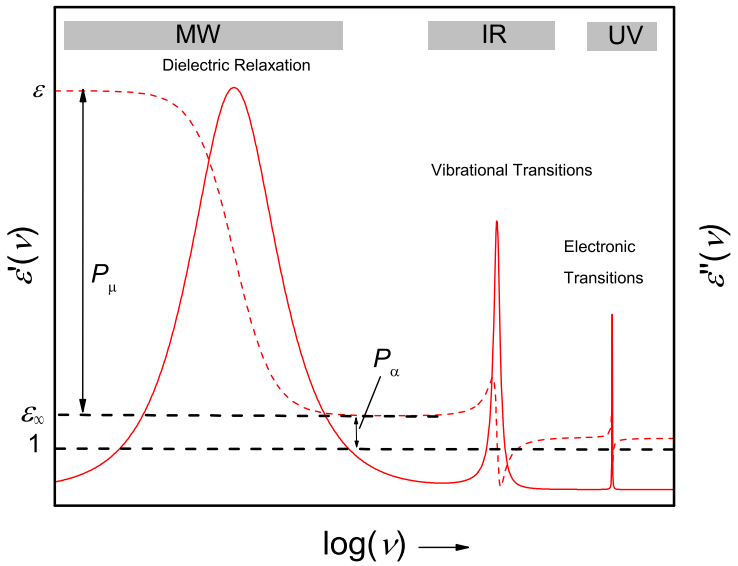

Figure 1.2: Schematic complex permittivity spectrum, with $\varepsilon'(\nu)$ (dashed line) and $\varepsilon''(\nu)$ (solid line), covering frequencies from the microwave (MW) regime to infrared (IR), and up to the ultraviolet (UV) region.

Since the present work does not treat intramolecular resonance processes, but focuses on the dielectric relaxation in the microwave frequency range, various mathematical descriptions of the dielectric relaxation functions will be presented in the following chapter.

1.2 Empirical Relaxation Models

Numerous empirical and semi-empirical approaches have been proposed in literature to characterize dielectric relaxation phenomena. In general, the dielectric spectra of liquids and solutions (far from their glass-transition temperature) can be decomposed into their individual contributions and described with a suitable linear combination of n single relaxation processes:

$$\hat{\varepsilon}(\omega) = \varepsilon_\infty + \sum_{j=1}^{n} (\varepsilon_j - \varepsilon_{\infty,j}) F_j(\omega) \tag{1.27}$$

All single processes are assumed to be linearly independent and each process, j, is characterized by its own band-shape function, $F_j(\omega)$, and amplitude, S_j:

$$\varepsilon - \varepsilon_\infty = \sum_{j=1}^{n} (\varepsilon_j - \varepsilon_{\infty,j}) = \sum_{j=1}^{n} S_j \text{ with } \varepsilon_{\infty,j} = \varepsilon_{j+1} \tag{1.28}$$

Yet, it should be emphasized that many of the proposed models are (semi-) empirical and thereby their physical meaning is often not easy to derive. In the following, models used in this work will be presented.

1.2.1 The Debye Equation

The simplest approach to model dielectric relaxations was introduced by Debye [59], who assumed the decrease of the orientational polarization after the cut-off of the external electric field to be directly proportional to the momentary polarization itself [60]. One thus obtains a differential time law of first order

$$\frac{\partial}{\partial t}\vec{P}_\mu(t) = -\frac{1}{\tau}\vec{P}_\mu(t) \tag{1.29}$$

where τ is the relaxation time of this process, characterizing the dynamics of the system. Solving the differential equations leads to

$$\vec{P}_\mu(t) = \vec{P}_\mu(0)\exp\left(-\frac{t}{\tau}\right) \tag{1.30}$$

Comparing Eqs. 1.21 and 1.30 yields the step response function in the time domain

$$F_P^{or}(t) = \exp\left(-\frac{t}{\tau}\right) \tag{1.31}$$

and after application of Eq. 1.24 the pulse response function of the Debye relaxation is obtained:

$$f_P^{or}(t) = \frac{1}{\tau}\exp\left(-\frac{t}{\tau}\right) \tag{1.32}$$

According to Eq. 1.26 the complex permittivity can be obtained by Laplace transformation of the pulse response function

$$\hat{\varepsilon}(\omega) = \varepsilon_\infty + (\varepsilon - \varepsilon_\infty)\cdot\mathcal{L}_{\mathrm{i}\omega}\left[\frac{1}{\tau}\exp\left(-\frac{1}{\tau}\right)\right] \tag{1.33}$$

Using the identity $\mathcal{L}_s\left[\exp(\mathrm{a}x)\right] = (\mathrm{s}-\mathrm{a})^{-1}$ [51] the complex permittivity can be written as the Debye (D) formula

$$\hat{\varepsilon}(\omega) = \varepsilon_\infty + \frac{\varepsilon - \varepsilon_\infty}{1 + \mathrm{i}\omega\tau} \tag{1.34}$$

The comparison of the Eqs. 1.34 and 1.26 provides the relaxation function, $F_\mathrm{D}(\omega)$, of the Debye equation

$$F_\mathrm{D}(\omega) = \frac{1}{1 + \mathrm{i}\omega\tau} \tag{1.35}$$

Eventually, the real and the imaginary parts of $\hat{\varepsilon}(\omega)$ can easily be obtained from Eq. 1.34

$$\varepsilon'(\omega) = \varepsilon_\infty + \frac{\varepsilon - \varepsilon_\infty}{1 + \omega^2\tau^2} \tag{1.36}$$

$$\varepsilon''(\omega) = \omega\tau\frac{\varepsilon - \varepsilon_\infty}{1 + \omega^2\tau^2} \tag{1.37}$$

The dispersion curve, plotted as $\varepsilon' = \varepsilon'(\ln(\omega))$, is a point symmetric, monotonically decreasing function with the inflection point at $\omega = 1/\tau$. The absorption curve, $\varepsilon'' = \varepsilon''(\ln(\omega))$, yields an axis-symmetric band reaching its maximum at $\omega = 1/\tau$.

1.2.2 Extensions of the Debye Equation

For many condensed systems deviations from the mono-exponential relaxation described by the Debye band-shape function occur. In this case, the assumption of just *one* relaxation time is dropped and the analysis of these dielectric spectra is improved by the introduction of the concept of a continuous relaxation time distribution function, $g(\tau)$, proposed by Wagner [61]. The logarithmic distribution function, $G(\ln(\tau))$, is often preferred for practical reasons. The complex permittivity can be written as

$$\hat{\varepsilon}(\omega) = \varepsilon_\infty + (\varepsilon - \varepsilon_\infty) \int_0^\infty \frac{G(\ln(\tau))}{1 + \mathrm{i}\omega\tau} \mathrm{dln}(\tau) \text{ with } \int_0^\infty G(\ln(\tau))\mathrm{dln}(\tau) = 1 \tag{1.38}$$

If $G(\ln(\tau))$ is a delta function, this equation will reduce to a Debye function.
In the literature a lot of afford has been made to obtain the distribution function directly from experimental results, which turned out to be anything but straightforward and a generally accepted theory of the origin of the non-Debye behaviour is still lacking until today. However, the introduction of additional parameters into the Debye equation 1.34 made it possible to describe the relaxation behavior satisfactorily. These empirical parameters lead to symmetrical and/or asymmetrical broadening of the dispersion curves, which can be interpreted as a respective broadening of the distribution of relaxation times around its most probable relaxation time value τ_0 [51].

Cole-Cole equation
The Cole-Cole (CC) equation [62, 63] describes a symmetrical relaxation time distribution around a principal relaxation time τ_0 by introducing the parameter $\alpha \in [0...1[$ into the Debye equation

$$F_{\mathrm{CC}}(\omega) = \frac{1}{1 + (\mathrm{i}\omega\tau_0)^{1-\alpha}} \tag{1.39}$$

For $\alpha = 0$ the CC equation reduces to the Debye equation. Increasing the α-value results in a systematical broadening of the dispersion and the dissipative curves.

Cole-Davidson equation
An asymmetrical relaxation time distribution around the center of gravity τ_0 is given by the Cole-Davidson (CD) equation [64, 65]. The empirical parameter $\beta \in]0...1]$ introduces an asymmetric broadening of dispersion and absorption curves towards higher frequencies. The CD equation is

$$F_{\mathrm{CD}}(\omega) = \frac{1}{(1 + \mathrm{i}\omega\tau_0)^{\beta}} \tag{1.40}$$

and it reduces to the Debye equation for $\beta = 1$.

Havriliak-Negami equation
Combining both parameters $\alpha \in [0...1[$ and $\beta \in]0...1]$, leads to the Havriliak-Negami (HN) equation [66] for broad, asymmetric relaxation time distributions:

$$F_{\mathrm{HN}}(\omega) = \frac{1}{(1 + (\mathrm{i}\omega\tau_0)^{1-\alpha})^{\beta}} \tag{1.41}$$

Consequently, the HN equation is used for the description of broad and asymmetric dispersion and dissipative curves. For $\alpha = 0$ and $\beta = 1$ the Debye band-shape function is obtained.

Furthermore, corrections for the unphysical behavior of the mentioned equations in higher frequency regions (THz and far-infrared regime) can be introduced. As the Debye, but especially the broader CC, CD and HN equations, decay too slowly a termination at higher frequencies is necessary, which accounts for the inertia effects of the relaxing species. However, as this correction was not needed for the present work, it is not going to be elucidated further. For more details see [67].

1.3 Microscopic Relaxation Models

So far dielectric relaxation has been discussed on a macroscopic level and the formal description of the experimental data using the equations in the previous section only yields macroscopic parameters, such as amplitude, S_j, and relaxation time, τ_j. In order to establish the link between the macroscopic and the microscopic properties some suitable theoretical models will be presented in the following.

1.3.1 The Onsager Equation

The Onsager model [51, 68] is based on the concept of a single dipole being placed into a cavity, which itself is embedded in an infinite continuum characterized by its macroscopic properties. Assuming a spherical cavity and neglecting specific interactions as well as the anisotropy of the surrounding electric field yields the equation

$$\varepsilon_0(\varepsilon - 1)\vec{E} = \vec{E}_h \cdot \sum_j \frac{\rho_j}{1 - \alpha_j f_j} \left(\alpha_j + \frac{1}{3k_{\mathrm{B}}T} \cdot \frac{\mu_j^2}{1 - \alpha_j f_j} \right) \tag{1.42}$$

where ρ_j is the dipol density, α_j the polarizability, f_j the reaction field factor and μ_j the dipole moment of the species j.
For the case of spherical cavity, the cavity field $\vec{E}_h$ can be expressed as

$$\vec{E}_h = \frac{3\varepsilon}{2\varepsilon + 1}\vec{E} \tag{1.43}$$

with ε denoting the permittivity of the continuum dielectric.
Combining Eqs. 1.42 and 1.43 leads to the general form of the Onsager equation

$$\frac{\varepsilon_0(\varepsilon-1)(2\varepsilon+1)}{3\varepsilon} = \sum_j \frac{\rho_j}{1-\alpha_j f_j}\left(\alpha_j + \frac{1}{3k_\mathrm{B}T}\cdot\frac{\mu_j^2}{1-\alpha_j f_j}\right) \tag{1.44}$$

For a pure single-component dipole liquid with non-polarizable molecules, exhibiting just one dispersion step, this equation reduces to

$$\frac{(\varepsilon-\varepsilon_\infty)(2\varepsilon+\varepsilon_\infty)}{\varepsilon(\varepsilon_\infty+2)^2} = \frac{\rho\mu^2}{9\varepsilon_0 k_\mathrm{B}T} \tag{1.45}$$

Hence, the dipole moment of a species can be calculated from the above equation if the density, the static permittivity and ε_∞ are known. However, the Onsager equation is only valid for systems without dipole-dipole correlations, which generally does not necessarily hold for liquids.

1.3.2 The Kirkwood-Fröhlich Equation

To account for the shortcoming of the lack of specific particle interactions Kirkwood and Fröhlich [69, 70] introduced, with the help of statistical mechanics, the correlation factor g_K. The Kirkwood-Fröhlich equation reads

$$\frac{(\varepsilon-\varepsilon_\infty)(2\varepsilon+\varepsilon_\infty)}{\varepsilon(\varepsilon_\infty+2)^2} = \frac{\rho\mu^2}{9\varepsilon_0 k_b T}\cdot g_\mathrm{K} \tag{1.46}$$

The correlation factor describes the orientation correlation between the dipole and the neighbor molecules. Taking only nearest-neighbor interactions into account, the factor can be written as [51]

$$g_\mathrm{K} = 1 + z\,\langle\cos\theta_{ji}\rangle \tag{1.47}$$

where θ_{ji} denotes the angle between the orientation of the jth and ith dipole, and z gives the number of nearest neighbors. From Eq. 1.47 it becomes clear that for a preferentially parallel alignment the factor becomes $g_\mathrm{K} > 1$, whereas for antiparallel orientation $g_\mathrm{K} < 1$ will be found. For $g_\mathrm{K} = 1$ a fully random (statistical) alignment is present and the Kirkwood-Fröhlich equation 1.46 reduces to the Onsager equation 1.45.

1.3.3 The Cavell Equation

For the description of dielectric systems with more than one dispersion step a more general expression in the form of the Cavell equation is used [71, 72]:

$$\frac{\varepsilon + A_j(1-\varepsilon)}{\varepsilon} S_j = \frac{N_\mathrm{A}c_j}{3\varepsilon_0 k_\mathrm{B}T}\cdot\mu_{\mathrm{eff},j}^2 \tag{1.48}$$

The Cavell equation connects the dispersion amplitude, S_j, of the species j with the molar concentration, c_j, and the effective dipole moment, $\mu_{\mathrm{eff},j}$, of that species. A_j is the cavity field factor of the species j and has the value of $A_j = 1/3$ for spherical particles. For ellipsoidal cavities with half axes $x_j > y_j > z_j$ the cavity field factor can be calculated by [51, 73]

$$A_j = \frac{x_j y_j z_j}{2} \int_0^\infty \frac{ds}{(s + x_j)^{3/2}(s + y_j)^{1/2}(s + z_j)^{1/2}} \tag{1.49}$$

For relaxing water molecules the assumption of a spherical cavity field with $A_j = 1/3$ is reasonable, while for dipoles with a non-spherical shape A_j has to calculated from their geometry [72]. Thus, for prolate ellipsoids ($x_j > y_j = z_j$) Scholte [73] derived the elementary function,

$$A_j = \frac{-1}{p_j^2 - 1} + \frac{p_j}{\sqrt{p_j^2 - 1}^3} \ln(p_j + \sqrt{p_j^2 - 1}) \tag{1.50}$$

while for the oblate shape ($x_j < y_j = z_j$) the equation is given as

$$A_j = \frac{1}{1 - p_j^2} - \frac{p_j}{\sqrt{1 - p_j^2}^3} \cos^{-1} p_j \tag{1.51}$$

where p_j is the ratio x_j/y_j.
The effective dipole moment, $\mu_{\mathrm{eff},j}$, can be calculated through the Eq. 1.48 if c_j is known and it is related to the apparent dipole moment, $\mu_{\mathrm{ap},j}$, of the species

$$\mu_{\mathrm{eff},j} = \sqrt{g_j} \cdot \mu_{\mathrm{ap},j} \tag{1.52}$$

where g_j is an empirical factor being a measure for the orientational correlations, similar to the Kirkwood factor g_{K} (Eq. 1.46). The apparent dipole moment is connected to the gas phase dipole moment, μ_j, *via*

$$\mu_{\mathrm{ap},j} = \frac{\mu_j}{1 - f_j \alpha_j} \tag{1.53}$$

The factor $(1 - f_j\alpha_j)^{-1}$ accounts for reaction field effects, with α_j being the polarizability and f_j the reaction field factor of species j.
For a spherical cavity of radius r_j, the reaction field factor can be written as [51]

$$f_j = \frac{1}{4\pi\varepsilon_0 r_j^3} \cdot \frac{2\varepsilon - 2}{2\varepsilon + 2} \tag{1.54}$$

while for an ellipsoidal particle with the half axes $x_j > y_j > z_j$ the reaction field factor can be calculated by the general expression [73]

$$f_j = \frac{3}{4\pi\varepsilon_0 x_j y_j z_j} \cdot \frac{A_j(1 - A_j)(\varepsilon - 1)}{\varepsilon + (1 - \varepsilon)A_j} \tag{1.55}$$

1.3.4 Debye Model of Rotational Diffusion

In order to connect the relaxation time to molecular properties, Debye [59] considered a dielectric as a simple system consisting of non-interacting spherical, inelastic dipoles. The frequent and uncorrelated collisions of the particles in this system lead to a set of infinitesimally small changes in the orientation of the dipoles. In this mechanism of rotational diffusion of dipolar particles, however, some non-negligible approximations are applied: dipole-dipole interactions and inertia effects are neglected, the Lorentz field was assumed as the inner field, and the laws of hydrodynamics were assumed to be valid, which in fact describe macroscopic properties but are used on the microscopic level in this case. By making these assumptions, the dipolar correlation function, $C_1(t)$, can be written as

$$C_1(t) = \exp(-\frac{t}{\tau_{\mathrm{rot}}}) \tag{1.56}$$

The microscopic relaxation time τ_{rot} can be calculated from the rotational friction coefficient, ζ, by

$$\tau_{\mathrm{rot}} = \frac{\zeta}{2k_{\mathrm{B}}T} \tag{1.57}$$

Applying the laws of hydrodynamics to a rotating sphere in a viscous medium, the Stokes-Einstein-Debye equation is obtained:

$$\tau_{\mathrm{rot}} = \frac{3V_{\mathrm{m}}\eta'}{k_{\mathrm{B}}T} \tag{1.58}$$

where V_{m} represents the volume of the sphere and η' is the microscopic dynamic viscosity, *i.e.*, the viscosity in the vicinity of the relaxing dipole. However, the relation between the microscopic dynamic viscosity and the experimentally accessible macroscopic dynamic viscosity, η, is usually unknown. To create a link between the relaxation time and the macroscopic viscosity, Dote et al. [74] proposed a more general expression for the microscopic relaxation time:

$$\tau_{\mathrm{rot}} = \frac{3V_{\mathrm{eff}}\eta}{k_{\mathrm{B}}T} + \tau^0_{\mathrm{rot}} \tag{1.59}$$

The empirical axis intercept, τ^0_{rot} , is often interpreted as the correlation time of the freely rotating dipole. V_{eff} is related to the molecular volume, V_{m}, *via*

$$V_{\mathrm{eff}} = V_{\mathrm{m}} C f_\perp \tag{1.60}$$

where the shape factor, $f_\perp$, accounts for deviations from spherical shape and C represents the hydrodynamic friction factor, which connects the microscopic and macroscopic viscosity. The latter is an empirical parameter and has its limiting values of $C = 1$ for *stick* and $C = 1 - f_\perp^{-2/3}$ for *slip* boundary conditions of rotational friction. The shape parameter can be obtained from the geometry of the relaxing particle. For prolate spheroids the factor is given by [75]

$$f_\perp = \frac{\frac{2}{3}\left[1-(\alpha_\perp)^4\right]}{\frac{[2-(\alpha_\perp)^2](\alpha_\perp)^2}{[1-(\alpha_\perp)^2]^{1/2}} \ln\left[\frac{1+[1-(\alpha_\perp)^2]^{1/2}}{\alpha_\perp}\right] - (\alpha_\perp)^2} \tag{1.61}$$

with $\alpha_\perp$ representing the ratio between particle volume and the volume swept out by the particle during rotation about an axis perpendicular to the symmetry axis. For a prolate ellipsoid with a major axis x_j and the minor axis y_j this ratio is determined by $\alpha_\perp = y_j/x_j$. The corresponding $f_\perp$ value for oblate spheroids with the long axis x_j and short axis y_j can be calculated by [76]

$$f_\perp = \frac{\frac{2}{3}\left[1-(\beta_\perp)^4\right]}{\frac{[2-(\beta_\perp)^2](\beta_\perp)^2}{[1-(\beta_\perp)^2]^{1/2}}\arctan\left[\left({\beta_\perp}^2-1\right)^{1/2}\right]-(\beta_\perp)^2} \tag{1.62}$$

where $\beta_\perp = x_j/y_j$.

1.3.5 Relaxation by Discrete Jumps - The Case of Water

The continuous reorientation mechanism of rotational diffusion, presented in the previous section, can be successfully applied to systems consisting of large solute molecules dissolved in a solvent consisting of small, rigid molecules. However, in some systems the above relations do not hold anymore [51]. For this case, Kauzmann [77] introduced the concept of reorientation due to instantaneous jumps over finite angles. In the jump model, the system is regarded as a molecular crystal, where molecules are situated in different potential wells for finite time intervals and the reorientation is represented by the process of a molecule going from one potential well to another. The probability of the molecule to attain a certain orientation is given by the height of the potential energy barrier between the two states. For small angles the model of Kauzmann reduces to the Debye model of rotational diffusion [51].

One of the most prominent examples of jump-relaxation is the water relaxation. Although many studies on the nature of the water relaxation exist [50, 78–81], a consensus on the microscopic picture is still lacking. Arguably the most sophisticated molecular model on water reorientation and its dynamics is given by Laage *et al.* [82]. In this "wait-and-switch-type" model the reorientation of water molecules can be described as depicted in Figure 1.3. The first step involves an elongation of a H-bond in the local tetrahedrally ordered structure, and the approach of a new hydrogen bond acceptor, *e.g.* from the second shell (Figure 1.3(a)). As soon as the distance between the new acceptor and the initial partner is equal, the rotating water molecule performs a large-amplitude angular jump through the transition state in which a symmetric bifurcated H-bond is formed between the initial and final H-bond acceptor (Figure 1.3(b)). Subsequently, the surrounding water molecules have to adjust to the new situation by reorganization of the frame around the rotating molecule, reaching the energetically most favorable arrangement (Figure 1.3(c)). Both steps, large angular jump and the frame reorientation, can be combined in a so-called extended jump model (EJM) and, assuming both processes to be independent, the overall EJM reorientation time, τ^{EJM}, can be written as [82]

$$\frac{1}{\tau^{\mathrm{EJM}}} = \frac{1}{\tau^{\mathrm{jump}}} + \frac{1}{\tau^{\mathrm{frame}}} \tag{1.63}$$

The jump and the frame contribution occur both at the picosecond timescale at 298 K, with $\tau^{\text{jump}} < \tau^{\text{frame}}$. On this basis, Laage *et al.* were also able to analyze, at least qualitatively, the effects of various solutes (hydrophobic or hydrophilic) on the dynamics of water in their hydration shells.

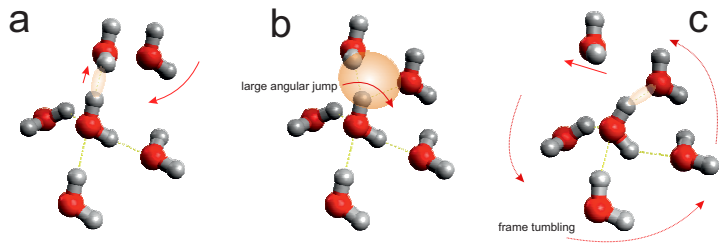

Figure 1.3: Schematic representation of the jump-reorientation mechanism of water.

At this point, it should be mentioned that the molecular correlation time, τ_{rot}, probed by dielectric spectroscopy is not necessarily the same as the reorientation correlation time probed by other techniques. For example, nuclear magnetic resonance (NMR), optical Kerr effect spectroscopy (OKE) or femtosecond infrared spectroscopy probe the second-rank order ($L = 2$) of the time-correlation function of the molecule reorientation, while DRS accesses correlations of rank $L = 1$. The correlation function of the dipole vector can be generally written as

$$C_L(t) = \langle P_L \left[\vec{\mu}(0) \cdot \vec{\mu}(t)\right] \rangle \tag{1.64}$$

where P_L is the Lth-rank Legendre polynomial. For rotational diffusion, the relation between the different rank molecular correlation times follows the relation

$$\tau_{\text{rot}}^{(L)} = \frac{\tau_{\text{rot}}}{L(L+1)} \tag{1.65}$$

with $\tau_{\text{rot}} = \tau_{\text{rot}}^{(1)}$, which is probed by DRS. However, the corresponding relation for the jump-relaxation mechanism involves the knowledge on the jump-angle distribution and the jump-probabilities. Thus, definite (simplified) mathematical relations can only be obtained for few limited cases [51], which will not be elucidated further in this work.

1.3.6 Microscopic and Microscopic Relaxation Time

Since the experimentally accessible dielectric relaxation time, τ, is a macroscopic property, it has to be converted into the corresponding microscopic rotational correlation time, τ_{rot}. Assuming that the underlying mechanism is due to rotational diffusion, Powles and Glarum

[83, 84] proposed that the macroscopic and microscopic correlation times are connected *via*

$$\tau = \frac{3\varepsilon}{2\varepsilon + \varepsilon_\infty} \cdot \tau_{\mathrm{rot}} \tag{1.66}$$

In the case of presence of several Debye relaxation processes, the generalized expression for the jth relaxation time is given by [83]

$$\tau_j = \frac{3\varepsilon_j}{2\varepsilon_j + \varepsilon_{\infty,j}} \cdot \tau_{\mathrm{rot},j} \tag{1.67}$$

where ε_j and $\varepsilon_{\infty,j}$ have the same definition as in Equation 1.28.
Taking into account dipole-dipole correlations, Madden and Kivelson [85] derived

$$\tau = \frac{3\varepsilon}{2\varepsilon + \varepsilon_\infty} \cdot \frac{g_{\mathrm{K}}}{\dot{g}} \cdot \tau_{\mathrm{rot}} \tag{1.68}$$

where g_{K} is the Kirkwood correlation factor and $\dot{g}$ is the dynamic correlation factor (dynamic coupling parameter). The latter is thought to be in the order of unity. Thus, for $g_{\mathrm{K}} = 1$ Equation 1.68 reduces to the Powles-Glarum equation 1.66.

1.4 Temperature Dependence of Relaxation Times

1.4.1 Arrhenius Equation

One of the oldest models for the description of rate constants of chemical reactions and transport properties is the Arrhenius Equation [86]. In the case of relaxation times it can be written as

$$\ln(\tau/\mathrm{s}) = \ln(\tau_0/\mathrm{s}) + \frac{E_{\mathrm{A}}}{RT} \tag{1.69}$$

The basis of this equation is the idea that the particles excited by thermal fluctuation can cross the temperature-independent energy barrier, E_{A}, to achieve the transition between two stable energetic states. The frequency factor, τ_0, is interpreted as the shortest relaxation time possible, since with increasing temperature τ reaches τ_0.

1.4.2 Eyring Equation

A comparable description of the temperature dependance is given by the Eyring equation [87], which is based on the the transition state theory. The relaxation time, τ, as a function of temperature can be expressed as

$$\ln(\tau/\mathrm{s}) = \ln\left(\frac{h}{k_{\mathrm{B}}T}\right) + \frac{\Delta G^{\neq}}{RT} \text{ with } \Delta G^{\neq} = \Delta H^{\neq} - T \cdot \Delta S^{\neq} \tag{1.70}$$

where $\Delta G^{\neq}$ is the Gibbs energy of activation, respectively $\Delta H^{\neq}$ and $\Delta S^{\neq}$ are the activation enthalpy and activation entropy.

For the analysis of relaxation times over a wide temperature range the temperature dependance of $\Delta H^{\neq}$ and $\Delta S^{\neq}$ cannot be neglected. According to thermodynamic laws, the Eyring Equation can be extended to

$$\ln(\tau/\mathrm{s}) = \ln\left(\frac{h}{k_\mathrm{B}T}\right) + \frac{1}{R}\left[\frac{\Delta H^{\neq}_{T^0}}{T} - \Delta S^{\neq}_{T^0} + \Delta C_p^{\neq}\left(1 + \ln\left(\frac{T^0}{T}\right) - \frac{T^0}{T}\right)\right] \tag{1.71}$$

where T^0 is the thermodynamic reference temperature (usually 298.15 K) and $\Delta C_p^{\neq}$ represents the heat capacity for the transition state, which is assumed to be constant.
However, for the limited temperature range of the present work ($5 \leq \vartheta/°C \leq 65$) the relaxation times could often (not always) be fitted assuming constant $\Delta H^{\neq}$ and $\Delta S^{\neq}$. In this case, the activation parameters can consequently be derived easily from the slope and the intercept of the linear plot $\ln(\tau T) = f(T^{-1})$.

Chapter 2

Experimental

2.1 Materials

Substances used in the framework of this thesis were purchased commercially in the highest affordable degree of purity. Table 2.1 provides details on the used chemicals. Chemicals were used as received, except for the following substances:

Acetylcholine chloride (AcChCl) was purchased from from Sigma Aldrich (purity $\geq 99\,\%$) and Alfa Aeser (purity $> 98\,\%$). Prior to use the salt was recrystallized three times from an ethanol (Sigma Aldrich, 99.9 %)/diethyl ether (VWR Chemicals, $\geq 99.7\,\%$) mixture and subsequently dried over Sicapent© for six days at room temperature at high vacuum ($p \leq 10^{-6}\,\mathrm{bar}$). The purity was checked by ^{1}H- and ^{13}C-NMR measurements (Avance III HD 400, 400 MHz, Bruker, Billerica, Massachusetts, USA). The water content determined by Karl Fischer titration (Metrohm 899 Coulometer) was $< 200\,\mathrm{ppm}$.

Monosodium glutamate (NaGlu) was purchased as a NaGlu·$X\,\mathrm{H_2O}$. The hydrate was recrystallized three times from an 2-propanol (Sigma Aldrich, $\geq 99.5\,\%$)/water (Millipore Milli-Q) mixture and the crystals were subsequently dried for four days over Sicapent© at 80 °C and at a reduced pressure of $p \leq 10^{-6}\,\mathrm{bar}$. The absence of unwanted impurities was ensured by ^{1}H- and ^{13}C-NMR measurements (Avance III HD 400, 400 MHz, Bruker, Billerica, Massachusetts, USA). The final content of crystal water, as determined by pH titration, was found to be $(6.8 \pm 0.2)\,\%$ and $(5.8 \pm 0.1)\,\%$, respectively, depending on the batch of recrystallized NaGlu. This non-negligible amount of water was accounted for during sample preparation.

Lithium chloride (LiCl) was dried for four days at pressures of $p \leq 10^{-9}\,\mathrm{bar}$ and at 150 °C prior to use. The water content, investigated by Karl Fischer titration, showed values of $< 880\,\mathrm{ppm}$.

Potassium fluoride (KF) was dried for four days at 120 °C under high vacuum ($p \leq$

Table 2.1: Overview of all chemicals, their purity and the supplier.

Neurotransmitters and chemically related substances

chemical	purity	supplier
Acetylcholine chloride (AcChCl)	$\geq 99\,\%$	Sigma Aldrich
	$> 98\,\%$	Alfa Aeser
Monosodium L-glutamate hydrate (NaGlu·$X\,H_2O$)	$\geq 99\,\%$	Sigma Aldrich
L-Glutamic Acid (HGlu)	$\geq 99.5\,\%$	Sigma Aldrich
Carbamylcholine chloride (CarCl)	$99\,\%$	Acros Chemicals
γ-Aminobutyric acid (GABA)	$\geq 99\,\%$	Sigma Aldrich
L-Glutamin (Gln)	$\geq 99.5\,\%$	Sigma Aldrich
DL-α-Aminobutryric acid (AABA)	$99\,\%$	Sigma Aldrich
n-Butylammonium chloride (BACl)	$99.5\,\%$	TCI

Inorganic salts

chemical	purity	supplier
Sodium chloride (NaCl)	$\geq 99\,\%$	Sigma Aldrich
Lithium chloride (LiCl)	$\geq 99.99\,\%$, Suprapur©	Merck
Potassium chloride (KCl)	$\geq 99.99\,\%$, Suprapur©	Merck
Potassium fluoride (KF)	$\geq 99.5\,\%$	Sigma Aldrich
Tetramethylammonium chloride (Me_4NCl, TMA)	$> 98\,\%$	Merck
Calcium chloride dihydrate ($CaCl_2{\cdot}2H_2O$)	$\geq 99\,\%$	Carl Roth
Magnesium chloride hexahydrate ($MgCl_2{\cdot}6H_2O$)	$\geq 99\,\%$	Merck

10^{-6} bar) over Sicapent© at 80 °C. Karl Fischer titration indicated a water content of < 440 ppm.

2.2 Sample Preparation and Handling

To avoid unnecessary water uptake the substances were stored in a dry-nitrogen-filled glove box with a dewpoint below −50 °C. All solutions were prepared gravimatrically on an analytical balance without the application of buoyancy corrections. The uncertainty of the prepared samples was better than ±0.001 g. Degassed Millipore Milli-Q water with an electrical resistivity of $\geq 18\,\mathrm{M\Omega cm}$ was used for the sample preparations. Prior to each measurement, the solutions were put into an ultrasonic bath for at least 15 minutes to further degas the samples and thus to suppress the problematic formation of gas bubbles during the experiment. Measurements at higher temperatures ($\vartheta \geq 45\,°\mathrm{C}$) were conducted under a saturated solvent atmosphere if possible. To avoid fast spoilage of the solutions of the biologically active substances the samples were stored in a refrigerator when not used for the measurements.

Table 2.2: Overview of the used equipment for DRS with the signal transmission line type, the frequency range and the corresponding wavelength of the electromagnetic wave in vacuum.

name	transmission line type	frequency range / GHz	wavelegth / m
TDR cells	coaxial line	0.01 - 1	30 - 0.3
Dielectric probe kit	coaxial line	0.05 - 50	6 - 0.006
A-Band	rectangular waveguide	27 - 40	0.011 - 0.007
E-Band	rectangular waveguide	60 - 89	0.005 - 0.003

2.3 Measurement of Dielectric Properties

To cover the microwave frequency region in DRS, which extends over several decades of the electromagnetic spectrum, different experimental setups have to be utilized. All instruments used in the present work are listed in Table 2.2. The lower frequency part of the dielectric spectra was acquired by a Vector Network Analyzer (VNA), which was used in combination with TDR-cells and the dielectric probe kit to cover the frequency range $0.01 \leq \nu/\mathrm{GHz} \leq 50$. Furthermore, a waveguide-transmission cell of the A-band apparatus connected to the VNA was used to perform transmission experiments in the frequency domain $27 \leq \nu/\mathrm{GHz} \leq 40$. The high-frequency wing ($60 \leq \nu/\mathrm{GHz} \leq 89$) was covered by the E-band apparatus, which operates on the principle of frequency-domain interferometry. Note that transmission cell types (A-Band, E-Band) do not require any kind of calibration, while for frequency-domain reflectometry setups (TDR cells and dielectric probe kit) calibrations with appropriate standards are necessary prior to measurement. In the following, all methods used for the dielectric-data acquisition will be presented.

2.3.1 Interferomentry

For frequencies $> 50\,\mathrm{GHz}$ collecting dielectric data with waveguides becomes more efficient as the coaxial line setups, discussed in Section 2.3.2, depend strongly on the restrictions determined by geometry of the coaxial cells. Thus, waveguide interferometers (IFM) based on traveling waves are employed at these frequencies. However, the receiver of the IFM setup is only capable of detecting the signal amplitude without any phase information. Hence, interferometry has to be used to retrieve this information and to determine the complex permittivity.

Instrumentation

A block diagram of the E-band ($60 \leq \nu/\mathrm{GHz} \leq 89$) instrument used in the Regensburg laboratories [88] is shown in Figure 2.1. The interferometer is based on a transmission

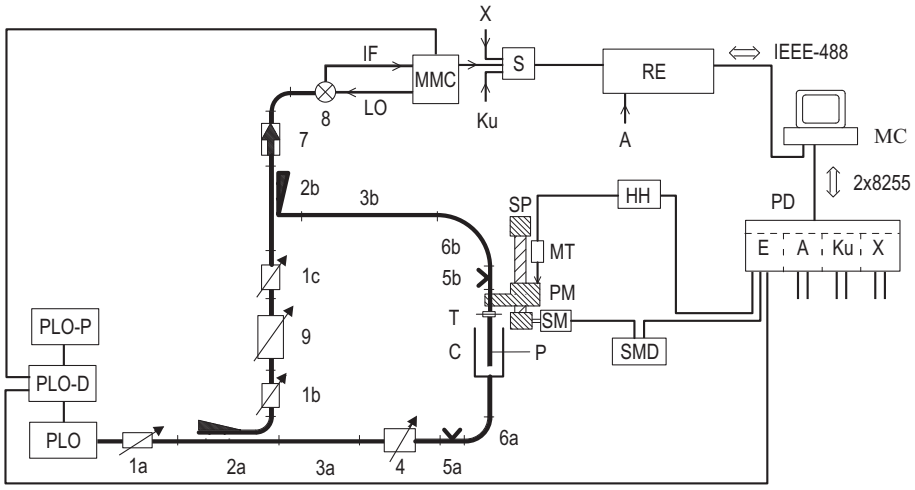

Figure 2.1: Block diagram of the E-band apparatus [88]: **1a, b, c:** variable attenuators; **2a, b:** directional couplers; **3a, b:** waveguide sections; **4:** precision phase shifter; **5a, b:** E/H tuners; **6a, b:** flexible waveguides; **7:** insulator; **8:** harmonic mixer; **9:** variable precision attenuator; **C:** cell, **HH:** bidirectional counter; **MC:** microcomputer; **MMC:** millimeter-wave to microwave converter; **MT:** digital length gauge; **P:** probe; **PLO:** phase locked oscillators; **PLO-D:** PLO-control unit; **PLO-P:** PLO-power supply; **PM:** probe mount; **RE:** precision receiver; **SM:** stepping motor; **SMD:** stepping motor control unit; **SP:** spindle and spindle mount; **T:** tapered transmission, double lines represent waveguides, while thick lines symbolize semi-rigid microwave cables and normal lines denote data transfer connections (analog or digital).

principle: a traveling wave with a certain frequency (60 GHz, 66 GHz, 72 GHz or 89 GHz), generated by phase-locked Gunn oscillators **PLO**, is split into a measuring path and a reference path by a directional coupler **2a**. The measuring path contains a phase shifter **4**, two sets of E/H-Tuners **5a, b** and the measuring cell **C**. The cell consists of a piece of waveguide filled with the sample, in which a gold plated ceramic probe **P** is immersed whose position in the z-direction is adjustable by a stepping motor **SM** and which can be determined by a precision gauge **MT**. A mica window separates the measuring cell from the preceding waveguide. A polyethylene tube can be mounted around **P** and **C** to perform measurements under a nitrogen or solvent saturated atmosphere if needed. The temperature of the sample in the cell is measured with a Pt-100 temperature sensor and it is controlled by a circulating thermostat (Lauda RK 20) with a precision $\pm 0.02\,^{\circ}\mathrm{C}$. Eventually, the measuring signal is recombined with the reference path, which comprises a precision attenuator **9**, at **2b** after passing the sample. The relative amplitude, A, of the recombined beams is measured as a function of optical path length, z_0, after mixing for frequency conversion.

Besides the E-Band equipment, waveguide transmission cells for X-Band ($8.5 \leq \nu/\mathrm{GHz} \leq 12$), Ku-band ($12.5 \leq \nu/\mathrm{GHz} \leq 18$) and A-band ($27 \leq \nu/\mathrm{GHz} \leq 40$) are available at the

Regensburg laboratories. However, the interferometric measurement described above is only required for the E-band region. For the remaining bands phase-sensitive transmission measurements can be performed with a vector network analyzer (Section 2.3.2).

Theory and Measurement Principle

For each individual frequency, several steps are required to obtain the attenuation coefficient and the medium wavelength of sample, which are prerequisite for the determination of $\hat{\eta}(\nu)$. The time-dependent electric field in the reference beam can be described by equation 1.8 for harmonically oscillating fields and thus reads:

$$\hat{E}_1(t) = E_0 \exp(\mathrm{i}\omega t). \tag{2.1}$$

Defining x as the relative distance from the interference minimum, z_0', as $x = z_0 - z_0'$, with z_0 being the absolute optical path length of the transmission cell, the electrical component of the electromagnetic field in the measuring beam can be written as

$$\hat{E}_2(t, x) = E_0 \exp(-\alpha x) \exp(\mathrm{i}(\omega t + \Delta\phi - \beta x)) \tag{2.2}$$

where α is the absorption coefficient of the sample and β is the phase constant. The phase constant is related to the medium wavelength, λ_M, through

$$\beta = \frac{2\pi}{\lambda_\mathrm{M}} \tag{2.3}$$

The damping coefficient and the phase constant can be combined in the form of the complex propagation constant, $\hat{\gamma}$, *via*

$$\hat{\gamma} = \alpha + \mathrm{i}\beta \tag{2.4}$$

The term $\Delta\phi$ in Eq. 2.2 accounts for the condition of destructive interference of the two waves and has to satisfy the equation

$$\Delta\phi = (2n + 1)\pi \text{ with } n \in \mathbb{Z} \tag{2.5}$$

At the receiver, the superposed signal of the measuring and the reference beam (assuming $\Delta\phi = \pi$) is detected:

$$\hat{E}(t, x) = \hat{E}_1(t) + \hat{E}_2(t, x) = E_0 \exp(\mathrm{i}\omega t)[1 + \exp(-\alpha x) \exp(\mathrm{i}(\pi - \beta x))] \tag{2.6}$$

The experimentally accessible quantity is the magnitude of the detected signal, P, and it is defined by the squared amplitude of the electric field,

$$P = \hat{E} \cdot \hat{E}^* = E_0^2 \cdot I(x) \tag{2.7}$$

where $I(x)$ represents the interference function,

$$\begin{aligned} I(x) &= [1 + \exp(-\alpha x) \exp(\mathrm{i}(\pi - \beta x))] \cdot [1 + \exp(-\alpha x) \exp(\mathrm{i}(\pi - \beta x))] \\ &= 1 + \exp(-2\alpha x) + \exp(-\alpha x) \cdot 2\cos(-\pi + \beta x) \end{aligned} \tag{2.8}$$

The magnitude of the signal, P, is not measured directly but it is expressed through the relative attenuation of the signal, $A(x)$, on a logarithmic scale, which is defined as

$$A(x) = 10 \lg \frac{P(x)}{P_{\text{ref}}} \tag{2.9}$$

Since P_{ref} is unknown, the measured attenuation is normalized to A_0 which is resulting from the signal $P_0 = E_0^2$,

$$\begin{aligned} A_{\text{rel}} &= A(x) - A_0 \\ &= 10 \lg \frac{P(x)}{P_{\text{ref}}} - 10 \lg \frac{P_0}{P_{\text{ref}}} \\ &= 10 \lg \frac{P(x)}{P_0} \\ &= 10 \lg \frac{E_0^2 \cdot I(x)}{E_0^2} \\ &= 10 \lg I(x) \end{aligned} \tag{2.10}$$

Inserting equation 2.8 and introducing the conversion constant $p = \left(20 \lg e \cdot \frac{\text{dB}}{\text{Np}}\right)^{-1}$ yields the following equation [88]:

$$\begin{aligned} A(x) = A_0 &+ 10 \lg \left[1 + \exp\left(-2p\alpha_{\text{dB}}x\right)\right] \\ &+ 10 \lg \left[-2 \cos\left(\frac{2\pi}{\lambda_{\text{M}}}x\right) \cdot \exp\left(-p\alpha_{\text{dB}}x\right)\right] \end{aligned} \tag{2.11}$$

At the beginning of the measurement the reference path is completely closed and the probe is descended as far as possible (z_0=0). The amplitude can be adjusted to its maximum, A_{max}, by the use of E/H-tuners. Next, the probe is moved until the amplitude shows the value of $A \approx 1/2 \cdot (A_{\text{max}} + 10)$ (in dB). At this position z_0', the instrument is aligned fully to destructive interference using the phase shifter and the attenuator. After moving the probe to its starting position, the measurement is started. The relative amplitude is registered as a function of the probe position at equally spaced distances while the probe is elevated until the total path length of $2 \cdot z_0'$.
Using a nonlinear fit by means of a least squares fitting procedure the interference data $A(x)$ can be fitted. The fitting was carried out with the mathematical package TableCurve 2D V5.1 [89]. The values of the power attenuation coefficient, $\alpha_{\text{dB}} = \alpha/p$, (in dB/m) and the medium wavelength, $\lambda_{\text{M}} = 2\pi/\beta$, can be determined simultaneously for each frequency. Finally, the complex permittivity can be calculated using the obtained $\alpha(\nu)$, $\lambda_{\text{M}}(\nu)$ and the conductivity, κ, of the sample:

$$\varepsilon'(\nu) = \left[\left(\frac{1}{\lambda_{\text{c,10}}^{\text{vac}}}\right)^2 + \left(\frac{1}{\lambda_{\text{M}}(\nu)}\right)^2 - \left(\frac{\alpha(\nu)}{2\pi}\right)^2\right] \cdot \left(\frac{c_0}{\nu}\right)^2 \tag{2.12}$$

$$\varepsilon''(\nu) = \frac{\alpha(\nu)}{\pi\lambda_{\mathrm{M}}(\nu)} \cdot \left(\frac{c_0}{\nu}\right)^2 - \frac{\kappa}{2\pi\nu\varepsilon_0} \tag{2.13}$$

The equations 2.12 and 2.13 can be obtained by solving the wave equation for a rectangular waveguide of a certain geometry [90]. The cut-off wavelength, $\lambda_{\mathrm{c},mn}$, denotes the highest wavelength (lowest frequency) able to pass the waveguide with the corresponding propagation mode. The fundamental mode, TE_{10}, ($m = 1$ and $n = 0$) is used for the measurement as it is the only field type which exists in a frequency range where no other mode is able to propagate, as higher order modes damp out very quickly. For a rectangular waveguide with $a = 2b$, where a is the width and b is the height, the technically useful range is restricted to

$$0.53 \leq \frac{\lambda}{\lambda_{\mathrm{c},10}} \leq 0.8 \tag{2.14}$$

The cut-off wavelength for an empty waveguide with the same geometry yields $\lambda_{\mathrm{c},10}^{\mathrm{vac}} = 2a$ [58]. The maximum error in ε'' is approximately 2 % with respect to the static permittivity, ε, of the sample [91].

2.3.2 Vector Network Analysis

In recent years vector network analyzers have markedly gained in importance considering the conduction of precise and fast dielectric relaxation spectroscopy experiments. A great variety of network analyzers operating in the kHz to GHz regime are commercially available [92]. Measuring both the amplitude and the phase of electromagnetic signals simultaneously, information on the reflection and the transmission of an electrical network is obtained and therefore the scattering parameter matrix, $\hat{S}$, can be determined. For a two-port network, $\hat{S}$ is defined as

$$\begin{pmatrix} \hat{b}_1 \\ \hat{b}_2 \end{pmatrix} = \begin{pmatrix} \hat{S}_{11} & \hat{S}_{12} \\ \hat{S}_{21} & \hat{S}_{22} \end{pmatrix} \begin{pmatrix} \hat{a}_1 \\ \hat{a}_2 \end{pmatrix} \tag{2.15}$$

where $\hat{a}_j$ and $\hat{b}_j$ denote the power of incident and reflected waves at port j [93]. For one-port measurements only the scattering parameter $\hat{S}_{jj}$ is needed. This parameter is equivalent to the relative complex reflection coefficient, $\hat{\Gamma}$. However, the reflection coefficient measured by the VNA, $\hat{\Gamma}_m$, differs from the actual reflection coefficient, $\hat{\Gamma}_a$. Thus, the systematic deviations - errors in directivity, e_{d}, frequency response, e_{r}, and source match, e_{s}, - have to be corrected by measuring three known reference standards. The obtained actual reflection coefficient at the coaxial probe aperture yields [94]

$$\hat{\Gamma}_{\mathrm{a}} = \frac{\hat{\Gamma}_{\mathrm{m}} - e_{\mathrm{d}}}{e_{\mathrm{s}}(\hat{\Gamma}_{\mathrm{m}} - e_{\mathrm{d}}) + e_{\mathrm{r}}} \tag{2.16}$$

The reflection coefficient $\hat{\Gamma}_{\mathrm{a}}$ can be linked to the normalized aperture admittance, $\hat{Y}$, by

$$\hat{\Gamma}_a = \frac{1 - \hat{Y}}{1 + \hat{Y}} \tag{2.17}$$

Open-ended Coaxial Probe

Dielectric spectra were recorded in the frequency range $0.05 \leq \nu/\mathrm{GHz} \leq 50$ with an Agilent E8364B VNA in combination with a dielectric probe kit (85070E). Additionally, a electronic calibration module (ECal, Agilent N4693) was available for correction of parasitic effects, which comprise *e.g.* phase errors due to the thermal expansion of the instrumentation. The ECal module measures well known reflection standards during the experiment and uses this data for the calculation of error terms, thus stabilizing the calibration [95]. However, it was found that for samples of low conductivity the accuracy does not improve noticeably. Hence, the ECal module was only used for a limited set of (conductive) samples in the framework of this thesis, as experience shows that the calibration of the VNA is more tedious in the presence of the ECal module. The probe kit consists of two different probes providing reliable dielectric data in distinct frequency ranges, namely the high temperature probe (85070E-20) in the region $0.05 \leq \nu/\mathrm{GHz} \leq 20$ and the performance probe (85070E-50) with the frequency range of $1 \leq \nu/\mathrm{GHz} \leq 50$. The probes are mounted on the bottom of temperature controlled cells. The temperature is adjusted by a Huber CC505 thermostat and measured with an Agilent 34970A datalogger, using a platinum resistance thermometer (Pt-100). The accuracy of the thermostat is $\pm 0.02\,^{\circ}\mathrm{C}$. The sample is poured into the cell to establish the contact with the open-ended coaxial probe. The upper opening of the cell can be sealed to avoid contact with the atmosphere and to contain evaporation of the sample at higher temperatures. Figure 2.2 shows a schematic representation of the oped-ended coaxial probe setup. The coaxial cables must not be rearranged during the calibration and the measurements, as any kind on mechanical stress may lead to the appearance of significant errors in the measured reflection coefficient.
The complex dielectric parameter of the sample, $\hat{\eta}_\mathrm{m}$, is calculated from the normalized aperture admittance, $\hat{Y}$, by using a simplified coaxial aperture opening model and solving the following equation numerically [94, 96]:

$$\hat{Y} = \frac{\mathrm{i}\hat{k}_\mathrm{m}^2}{\pi \hat{k}_\mathrm{c} \ln\left(D/d\right)} \left[\mathrm{i} \left(I_1 - \frac{\hat{k}_\mathrm{m}^2 I_3}{2} + \frac{\hat{k}_\mathrm{m}^4 I_5}{24} - \frac{\hat{k}_\mathrm{m}^6 I_7}{720} + \ldots \right) + \left(I_2 \hat{k}_\mathrm{m} - \frac{\hat{k}_\mathrm{m}^3 I_4}{6} + \frac{\hat{k}_\mathrm{m}^5 I_6}{24} - \ldots \right) \right] \tag{2.18}$$

In Eq. 2.18, $\hat{k}_\mathrm{c} = \omega\sqrt{\hat{\eta}_\mathrm{c}\varepsilon_0\mu_0}$ and $\hat{k}_\mathrm{m} = \omega\sqrt{\hat{\eta}_\mathrm{m}\varepsilon_0\mu_0}$ denote the propagation constants within the coaxial probe head and the sample, respectively. D and d represent the outer and inner conductor radii of the coaxial line. The determination of the normalized aperture admittance used in the Agilent 85070C software package comprises the numerical calculation of the first 28 probe constants, I_n, and a further empirical optimization of the obtained constants as described in Ref. [94].
The calibration was performed according to Eq. 2.16 using three known dielectric substances: air (open), purified mercury (short) and a third reference liquid with similar dielectric properties as the investigated dielectric (load). For all measurements of the

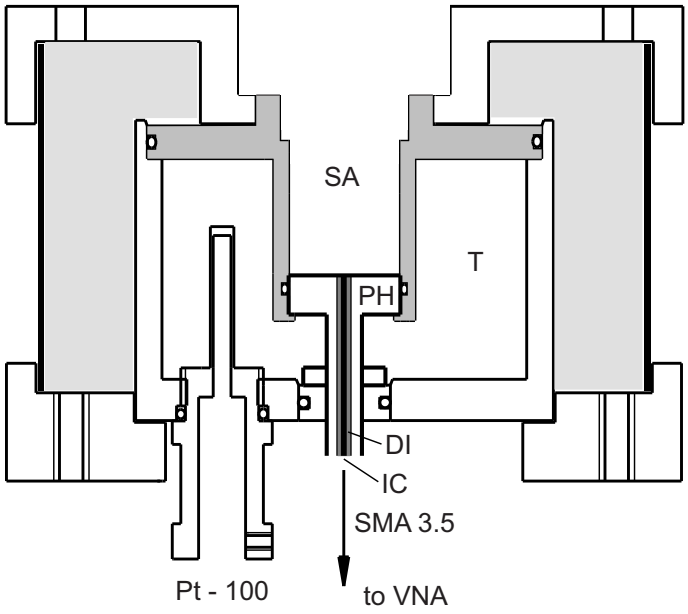

Figure 2.2: Scheme of the VNA open-ended coaxial probe cells. **PH**: coaxial probe head; **SA**: sample space; **T**: thermal casing; **IC**: inner conductor of the probe head; **DI**: dielectric material.

aqueous solutions in this work water, whose dielectric properties are well known [97], was chosen as an appropriate calibration standard at all investigated temperatures.

For each spectrum the average value of at least two measurements of independent calibrations was used.

Cut-off Type Coaxial Cells - TDR Cells

The low-frequency limit specified by the manufacturer of the open-ended coaxial 85070E-20 probe is 0.2 GHz. However, it was found that for low-conductivity samples of sufficient permittivity this limit could be extended down to ∼0.05 GHz by careful calibration [98, 99]. The validity of the data obtained at 0.2 GHz could be tested by crosschecking with known standards. In order to extend the investigation to even lower frequency values cut-off type coaxial cells were used. The cut-off type coaxial cells, or TDR cells, were previously developed for a time-domain reflectometry setup [100, 101]. Connecting them to the VNA allows the measurement of the reflection coefficient in the ν-domain and yields the complex permittivity data in the frequency region $0.01 \leq \nu/\mathrm{GHz} \leq 1$. The low-frequency limit of the TDR cells is determined by low-frequency limit of 10 MHz of the VNA. The geometry of these cells differs from the open-ended coaxial probes and thus it requires a different

mathematical expression for the normalized aperture admittance [102]:

$$\hat{Y} = g\sqrt{\hat{\eta}(\omega)}\tanh\left(\frac{\mathrm{i}\omega l}{c}\cdot\sqrt{\hat{\eta}(\omega)}\right) + \mathrm{i}\omega\hat{\eta}(\omega)Z_{\mathrm{L}}C_{\mathrm{s}} \tag{2.19}$$

where Z_{L} is the wave resistance of the feeding line (typically 50 Ω) and C_{s} is the discontinuity capacity of the coaxial to circular waveguide transition [102]. D and d denote the radii of the outer and inner conductor, and l is the electrical pin-length of the inner conductor inside the cell. The factor g represents the ratio between the feeding line impedance, Z_{L}, and the impedance of the empty cell, $Z_0 = \frac{1}{2\pi}\sqrt{\frac{\mu_0}{\varepsilon_0}}\cdot\ln(\frac{D}{d})$ [100]. The eqs. 2.17 and 2.19 can be solved numerically and consequently the generalized complex permittivity, $\hat{\eta}(\omega)$, is obtained.
The TS3 cut-off type cell ($l = 6.05\,\mathrm{mm}$; $g = 0.4282$) [101] was found to give the most accurate results for aqueous systems studied in this work. The discontinuity capacity, estimated from cell geometry and literature values [102, 103], was set to $C_{\mathrm{s}} = 40\,\mathrm{fF}$. After an one-port calibration of the VNA at the cable-cell connector interface in the frequency region of interest using the ECal module, as implemented in the Agilent software, a three-point calibration with respect to the sample - coaxial line interface - using open, short and load - is performed in order to correct for the three errors in directivity, frequency response and source match (equation 2.16). For open calibration an empty cell (air) was used. For short NaCl(aq)($b \approx 5$ mol kg^{-1}) was measured. The dielectric parameters of the NaCl solution were previously determined from the measurements with open-ended coaxial probes (Section 2.3.3). Nevertheless, it was shown by Hunger [103] that the dielectric parameters are not crucial as long as the conductivity, which is the major contribution to $\hat{\eta}(\omega)$ in this frequency range, is high enough and accurately known. For load water was chosen as its properties are similar to the properties of the investigated samples. The temperature was measured by a Pt-100 resistance connected to a high precision thermometer (ASL F250) and was adjusted with a Julabo FP 45 thermostat with an accuracy of ±0.05 °C. For the numerical calculation of $\hat{\eta}(\omega)$ software based on Maple 2016 [104] was used.
Figure 2.3 shows an exemplary spectrum of an aqueous γ-aminobutyric acid (GABA) solution (c(GABA) = 0.3891 mol L^{-1}) at 25 °C in the frequency range 0.01 – 89 GHz and the coverage of the frequency range by the different methods.

Padé-Calibration

Increasing deviations of dielectric properties of the sample from the calibration liquid (load) lead to increasing inaccuracies of the obtained spectra. In this case, an additional correction of the conductivity-corrected raw spectra, $\hat{\varepsilon}_{\mathrm{raw}}(\nu)$, can be performed (Section 2.3.3). This secondary calibration procedure accounts for imperfections of the model for aperture admittance. Application of a complex Padé approximation [105] yields the corrected spectra, $\hat{\varepsilon}_{\mathrm{corr}}(\nu)$, from the raw data, $\hat{\varepsilon}_{\mathrm{raw}}(\nu)$, *via*

$$\hat{\varepsilon}_{\mathrm{corr}}(\nu) = P_{n/m}\left[\hat{\varepsilon}_{\mathrm{raw}}(\nu)\right] = \frac{\hat{A}_0(\nu) + \hat{A}_1(\nu)\hat{\varepsilon}_{\mathrm{raw}}(\nu) + \ldots + \hat{A}_n(\nu)\left[\hat{\varepsilon}_{\mathrm{raw}}(\nu)\right]^n}{1 + \hat{B}_1(\nu)\hat{\varepsilon}_{\mathrm{raw}}(\nu) + \ldots + \hat{B}_m(\nu)\left[\hat{\varepsilon}_{\mathrm{raw}}(\nu)\right]^m} \tag{2.20}$$

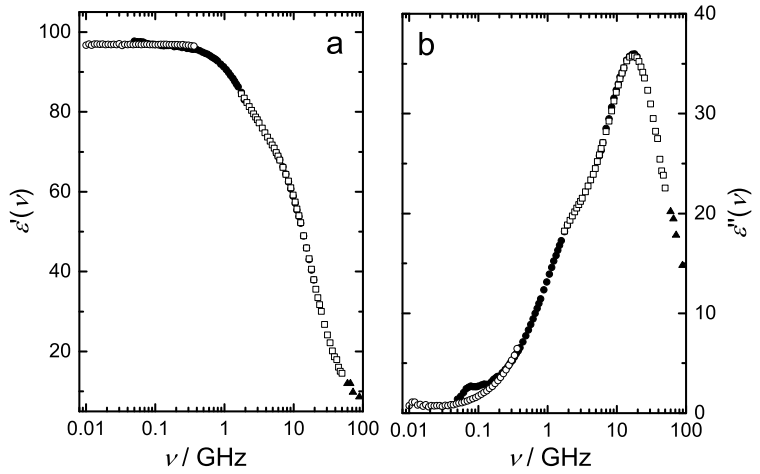

Figure 2.3: (a) Dielectric permittivity and (b) dielectric loss spectrum of 0.3891 mol L^{-1} GABA in water. Open circles (○) indicate the data obtained by TS3 cut-off type cell. The dielectric spectra determined by the high temperature probe and the performance probe are denoted by filled circles (●) and open squares (□), respectively. The E-band interferometer data is shown by filled triagles (▲).

In equation 2.20, the complex approximation constants, $\hat{A}_n(\nu)$ and $\hat{B}_m(\nu)$, can be obtained either analytically or by a complex linear fit algorithm [101] from a set of secondary standards with known dielectric properties. Water [97], propylene carbonate (PC; Sigma Aldrich, 99.7 %) [106, 107], diemethylacetamid (DMA; Sigma Aldrich, $\geq$ 99.9 %)[106, 108] and formamide (FA; Sigma Aldrich, $\geq$ 99.5 %)[108] were found to be most suitable calibration standards, covering a large range of dielectric permittivities. A calibration up to $n = 1$ and $m = 1$ was sufficient for the systems investigated in the framework of this thesis. The whole data processing procedure was implemented in a combination of MATLAB [109] and MAPLE [104] scripts.

Waveguide Transmission Cells

Since the VNA enables simultaneous measurements of the phase and amplitude of the signals up 50 GHz, the connection of Ku-band ($8 \leq \nu/\mathrm{GHz} \leq 12$), X-band ($12 \leq \nu/\mathrm{GHz} \leq 18$), and A-band ($27 \leq \nu/\mathrm{GHz} \leq 40$) waveguide transmission cells, which were previously used for interferometry experiments (Section 2.3.1), to Agilent E8364B vector network analyzer allows a direct measurement of the complex scattering parameter, $\hat{S}_{21}(z)$, as a function of the relative optical path length, z, at all relevant frequencies [103]. In this transmission setup the medium wavelength, λ_m, and the absorption coefficient, α, can be determined from $\hat{S}_{21}(z)$ at each frequency and the complex permittivity spectra can thus be obtained from eqs. 2.12 and 2.13. A personal computer was used to control the stepper motor, VNA and the precision gauge for the determination of the z position of the

waveguide probe, thus allowing fast automated measurements. A Huber CC505 thermostat controlled the temperature of the A-band cells with an accuracy of ±0.02 °C. The temperature was recorded with an Agilent 34970A datalogger and measured by a platinum resistance thermometer (Pt-100). For the Ku- and X-band a Julabo FP 50 thermostat with a temperature control ability of ±0.05 °C was used.
As already pointed out above, the big advantage of waveguide transmission cells is their ability to provide accurate permittivity data without the need for calibration. Thus, A-band measurements were used to crosscheck the validity of the data obtained by the performance probe. The permittivity data determined by the 50 GHz probe head were replaced by the A-band data in the case of strong deviations. Since the sample volumes required for the Ku- and X-band measurements are comparably large, it was refrained from using these cells in the present work.

2.3.3 Processing of Experimental Data

To retrieve information on the physical properties of the investigated samples from their permittivity spectra, suitable superpositions of empirical relaxation functions (Section 1.2) have to be found. As a starting approximation, the frequency-dependent complex permittivity data is corrected for the experimental conductivity, κ, to obtain $\hat{\varepsilon}(\nu)$ (eqs. 1.19 and 1.20). Subsequently, the conductivity is treated as an additional fit parameter, κ_{fit}, and it is thus slightly adjusted to improve the fit quality (Eq. 2.21). The main difference between the experimental and adjusted conductivity values traces back to fringing the field effects, caused by the geometry of the VNA probe heads [110] and the relative deviation of κ_{fit} from κ normally does not exceed ∼10 %. The fitting of the spectra is performed with a fitting procedure [111] integrated into the Igor software package [112]. A nonlinear least squares fit based on the Levenberg-Marquardt algorithm is used [113].

Finding the appropriate models to describe the so obtained complex permittivity spectra is not straightforward as many different combinations of the broad relaxation modes are possible, and a good formal description of the spectra does not necessarily mean that the obtained fitting parameters are physically reasonable. However, there are some criteria which help to find the appropriate fit model:

⇒ The quality of the fit is represented by the reduced error function, χ_r^2, which should be minimized in order to obtain the best fit. The error function reads

$$\chi_r^2 = \frac{1}{2m-n} \sum_{i=1}^{m} \left[\left(\varepsilon'(\nu_i) - \varepsilon'(\nu_i)_{\text{cal}}\right)^2 + \left(\varepsilon''(\nu_i) - \varepsilon''(\nu_i)_{\text{cal}}\right)^2 \right] \tag{2.21}$$

where m denotes the number of data triples $(\nu_i, \varepsilon'(\nu_i), \varepsilon''(\nu_i))$ and n is the number of adjustable parameters.

⇒ The fitting parameter should be physically reasonable, *i.e.*, no negative relaxation times

or amplitudes.

⇒ The number of relaxation modes should be reasonably small.

⇒ The fitting model should not change with changing concentration or temperature, except for specific physical reasons.

Besides, care should be taken about the data point density in the obtained spectra. The density should be comparable over the whole frequency range.

Zasetsky's Computational Analysis

To get an objective view on the possible relaxation processes a procedure introduced by Zasetsky and Buchner [114] was used in order to analyze the dielectric permittivity spectra. This method is based on a quasi-linear least squares minimization procedure with constraints for least squares fitting of experimental spectra in the frequency domain. The solution of this mathematical problem retrieves the probability, $P(\tau)$, of finding a Debye-type mode (Eq. 1.34) at the relaxation time τ. Thus, not only the possible number of relaxation modes, but also their relative strength, *i.e.*, relative amplitudes, can be obtained. Empirical band shapes, *e.g.* Cole-Cole modes (Eq. 1.39) or Cole-Davidson modes (Eq. 1.40), are described by small sets of Debye modes, which are symmetrically or asymmetrically distributed around a main mode. However, this fitting routine does not guarantee any physical meaning behind the resolved relaxation processes. Nevertheless, since this procedure does not require any knowledge on the relaxation mechanism of the investigated spectra, this bias-free approach provides hints on the existing processes which may facilitate the analysis of the spectra.

2.4 Supplementary Measurements

2.4.1 Density

Density measurements were performed using a vibrating tube densimeter (DMA 5000 M, Anton Paar, Graz, Austria). An U-shaped tube made of borosilicate glass is filled with the sample and excited to vibrate at its characteristic frequency. This frequency is related to the density of the sample. A precise determination of the eigenfrequency yields the density, ρ, by

$$\rho = K_A \cdot Q^2 \cdot f_1 - K_B \cdot f_2 \tag{2.22}$$

where K_A and K_B are apparatus constants, Q is the quotient of the period of the oscillating tube and the reference oscillator, and f_1 and f_2 are correction terms for temperature, viscosity and nonlinearity. According to the manual the instrument has an accuracy of $\pm 5 \cdot 10^{-6}\,\mathrm{g{\cdot}cm^{-3}}$. The temperature is controlled by Peltier-elements within $\pm 0.001\,^{\circ}\mathrm{C}$ and

measured by an integrated Pt-100 resistance thermometer. The temperature range of $0 \leq \vartheta/°C \leq 90$ is accessible.

2.4.2 Viscosity

For the determination of dynamic viscosity, η, an Automated Microviscometer (AMVn, Anton Paar, Graz, Austria) was used. The measuring principle is based on the determination of the rolling time of a steel ball in a glass capillary which is mounted in the heating block of the instrument. The angle of the block can be adjusted as desired and the rolling time, t, at a given angle is used to calculate the viscosity, η, through the equation

$$\eta = K \cdot (\rho_B - \rho) \cdot t \tag{2.23}$$

K is a calibration constant determined before the measurement through calibration (using the same equation), ρ_B is the density of the steel ball and ρ is the density of the investigated solution. The calibration was carried out manually with a suitable calibration liquid of known viscosity and density. For all measurements inclination angles of 30 ° and 70 ° were used. The uncertainty of the so gained data is $\leq 2\,\%$. However, especially for temperature dependent measurements of one sample up to three calibrations with different liquids and differently sized capillaries could be necessary as the viscosity changes drastically with temperature. In this case the choice of which liquid and which capillary to use at which temperature is crucial and not straightforward, and the uncertainty limit of 2% may be exceeded.
The temperature in the heating block is measured by Pt-100 resistance sensors and the measurements can be conducted in the temperature region $5 \leq \vartheta/°C \leq 100$.

2.4.3 Electrical Conductivity

The electrical conductivity, κ, was determined by a frequency-dependent measurement of the resistance using two-electrode capillary cells. After filling, the cells (calibrated with KCl(aq) [115]; cell constants C = 7 - 98 cm^{-1}) are introduced into a home-built precision thermostat with a temperature stability of $< 0.003\,°C$. An open/short calibration of the switchboard and the HAMEG Programmable LCR bridge HM 8118 is necessary prior to connecting the cells. The measurement is started and controlled using a program written in the programming language LabVIEW. The temperature is measured by a Pt-100 sensor, which is connected to a ASL F250 high precision thermometer and adjusted by Huber Unistat 705 thermostat with a temperature stability of $\pm 0.005\,°C$. The accessible temperature range of the instrumentation is $-35 \leq \vartheta/°C \leq 65$.
The resistance of the samples in a given cell, $R(\nu)$, is determined at a frequency range $0.2 \leq \nu/kHz \leq 10$ in order to avoid polarization effects at the surface of the electrodes. Eventually, the exact resistance, R_∞, is obtained by extrapolation of the frequency-dependent resistance, $R(\nu)$, using the empirical equation

$$R(\nu) = R_\infty + \frac{B}{\nu^a}. \tag{2.24}$$

where B and a are fitting parameters with $0.5 \leq a \leq 1$, whereas B is cell-specific [116]. The conductivity is finally obtained *via* $\kappa = C/R_\infty$ with an estimated overall uncertainty of $\leq 0.5\,\%$.

2.5 Quantum Mechanical Calculations

To facilitate the interpretation of the experimental results, molecular properties of the investigated solutes were obtained by density functional theory (DFT) calculations using the B3LYP hybrid functional, run on GAUSSIAN 09 software [117]. For all calculations either 6-31++G(d,p) or 6-31G(d,p) basis sets were used. The low-energy geometries of various conformers of the molecules, and thus their sizes, shapes and volumes, were obtained in this way. Note that when analyzing the geometry from the obtained coordinates, the van der Waals radii [118] of the atoms between which distances are calculated have to be taken into account. The dipole moments were obtained assuming the center of mass as the pivot. To account for solvent effects, the polarizable continuum model (PCM) [119–121] was applied. In this model the solvent (water) is considered as a continuum with an appropriate static permittivity and the solute is placed in a cavity within the solvent reaction field. The so obtained dipole moments are equivalent to apparent dipole moments, μ_{ap}, as defined by Equation 1.53.

2.6 Statistical Mechanical Calculations

Since dielectric spectroscopy does not deliver any direct information on the microscopic arrangement of solvent and solute molecules in solution, statistical mechanical calculations using the 1D- and 3D-RISM (Reference Interaction Site Model) [122] approach were performed for selected systems. Solving 1D-RISM Ornstein-Zernike integral equation [123] coupled with the 1D-Kovalenko-Hirata closure [124], and the 3D-RISM integral equation [122] combined with the 3D-Kovalenko-Hirata closure [125] atom-atom (site-site) distribution functions can be obtained, which provide insights into solution structure in terms of specific site-site interactions and coordination numbers. The 1D-RISM calculation yields statistically averaged atom-atom (site-site) radial pair distribution functions (PDFs), $g_{\alpha\beta}(r)$, for atom (site) α on the reference molecule interacting with atom (site) β of the surrounding species, while the 3D-RISM method provides spatial distribution functions (SDFs), $g_\beta(\vec{r})$, for atoms (sites) β around the reference molecule [122, 123]. All calculations were performed by Prof. Dr. Fedotova and Dr. Kruchinin (G.A. Krestov Institute of Solution Chemistry of the Russian Academy of Science, Ivanovo, Russia) using the rism1d and rism3d.snglpnt codes from the AmberTools 14 package [126] and the MDIIS (Modified Direct Inversion in the Iterative Subspace) iterative scheme [127]. The sizes of the 1D- and 3D-grids, used for solving RISM equations, were chosen to be large enough to accommodate the solute complex together with sufficient solvation space around it in order to suppress significant numerical errors. The interactions potentials between

the different sites were represented by short-range Lennard-Jones and long-range Coulomb contributions. For all calculations the solvent water was modeled by the the modified SPC/E water model (MSPC/E) [128].

Chapter 3

Neurotransmitters and Chemically Related Substances

Neurotransmitters (NTs) are endogenous substances that act as chemical messengers by transmitting signals from a neuron to a target cell across a synaptic cleft. Stored in secretory vesicles their release can be triggered by the arrival of an nerve pulse at the synapse. Subsequently, the neurotransmitter crosses the synaptic gap and binds to specific proteins in the membrane of the post-synaptic neuron or cell [129].

Besides their categorization upon whether they bind to metabotropic or an ionotropic receptor (metabotropic receptors are members of the G-protein coupled receptor family while ionotropic receptors are ligand-gated ion channels), neurotransmitters are generally classified according their overall effects on the neurons, *i.e.*, excitatory or inhibitory. Major excitatory neurotransmitters include glutamate (Glu), epinephrine and norepinephrine. Glycine, γ-aminobutyric acid (GABA) and serotonin are prominent representatives of the class of inhibitory neurotransmitters, while some others can exert both excitatory and inhibitory effects, depending on the type of receptors that are targeted [130, 131].

Certainly, the interaction of the NTs with its surrounding aqueous medium is decisive for their biological action [1]. Investigations of the properties of these biomolecules in water could provide valuable information on the processes occurring in living organisms. Using dielectric spectroscopy, the structure and dynamics of such biologically important substances can be studied in aqueous solution. A deeper insight into the physico-chemical properties of the NT solutions in terms of solute-solute and solute-solvent interactions can be gained. Further, the role of specific functional groups can be examined by additionally investigating chemically related compounds. Therefore, the following chapter presents a dielectric relaxation study of binary aqueous solutions of various neurotransmitter and chemically related substances.

3.1 Acetylcholine Chloride and Carbamylcholine Chloride

3.1.1 Introduction

Acetylcholine ($AcCh/AcCh^+$, Figure 3.1(a)) is one of the most important neurotransmitters in living organisms and was the first NT to be identified [132]. It is the main NT involved in the nervous excitation in the peripheral and central nervous system. After release into the synaptic cleft by depolarization, AcCh is able to act at two structurally different receptor types at the postsynaptic membrane, namely muscarinic and nicotinic receptors, which trigger the opening of ion channels. The binding ability and thus the particular biological activity of AcCh is strongly linked to its chemical structure. Especially, the onium moiety was found to play a major role in the binding process in terms of formation of cation-π bonds, which arise from the interaction of the $-N^+(CH_3)$ group with the surrounding aromatic cage in the specific binding-sites of the cholinergic proteins [133–136]. Moreover, the high conformational flexibility of the AcCh cation was reported to be decisive for its binding affinities [133, 137]. The *trans, gauche* and the *trans, trans* conformers, with respect to the torsion angles ϕ_1 and ϕ_2 shown in Figure 3.1(a), were found to be the most prominent in aqueous solution [137, 138]. In particular, the *trans, trans* conformer is recognized by acetylcholinesterase and muscarinic receptors, whereas the folded *trans, gauche* form preferably interacts with nicotinic receptors [139–141].

Undoubtedly, AcCh has high biological relevance and malfunctions in the natural AcCh recognition cycle have also been linked with Alzheimer's disease [142]. However, acetylcholine is not used as a drug due to its broad-ranging actions which render it of limited therapeutic value.

On the other hand, carbamylcholine (carbachol, Car/Car^+, Figure 3.1(b)), a synthetic derivative of AcCh, is frequently used as a miotic agent for the treatment of glaucoma [143, 144]. Carbachol stimulates primarily muscarnic receptors, with a reduced affinity towards the nicotinic receptor types [134, 143]. Due to its stability towards hydrolysis by acetylcholinesterase it shows a longer duration of action [144]. However, the exact mechanisms by which AcCh and its derivative Car act are still not completely understood and in spite of their importance in the pharmacological field studies on the properties of "simple" aqueous solutions of the two NTs are scarce. Whereas for AcCh some experimental [11, 145, 146] and theoretical studies [147] investigating its hydration can be found, appropriate studies on the hydration and dynamics of carbachol are still lacking.

To deepen the knowledge on the biological action of the two choline-based NTs, dielectric spectra of aqueous solutions of the chloride salts, AcChCl and CarCl, were recorded at 25 °C. For AcChCl the concentration range of $0.07 \lesssim c/\mathrm{M} \lesssim 0.53$ ($\mathrm{M} \mathrel{\hat{=}} \mathrm{mol\,L^{-1}}$) was covered (note: solubility limit of AcChCl in water is $\sim 0.55\,\mathrm{mol\,kg^{-1}}$), while CarCl(aq) was investigated in the range $0.07 \lesssim c/\mathrm{M} \lesssim 0.83$. Temperature-dependent spectra of AcChCl(aq) were recorded at two selected molalities ($b(\mathrm{AcChCl}) = 0.2621\,\mathrm{mol\,kg^{-1}}$ and $b(\mathrm{AcChCl}) = 0.3738\,\mathrm{mol\,kg^{-1}}$) to retrieve information on activation parameters of the

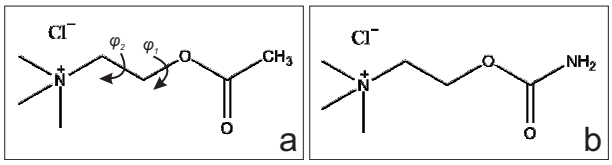

Figure 3.1: Chemical structures of (a) acetylcholine chloride and (b) carbamylcholine chloride.

present relaxation processes. Further insight into the structure of AcChCl(aq) solutions was gained by 1D- and 3D-RISM calculations, which were performed and kindly provided by Prof. Dr. Fedotova and Dr. Kruchninin (G.A. Krestov Institute of Solution Chemistry of the Russian Academy of Science, Ivanovo, Russia) [148]. Additionally, precise conductivity measurements of dilute AcChCl(aq) and CarCl(aq) solutions, provided by Prof. Dr. Marija Bešter-Rogač from the University of Ljubljana, yielded information on the extent of IP formation in these systems [149].

The acquisition and analysis of the dielectric spectra of the two NTs will cover the first part of this section, followed by a discussion of the DRS results. The DR results will start with a short discussion of the activation parameters of AcCh relaxations. The last part of this section will focus on structure and dynamics, which was deduced from the DR experiment complemented by RISM calculations and dilute-solution conductivity measurements, of the present AcChCl(aq) and CarCl(aq) solutions and their respective differences.

3.1.2 Data Acquisition and Processing

The AcChCl(aq) and CarCl(aq) samples were prepared as described in Section 2.1 and 2.2. The densities, viscosities and conductivities of the solutions were measured according to the procedures presented in Section 2.4. The ρ, η and κ values of the AcChCl(aq) and CarCl(aq) solutions are summarized in Tables A.1, A.2 and A.3. For all samples, the permittivity spectra were recorded in the frequency range $0.05 \leq \nu/\mathrm{GHz} \leq 89$ (Dielectric probe kit VNA setup + E-band interferometer, Section 2.3). The temperature-dependent measurements of AcChCl(aq) were performed in the temperature range $5 \leq \vartheta/^{\circ}\mathrm{C} \leq 65$ in 10 °C intervals with a temperature stability of ±0.05 °C. As pointed out in Section 1.1.2, the conductivity term, which scales with ν^{-1}, determines the low-frequency limit, ν_{min}, at which the experimental noise in η'' exceeds the dielectric loss, ε''. Thus, an increase in ν_{min} with increasing conductivity, *i.e.*, increasing c, can be observed. Consequently, noisy permittivity data in the region 0.05 GHz – ν_{min} was always discarded from the spectra. For the present AcChCl(aq) and CarCl(aq) samples ν_{min} was always in the region $0.1 \lesssim \nu_{\mathrm{min}}/\mathrm{GHz} \lesssim 0.4$.

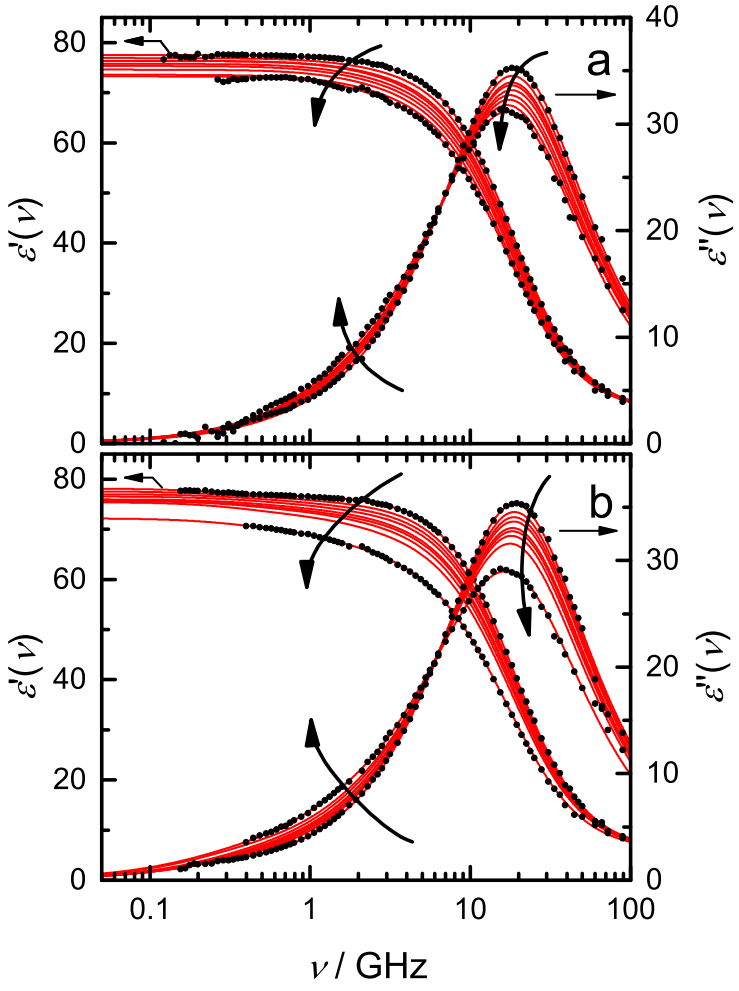

Figure 3.2: Relative permittivity, $\varepsilon'(\nu)$, and dielectric loss, $\varepsilon''(\nu)$, spectra of (a) AcChCl(aq) ($0.07496 \leq c/\mathrm{mol\,L^{-1}} \leq 0.5334$) and (b) CarCl(aq) ($0.07434 \leq c/\mathrm{mol\,L^{-1}} \leq 0.8338$) at 25 °C. Symbols denote the experimental data. Solid lines represent the fits. For visual clarity data points are only shown for selected samples. Arrows indicate the trend with increasing solute concentration.

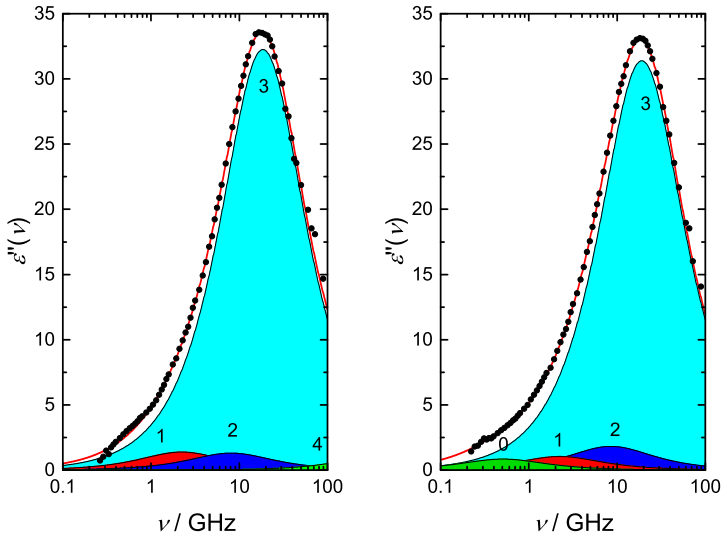

Figure 3.3: Dielectric loss spectrum of (a) 0.2510 M AcChCl(aq) and (b) 0.3193 M CarCl(aq) at 25 °C. Symbols denote experimental data, lines indicate the fits. The shaded areas show the individual contributions of the D+D+D+D model.

3.1.3 Choice of Relaxation Model and Assignment of Modes

AcChCl(aq) and CarCl(aq) concentration series. Figure 3.2 shows the evolution of the experimental spectra with increasing solute concentration. A superposition of up to five HN-equations (Equation 1.41) were tested to model the experimental spectra. Following the criteria presented in Section 2.3.3 and Zasetsky's analysis shown in Figures A.1 and A.2, only a superposition of four Debye (Equation 1.34) modes (D+D+D+D model) yielded a consistent set of relaxation parameters for both neurotransmitter systems at 25 °C. The parameters obtained from these fits are shown in Tables 3.1 and 3.2. The modes are numbered from lower to higher frequencies. In the following discussion $j = 1, .., 4$ will be used to designate only AcChCl(aq) modes, while modes in CarCl(aq) will be defined as $l = 0, .., 3$ for the sake of clarity (Figure 3.3).
The static permittivities of the two different systems decreased continuously with increasing neurotransmitter concentration (Figures A.4 and A.5). The spectra of both sets of samples were dominated by a high-amplitude mode $j, l = 3$ centered at ~ 19 GHz ($\tau_3 \approx 8.5$ ps), as can be seen in Figure 3.3. Based on its location and amplitude, mode 3 can be unambiguously assigned to the cooperative reorientation of bulk water molecules [22, 150]. Its amplitude, S_3, decreased systematically with increasing solute concentration (Figures A.4 and A.5). Also apparent from the AcChCl(aq) spectra is the appearance of a low-intensity mode $j = 4$ centered above the present upper-frequency limit at ~ 500 GHz ($\tau_4 \approx 0.3$ ps). Dielectric studies up to the THz regime indicate the presence of a similar high-frequency mode in neat water [150]. Currently, it can be attributed to the fast switch of H-bond connections between adjacent H_2O molecules *via* an triangular transition state, as depicted

Table 3.1: Static permittivity, ε, relaxation amplitudes, S_j, relaxation times, τ_j ($j = 1, .., 4$), infinite frequency permittivity, ε_∞, of AcChCl(aq) at 25 °C and the reduced error function, χ_r^2, of the D+D+D+D fitting model.[a,b]

c	ε	S_1	τ_1	S_2	τ_2	S_3	τ_3	S_4	τ_4	ε_∞	χ_r^2
0[c]	78.37	–	–	–	–	72.42	8.35	2.43	0.278	3.52	0.0056
0.07496	77.5	0.74	118.7	0.76	20.5	69.8	8.56	2.71	0.278F	3.52F	0.0601
0.1501	76.9	1.72	79.5	1.17	19.3	67.6	8.61	2.88	0.278F	3.52F	0.1329
0.2005	76.4	2.23	73.0	1.73	22.7	65.9	8.62	2.94	0.278F	3.52F	0.1313
0.2510	76.3	2.77	71.6	2.6F	19.7	64.5	8.59	2.95	0.278F	3.52F	0.1057
0.3013	75.8	2.49	83.8	3.8F	22.0	63.1	8.53	2.88	0.278F	3.52F	0.0795
0.3521	75.3	2.65	86.2	4.19	22.8	61.9	8.67	3.12	0.278F	3.52F	0.1460
0.4027	74.6	2.91	80.5	4.32	22.1	60.7	8.76	3.18	0.360	3.52F	0.1204
0.4538	73.6	3.08	76F	4.29	19.8	58.8	9.04	3.88	0.862	3.52F	0.1358
0.5334	73.2	3.59	71.2	5.32	23.0	57.4	8.96	3.43	0.632	3.52F	0.1199

[a]Units: c in mol L^{-1}; τ_j in ps. [b]Parameter values followed by "F" were fixed during fitting; [c]taken from Ref. [97].

in Figure 1.3(b). This "fast-water" process does not necessarily indicate the existence of a new, distinct water-species but it rather represents a different step on the timescale of the cooperative H_2O reorientation process (Section 1.3.5) [82]. Since the characteristic frequency of mode 4 lies outside the studied frequency range, it was not possible to resolve this process completely, as has been found for various aqueous electrolyte systems [55, 98, 151] and systems involving small, biologically active molecules in water [152, 153]. Accordingly, its relaxation time, τ_4, was fixed to its neat water value 0.278 ps [154] during fitting to reduce scatter (except for c(AcChCl)$\geq$ 0.4027 mol L^{-1}, Table 3.1). The infinite-frequency permittivity was assumed to be concentration-independent and, consequently, it was fixed to the neat water value of $\varepsilon_\infty = 3.52$ during the fit for all AcChCl(aq) solutions. This is supported by rather recent THz studies on concentrated NaCl(aq) solutions, which indicate only a weak concentration dependence of ε_∞ [155]. The fast-water mode was not resolved for CarCl(aq). However, the value of $S_4 + \varepsilon_\infty$ of AcChCl(aq) is comparable with $\varepsilon_\infty \approx 6$ of the CarCl(aq) solutions (Tables 3.1 and 3.2). This means that the fast-water mode is also present for CarCl(aq), but it is shifted too far outside the covered frequency range, and thus ε_∞ automatically comprises the unresolved fast-water contribution .

Additionally, a distinct mode at $\sim$ 8 GHz ($\tau_2 \approx$ 20 ps) appeared upon addition of AcChCl(aq) and CarCl(aq) to water. Its amplitude, S_2, increased with increasing solute concentration (Figures A.4 and A.5). Due to its proximity to the dominant bulk water mode 3 and its comparably low intensity, mode 2 was difficult to separate at low solute content, especially for AcChCl(aq) (S_2 at c(AcChCl) = 0.2510 mol L^{-1} and 0.3038 mol L^{-1} had to be fixed; Table 3.1). Note that for AcChCl(aq) the exclusion of this mode during

Table 3.2: Static permittivity, ε, relaxation amplitudes, S_l, relaxation times, τ_l ($l = 0, .., 3$), infinite frequency permittivity, ε_∞, of CarCl(aq) at 25 °C and the reduced error function, χ_r^2, of the D+D+D+D fitting model.[a,b]

c	ε	S_0	τ_0	S_1	τ_1	S_2	τ_2	S_3	τ_3	ε_∞	χ_r^2
0.07434	78.1	1.37	604	0.36	119	–	–	70.5	8.42	5.90	0.0911
0.1567	77.6	1.24	531	1.14	123	2.18	19.8	67.3	8.29	5.67	0.0786
0.2004	77.0	1.22	416	1.43	116	2.43	21.1	66.2	8.31	5.73	0.0690
0.2459	76.5	1.22	400F	1.68	116	3.30	20.2	64.7	8.29	5.66	0.0525
0.3193	76.0	1.69	314	2.08	71.3	3.63	18.7	62.8	8.35	5.80	0.0568
0.3524	75.8	1.68	360	2.01	91.7	4.27	20.2	62.0	8.36	5.83	0.0801
0.4037	75.7	1.91	350F	2.72	79.0	5.52	18.4	59.7	8.34	5.80	0.0501
0.4985	75.4	2.47	400F	3.47	75.3	6.56	16.9	56.9	8.40	5.98	0.0494
0.8338	72.2	2.00	464	4.44	101	12.1	19F	47.8	8.34	5.86	0.127

[a]Units: c in mol L^{-1}; τ_l in ps. [b]Parameter values followed by "F" were fixed during fitting.

the fitting, and thus using a D+D+D model instead of the D+D+D+D, led to a better nominal description of the spectra at low c(AcChCl) (χ_r^2 up to 20 % lower). This is also indicated by Zasetsky's analysis shown in Figure A.1 where a mode with the respective characteristic relaxation time ($\sim$ 20 ps) was discernible only at higher AcChCl concentrations. However, using the D+D+D model led to inconsistent and partly unphysical evaluation results of the fitting parameters and was thus discarded. The magnitude and the relaxation time of mode 2 is typical for so-called "slow-water", which originates from the relaxation of water molecules slowed down in their dynamics by hydrophobic [156–160] and/or (moderately) hydrophilic [154, 160] hydration of the solute. Whereas the latter hydration effect arises from electrostatic interaction of the water dipoles with charged or dipolar groups of the solute (H-bonds and/or Coulombic interactions), the former effect is the result of a steric effect, where hydrophobic groups prevent the approach of a fifth water molecule to the tetrahedrally coordinated H_2O molecules (Figure 1.3), and as such impede molecular reorientation [82, 161]. The retardation factor of slow-water compared to the bulk reorientation, determined by excluded-volume effects and the balance of solute-solvent *vs.* solvent-solvent interaction strengths [82], was found to be $r = \frac{\tau_2}{\tau_3} \approx 2.5$ in the present solutions. A similar moderately retarded water species was also reported for aqueous solutions of Me_4NCl (Section 4.2), biologically active amino acids, such as ectoine [152] and L-proline [162], and biological macromolecules, *e.g.* proteins [163, 164].

In contrast to spherical chloride ions, which do not have a permanent dipole moment, acetylcholine ($AcCh^+$) and carbamylcholine (Car^+) cations are dipolar species as their positive charge does not coincide with their center of mass. Judging by the location of process 1 ($\sim$70 – 120 ps) and the steady increase of S_1 with increasing solute concentration, mode 1 can be assigned to the reorientation of the dipolar $AcCh^+$(aq) and Car^+(aq) cations

(Tables 3.1 and 3.2). The relaxation strengths and relaxation times are rather similar for $AcCh^+$(aq) and Car^+(aq), as would be expected from their structural resemblance (Figure 3.1), with a slightly higher mean relaxation time value for Car^+(aq) ($\bar{\tau}_1 \approx 100\,\mathrm{ps}$) compared to $AcCh^+$(aq) ($\bar{\tau}_1 \approx 80\,\mathrm{ps}$).
For CarCl(aq) an additional low-frequency mode $l = 0$, centered at $\sim$0.4 GHz, was resolved (Table 3.2). The location of this mode in the MHz regime and its rather small amplitude is compatible with an ion-cloud (IC) relaxation process, also called the Debye-Falkenhagen-Effect [165]. It is a well known phenomenon in electrolyte solutions, which manifests itself in a distinct relaxation process with a relaxation time scaling with $1/\kappa$. Although its contribution was thought to be rather small in electrolyte solutions, fairly recent results indicate that this is not necessarily the case, in particular at low electrolyte concentrations [55, 166]. The IC effect is generally always present in the DR spectra of solutions containing charged species. However, currently there is no theory available to predict or quantify the contribution of IC relaxation to the overall dielectric spectrum.
As dipolar ionic aggregates, *e.g.* carbamylcholine chloride ion pairs (IPs), would be expected to contribute in the lower frequency range compared to the Car^+(aq) relaxation of mode 1, the assignment of mode 0 to the relaxation of dipolar ionic aggregates would also be conceivable and it will be discussed further below.

Temperature-dependent AcChCl(aq) spectra. The typical effect of temperature on the AcChCl(aq) permittivity spectra is shown in Figure 3.4. The D+D+D+D fitting model, applied for the concentration-dependent measurements of AcChCl(aq) at 25 °C, also yielded the best description for the spectra at 5 °C and 15 °C. However, due to the disappearance of mode 2 at $\vartheta \geq 35\,^\circ\mathrm{C}$ different fitting models had to be used at higher temperatures. Mode 3 was fitted with a Cole-Cole equation (Equation 1.39) at 35 °C and 45 °C. The necessity to utilize the broader CC equation instead of the D mode might reflect the presence a small slow-water contribution in the proximity of the bulk water mode 3, which however could not be resolved as a distinct process. Since the amplitude of a mode scales linearly with concentration (Equation 1.48), it can be said at this stage that the amount of slow-water decreases rather fast with increasing temperature. At $\vartheta = 55\,^\circ\mathrm{C}$ and $\vartheta = 65\,^\circ\mathrm{C}$ the "narrower" Debye equation was used to fit mode 3, which indicates total disappearance of the slow-water species at such high temperatures.
The static permittivity, ε, decreased as the densities of the liquids decrease and thermal fluctuations increase with ϑ (Figure A.6). Bulk-water amplitude, S_3, showed a overall linear decrease with increasing temperature, except for the region between $\vartheta = 35\,^\circ\mathrm{C}$ and $\vartheta = 45\,^\circ\mathrm{C}$, where a small maximum in S_3 can be observed (Figure A.6). This deviation from the decreasing behavior might be traced back to the incorporation of the unresolved slow-water contribution to the bulk-water process, expressed in the form of a CC fitting mode.
In contrast to S_2 and S_3, the fairly scattering amplitude of the $AcCh^+$(aq) reorientation process, S_1, showed no decrease with increasing temperature, most probably reflecting problems in the accurate determination of the small amplitude S_1 at these temperatures. Thus, in the following it was abstained from a detailed discussion of $S_1(T)$. Relaxation

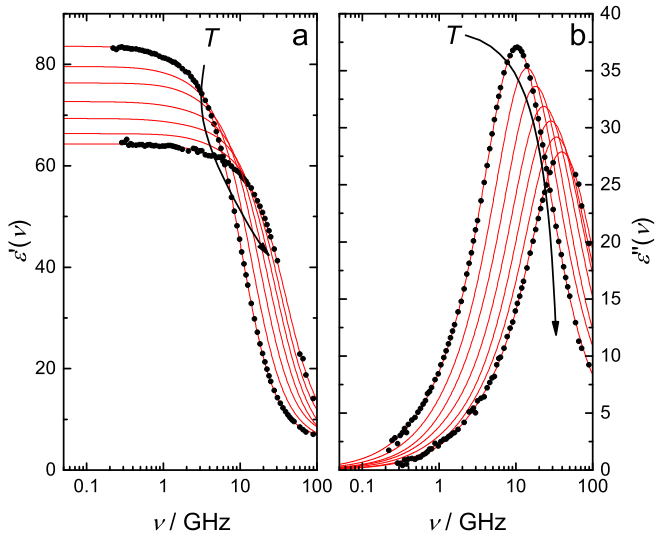

Figure 3.4: (a) Relative permittivity, $\varepsilon'(\nu)$, and (b) dielectric loss, $\varepsilon'(\nu)$, spectra of 0.2621 mol kg^{-1} AcChCl(aq) in the temperature range $5 \leq \vartheta/°C \leq 65$ in steps of 10 °C. Symbols indicate the experimental data, while solid lines denote the overall fits. For visual clarity only data points at 5 °C and 65 °C are shown.

times of modes 1-3 decreased with increasing temperature. The values of ε_∞ and the relaxation times of fast-water mode 4 were (partly) fixed to the neat water values [97] for the reasons discussed above. As the fast-water contribution is located at the edge of the accessible frequency range, its actual, rather scattery amplitude values should not be over-interpreted, although the inclusion of mode 4 was essential to obtain a stable fit of the temperature-dependent spectra. All parameters of the temperature-dependent D(+D)+D(CC)+D fitting model (brackets indicate that the mode could not be resolved over the whole temperature range) are summarized in Table 3.3.

3.1.4 Activation Parameters of AcChCl(aq) Relaxation Processes

The relaxation times, τ_j, investigated as a function of temperature in the range $5 \leq \vartheta/°C \leq 65$ ($278.15 \leq T/K \leq 338.15$) were fitted to the Eyring equation. It should be noted that the activation parameters were not derived for the disappearing slow-water mode. The same applies for the relaxation time of the fast-water mode, τ_4, which was fixed to the neat water value almost throughout the whole temperature range. Consequently, activation parameters were only obtained for the $AcCh^+$ reorientation process (mode 1) and the bulk-water relaxation (mode 3). For both processes the extended Eyring equation (Equation 1.71) yielded a better description than the assumption of temperature-independent activation enthalpies and entropies (Equation 1.70). The obtained activation parameters are summarized in Table 3.4. The corresponding fits of the relaxation times of 0.3738 mol kg^{-1}

Table 3.3: Static permittivity, ε, relaxation amplitudes, S_j, relaxation times, τ_j ($j = 1,..,4$), infinite frequency permittivity, ε_∞, of AcChCl(aq) at different temperatures, ϑ, and the reduced error function, χ_r^2, of the D(+D)+D(CC)+D and fitting model.[a,b]

ϑ	ε	S_1	τ_1	S_2	τ_2	S_3	α_3	τ_3	S_4	τ_4	ε_∞	χ_r^2
$b = 0.2621\,\mathrm{mol\,kg^{-1}}$ (0.2510 M at 25,°C)												
5	83.6	2.60	162	6.78	27.8	67.8	–	14.7	2.47	0.480	3.96F	0.02177
15	79.6	2.08	125	5.07	25.2	65.9	–	11.0	2.85	0.831	3.68F	0.03491
25	76.3	2.77	71.6	2.6F	19.7	64.5	–	8.59	2.95	0.278F	3.52F	0.1057
35	72.7	1.28	115	–	–	67.1	0.035	6.90	1.13	0.212F	3.2F	0.1050
45	69.3	1.16	110	–	–	64.1	0.031	5.58	1.33	0.17F	2.78F	0.1336
55	66.3	2.82	43.0	–	–	57.5	–	4.70	3.22	0.189F	2.8F	0.1395
65	64.3	3.02	43.7	–	–	55.0	–	4.00	3.70	0.128F	2.58F	0.1118
$b = 0.3738\,\mathrm{mol\,kg^{-1}}$ (0.3521 M at 25,°C)												
5	83.0	2.79	241	9.82	33F	63.5	–	14.9	2.92	0.509F	3.96F	0.09251
15	78.7	2.39	129	8.03	26.5	62.2	–	10.8	2.41	0.288	3.68F	0.03621
25	75.3	2.65	86.2	4.19	22.8	61.9	–	8.67	3.12	0.278F	3.52F	0.1460
35	71.8	2.99	62.7	–	–	63.2	0.017	7.11	2.42	0.212F	3.2F	0.0873
45	68.6	2.45	71.2	–	–	60.8	0.020	5.79	2.63	0.17F	2.78F	0.1417
55	65.5	3.52	35.1	–	–	55.7	–	4.85	3.39	0.189F	2.84F	0.1019
65	63.1	3.38	39.5	–	–	53.5	–	4.13	3.62	0.128F	2.58F	0.3135

[a]Units: ϑ in °C; τ_j in ps. [b]Parameter values followed by "F" were fixed during fitting.

Table 3.4: Eyring activation enthalpies, $\Delta H^{\neq}_{298.15}$„ entropie, $\Delta S^{\neq}_{298.15}$, and heat capacities, $\Delta C^{\neq}_{p}$, obtained from the fits of relaxation times, τ_1 and τ_3, of the investigated AcChCl(aq) solutions as a function of T.

τ_j	$\Delta H^{\neq}_{298.15}$ / kJ mol^{-1}	$\Delta S^{\neq}_{298.15}$ / J K^{-1} mol^{-1}	$\Delta C^{\neq}_{p}$ / J K^{-1} mol^{-1}
		Neat water	
τ^a_b	15.9 ± 0.2^a	20.4 ± 0.7^a	-160 ± 22^a
	AcChCl(aq) $b = 0.2621$ mol kg^{-1} (0.2510 M at 25 °C)		
τ_1	20 ± 3	16 ± 10	-530 ± 270
τ_3	15.1 ± 0.1	17.7 ± 0.4	-92 ± 9
	AcChCl(aq) $b = 0.3738$ mol kg^{-1} (0.3521 M at 25 °C)		
τ_1	24 ± 4	29 ± 14	-447 ± 342
τ_3	14.7 ± 0.4	16 ± 1	-93 ± 33

[a]Taken from Ref. [78]

AcChCl(aq) to the extended Eyring equation are shown in Figure 3.5.

The activations parameters obtained for the $AcCh^+$ reorientation show large uncertainties and are thus not very reliable (Table 3.4). The only reasonable statement which can be made here is that the parameters of both AcChCl(aq) solutions are comparable within their (fairly large) errors, indicating no significant changes in the nature of the relaxation mode 1 at different concentrations.

On the other hand, τ_3 could be fitted more accurately (Table 3.4) and the derived eyring activation parameters allow a slightly more detailed discussion. Even though the assumption of constant $\Delta H^{\neq}$ and $\Delta S^{\neq}$ would yield acceptable fits for τ_3, introducing temperature-dependence of the parameters improves the quality of the plot (adjusted R^2 of the fit: 0.9962 *vs* 0.9982). Furthermore, the necessity to use temperature-dependent activation parameters is consistent with previous studies on the temperature dependence of the water relaxation [78, 167, 168]. Although water relaxation dynamics is essentially decoupled from the viscosity [22, 169], plots of $\ln(\eta T)$ *vs* T^{-1} show a particularly pronounced non-linear behaviour (Figure A.3), similarly implying temperature-dependence of activation parameters with regard to these transport properties.

Both quantities, $\Delta H^{\neq}_{298.15}(\tau_3)$ and $\Delta S^{\neq}_{298.15}(\tau_3)$, are lowered compared to the neat water value (Table 3.4). The reduced activation enthalpies for the AcChCl(aq) solutions compared to neat water value might reflect the slight fragility of the Cl^- hydration shells. Chloride anions in aqueous solution show low residence times of H_2O in its hydration sheath and the corresponding rotational correlation times of hydrating water molecules are somewhat lowered compared to neat water [34, 170]. Thus, the water relaxation process, which involves breaking of hydrogen bonds, is enthalpically facilitated in the vicinity of the chloride anion. The question weather this decrease is dominated by the labile Cl^- hydration structure only, or if certain entities of the $AcCh^+$ molecule might contribute to this

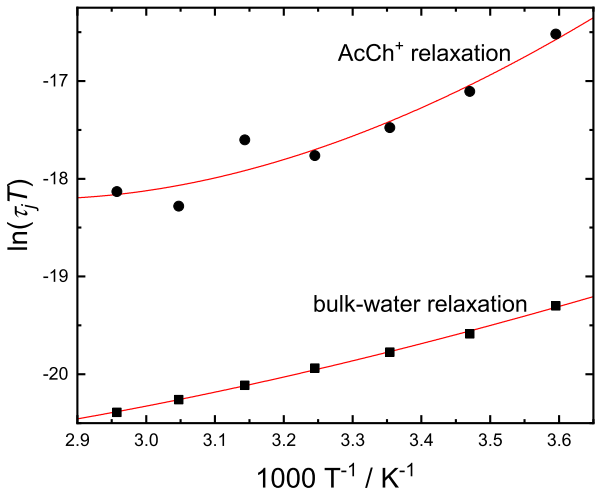

Figure 3.5: Plots of $\ln(\tau_j T)$ as a function of T^{-1} for the $AcCh^+$ relaxation ($j = 1$, ●) and the bulk-water relaxation process ($j = 3$, ■). The fits to the (extended) Eyring equation are denoted by solid lines.

effect as well can not be answered here. In any case, the reduction of $\Delta H^{\neq}_{298.15}(\tau_3)$ scales with increasing solute concentration, as can be seen in Table 3.4. Similarly, $\Delta S^{\neq}_{298.15}(\tau_3)$ decreases with increasing c(AcChCl), suggesting that the transition state for the cooperative water relaxation is more "ordered" compared to neat water in the presence of $AcCh^+$ and Cl^- ions.

3.1.5 Solute Relaxations

Ion-cloud/ion pair relaxation process. Using the Cavell equation (Eq. 1.48) the amplitudes of the resolved solute-related relaxation modes can be analyzed quantitatively. Under the assumption that mode 0 of CarCl(aq), which could not be resolved for AcChCl(aq), originates from a CarCl-IP-relaxation exclusively, concentrations of the ion pairs and therefore association constants can be derived. Since both ions, Cl^- and the onium group, are known to be weakly hydrated [22, 156], contact ion pairs (CIPs), rather than solvent-shared (SIPs) or solvent-separated ion pairs (2SIPs), can be considered as the most likely IP species for CarCl(aq). Among the few possible CIP structures two distinct limiting cases stand out: a "linear" arrangement, where Cl^- is directly coordinated to the cationic $-N(CH_3)_3$ group (Figure A.7(a)), and a "bidentate" structure, where Cl^- is bound simultaneously by the onium and the $-NH_2$ group of the same Car^+ molecule (Figure A.7(b)). The exact geometries and the apparent dipole moments of the respective aggregate were obtained from Gaussian 09 at the B3LYP/6-31G(d,p) level using the PCM solvation model.

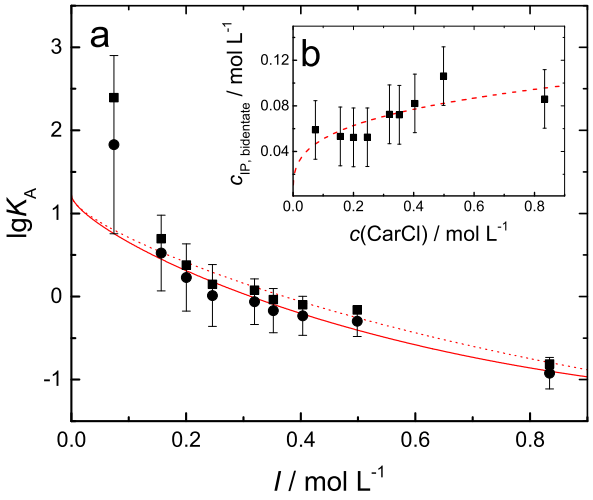

Figure 3.6: (a) Association constant, K_A (in M^{-1}), for the formation of the "linear"-type (●) and the "bidentate"-type (■, error bars not shown) CIPs of CarCl(aq) as a function of ionic stregnth, I, at 25 °C. The Guggeheim-type fits are denoted as a solid line for the "linear" aggregate and as a dotted line for the "bidentate" case. Inset (b) shows the concentration of the "bidentate"-type IP as a function of the overall CarCl(aq) concentration.

Assuming no orientational correlations between the IPs and the surrounding dipoles, *i.e.*, $g_{IP} = 1$ (Equation 1.52), c_{IP} were calculated from Equation 1.48. The association constants were subsequently obtained *via*

$$K_A = \frac{c_{IP}}{c_+ c_-} \tag{3.1}$$

where c_+ and c_- are the concentration of the "free" cation and "free" anion, respectively. The K_A (in M^{-1}) values were fitted as a function of the stoichiometric ionic strength, $I(= c)$, using an extended Guggenheim-type equation [171]

$$\lg K_A = \lg K_A^\circ - \frac{2A_{DH}\,|z_+ z_-|\,\sqrt{I}}{1+\sqrt{I}} + B \cdot I + C \cdot I^{3/2} \tag{3.2}$$

In Equation 3.2, K_A° is the standard-state (infinite dilution) association constant, $z_\pm$ are the ion charge numbers, $A_{DH} = 0.5115\,(\mathrm{L\,mol^{-1}})^{1/2}$ is the Debye-Huckel constant for activity coefficients in water at 25 °C, and B and C are adjustable parameters.
The acquired K_A values for the two most probable IP types and the respective Guggenheim-type fits are shown in Figure 3.6. The association constants of the "linear" and the "bidentate" aggregate deviate only weakly from each other and the respective infinite dilution association constants of $\lg K_A^\circ = 1.2 \pm 0.4$ ($K_A^\circ = 16 \pm 5$) and $\lg K_A^\circ = 1.2 \pm 0.3$ ($K_A^\circ = 16 \pm 4$), obtained from the fit to Equation 3.2, are completely identical.

At this point, it is instructive to compare the present DRS results with dilute-solution electrical conductivity data [149]. The obtained limiting molar conductivities, Λ_0, and the infinite dilution association constants, K_A°, of AcChCl(aq) and CarCl(aq) in the temperature range $5 \leq \vartheta/°C \leq 40$ are summarized in Tables A.4 and A.5. Details on the dilute-solution conductivity procedure will not be given here and can be found elsewhere [172–174]. To sum up shortly, the electrical conductivities of dilute (low mM regime) AcChCl(aq) and CarCl(aq) solutions were measured and subsequently converted to molar conductivities, $\Lambda = \kappa/c$. The Λ values were evaluated with Barthel's low-concentration chemical model, which yielded the limiting molar conductivities, Λ_0, and the infinite dilution formation constants, K_A° [175]. The obtained infinite dilution formation constant of CarCl(aq) IPs at 25 °C of $\lg K_A^\circ = 0.497$ ($K_A^\circ = 2.93\,M^{-1}$) is significantly lower than the respective DRS value of $\lg K_A^\circ = 1.2$, indicating an overestimation of the S_0 values. Undoubtedly, the ion-cloud contribution to S_0 is not insignificant. The predicted relaxation time for the rotational diffusion of the two presumed CIP species (Figure A.7) would be expected to be located between ~ 40 ps and ~ 300 ps, depending on the applied boundary conditions (*slip* or *stick*; Section 1.3.4). These values are lower than the mean relaxation time of mode 0, $\bar{\tau}_0 \approx 450$ ps, which supports the argument of a strong IC contribution, shifting the relaxation time to lower frequencies. In this context, the question arises whether mode 0 is purely due to IC relaxation, without any IP contribution. Although this picture is conceivable, it is rather unlikely. The amplitude of an IC relaxation typically shows a rise and subsequent decline at lower electrolyte concentrations, followed by its total disappearance from the spectra at higher c [99]. Although S_0 is fairly scattering (Table 3.2), no such trend can be observed. In broad terms, even a slight increase with rising c may be postulated. Most likely, mode 0 is a composite process, comprising both, the IC relaxation at lower c and an IP relaxation, which dominates at high c and counteracts the decline of the IC contribution in this concentration range. Unfortunately, a separation of the two processes is currently impossible due to the lack of appropriate theories.

Interestingly, no equivalent IC/IP mode could be resolved for AcChCl(aq), which indicates that the IC effect in AcChCl(aq) solutions is less pronounced and/or that the tendency of IP formation of acetylcholine chloride IPs is too low to be detected as a distinct mode. The infinite dilution association constant for $AcCh^+$-Cl^--IPs, which was obtained from dilute-solution conductivity measurements, was found to be $\lg K_A^\circ = 0.391$ ($K_A^\circ = 2.46\,M^{-1}$) at 25 °C (Table A.4), which is indeed lower than the respective CarCl(aq) value (Table A.5). Low concentrations of $AcCh^+$-Cl^--IPs (note that AcChCl(aq) were studied in a smaller concentration range compared to CarCl(aq) due to solubility limits) and limitations in the sensitivity of the DRS method made the contribution of an AcChCl(aq) IP mode practically invisible in the DR spectra. It should be also noted that the calculated dipole moment of the $AcCh^+$-Cl^- CIP species of $\mu_{ap}^{calc} = 16.4$ D (Gaussian 09, B3LYP/6-31G(d,p) level using the PCM solvation model) with Cl^- being coordinated to the onium moiety, similar to Figure A.7(a), is slightly lower than respective Car^+-Cl^- values, implying a somewhat reduced relaxation strength of AcChCl(aq) aggregates compared to CarCl(aq) IPs in the DR spectra.

The extent of ion pairing in AcChCl(aq) and CarCl(aq) solutions is low, but not insignif-

icant. The conductivity-deduced standard-state association constants for IP formation of the chloride salts of the two neurotransmitters can be directly compared with those of structurally related compounds, such as short-chain tetraalkylammonium (Me_4NCl: $K_A^\circ = 1\,M^{-1}$ (Section 4.2), $2.17\,M^{-1}$ [176], $0.8\,M^{-1}$ [177]; Me_4NBr: $K_A^\circ = 2.78\,M^{-1}$ [176]; Et_4Cl: $K_A^\circ = 2.3\,M^{-1}$ [178]; Et_4Br: $K_A^\circ = 3.55\,M^{-1}$ [176]) and choline-based salts (choline chloride: $K_A^\circ = 1.99\,M^{-1}$ [173]; chlorocholine chloride: $K_A^\circ = 3.02\,M^{-1}$ [173]; all at 25 °C). The association constant for choline chloride (ChCl(aq)) is lower than the present AcChCl(aq) and CarCl(aq) values. The introduction of a acetyl and carbamoyl group evidently leads to a stronger binding of the chloride anion. If the "bidentate" Car^+-Cl^- aggregate (Figure A.7(b)) was indeed formed in aqueous solution, the higher standard-state association constant of Car^+-Cl^-(aq) complexes compared to $AcCh^+$-Cl^-(aq), Ch^+-Cl^-(aq) and Me_4N^+-Cl^-(aq) IPs might be attributed to the chelate effect, which predicts a higher stability of multidentate complexes compared to monodentate species due to favorable entropy changes associated with the chelate formation [179]. However, the extent of ion pairing is governed by a very subtle interplay between the level of hydration and the interactions of the ions of opposite charge, which makes it a quite complex physicochemical issue. Thus, the "intuitive" discussion about a possible chelate effect should be taken with a grain of salt. Further experiments would certainly help to confirm (or refute) the possible formation of such species.

$AcCh^+$ and Car^+ reorientation process. The effective dipole moments of $AcCh^+$(aq) and Car^+(aq) obtained from the evaluation of S_1 *via* Equation 1.48 are shown in Figure 3.7. The dipole moments of both cations are rather similar ($\sim 10-8\,D$) and they decrease systematically with increasing c, although a slightly steeper decrease can be observed for $\mu_{eff}(AcCh^+)$ compared to $\mu_{eff}(Car^+)$. Note that, as the actual error of the dielectric measurement is not known, the error bars of μ_{eff} were obtained from an empirical polynomial fit of $S_1(c)$ using $2 \cdot \sigma_{fit}$ as ΔS_1.

A decreasing μ_{eff} with c can generally be interpreted as (i) changes of the apparent dipole moment, *i.e.*, changes in the geometry of the relaxing species, or (ii) a drop in orientational correlations between the relaxing species and the neighbouring dipoles. While the latter covers the solvent-solute and solute-solute interactions, the former is mainly governed by conformational changes of the relaxing dipole. Various experimental [37, 180] and computational studies [36, 38, 137, 138, 181, 182] on the conformational behaviour of acetylcholine in different media reported a high flexibility of the $AcCh^+$ cation. The situation is similar for CarCl [183]. It could be shown by Vistoli *et al.* [36, 182] that the distribution of conformers correlates with the polarity of medium embedding the $AcCh^+$ cation. Thus, the proportion of unfolded conformers, bearing a higher dipole moment compared to the folded form, is increased in polar media and *vice versa*. Taking the static permittivity, ε, of the present AcChCl(aq) CarCl(aq) as a measure for the polarity, one might attribute the decrease in μ_{eff} to the decreasing ε with rising c ($\Delta\varepsilon \approx 5-6$, Table 3.1 and Table 3.2). Vistoli *et al.* reported a drop of the mean $AcCh^+$ dipole moment of $\sim 1\,D$ when putting the cation out of water into vacuum ($\Delta\varepsilon \approx 80$) [36], which implies that this conformational effect, if present at all in the investigated solutions, cannot account for the significant drop

of μ_{eff} with c. Note that the mean dipole moment of 8.9 D for $AcCh^+$ embedded in water as reported by Vistoli *et al.* [36] is in excellent agreement with the present $\mu_{\text{eff}}(AcCh^+)$ values ($\bar{\mu}_{\text{eff}}(AcCh^+) = 9\,\text{D}$).
Interestingly, $\mu_{\text{eff}}(AcCh^+)$ converges to the calculated apparent dipole moment value of the $AcCh^+$ cation in water of $\mu_{\text{ap}}^{\text{calc}} = 7.6\,\text{D}$ at higher c(AcChCl) (Figure 3.7(a)). Figure 3.8 shows the DFT-calculated low-energy structures and the respective dipole moments of AcCh+x·H_2O clusters with the x hydrating water molecules being taken into account explicitly. The calculated dipole moments increase continuously when going from 7.6 D for the "naked" cation ($x = 0$) to 13.3 D for AcCh+2·H_2O. This suggests that (at least for $x \leq 2$) the dipole moments of the hydrating H_2O molecules align preferentially parallel to the AcCh dipole. Although only one conformational arrangement was calculated for each hydrated species respectively, the obtained calculated dipole moments compare well with the experimental values (Figure 3.7(a)). The marked decrease of $\mu_{\text{eff}}(AcCh^+)$ with c (11.4 D $\rightarrow$ 7.6 D) might suggest a continuous loss of dipolar correlation between the water molecules and the $AcCh^+$ cation ($x \approx 2 - 1 \rightarrow x \approx 0$) with increasing c, *i.e.* dehydration. At this stage, it is instructive to analyze the relaxation time of the $AcCh^+$ reorientation process, τ_1. Using Equation 1.59 (empirical intercept $\tau_{\text{rot}}^0 = 0$) and 1.60, the hydrodynamic friction coefficient, C, can be calculated as function of solute concentration, which is commonly regarded as measure for the solute-solvent interaction strength. As can be seen in Figure 3.10(a), the C values decrease with increasing c. The decline and the gradual approach to the *slip*-value suggests decreasing coupling, and thus a reduction of interaction, between the reorienting dipole and the surrounding solvent. Note that in this analysis V_{m} was taken from DFT-calculated geometry of the "naked" cation and as such was set to be constant. The decrease in the effective volume, V_{eff}, was directly accounted in the decline of the hydrodynamic friction factor (Eq. 1.60). This is not necessarily true, as a decrease in V_{m}, implying decreasing size of the rotating aggregate, would result is a similar effect on V_{eff} (Eq. 1.60). The latter would also mean that the solute hydrates rotate as one species as a whole. In either way, both effects suggest a decrease of solute-solvent interactions. Since the exact changes in V_{m} as a function of c are not known, it is most appropriate to use the friction factor as measure for the interaction of the solute with its surrounding, while V_{m} is held constant.
Note that the experimental dipole moments for Car^+(aq) are lower than the calculated values (Figures 3.7(b) and 3.9), which most probably indicates that the low-energy conformations obtained from DFT calculations are of minor importance in real aqueous solutions. However, some qualitative information can still be obtained from the theoretical structures of Car+x·H_2O clusters. Similarly to the AcCh calculations, the obtained apparent dipole moments scale with the number of hydrating water molecules (Figure 3.9). Further, the hydrodynamic friction coefficient, C, shows a decrease with increasing CarCl concentration (Figure 3.10(b)). Accordingly, the decrease in $\mu_{\text{eff}}(Car^+)$ might be attribute to a dehydration effect, similar to the case of AcChCl. It should be pointed out that the overall effects, which express themselves in slopes of $\mu_{\text{eff}}(Car^+)$ and $C(c)$, are generally less pronounced in the CarCl(aq) solutions.
Undoubtedly, the hydration plays a major role in unraveling the properties of the aqueous

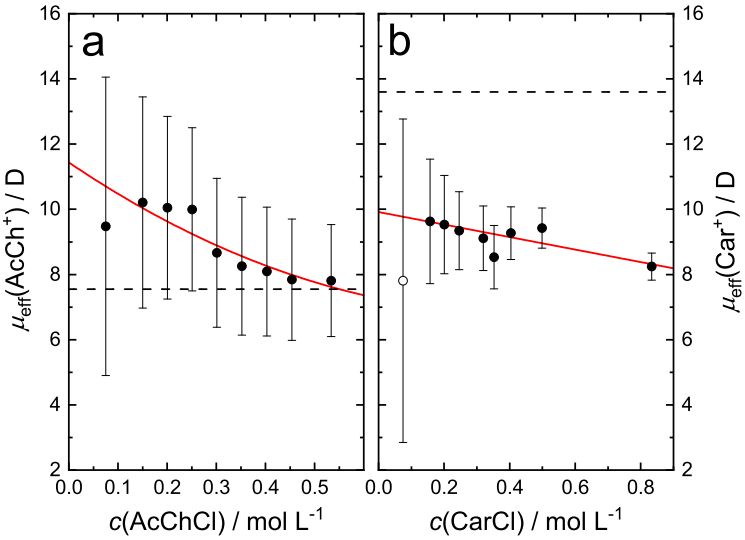

Figure 3.7: Effective dipole moments, μ_{eff}, of (a) $AcCh^+$(aq) and (b) Car^+(aq) as obtained from the DR spectra at 25 °C. The symbols denote the experimental data, solid lines represent empirical weighted fits. Unfilled symbols were neglected in the fit. The dashed line indicates the the calculated (Gaussian 09, B3LYP/6-31G(d,p) with the PCM solvation model) apparent dipole moments of the respective cations.

solutions of the two neurotransmitters, which will be the topic of the following section.

3.1.6 Solvent Relaxations - Hydration of AcChCl and CarCl

Knowing the relaxation amplitudes of the solvent modes, the concentration of the respective water species, and thus effective hydration numbers, can be derived from Eq. 1.48. To obtain the concentration of bulk-like water the apparent bulk-water amplitude, S_{b}^{ap}, has to be used, which is calculated as

$$S_{\text{b}}^{\text{ap}} = S_3 + S_4 + \varepsilon_\infty(c) - \varepsilon_\infty(0) \tag{3.3}$$

For the case where the fast-water process (mode 4) was not resolved, S_4 was set to zero. Prior to inserting S_{b}^{ap} into the Cavell equation, the apparent bulk-water amplitude has to be corrected for the effect of "kinetic depolarization", which arises from the inhibition of rotation of solvent molecules caused by the movement of ions in the applied electric field. The approach of Sega, Kantorovich and Arnold (SKA) [184] was used throughout the present work. A detailed discussion of this correction can be found in the Chapter B of the Appendix.
In order to obtain concentrations from Equation 1.48 the effective dipole moment, $\mu_{\text{eff},j}$, of the relaxing species has to be known. In particularly, the orientational correlation factor,

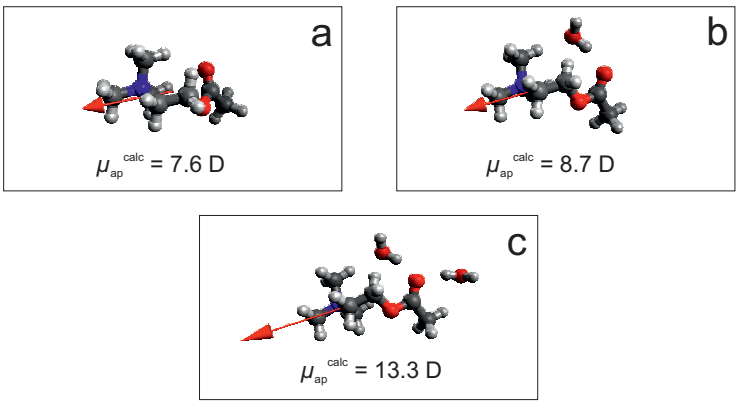

Figure 3.8: Lowest-energy structures of (a) AcCh, (b) AcCh+1·H_2O and (c) AcCh+2·H_2O species as obtained by Gaussian 09 at the B3LYP/6-31G(d,p) level using the PCM solvation model. Blue: nitrogen, red: oxygen, dark-gray: carbon, light-gray: hydrogen. The arrows indicate the dipole moments.

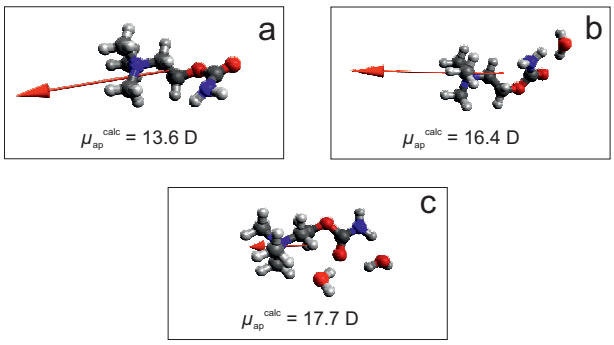

Figure 3.9: Lowest-energy structures of (a) Car, (b) Car+1·H_2O and (c) Car+2·H_2O species as obtained by Gaussian 09 at the B3LYP/6-31G(d,p) level using the PCM solvation model. Blue: nitrogen, red: oxygen, dark-gray: carbon, light-gray: hydrogen. The arrows indicate the dipole moments.

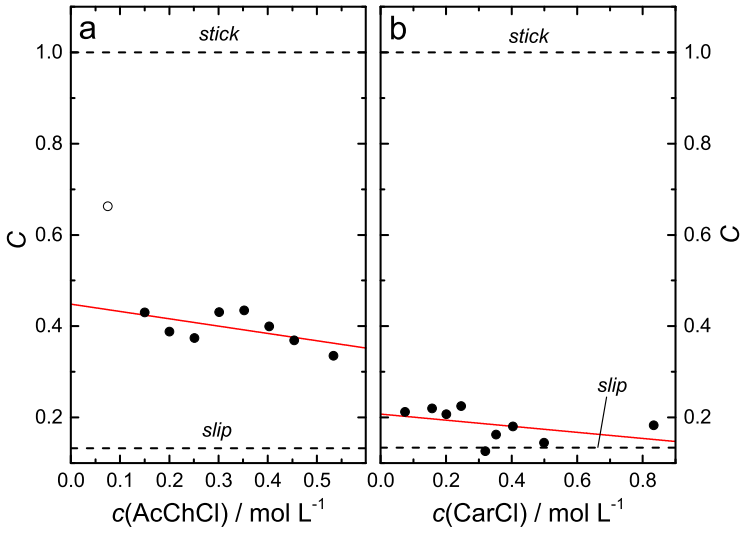

Figure 3.10: The hydrodynamic friction coefficient, C, as a function of (a) c(AcChCl) and (b) c(CarCl). Solid lines denote linear fits. Hollow symbols were not included in the fitting.

g_j, is usually unknown and it is not independently accessible from the experiment (Equation 1.52). However, for the bulk-like water relaxation in low-to-moderately concentrated solutions, it can be circumvented by normalizing Equation 1.48 with respect to neat water. This assumption was found to break down at too high c [156] and in the solvation shell of ions [185]. The latter implies that the orientational correlation factor of moderately retarded H_2O molecules, which arise from interactions with the solute, might be different from the bulk-like water and thereby from the neat water value. However, due to the lack of precise knowledge of the orientational correlation factor for the water species in this process, the normalization to neat water was also used for the analysis of the slow-water mode as a first approximation.
The effective total hydration number, Z_t, of the dissolved neurotransmitters is determined as the difference between the total (analytical) water concentration, c_w, and the "free" bulk water concentration, c_b, divided by the solute concentration, c, yielding

$$Z_t = \frac{c_w - c_b}{c} \tag{3.4}$$

Z_t comprises all water molecules whose dynamics are slowed down sufficiently by the presence of the solute so as to make them distinguishable from bulk water. Depending on the strength of the solute-solvent interactions, this might include water dipoles which "disappear" completely from the DR spectrum and/or solvent molecules which are moderately retarded in their dynamics and thus appear as a distinct mode at lower frequencies compared to the bulk-water mode. While the latter corresponds to the slow-water mode, which could be directly observed in the present AcChCl(aq) and CarCl(aq) DR spectra, the former is often referred as "frozen" or irrotationally bound (ib) water, caused by strong

solute-water interactions [22]. The effective hydration number of ib-water can be defined as

$$Z_{\mathrm{ib}} = Z_{\mathrm{t}} - Z_{\mathrm{s}} \tag{3.5}$$

where Z_{s} is the number of moderately bound water molecules per unit of solute concentration:

$$Z_{\mathrm{s}} = \frac{c_{\mathrm{s}}}{c} \tag{3.6}$$

with c_{s} being retrieved from Equation 1.48 and the slow-water amplitude, S_2.
The thus obtained hydration number refers to the whole salt. To acquire the more interesting single ion values, ionic additivity has to be assumed and the effective hydration number of a model salt, $\mathrm{C}_n\mathrm{A}_m$, can be written as $Z_i(\mathrm{C}_n\mathrm{A}_m) = Z_i(\mathrm{C}^{m+}) + Z_i(\mathrm{A}^{n-})$ (i = t, s, ib). Strictly speaking, this assumption is only valid at infinite dilution. However, it was found to hold (at least approximately) at finite solute concentrations [22]. Additionally, it is required to make appropriate "single ion" assumptions for the Z_i values for one of the ions. Taking into account previous dielectric measurements of salts such as $\mathrm{Et_4NCl(aq)}$ [156] $Z_{\mathrm{t}}(\mathrm{Cl}^-) \approx 0$ could be readily adopted for all concentrations [22].
Note that in the above approach, all water dipoles which bear the same dynamics are regarded as one distinct species (slow-water or bulk-like water) and they are treated as if they can rotate freely (though at different timescales). However, this is not necessarily the case in solution, as some molecules might be confined in their rotational angle due to intermolecular interactions and consequently these dipoles cannot fully contribute to $S_{\mathrm{b}}^{\mathrm{ap}}$ or S_2, respectively. This leads to non-integer numbers of Z_{t}, Z_{s} and Z_{ib}.
The obtained hydration numbers of the two neurotransmitter cations, $\mathrm{AcCh^+(aq)}$ and $\mathrm{Car^+(aq)}$, as a function of concentration are shown in Figure 3.11. For both neurotransmitters the total hydration number, Z_{t}, and the number of irrotationally bound $\mathrm{H_2O}$ dipoles, Z_{ib}, decrease with rising c. This decrease of hydration numbers is physically reasonable as hydration shells of solute molecules increasingly overlap at higher concentrations and, accordingly, the ratio of mobile water dipoles increases [186]. Interestingly, no such decrease could be observed for Z_{s}, as its value stayed virtually constant over the present concentration range for both cations. This peculiar behavior might be explained by regarding the dehydration of both neurotransmitters with increasing c as a flowing and gradual process: the amount of water molecules impeded in their dynamics, either moderately retarded or strongly bound water dipoles, decreases continuously with increasing steric crowding, *i.e.*, high solute concentrations. However, the initially "frozen" $\mathrm{H_2O}$ dipoles do not regain their full mobility, but rather contribute as slow-water in the DR spectra. Accordingly, $Z_{\mathrm{s}}(c)$ would be expected to decrease more slowly compared to $Z_{\mathrm{ib}}(c)$ [162]. In the case of $\mathrm{AcCh^+(aq)}$ and $\mathrm{Car^+(aq)}$, the effective number of water dipoles disappearing from the initial slow-water fraction equals the number of initially irrotationally bound $\mathrm{H_2O}$ dipoles, which recover some (but not all) of their mobility, leading to a constant Z_{s} over the whole concentration range.
Note that the overall dehydration of both neurotransmitters with increasing c is consistent with the discussion of their experimental dipole moments in the previous section (Section 3.1.5). Similar to the less steeper decrease of μ_{eff} (Figure 3.7) and C (Figure 3.10) for

Car^+(aq) with rising c in comparison to $AcCh^+$(aq), the obtained hydration numbers of Car^+(aq) drop noticeably slower (Figure 3.11), which supports the argument of a link between the hydration state and the effective dipole moment of the NT.
The Z_t and Z_s values of Car^+(aq) (Figure 3.11(b)) are generally slightly higher than those of $AcCh^+$(aq) in the present concentration range (Figure 3.11(a)). Accordingly, the respective effective hydration numbers at infinite dilution, obtained by extrapolation of $Z_i(c)$ to $c \to 0$, are systematically lower for $AcCh^+$(aq) (Table 3.5). Note that both Z_t^0 values, ~ 11 for $AcCh^+$(aq) and ~ 13 for Car^+(aq), are lower than the number of H_2O molecules which can be packed into the first solvation layer of the cations, which was found to be ~ 40 for both molecules (geometries obtained from Gaussian 09 at the B3LYP/6-31G(d,p) level with the PCM solvation model). The slight difference in the hydration strength might originate from the varying chemical structure of both molecules: the acetyl group in $AcCh^+$(aq) is replaced by a carbamoyl group in Car^+ (Figure 3.1). The difference between these two functional groups lies in the substitution of the hydrophobic methyl group by a polar amine moiety at the acyl carbon. The amine group of Car^+(aq) posses two hydrogen atoms, enabling the formation of H-bonds between -NH_2 and H_2O molecules. As indicated by the present results, these amide-water interactions effectively decelerate a higher number of water dipoles compared to the acetyl group, which thus lead to an increase in Z_s, and consequently Z_t. Note that within the error limits $Z_{ib}(Car^+) \approx Z_{ib}(AcCh^+)$ (Table 3.5), which implies that the -$NH_2 \cdots H_2O$ interactions are not strong enough to additionally "freeze" water molecules on the DR timescale. It should also be pointed out that the non-polar -CH_3 moiety itself slows down approximately $2-3$ H_2O molecules in its hydration layer, as reported by GHz-THz dielectric spectroscopy [187] and fs-IR experiments [188], hence contributing to the overall Z_s value of $AcCh^+$(aq).
As will be shown in Section 4.2 and as reported previously [156], $Z_{ib}(Me_4N^+) \approx 0$ and $Z_{ib}(Et_4N^+) \approx 0$, implying that the presence of strongly bound water in AcChCl(aq) and CarCl(aq) is most probably linked to the acetyl and carbamoyl moiety, respectively, with both of these groups "freezing" $\sim 4-3$ H_2O molecules at vanishing c. The neutron diffraction study by Hulme *et al.* [145] and a computational study of Margheritis and Corongiu [147] reported rather weak ether-oxygen-H_2O interactions, suggesting that the carbonyl group is mainly involved in the strong binding of the water dipoles. Hernández *et al.* [146] found evidence for pronounced bonding between the carbonyl oxygen of AcCh and water, which supports this view. Correspondingly, the calculated minimum-energy structures of AcCh+x·H_2O and Car+x·H_2O (Figures 3.8 and 3.9) show a preferential arrangement of the water molecules next to the carbonyl moiety, with the one of the water hydrogen directly interacting the carbonyl oxygen. A dielectric relaxation study combined with MD simulations on aqueous 1,3-dimethylurea solutions revealed ~ 2 H_2O molecules being irrotationally bound by its carbonyl group [189]. The $Z_{ib}^0 \approx 4-3$ found by DRS (see above) of AcCh and Car is slightly higher, but fairly consistent with these numbers (error of $Z_{ib}^0 \approx \pm 1$).
Although the interaction strength of water with an onium group (-N^+Me_3) is not high enough to irrotationally bind the solvent molecules of the DR timescale [173], about ~ 6 H_2O dipoles were found to be impeded in their dynamics by the closely-related Me_4N^+

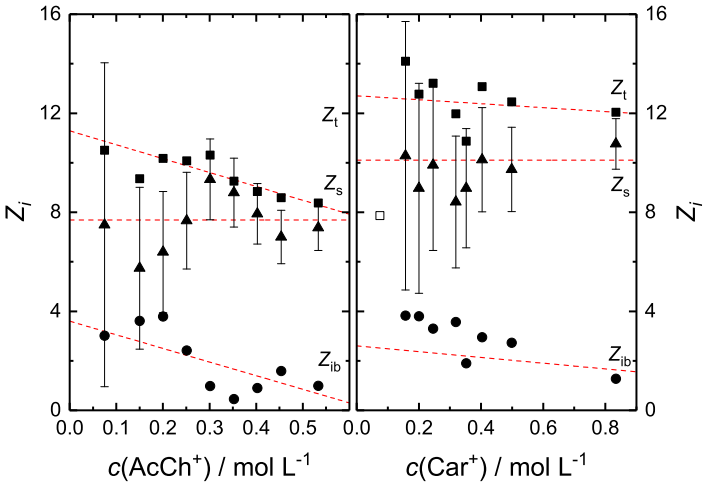

Figure 3.11: Total effective hydration numbers, Z_t(■), and the numbers of moderately retarded, Z_s(▲), and irrotationally bound water, Z_{ib}(●), of (a) AcCh$^+$(aq) and (b) Car$^+$(aq) as a function of concentration at 25 C. Dashed lines denote weighted linear fits. The intercept of $Z_{ib}(c)$, Z^0_{ib}, was fixed to $Z^0_t - Z^0_s$. Error bars of Z_t and Z_{ib} were omitted for the sake of clarity. Unfilled symbols were not included in the fits.

cation at vanishing c, so as they appear as a separate slow-water mode in the DR spectra (Section 4.2). Assuming additivity of hydration numbers of the functional groups of both NTs, this would suggest that $Z^0_s(\text{AcCh}^+) - Z^0_s(\text{Me}_4\text{N}^+) \approx 2$ and $Z^0_s(\text{Car}^+) - Z^0_s(\text{Me}_4\text{N}^+) \approx 4$ water molecules can be attributed to the non-onium parts of the molecules, respectively. Note that the obtained non-onium hydration number of AcCh coincides well with the number of water dipoles slowed down by hydrophobic hydration of a methyl group ($\sim 2-3$) [187, 188], as already mentioned previously.
The hydration numbers of the 0.3738 mol kg^{-1} AcChCl(aq) solution are shown as a function of temperature in Figure 3.12. While the number of irrotationally bound solvent molecules, Z_{ib}, which was fairly small, stayed constant within the error bars, the num-

Table 3.5: Infinite dilution hydration numbers, Z^0_t, Z^0_s and Z^0_{ib} of AcCh$^+$(aq) and Car$^+$(aq) at 25 C. The errors were obtained from the linear regression.

	Z^0_t	Z^0_s	$Z^{0\,a}_{ib}$
AcCh$^+$(aq)	11.3 ± 0.4	7.7 ± 0.3	3.6 ± 0.7
Car$^+$(aq)	12.7 ± 0.7	10.1 ± 0.3	2.6 ± 1

$^a Z^0_{ib}$ were calculated from the extrapolated Z^0_t and Z^0_s values according to $Z^0_{ib} = Z^0_t$ - Z^0_s

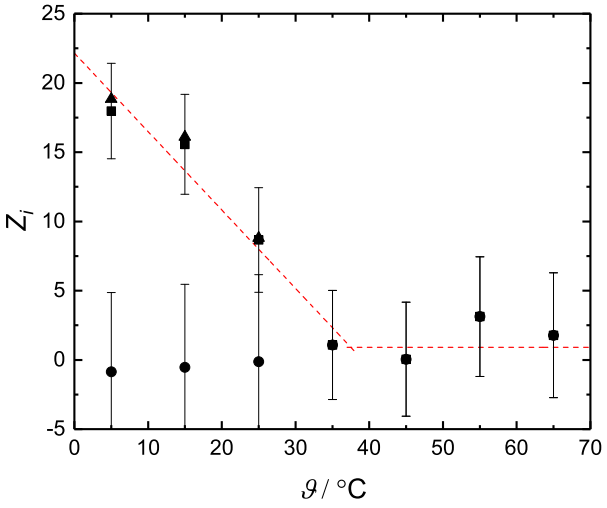

Figure 3.12: Total effective hydration numbers, Z_t(■), and the numbers of moderately retarded, Z_s(▲), and irrotationally bound water, Z_{ib}(●), of 0.3738 mol kg^{-1} AcCh$^+$(aq) and as a function of temperature, ϑ. Dashed lines are visual guides to $Z_t(\vartheta)$. Error bars of Z_s were omitted for the sake of clarity.

ber of moderately bound water molecules, Z_s, decreased rather fast with increasing T, consistent with increased thermal motion. Such rapid breakdowns of hydration with increasing temperature were previously reported for the dehydration of hydrophobic moieties (-CH_3) [160, 187]. It was thus concluded that the hydrophobic hydration effect is reduced at elevated temperatures. This effect might explain the vanishing of slow-water in the present AcChCl(aq) system. Accordingly, it may be deduced that the slow-water fraction in AcChCl(aq) solutions most probably originates to a large extend from the hydration of hydrophobic parts of the acetylcholine molecule, rather than hydrophilic moieties.

3.1.7 RISM Calculations of AcChCl(aq) solutions

To obtain further information on the solute-solvent interactions at a molecular level, RISM calculation of aqueous solutions of AcChCl were performed [148].
The minimum-energy conformation of AcCh$^+$ in water was obtained as follows. As a start Monte Carlo/Stochastic Dynamics calculations using the OPLSA-2005 force field with implicit water model were performed [190], which yielded 100 conformations for the AcCh cation. After removing redundant conformers, non-redundant minimum-energy conformations served as the input for the subsequent DFT calculations using the B3LYP density functional and a 6-31++G(d,p) basis set with the Poisson-Boltzmann finite element method as implemented in Jaguar (Schrödinger Suite 2017-3) to account for solvation effects [191–

194]. From the output of these QM calculations site charges were calculated with the ESP method [195]. The spatial configuration of acetylcholine ion with the corresponding numbering of atoms as well as the obtained configuration of the two obtained most stable conformers of AcCh, namely the *trans, gauche* (red) and *trans, trans* (green) conformers, are shown in Figure 3.13.
The 1D-RISM equations were solved on a 1D-grid of 16384 points with a spacing of $2.5 \cdot 10^{-3}$ nm with 10 MDIIS vectors. The 3D-RISM equations were solved on a 3D-grid of $270 \times 270 \times 256$ points with 4 MDIIS vectors and with a spacing of 0.025 nm. A residual tolerance of 10^{-6} was selected. The calculations were performed at varying AcChCl concentrations (c(AcChCl) = infinite dilution, 0.07, 0.15, 0.20, 0.25, 0.30, 0.35, 0.40, 0.45, 0.53 M) under ambient conditions.
The 1D-RISM theory provides site–site (atom-atom) radial pair distribution functions (PDFs), $g_{\alpha\beta}(r)$, describing the probability density of the distribution of sites (atoms) α and β belonging to different particles (molecules, ions) in the investigated system. In the present RISM study, only solute-solvent PDFs were calculated, yielding information on the hydration of the molecule. The analysis of $g_{\alpha\beta}(r)$ allows the determination of interatomic solute-solvent distances, $r_{\alpha\beta}$, and site-specific coordination numbers, $n_{\alpha\beta}$, *via*

$$n_{\alpha\beta} = 4\pi\rho_\beta \int_0^{r_{\min}} g_{\alpha\beta}(r) r^2 \mathrm{d}r \tag{3.7}$$

where ρ_β is the average number density of atoms/sites of kind β. The integration limit, $r_{\min}$ is defined by the position of the first minimum of the PDF and corresponds to the radius of the first coordination shell around atom/site α.
The spatial distribution functions (SDFs), $g_\beta(\vec{r})$, obtained by 3D-RISM theory, gives the distribution function of solvent atoms, β, around the solute molecule. These are commonly represented by isodensity surfaces at a certain probability level. Integration over the volume, V_s, occupied by the first hydration shell of the solute, yields the total coordination number of the solute, n_t:

$$n_\mathrm{t} = \rho_\beta \int_0^{V_\mathrm{s}} g_\beta(\vec{r}) \mathrm{d}V \tag{3.8}$$

As $AcCh^+$ is not spherical, its hydration shell is expected to be non-spherical as well. In this case, a special approximation for the first hydration shell of the solute as a closed surface with arbitrary shape as suggested by Fedotova and Kruchinin earlier [18] was used. The obtained hydration parameters of AcChCl(aq) were found to have a weak concentration dependence. The peak-heights as well as their positions of the PDFs practically did not change with varying c. The partial coordination numbers were found to decrease only by $\sim 7 - 8\,\%$ over the whole concentration range. Consequently, only the limiting cases, *i.e.*, infinite dilution and c(AcChCl) = 0.53 M, will be discussed here. Note that the changes in Z_t with increasing concentration are significant (Figure 3.11). This discrepancy points out the difference between the hydration number as obtained by DRS, which comprises (cooperative) dynamical information, and the coordination number obtained by RISM calculation, which gives the structural information of hydration of specific molecular sites.

As shown in Table A.6, the differences between the *trans, gauche* and the *trans, trans* conformers are rather small, with the largest differences being observed for the partial coordination numbers of the ether oxygen O7. The reasons for that will be discussed further below. The following discussion will mainly focus on the hydration structure of the *trans, gauche* conformer (unless otherwise specified) as the most interesting example.
In total ~ 30 water molecules can be found in the primary hydration shells of $AcCh^+$ at infinite dilution. Hence, most of the hydration water is not noticeably affected in their dynamics (Figure 3.11). The PDFs of the onium-nitrogen and the water oxygen, $g_{\mathrm{NOw}}(r)$, show a first intensive maximum at $\sim 0.428\,\mathrm{nm}$ (Figure 3.14(a), Table A.6). A similarly strong correlation can also be found in $g_{\mathrm{Cm2Ow}}(r)$ at $\sim 0.312\,\mathrm{nm}$ (Figure 3.14(b), Table A.6). Integration of $g_{\mathrm{Cm2Ow}}(r)$ yields $n_{\mathrm{Cm2Ow}} \approx 6$ and thus a total number of $n_{\mathrm{onium}} \approx 18$ for the $\text{-}N^+Me_3$ moiety. The height of the first peak of $g_{\mathrm{Hm2Ow}}(r)$ at ~ 0.235 (Figure 3.14(b), Table A.6) is less than unity, stating the absence of H-bonding between the methyl groups and the hydration water. The SDFs, shown in Figure 3.16, suggest that the water molecules are located close to the voids between the methyl groups. Similar hydration patterns with remarkably similar $g_{\mathrm{Cm2Ow}}(r)$ and $g_{\mathrm{Hm2Ow}}(r)$ were reported for the onium moieties of choline and chlorocholine by a combination of DRS and RISM calculations [173], for acetylcholine [145] and a phosphocholine lipid [196] both by a combination of neutron diffraction and MD simulation. The quoted studies found n_{onium} values of ~ 18, ~ 23 and ~ 17, respectively. A similar hydration structure was also found for trimethylamin-N-oxide (TMAO) [197] and glycine betaine [198]. Hulme *et al.* [145] could show that the H_2O molecules align their dipoles nearly tangentially to the $\text{-}N^+Me_3$ surface. These water molecules avoid bonds to the onium group and form H-bonds among each other instead. Given the similarities in the hydration patter, it is reasonable to assume an analogous situation for $AcCh^+$, and most likely also Car^+. Such a hydration feature is typical for the hydration of hydrophobic groups. A similar orientation of water molecules was also reported for the hydration of the Me_4N^+ cation [48, 49, 199, 200]. Obviously, the hydrophobic methyl groups shield the positive charge on the nitrogen. Although RISM calculations do not give any information on the dynamics of hydration water, this picture is consistent with the assignment of the major fraction of the slow-water, Z_{s}, to be due to the hydrophobic hydration of the onium group, as discussed above. Interestingly, the slow water relaxation mode was not resolved in the DR spectra of choline chloride and chlorocholine chloride in Reference [173]. However, some slow-down in the form of increasing "bulk-like" water relaxation time and increasing "bulk-like" water width parameter was detected, which indicates that in the case of choline and chlorocholine the deceleration of this fraction of water (although present) was not large enough to allow the detection of a separate slow-water mode.
The PDFs of the backbone CH_2 groups (b1 and b2) and the methyl group at the acyl carbon (m1) are shown in Figure A.8. The large distances between the water oxygens and these groups can be regarded as an evidence for their hydrophobic hydration.
From the comparison of the r_{O2Ow} and r_{O2Hw} distances (Table A.6) and the high intensities of the first peaks of the $g_{\mathrm{O2Ow}}(r)$ and $g_{\mathrm{O2Hw}}(r)$ (Figure 3.15(a)), it can be deduced that the carbonyl oxygen interacts with water by H-bonding. Approximately two H_2O molecules were found to be H-bonded to the hydrophilic carbonyl group (Table A.6), which is in

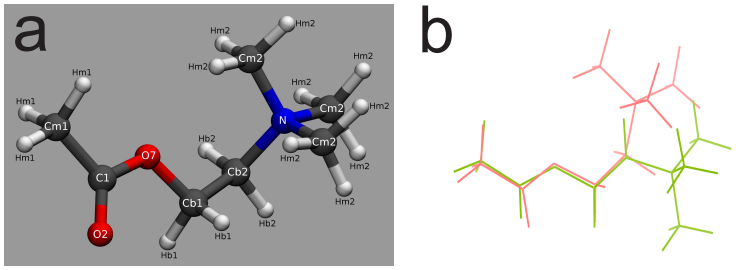

Figure 3.13: (a) The spatial configuration of AcCh with the corresponding numbering of atoms. (b) The configuration of the investigated *trans, gauche* (red) and *trans, trans* (green) conformers.

agreement with the results from neutron diffraction [145]. The SDFs depicted in Figure 3.16 show that the most probable location of water hydrogens is in the proximity of the carbonyl oxygen. This result is consistent with the discussion of the Z_{ib} values in the previous section (Section 3.1.6), where the presence of irrotationally bound water was discussed to be mainly linked to strong binding of water molecules to the carbonyl oxygen. The low intensities (less than unity) and the location of the first peaks of the PDFs $g_{\mathrm{O7Ow}}(r)$ and $g_{\mathrm{O7Hw}}(r)$ (Figure 3.15(b)) indicate only limited interaction of the ether oxygen with the water molecules. This result is consistent with previous studies on $AcCh^+$ hydration [145, 147].
As noted above, the hydration of the ether oxygen shows some differences between the two conformers. The first peak of $g_{\mathrm{O7Ow}}(r)$ of the *trans, trans* conformer (Figure 3.15(b)) is markedly more pronounced compared to the *trans, gauche* conformation. Accordingly, the respective partial coordination number of the *trans, trans* conformer is higher by ~ 1. Probably, this discrepancy can be explained by the close locations of one of the methyl group in $\text{-N}^+\text{Me}_3$ moiety and the oxygen O7 atom in the *trans, gauche* conformation (Figures 3.13(b) and 3.16(a)). Such spatial arrangement can limit the access of water molecules to the O7 atom. In the case of *trans, trans* conformation, there are no steric limitation caused by the onium moiety and the interaction with the H_2O molecules is sterically feasible. The higher probability of H-bonding between the water molecules and the ether oxygen for the *trans, trans* conformer is also shown in SDFs of Figure 3.16(b). The small white region at O7 indicates a higher tendency of water H-atoms to be located near the ether oxygen, in contrast to the *trans, gauche* conformation, where no such feature could be observed (Figure 3.16(a)). As also noted in literature [36], the *trans, trans* conformation is thus best suited for the H-bond formation with water.

3.1.8 Concluding Remarks

The dielectric spectra of AcChCl(aq) and CarCl(aq) could be satisfactorily fitted with four Debye modes. In contrast to the spectra of AcChCl(aq), an ion pair/ion cloud relaxation mode could be resolved for CarCl(aq). However, due to the inability of separation of the

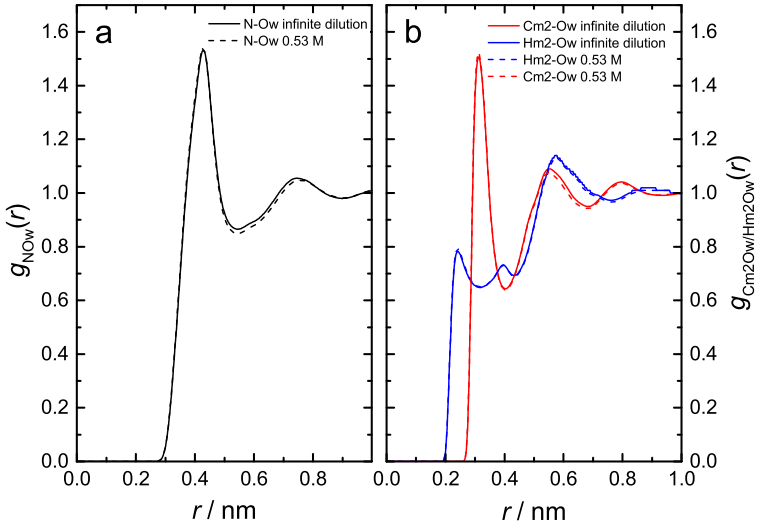

Figure 3.14: PDFs (a) g_{NOw}, (b) g_{Cm2Ow} and g_{Hm2Ow} for the *trans, gauche* conformer of AcCh in aqueous solution at infinite dilution and the highest concentration of 0.53 M.

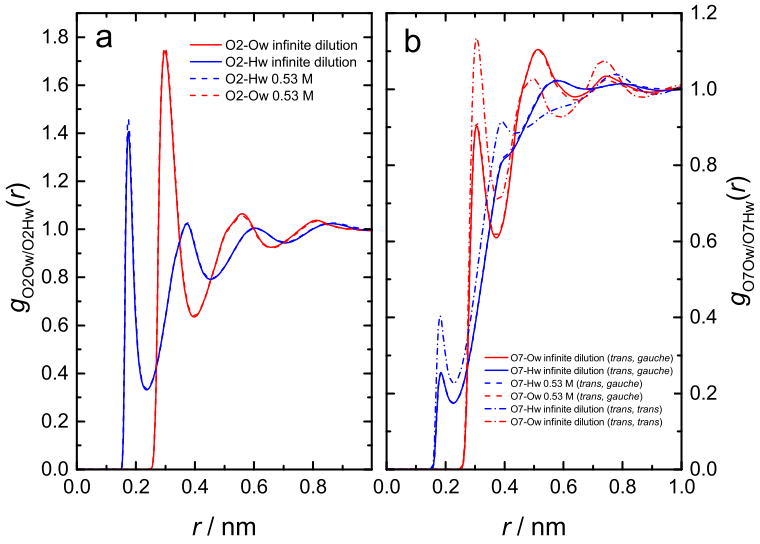

Figure 3.15: PDFs (a) g_{O2Ow}, g_{O2Hw} and (b) g_{O7Ow}, g_{O7Hw} for the *trans, gauche* conformer of AcCh in aqueous solution at infinite dilution and the highest concentration of 0.53 M. Additionally, g_{O7Ow} and g_{O7Hw} of the *trans, trans* conformer at infinite dilution are shown for comparison.

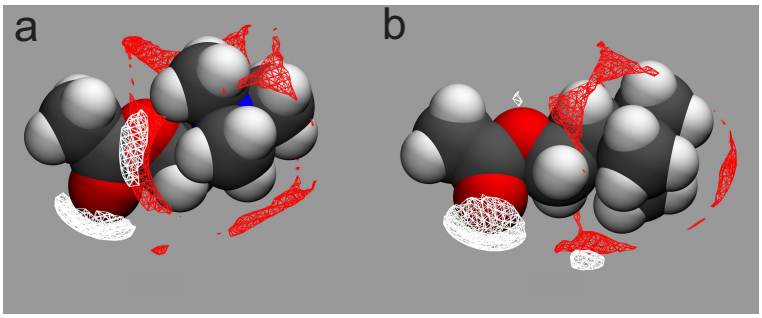

Figure 3.16: Spatial distribution functions of the oxygen (red) and hydrogen (white) atoms of water around (a) the *trans, gauche* conformation and (b) the *trans, trans* conformation of $AcCh^+$. The isodensity surfaces correspond to the SDF values of $g_{\text{AcCh-Ow}} = 3.5$ and $g_{\text{AcCh-Hw}} = 3.5$.

IC contribution from the dielectric spectra, the obtained association constants of Car^+-Cl^--IPs were too high compared to dilute-solution conductivity measurements. The latter indicate that IP formation is small but not negligible in aqueous solution of both salts, with a slightly higher formation constant for CarCl(aq) compared to AcChCl(aq). The analysis of the solute reorientation mode revealed a decrease of the effective dipole moment with increasing c for both NTs (Figure 3.7). Several reasons for the systematic change were discussed. A comparison of the experimental values with the calculated dipole moments of neurotransmitter-hydrates and the analysis of the relaxation time of the reorientation process suggests a dehydration effect to be responsible for this feature. Accordingly, the analysis of the solvent relaxation modes showed a decrease of hydration numbers of both NTs with increasing c (Figure 3.11). Whereas the number of strongly bound water dipoles, Z_{ib}, was virtually identical for both NTs, a higher number of moderately retarded water molecules, Z_{s}, was observed for Car^+(aq). The higher Z_{s} value of Car^+ was attributed to the presence of a hydrophilic -NH_2 moiety at Car instead of the hydrophobic methyl group at the acyl carbon of AcCh (Figure 3.1).

The statistical mechanical 1D- and 3D-RISM calculations of AcChCl(aq) solutions were in good agreements with the present DRS results. The strongest water-site interaction was observed for the carbonyl oxygen, which showed pronounced H-bonding to ~ 2 water molecules. This number is somewhat lower but rather comparable (given their errors) with the observed Z^0_{ib} value of $\sim 4-3(\pm 1)$ of AcCh and Car. The interaction of the ether-oxygen and water depended on the conformation of AcCh, but was markedly less pronounced compared to the carbonyl oxygen. The alleged most striking structural feature of both neurotransmitters is the onium headgroup. As discussed by Hulme *et al.* [145] a fast dehydration, especially of the -N^+Me_3 moiety, prior to bonding to hydrophobic binding sites of the receptor proteins is key for its biological activity. The dielectric results and in particular the RISM calculations showed strong features of hydrophobic hydration of the onium group in spite of its charge. The nitrogen atom is deeply buried inside a hydrophobic

shell. The ~ 18 water molecules in its primary hydration sheath preferably interact among each other rather than with the onium group. Such a hydrophobic hydration pattern would certainly facilitate the desolvation process.

3.2 Sodium Glutamate and Glutamine

3.2.1 Introduction

L-glutamic acid or rather the anion, L-glutamate (Glu^-, Glu, Figure 3.17(a)), which is its dominant corresponding form at neutral pH, is the most abundant amino acid and the major excitatory NT in the brain. Its concentration in a healthy brain is rather high (5-15 $mmol\,kg^{-1}$) and an overload of the Glu-receptors was reported to even lead to cell death ("excitotoxicity"). Further, Glu can be found at the crossroads of various metabolic pathways in living organisms [201] and salts of L-glutamic acid are used as flavor enhancer in food industry [202].
Mainly because of its undeniable importance, malfunctions considering the metabolism and molecular recognition of Glu^- are often linked to various diseases and brain dysfunctions [203, 204]. Despite recent insights into the reception mechanism of L-glutamate [201, 204–206], the full action of binding of Glu^- to its receptors, which is evidently connected to its hydration and ion-binding properties, is still not completely understood. The ability of Glu^- to bind to many different kinds of proteins (almost all cells in the human brain express Glu-receptors [201]) was discussed to be linked to its conformational flexibility, with rather low energy barriers between the different geometric arrangements [207].
Previous neutron diffraction [208] and molecular dynamics (MD) simulation studies [15, 209] of aqueous solutions of monosodium glutamte (NaGlu) suggested that the presence of Glu^- leads to a disruption of the H-bond water structure. Furthermore, the propensity for the association into Na^+-Glu^--IPs and and even the possibility of Glu^-–Glu^- aggregates were reported.
The structurally related L-Glutamine (Gln, Figure 3.17(b)) is synthesized in the body from Glu and ammonia by the enzyme glutamine synthetase. Reduced levels of glutamine synthetase might result in too high extraceullular Glu concentration, which was identified to trigger some forms of epilepsy [210]. L-Glutamine is one of the most abundant, nonessential amino acids in the human body with intracellular and extracellular concentrations of 2-20 mM and 0.7 mM, respectively [211]. Owing to the differing chemical side-chain structure of Glu and Gln (carboxylate at Glu^- and carbamoyl moiety at Gln), glutamine is inactive towards Glu-receptors [201]. Gln is not classified as a neurotransmitter, in contrast to Glu^-, but plays a key regulatory role in several cell specific processes, such as metabolism, respiratory burst, cell defense, cell repair, cell proliferation and apoptosis. A more detailed description of the biological relevance of Gln can be found in Ref. [211].
Being proteinogenic amino acids, Glu and Gln are prominent constituent of proteins and are involved in protein-synthesis and degradation. In particular, regions of neighbouring, repeating Gln units can often be identified in proteins responsible for RNA and DNA syn-

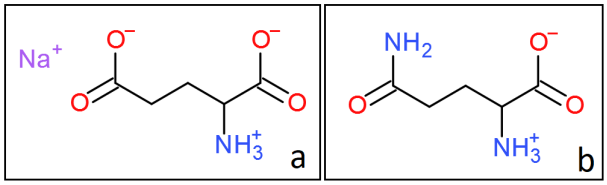

Figure 3.17: Chemical structures of (a) NaGlu and (b) Gln.

thesis [212]. Elongations of such polyglutamine regions (also called PolyQ) are associated with protein misfolding and the development of many degenerative diseases, such as the currently incurable Huntington's disease [212, 213]. Thus, it is not surprising that PolyQ has been a subject of intense research during the last decade [214–216]. The toxicity of PolyQ regions is thought to be related to their propensity to self-association [217, 218]. This aggregation was discussed to be driven by the formation of energetically favorable Gln-Gln H-bonds, which outweigh the Gln-water interactions [219, 220]. Neutron diffraction studies coupled with computational modeling of Gln solutions by Rhys *et al.* [221, 222] claimed that a fairly high number of $\sim 20\,\%$ of Gln molecules are located in "hydrophilic aggregates" (contrary to the classical hydrophobically driven association) in a $\sim 0.2\,\mathrm{M}$ Gln(aq) solution [222]. In contrast to Glu(aq), the bulk-water structure was found to be essentially unchanged upon addition of Gln.
Undoubtedly, the biological action of Glu^- and Gln is manifold and their great biochemical significance is indisputable. To gain a deeper insight into the physico-chemical behaviour of these two amino acids, aqueous solutions of NaGlu and Gln were investigated by the means of dielectric relaxation spectroscopy. Dielectric spectra ($0.05 \leq \nu/\mathrm{GHz} \leq 89$) were recorded and analyzed in the concentration range of $0.1 \lesssim c(\mathrm{NaGlu})/\mathrm{mol\,L^{-1}} \lesssim 1.9$ and $0.05 \lesssim c(\mathrm{Gln})/\mathrm{mol\,L^{-1}} \lesssim 0.23$ at $25\,^\circ\mathrm{C}$, respectively. Further, to investigate the effect of protonation on the behaviour of glutamate, measurements of aqueous solutions of L-glutamic acid (HGlu) with varying degree of protonation, adjusted by addition of NaOH and HCl, were performed at $25\,^\circ\mathrm{C}$.
According to our knowledge, this is the first broadband DRS study of NaGlu(aq) and Gln(aq) solutions at the given frequency and concentration range, although some DR studies of aqueous glutamate solutions within a rather limited ν and concentration region can be found in literature [223, 224].

3.2.2 Data Acquisition and Processing

The NaGlu(aq), HGlu+NaOH/HCl(aq) and Gln(aq) samples were prepared as described in Section 2.1 and 2.2. The pH-values of the amino acid samples were checked at room temperature with a pH-meter (pHenomenal PCL 1000, VWR, Germany) with a calibrated glass electrode. The densities, viscosities and conductivities, determined as described in Section 2.4, are shown in Tables A.7, A.8 and A.9. The permittivity spectra of all samples were recorded in the frequency range $0.05 \leq \nu/\mathrm{GHz} \leq 89$ (Dielectric probe kit VNA

Table 3.6: Static permittivity, ε, relaxation amplitudes, S_j, relaxation times, τ_j ($j = 1, .., 3$), and the infinite frequency permittivity, ε_∞, obtained from the D+D+D model fit of dielectric spectra of NaGlu(aq) solutions at 25 °C.[a,b]

c	ε	S_1	τ_1	S_2	τ_2	S_3	τ_3	ε_∞	χ^2_r
0.101	80.0	3.96	90F	3.63	13.9	66.7	8.14	5.70	0.0323
0.206	81.5	7.72	93.9	3.89	17.6	64.2	8.12	5.68	0.0748
0.406	85.2	14.4	98.1	5.18	21.2	59.5	8.13	6.12	0.0662
0.601	88.6	20.2	109	7.20	24.0	55.1	8.10	6.17	0.0834
0.783	92.1	25.5	121	8.73	26.7	51.4	8.16	6.39	0.1087
0.965	95.6	30.4	134	10.5	29.8	48.2	8.17	6.47	0.1317
1.14	98.5	36.4	144	9.65	29.6	45.7	8.38	6.69	0.0675
1.30	102	41.5	158	11.4	29.2	42.3	8.34	6.87	0.1427
1.44	106	46.0	176	11.7	34.3	41.1	8.64	6.91	0.0687
1.60	109	51.8	190	12.7	32.5	37.8	8.53	6.98	0.1084
1.75	113	56.7	212	12.9	38.4	36.7	8.83	7.13	0.0956
1.90	116	61.4	227	12.8	40.1	35.0	9.04	7.30	0.0782

[a] c in mol L^{-1}, τ_j in ps; [b] parameter values followed by "F" were fixed during fitting.

setup + E-band interferometer, Section 2.3). As mentioned previously, in conductive systems the electrical conductivity determines the effective low-frequency limit, $\nu_{\min}$, at which the experimental noise in η'' exceeds the magnitude of the dielectric loss, ε''. Thus, in the NaGlu(aq) spectra an increase in $\nu_{\min}$ with increasing conductivity, *i.e.*, increasing c(NaGlu), could be observed. The noisy permittivity data in the region 0.05 GHz – $\nu_{\min}$ was always discarded from the spectra and $\nu_{\min}$ was in the region $0.17 \lesssim \nu_{\min}/\text{GHz} \lesssim 0.24$ for the present NaGlu(aq) solutions. For the HGlu+NaOH/HCl(aq) spectra $\nu_{\min}$ was always between 0.05–0.15 GHz.

3.2.3 Relaxation Models and Assignment of Modes

Combinations of up to six HN-equations (Equation 1.41) were tested to fit the dielectric spectra. Taking into account the criteria discussed in Section 2.3.3 a sum of three Debye modes (D+D+D model) was found to best describe the DR spectra of NaGlu(aq) and Gln(aq), while a forth Debye mode was required in some of the HGlu+NaOH/HCl(aq) spectra. The best-fitting parameters are summarized in Tables 3.6, 3.7 and 3.8. The DR spectra of NaGlu(aq), HGlu+NaOH/HCl(aq) and Gln(aq) are shown in Figures 3.19, A.15 and 3.20. The decomposition of exemplary spectra of NaGlu(aq) and Gln(aq) into the individual modes is illustrated in Figure 3.18.

Due to low solubility of Gln in water ($\sim$ 0.27 mol kg^{-1} for Gln *vs.* $\sim$ 2.3 mol kg^{-1} for

Table 3.7: Static permittivity, ε, relaxation amplitudes, S_l, relaxation times, τ_l ($l = 0, .., 3$), and the infinite frequency permittivity, ε_∞, obtained from the (D+)D+D+D model fit of dielectric spectra of HGlu+NaOH/HCl(aq) solutions at 25 °C.[a,b]

pH	c_0(HGlu)	ε	S_0	τ_0	S_1	τ_1	S_2	τ_2	S_3	τ_3	ε_∞	χ^2_r
1.6	0.06132	79.2	1.61	959	1.7	180	4.06	16.0	66.4	8.04	5.47	0.1032
3.1	0.05964	79.4	–	–	1.6	95.3	2.99	18.6	69.3	8.06	5.45	0.1067
4.2	0.05928	79.6	0.239	462	2.0	93.5	2.80	17.0	69.0	8.09	5.51	0.0823
10.9	0.05869	78.9	1.53	441	1.0	165	2.00	15.5	68.7	8.18	5.73	0.0948
12.6	0.05848	76.7	–	–	2.6	171	1.56	20.3	66.9	8.18	5.69	0.1326

[a] c in mol L^{-1}, τ_l in ps; [b] parameter values followed by "F" were fixed during fitting.

Table 3.8: Static permittivity, ε, relaxation amplitudes, S_k, relaxation times, τ_k ($k = 1, .., 3$), and the infinite frequency permittivity, ε_∞, obtained from the D+D+D model fit of dielectric spectra of Gln(aq) solutions at 25 °C.[a,b]

c	ε	S_1	τ_1	S_2	τ_2	S_3	τ_3	ε_∞	χ^2_r
0[c]	78.37	–	–	72.42	8.35	2.43	0.278	3.52	0.0056
0.04758	78.8	1.53	50.7	71.5	8.30	2.26	0.278F	3.52F	0.0202
0.1092	80.0	3.40	63.9	70.7	8.37	2.43	0.278F	3.52F	0.0424
0.1716	81.4	5.95	61.7	69.5	8.33	2.38	0.278F	3.52F	0.0790
0.1878	81.8	6.43	64.1	69.4	8.36	2.41	0.278F	3.52F	0.0641
0.2166	82.3	7.14	67.3	68.9	8.41	2.73	0.278F	3.52F	0.0777
0.2310	82.6	7.67	67.5	68.5	8.50	2.83	0.278F	3.52F	0.0768

[a] c in mol L^{-1}, τ_k in ps; [b] parameter values followed by "F" were fixed during fitting; [c] taken from Ref. [97].

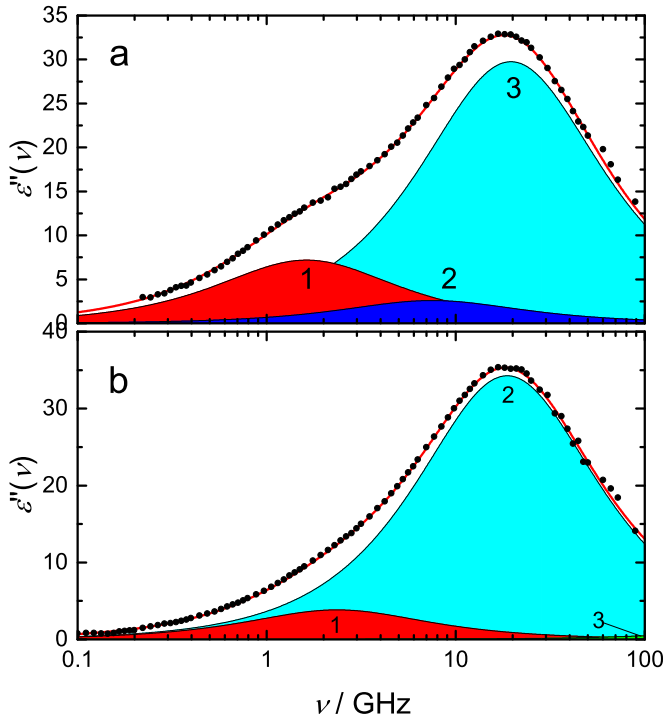

Figure 3.18: Dielectric loss, $\varepsilon''(\nu)$, spectrum of (a) 0.406 M NaGlu(aq) and (b) 0.2310 M Gln(aq) solution at 25 °C. The symbols denote the experimental values and the lines indicate the fits. The shaded areas show the contributions of the D+D+D model.

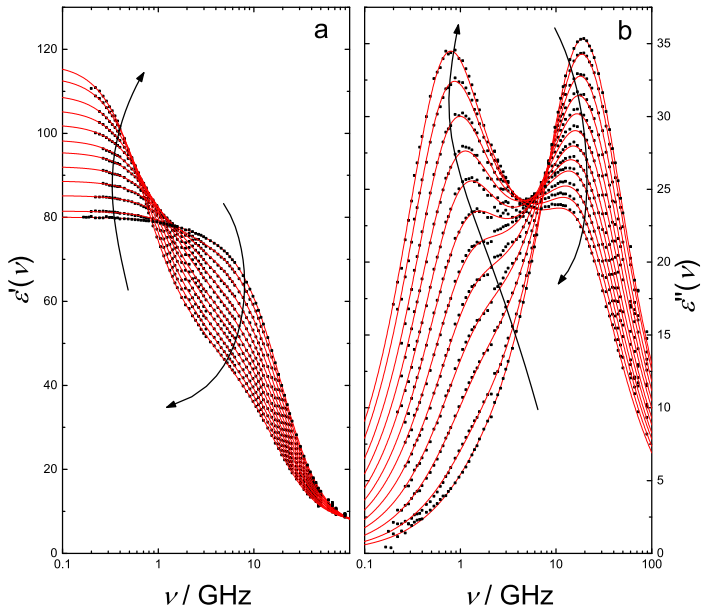

Figure 3.19: Relative permittivity, $\varepsilon'(\nu)$, and dielectric loss, $\varepsilon''(\nu)$, spectra of NaGlu(aq) ($0.101 \leq c/\mathrm{mol\,L^{-1}} \leq 1.90$) at 25 °C. Symbols denote the experimental data. Solid lines represent the fits. Arrows indicate the trend with increasing solute concentration.

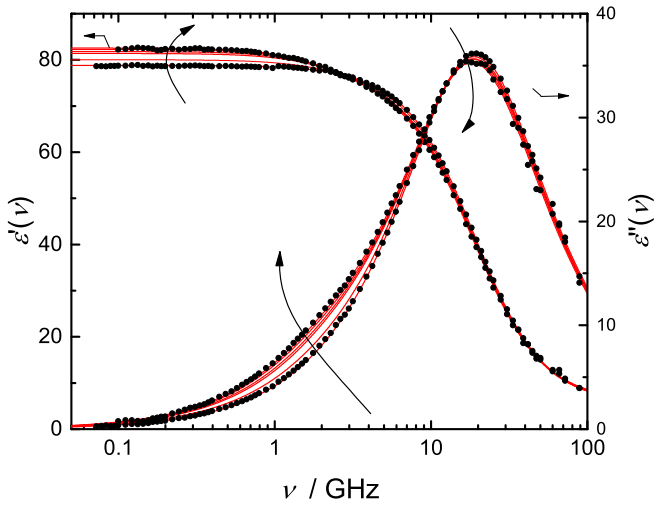

Figure 3.20: Relative permittivity, $\varepsilon'(\nu)$, and dielectric loss, $\varepsilon''(\nu)$, spectra of Gln(aq) ($0.04758 \leq c/\mathrm{mol\,L^{-1}} \leq 0.2310$) at 25 °C. Symbols denote the experimental data. For visual clarity experimental points are only shown for selected samples. Solid lines represent the fits. Arrows indicate the trend with increasing solute concentration.

NaGlu [225]) and thus a narrower investigated concentration range, the observed effects of increasing solute concentration are less pronounced in the spectra of Gln(aq) (Figure 3.20) compared to NaGlu(aq) (Figure 3.19). However, there are some unmissable similarities between the two sets of spectra. The static permittivity, ε, increased continuously with increasing solute concentration (Table 3.6 and 3.8, Figures A.12 and A.13) and the slope $\mathrm{d}\varepsilon/\mathrm{d}c = 20\,\mathrm{L\,mol^{-1}}$ was found to be equal for both systems. Similar increasing trends of ε were observed previously for various amino acid solutions [162, 226–228]. An increase of ε upon addition of a solute into the solvent (water) indicates the presence of highly dipolar solute-related species in solution, whose squared dipole moment normalized by the effective volume of this species is higher than the respective solvent value (Eq. 1.48).

Upon addition of the amino acid, a mode $j, k = 1$ centered at $\sim 0.7{-}1.8\,\mathrm{GHz}$ ($\sim 90{-}230\,\mathrm{ps}$) for NaGlu(aq) and $\sim 2.5 - 3.2\,\mathrm{GHz}$ ($\sim 50 - 70\,\mathrm{ps}$) for Gln(aq) appeared in both sets of spectra. Its relaxation time and amplitude increased with rising c (Table 3.6 and 3.8, Figures A.12 and A.13). At $c(\mathrm{NaGlu}) \geq 1.44\,\mathrm{M}$ it even became the most intense relaxation process in the DR spectra. Judging by its relaxation time and given the fact that the $\mathrm{Glu^-}$ anion and the Gln zwitterion are dipolar molecules, it is reasonable to assign this process to the reorientation of the amino acid dipoles. Note that the spherical $\mathrm{Na^+}$ cation does not posses a permanent dipole moment and is thus "invisible" in the DR spectra.

Further, all spectra exhibited a mode centered at $\sim 19\,\mathrm{GHz}$ ($\sim 8.5\,\mathrm{ps}$), which was dominant for the most spectra (except for NaGlu(aq) at $c \geq 1.44\,\mathrm{M}$). The amplitude of this mode,

which corresponds to process $j = 3$ in Figure 3.18(a) and mode $k = 2$ in Figure 3.18(b), respectively, decreased with increasing solute concentration (Table 3.6 and 3.8, Figures A.12 and A.13). It can unambiguously be assigned to the cooperative relaxation of the H-bond network of bulk-like water molecules, based on its location and intensity [22].
Besides the marked similarities, there are also some noticeable differences. As mentioned further above (Section 3.1), investigations of pure water up to the terahertz regime [150] show evidence for the presence of an additional, less intense relaxation process at $\sim$ 600 GHz, designated as fast-water (Section 3.1). Since this process is centered outside the studied frequency, it could only be resolved for Gln(aq) by fixing its relaxation time and the infinite-frequency permittivity to the neat water values (Table 3.8), while for NaGlu(aq) it was found that a similar approach yielded a worse description of the experimental spectra. Accordingly, the fast-water process was not resolved directly in the DR spectra of NaGlu(aq), but was incorporated into ε_∞, as implied by its rather high value of $\varepsilon_\infty \approx 6 - 7$ (Table 3.6). Accordingly, in the following the fast water contribution in such case was taken into account in the calculation of the total apparent bulk-water amplitude by $S_\mathrm{b}^\mathrm{ap} = S_3 + \varepsilon_\infty(c) - \varepsilon_\infty(0)$ (in contrast to Eq. 3.3). Note that the inability to directly resolve the fast-water mode might indicate that this process is shifted to higher frequencies compared to neat water, induced by the the presence of Na^+ and Glu^- ions.
Moreover, in contrast to Gln(aq), an additional relaxation, located at $\sim 4-11$ GHz ($\sim 14-40$ ps), was discernible in the NaGlu(aq) spectra (Table 3.6). This observation is consistent with the "unbiased" results of the Zasetsky analysis of the dielectric spectra, which suggests the presence of a similar process in the NaGlu(aq) spectra (Figure A.9), while no such mode was discernible in the Zasetsky plot of the Gln(aq) spectra in the investigated concentration range (Figure A.11). Its amplitude, S_2, increased with increasing c (Table 3.6, Figure A.12). The magnitude and relaxation time is typical for slow-water, which originates from H_2O dipoles slowed down in their dynamics either by hydrophobic or moderately hydrophilic hydration of the solute [152, 154, 156–160, 162–164] (Section 3.1). For the present NaGlu(aq) spectra the retardation factor for the slow-water fraction, $r = \tau_2/\tau_3$, increased with concentration from ~ 1.7 to ~ 4.4 (Figure A.14).
The fitting model applied to the DR spectra of the HGlu+NaOH/HCl solutions and the assignment of modes are essentially equal to NaGlu(aq), which is not surprising since Glu^- is the single deprotonated form of HGlu. However, for some of the spectra an additional low-frequency mode $l = 0$ (Table 3.7) was resolved. The neglect of this mode during fitting resulted in higher χ_r^2 values and the retrieved parameters became unphysical. Based on its location and intensity, two different relaxation mechanisms would to come into question to explain its appearance. On the one hand, relaxation of dipolar IPs, consisted of protonated/deprotonated HGlu molecules and Na^+ and Cl^-, respectively, would be conceivable for such a process. On the other hand, the effect of IC-relaxation [55, 165] in low-concentrated electrolyte solutions is always present (Section 3.1). To fully clarify this issue measurements of a proper concentration series of HGlu+NaOH(aq) and HGlu+HCl(aq) would be necessary.
Here, it should be pointed out that the solubility of HGlu in water is rather low ($\sim 0.06\,\mathrm{mol\,kg^{-1}}$), which restricts the execution of extended concentration dependent dielectric

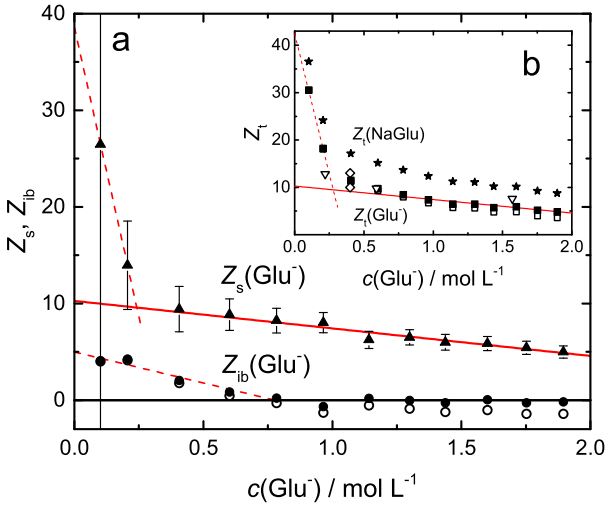

Figure 3.21: (a) The number of moderately retarded, $Z_s(Glu^-)$ (▲), and irrotationally bound water, $Z_{ib}(Glu^-)$ (●, ○), of Glu^-(aq) as a function of glutamate concentration, $c(Glu^-)$. (b) Total hydration number of NaGlu, $Z_t(NaGlu)$ (★), and resulting values for the glutamate anion, $Z_t(Glu^-)$ (■, □). Open symbols for $Z_t(Glu^-)$ (□) and $Z_{ib}(Glu^-)$ (○) were calculated assuming fully hydrated Na^+(aq) ions; closed symbols assume partial dehydration of the cation (see text). Solid and dashed lines show empirical straight line fits in the higher and lower concentration region, respectively. For clarity error bars are only shown for $Z_s(Glu^-)$. Also included in (b) are the simulation results of Leenders *et al.* [229] (◇) and Daub *et al.* [15] (▽) for the total number of H_2O molecules coordinating the carboxylate moiety of Glu^-.

studies on this system. At the same token, the intensity of the resolved solute-related relaxation modes is rather low (Table A.15). The resolution of such relaxation processes, especially in conductive systems, can be fairly problematic due to the limited sensitivity of the DRS experiment. Thus, in particular the parameters of the weak amino acid mode $l = 1$ should be taken with a grain of salt in the HGlu+NaOH/HCl(aq) systems (Table A.15). Despite this limitation, some (semi-)quantitative information can still be deduced from the relaxation parameters of this system, which will be discussed in the following section.

3.2.4 Solvent Relaxations - Hydration

NaGlu(aq). As described in Section 3.1.6, the amplitudes of the solvent-related relaxation modes ($j, l = 2, 3$ for NaGlu(aq) and HGlu+NaOH/HCl(aq); $k = 2$ for Gln(aq)) can be analyzed quantitatively to obtain hydration numbers.

Figure 3.21 shows the thus obtained Z_t data for NaGlu(aq) and the derived single ion values, $Z_t(Glu^-)$, $Z_s(Glu^-)$ and $Z_{ib}(Glu^-)$, as a function of glutamate concentration. Since for sodium ions $Z_s(Na^+) = 0$, it can readily be assumed that $Z_t(Na^+) = Z_{ib}(Na^+)$ [55, 186]. Thus all detected slow water can be assigned to glutamate, yielding $Z_s(Glu^-)$ values that drop linearly for $c(\text{NaGlu} \geq 0.406\,\text{M}$ (Figure 3.21(a)). Under the assumption of additivity of ionic hydration numbers, *i.e.*, that the hydration shell of Na^+ is unaffected by the presence of glutamate (or to be more precise: equally affected as in non-associating NaCl(aq) solutions [55]), the values denoted by open symbols in Figure 3.21 were obtained for $Z_t(Glu^-)$ and $Z_{ib}(Glu^-)$, with increasingly negative numbers for the latter at $c(\text{NaGlu}) > 0.7\,\text{M}$. This unphysical result possibly reflects uncertainties in the experimental data and the assumptions made during the correction of the bulk water amplitude for kinetic depolarization (Chapter B of the Appendix). On the other hand, additivity of ionic hydration numbers strictly speaking only applies to infinitely diluted solutions. When going to higher concentrations increasing solute-solute interactions might lead to a break down of this assumption. For the present NaGlu(aq) solutions the latter means that the concentration-dependent $Z_t(Na^+)$ (obtained from reanalysis of the data from Refs. [55, 186]), used for the calculation of $Z_t(Glu^-)$ and $Z_{ib}(Glu^-)$, might not well represent the actual situation in the NaGlu solutions. Collis *et al.* [209] deduced from their MD simulation that Na^+ is hydrated by only 3.8 H_2O molecules on average in a 2 M NaGlu(aq) solution. Scaling the concentration dependence of $Z_t(Na^+)$ linearly to meet the simulation result yielded the closed symbols shown for $Z_t(Glu^-)$ and $Z_{ib}(Glu^-)$ in Figure 3.21. Although these results should be taken with a grain of salt, it is appealing that now $Z_t(Glu^-)$ follows the solid line fitting of $Z_s(Glu^-)$ and accordingly $Z_{ib}(Glu^-) \approx 0$ for $c(\text{NaGlu}) \geq 0.783\,\text{M}$. Either way, the present DRS results suggest that at least for intermediate to high solute concentrations glutamate is only able to retard but not to "freeze" hydrating water molecules on the timescale of the experiment.

The effective hydration numbers for $c(\text{NaGlu}) < 0.4\,\text{M}$ should not be over-interpreted, as the errors in Z_i diverge with decreasing solute concentration due to finite estimated uncertainties in S_2 and S_3 (standard deviation of an empirical polynomial fit) but vanishing c(NaGlu). However, it is interesting to note that a linear fit through the first two $Z_t(Glu^-)$ and $Z_s(Glu^-)$ extrapolates to ~ 42 and ~ 37, respectively. Both values are comparable to the number of water molecules (~ 40) which can be arranged in the first hydration layer of Glu^- according to its solvent accessible surface area (Gaussian 09 at the B3LYP/6-31++G(d,p) level with the PCM solvation model, Figure A.17(a)) and suggest that at infinite dilution almost all first-shell hydration water is retarded at least by a factor $r = 1.5$ (Figure A.14), irrespective if they are in the proximity of hydrophobic or hydrophilic patches of Glu. However, this hydration shell is very fragile as $Z_t(Glu^-)$ and $Z_s(Glu^-)$ rapidly drop up $c \approx 0.3\,\text{M}$ (Figure 3.21). This concentration is close to the concentration (0.45 M) where the average distance between the solute ions becomes so small that their second hydration shells start to overlap, which might suggest that a major fraction of the moderately retarded H_2O molecules in the first hydration shell quickly regain their mobility as the the neighbouring solvent molecules in the subsequent hydration layer are continuously replaced by hydrated Glu^- anions. If this picture was in deed true (and not

just an artifact of the experiment), the hydration of Glu^- at low c would be thought to be governed by cooperative effects, similar to dilute aqueous 1-ethyl-3-methyl-imidazolium chloride solution [230], between the functional groups *and* neighbouring water molecules. However, due to the lack of further (microscopic) information this is as far as can be speculated at this stage.

Classical and *ab initio* molecular dynamics simulations (AIMD) by Leenders *et al.* [229] of $\sim 0.4\,\mathrm{M}$ Glu^- solutions found that all four carboxylate oxygens are on average equally well hydrated, indicating ∼10 water molecules coordinating the carboxylate groups in AIMD and ~ 13 in classical MD simulations. These numbers are well comparable to the present results of $Z_\mathrm{t}(Glu^-) \approx 11.6$ (Figure 3.21(b)). Daub *et al.* [15] reported $CN_1 = 9.8$ and $CN_1 = 7.6$ in the coordination shell of the -COO^- groups in 0.59 and 1.57 M NaGlu(aq) using MD simulations, whereas the corresponding $Z_\mathrm{t}(Glu^-)$ values are 9.9 and 5.8. Note that for NaGlu(aq) the first hydration shells of the ions start to overlap at $\sim 1.2\,\mathrm{M}$. Therefore, $CN_1 > Z_\mathrm{t}$ at 1.57 M might reflect that some H_2O molecules simultaneously hydrate two Glu^- anions and thus are double-counted in the simulation. The reported CN_1 value of 12.2 at 0.22 M deviates from $Z_\mathrm{t}(Glu^-) = Z_\mathrm{ib}(Glu^-) + Z_\mathrm{s}(Glu^-) \approx 16.7$ when using the dashed line at Figure 3.21(a) for estimating Z_s at $c(Glu^-) = 0.22\,\mathrm{M}$ but agrees well with $Z_\mathrm{t}(Glu^-) \approx 13.4$ when the corresponding solid line is used (in both cases $Z_\mathrm{ib}(Glu^-) \approx 3.7$).

Nevertheless, the good agreement would suggest that at $c \approx 0.4\,\mathrm{M}$ the hydrophobic sites of Glu^- and also its ammonium group are dehydrated in the sense that the dynamics of H_2O molecules in their proximity cannot be distinguished from bulk water anymore. Especially the role of the onium group and its influence on the water solvent structure is not completely clear. Despite its positive charge, the formed $NH_3^+ \cdots OH_2$ H-bonds were reported to be rather weak and the hydration shell around the (alkyl-)ammonium cations is often classified as labile [170, 231–234]. On the other hand, other studies reported a rather stable hydration shell around the ammonium group [235, 236]. This discrepancy will be the subject of a more detailed discussion in Section 3.3, where the effect of the location of the -NH_3^+ with respect to the carboxylate moiety on the solution structure will be investigated on the example of γ- and α-aminobutyric acid. Although the former picture of a labile -NH_3^+ hydration sheath would be consistent with the agreement between present Z_t values and CN_1 of the caboxylate groups from literature,* the existence of irrotationally bound water at $c(Glu^-) < 0.7\,\mathrm{M}$ indicates at least some strong binding of water in the vicinity of the onium cation at the Glu^- backbone, as recent DRS studies on aqueous sodium carboxylate solutions revealed that even though a "structurally isolated" (no other functional groups in its vicinity) -COO^- moiety affects the dynamics of $\sim 5-6$ water molecules it is unable to "freeze" them on the DR timescale [160, 237]. Note that DRS measurements of aqueous glycine [226] revealed that effectively 4.2 water molecules are irrotationally bound by glycine at infinite dilution, which is in good agreement with

*It should be pointed out that exact numerical equivalence of DRS hydration numbers and coordination numbers, CN_1, from scattering experiments and computer simulations cannot be expected as DRS probes the dynamics not geometry.

the present value of $Z^0_{\mathrm{ib}}(\mathrm{Glu}^-) \approx 5$. As will be discussed in Section 3.3, the strongly bound water in aqueous α-amino acid solutions is most likely the result of an interplay between the hydration of the -COO^- and -NH_3^+ at the backbone (*i.e.*, cooperative binding) rather than just the ammonium group alone.
The Z_{t} values of Glu^- decrease continuously with rising c ($Z_{\mathrm{t}} \approx 5$ at 1.90 M, Figure 3.21). Mutual competition of ions for the decreasing number of solvent molecules is certainly one reason, as the second hydration shells start to overlap at ~ 0.45 M already and first shells at ~ 1.2 M. This crowding effect probably also explains why - similar to aqueous ectoine [152] and proline [162]- only at low c some of the hydration H_2O molecules are effectively frozen ($Z_{\mathrm{ib}} > 0$). However, another possible reason for the systematic drop of $Z_{\mathrm{t}}(c)$ is the increasing formation of solute-solute aggregates ($\mathrm{Glu}^- \cdots \mathrm{Glu}^-$ and $\mathrm{Na}^+ \cdots \mathrm{Glu}^-$-IPs) observed with neutron scattering [208] and MD simulations [209] and corroborated by the present dielectric spectra, as will be discussed in Section 3.2.5.

HGlu+NaOH/HCl(aq). The analysis of the solvent-modes is slightly more complex for the pH-dependent DR spectra of HGlu(aq). Apart from the experimental difficulties associated with the low HGlu concentrations, the evaluation of the solvent-related modes is complicated by the simultaneous presence of several protonated/deprotonated HGlu species at once, depending on the pH. The overall (average) Z_{i} of the HGlu species at different pH are shown in Figure 3.22. Interestingly, the Z_{s} values increase continuously with decreasing pH. This increase suggests that changes in the charge distribution and polarity of the solute molecules induced by increasing protonation lead to an effective increase of the number of moderately retarded water molecules around the solute. Considering that ~ 40 H_2O molecules can be packed in the first hydration shell around Glu^- (the geometry and size should not be severely different for the other forms) the obtained Z_{s} value of ~ 50 at pH = 1.6 would indicate retardation of water dynamics beyond the first hydration layer. However, it should be pointed out that the error bars shown in Figure 3.22 were estimated from the standard deviation of an empirical polynomial fit of the solvent amplitudes. The real errors are most likely higher, given the low concentrations of the HGlu+NaOH/HCl(aq) solutions and the limits in the sensitivity of the DRS setup.
For an in-depth analysis of the hydration structure of each single species the compositions of the solutions have to be known and the obtained overall hydration numbers have to regarded as combinations of the individual hydration numbers of each species. Generally, four different forms of the glutamic acid are conceivable: the protonated H_2Glu^+, the neutral HGlu, the single deprotonated Glu^- and the double deprotonated Glu^{2-} molecules. Knowing the pK_{a} values of the individual acidic groups of HGlu [225], the composition of the solutions can be readily determined for each pH (Figure A.16). Assuming additivity and concentration-independence of the hydration numbers at such low solute concentrations individual hydration numbers of irrotationally bound water molecules, $Z_{\mathrm{ib}}(\text{species } m)$, of each species m could be determined by fitting the Z_{ib} values to

$$Z_{\mathrm{ib}} = \sum_m Z_{\mathrm{ib}}(\text{species } m) \cdot \frac{c(\text{species } m)}{c_0(\mathrm{HGlu})} \tag{3.9}$$

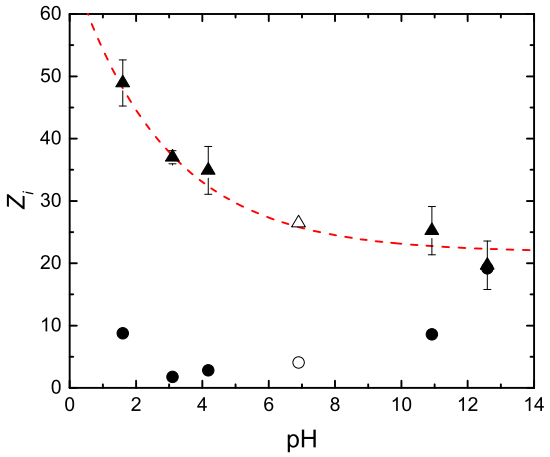

Figure 3.22: Overall numbers of irrotationally, Z_{ib} (●), and moderately bound water, Z_s (▲), in the ∼ 0.06 M HGlu+NaOH/HCl(aq) solutions as a function of pH at 25 °C. The dashed line is a guide to the eye. The error bars of Z_{ib} were omitted for the sake of clarity. The hollow symbols denote the corresponding hydration numbers of Glu^- (pH = 6.9) obtained from the DR spectra of 0.206 M NaGlu(aq) solutions.

Table 3.9: Effective number of irrotationally bound water dipoles per each protonated/deprotonated form of HGlu, Z_{ib}(species m), as obtained from the DR spectra of 0.06 M HGlu+NaOH/HCl(aq) at 25 °C.

	H_2Glu^+	HGlu	Glu^-	Glu^{2-}
Z_{ib}(species m)	∼11	∼1	∼5	∼14

in a nonlinear least-squares fitting routine using MATLAB (Mathworks) [109]. Table 3.9 summarizes the obtained individual numbers of irrotationally bound water molecules per equivalent of each species.

The thus obtained Z_{ib} value of Glu^- is consistent with the extrapolated infinite dilution value of $Z^0_{ib}(Glu^-) \approx 5$ as obtained from the DR spectra of NaGlu(aq) (Figure 3.21(a)). Here, it should be noted that taking into account all sources of errors in the determination of Z_{ib}(species m), the relative uncertainty of the values may exceed 40 %. Therefore, the obtained Z_{ib} in Table 3.9 should not be taken as absolute values but rather treated with some caution.

Nevertheless, the hydration results indicate that the number of strongly bound H_2O molecules is linked to the overall charge of the species, as *prima facie* would intuitively be expected from a continuum electrostatic point of view. On the other hand, glutamic acid molecules are structurally rather complex. For instance, Glu^- possess one positively charged and

two negatively charged patches at the molecule (Figure 3.17(a)), constituting an overall charge of -1. However, its Z_{ib} value is markedly lower than $Z_{ib}(H_2Glu^+)$ and $Z_{ib}(Glu^{2-})$ (Table 3.9). This result might imply that not only short-range but also long-range interactions determine the hydration characteristics of HGlu and its protonated/deprotonated forms. These long-range effects might reflect themselves in the structure breaking ability of Glu^- on bulk water, as reported in literature [15, 208, 209]. On the other hand, Leenders *et al.* [229] found, using MD simulations, that the -COOH group is an efficient H-bond donor and the lifetime of these bonds was reported to be significantly longer compared to $-COO^- \cdots$H-OH acceptor bonds. This difference was discussed to be associated with the higher flexibility of the -OH group in -COOH compared to the C-O bonds in $-COO^-$ and thus a more favorable arrangement of water molecules around the former. Such strong binding of water molecules might result in an increase of Z_{ib}, in particularly it might explain why $Z_{ib}(H_2Glu^+)$ is higher than $Z_{ib}(Glu^-)$. However, the overall coordination number of the protonated carboxylate moieties was found the smaller than for $-COO^-$ [229]. Further, $Z_{ib}(HGlu) < Z_{ib}(Glu^-)$, which suggest that the stronger $-COOH\cdots H_2O$ bonds cannot fully explain the trends in Z_{ib} of the different forms. Most likely, their hydration structure and dynamics is governed by both effects: rather unspecific long-range (coulombic) interactions and specific (probably cooperative) short-range effects, *e.g.* H-bonds.

Gln(aq). The Z_{ib} values of Gln are shown in Figure 3.23. Since no slow-water mode was discernible in the dielectric spectra of Gln(aq), $Z_{ib} = Z_t$ can be assumed. The Z_{ib} values of Gln(aq) are virtually constant over the investigated concentration range, indicating that effectively $Z_{ib} = Z_{ib}^0 = 6.4 \pm 0.3$ water dipoles are strongly bound by one Gln molecule. Note that the solvent accessible surface area of the DFT-calculated Gln structure in Figure A.18(a) suggest that in total ~ 41 water molecules can be packed around the Gln zwitterion. The literature data on the hydration numbers of Gln varies significantly, depending on the utilized technique. Freezing point depression measurements suggested a hydration number of 0 for the Gln molecule [238]. Burakowski and Gliíski reported an infinite dilution value of 4.13 for Gln from measurements of sound velocity in the solutions at 25 °C, while near-infrared spectroscopy measurements yielded a hydration number of 13.3 [239]. Similarly, millimeter spectroscopy experiments by Vorob'ev *et al.* revealed 15.0 water molecules being bound by the Gln zwitterion in a 0.07 M solution at 30 °C [240]. The present Z_{ib}(Gln) value of 6.4 is situated almost in the center of this rather wide range.

Although DRS, as a macroscopic technique, is not capable to provide a microscopic picture, it is reasonable to assumed that these "frozen" water dipoles are located at the charged backbone ($-COO^-$; $-NH_3^+$) and polar ($-CONH_2$) side-chain of the Gln zwitterion (Figure 3.17(b)).[†]

Because of the differing solubility limits of Gln and NaGlu, it is instructive to reduce the comparison of the hydration structure and dynamics between the two amino acids to a similar concentration range. The observed Z_{ib}(Gln) is slightly higher than $Z_{ib}(Glu^-) \approx 4$

[†]Given that the isoelectric point of Gln is pI=5.65 [225], the measured pH of the Gln solutions confirms that the zwitterionic form predominates in the present solutions (Table A.9).

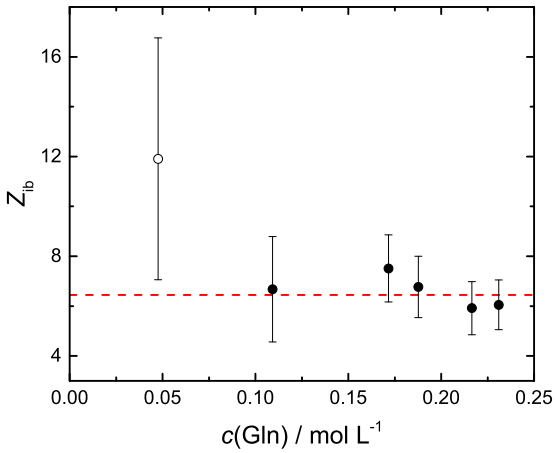

Figure 3.23: Number of irrotationally bound water molecules, Z_{ib}, of Gln as a function of glutamine concentration, c(Gln), at 25 °C. Dashed line shows an empirical linear fit with slope fixed to zero. The hollow symbol was not included in the fit.

at $c(\mathrm{Glu}^-) = 0.206\,\mathrm{M}$ (Figure 3.21(a)). On the other hand, the total number of water molecules impeded in their dynamics around Gln is significantly lower compared to Glu^- (Figure 3.21(b)), which reflects the substitution of a charged carboxylate by a carbamoyl moiety at the Gln side chain. Accordingly, this replacement results in the absence of slow-water in the Gln(aq) solutions, which is the major constituent of $Z_t(\mathrm{Glu}^-)$. Keeping in mind that the interaction of $-\mathrm{COO}^-$ moiety and H_2O is not strong enough to irrotationally bind water dipoles on the timescale of the DRS experiment [160, 237],[‡] the observed difference of $Z_{ib}(\mathrm{Gln}) - Z_{ib}(\mathrm{Glu}^-) \approx 2$ can be attributed to the hydration of the polar side chain group of the Gln molecule. This value is in good agreement with $Z^0_{ib}(\mathrm{Car}^+) = 2.6 \pm 1$, shown further above (Section 3.1.6), where the latter number was discussed to be linked to the hydrophilic hydration of the carbamoyl group and in particular its carbonyl oxygen.
The differences in the total numbers of water molecules impeded in their dynamics around Gln and Glu^- might be related to some biologically relavant properties of the Gln molecule. In spite of ~ 6 H_2O dipoles being irrotationally bound by the Gln zwitterion and its ability to form H-bonds with water [221], the solvating H_2O molecules were found to be rather easily replaced by Gln-Gln bonds, as suggested by the reported propensity of polyglutamine peptides to associate in water *via* side chain-side chain bonds [219, 220] and the formation of Gln-Gln aggregates in aqueous Gln solutions [221, 222]. The low solubility in water of Gln compared to Glu^- [225] and the markedly lower Z_t values of Gln(aq) suggest an

[‡]Note that the situation might be different for water near the backbone carboxylate compared to the "isolated" side chain $-\mathrm{COO}^-$ group due to the close proximity of the positively charged onium group at the former. This effect was already mentioned for the backbone-hydration of Glu^- and will be taken up in more detail in Section 3.3.

overall weaker hydration of Gln, which might explain its pronounced propensity towards aggregation, although some tendency towards aggregation was also reported Glu^- (see below). The tendency of polyglutamine peptides to associate is even easier to comprehend given that the hydration of the Gln side-chain is weaker compared to the charged backbone, as indicated by the present results.

3.2.5 Solute Relaxations

Relaxation time analysis. Assuming that the Glu^- dipoles, responsible for mode $j = 1$ in the DR spectra, relaxes by the mechanism of rotational diffusion, the corresponding relaxation times, τ_1 or, to be more precise, $\tau_{\mathrm{rot},1}$ (Eq. 1.67), can be analyzed using Equation 1.59. As can be seen in Figure 3.24(a), $\tau_{\mathrm{rot},1}(Glu^-)$ follows exceptionally well Equation 1.59, whereas $\tau_{\mathrm{rot},1}(Gln)$ shows a rather scattering behaviour with η (Figure 3.24(b)). The latter scatter might be explained by the comparably low Gln concentrations (due to the solubility limit) and the associated difficulties of precisely resolving the relaxation time of such relatively weak Gln relaxation processes. Note that the $\eta k_B^{-1}T^{-1}$ range scanned in Figure 3.24(b) corresponds roughly to the region of the first point in Figure 3.24(a). Accordingly, it was abstained from fitting the $\tau_{\mathrm{rot},1}(Gln)$ to Eq. 1.59.
The hydrodynamic friction factors of $C(Glu^-) = 0.25$ was obtained from the slope in Figure 3.24(a) (Equation 1.60). These coefficient can be regarded as measure for the interaction between the rotating particles and the surrounding medium and its value commonly lies between the upper *stick* ($C = 1$) and lower *slip* limits ($C = 0.23$ for Glu^-). The present values are within these theoretical limits.
Nevertheless, $C(Glu^-)$ is virtually equal to the *slip* value, which agrees well with the fairly fast dehydration of glutamate with increasing c, indicating that H_2O molecules in the "slippery" solvation sheath can be removed rather easily from the vicinity of Glu^- ions.
Note that no consistent results could be obtained from the analysis of the solute modes of the pH-dependent measurements of HGlu+NaOH/HCl(aq), due to the reasons mentioned above. Thus, it was refrained from presenting the corresponding results.
Dipole moments of Glu^- and Gln. The analysis of the amplitudes of the solute-modes, S_1, *via* Equation 1.48 yielded effective dipole moments of Glu^-(aq) and Gln(aq) (Figure 3.25). While $\mu_{\mathrm{eff}}(Gln)$ stays virtually constant in the investigated concentration range ($\sim 20.4\,D$), the effective dipole moment of Glu^- drops from an infinite dilution value of $\sim 22.2\,D$ to a plateau value of $\sim 20.1\,D$ for $c(Glu^-) > 0.8\,M$. The present dipole moment values are significantly higher than $\mu_{\mathrm{ap}}^{\mathrm{calc}}$ of Glu^- (14.2 D) and Gln (12.9 D) predicted by DFT calculations (B3LYP/6-31++G(d,p) and B3LYP/6-31G(d,p) level with the PCM solvation model using the center of mass for the pivot) of both molecules embedded into water (Figures A.17(a) and A.18(a)). Besides possible differences between the calculated conformations of Glu and Gln and their actual conformations in solution (which, however, are unknown), the enhanced experimental dipole moments might indicate preferential alignment between the dipoles of the reorienting molecules and dipoles in its proximity. Both hydrating solvent molecules and neighbouring solute dipoles are eligible to lead to such an effect. As can be seen in Figure 3.26(a), the effective dipole moment of the glutamate

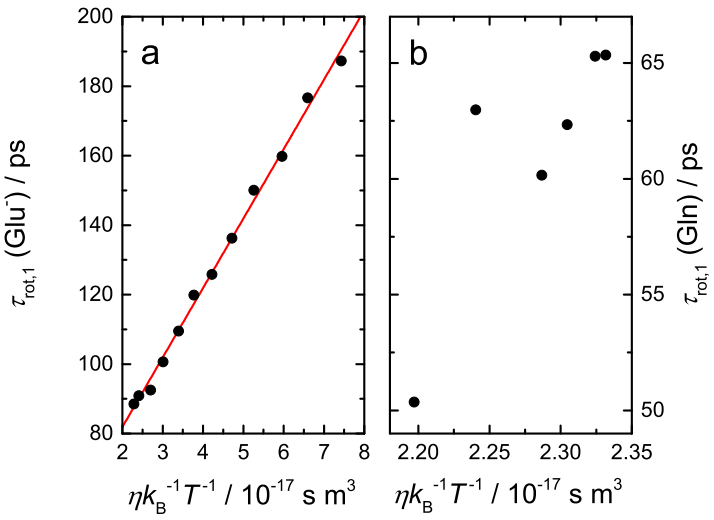

Figure 3.24: Rotational correlation time of the (a) Glu^-(aq) and (b) Gln(aq) reorientation as a function of $\eta k_B^{-1} T^{-1}$. Linear line denotes the fit to the modified Stokes-Einstein-Debye equation (Eq. 1.59).

molecules scales linearly with the number of tightly bound water molecules.[§] Similarly, quantum-chemical calculations of several $Glu^- + x{\cdot}H_2O$ clusters (Figure A.17) show an overall increase in the dipole moment with the number of explicit H_2O molecules interacting with the charged groups of glutamate.

However, the μ_{eff} value at $Z_{ib} \to 0$, *i.e.*, at high $c(Glu^-)$, is still significantly larger than the computational value of 14.2 D for the bare Glu^- anion. This discrepancy might be explained by preferential parallel alignment of Glu^- dipoles among each other. Molecular dynamics simulation by Collis *et al.* [209] reported the presence of glutamate-glutamate aggregates, where the side-chain -COO^- is H-bonded to the backbone ammonium group ("head-to-tail" aggregates). Clearly, no evidence for such long-lived (life-time≥rotational correlation time) aggregates could be deduced from the DR experiment, as these would have appeared as separate modes in the spectra. However, some kind of parallel arrangement and thus an increase of the dipole-dipole correlations is most likely responsible for the observed enhancement of the Glu dipole moment. It may be speculated that these rather short-lived structures might be stabilized by coordination of Na^+ to it, given the reported propensity of Glu^- to bind Na^+ cations (preferably at the backbone carboxylate) [209]. Such solute-solute interactions, which necessarily involve displacement of hydration water to a certain degree, are consistent with the observed fast drop of the total hydration number of Glu^- (Figure 3.21(b)).

[§]Note that correlations between Glu^- and moderately bound water dipoles ($Z_s \approx 5$), although less common, might also have an effect on the measured dipole moment value of glutamate.

The situation is somewhat different for aqueous glutamine at the first glance, but yet it provides a consistent picture. Keeping in mind that the decline of $\mu_{\text{eff}}(\text{Glu}^-)$ at low c is (most likely) governed by dehydration and remembering that Z_{ib} value of Gln stayed essentially constant over the investigated concentration range (Figure 3.23), no such decrease of $\mu_{\text{eff}}(\text{Gln})$ should be expected, which is in agreement with the present results (Figure 3.25(b)). Accordingly, no clear trend of $\mu_{\text{eff}}(\text{Gln})$ with Z_{ib} can be observed (Figure 3.26(b)). Analogous to Glu^-, the markedly higher experimental dipole moment of Gln compared to the computational value of the "bare" Gln molecule (Figure 3.25(b)) might reflect positive dipolar solute-solvent correlation ($Z_{\text{ib}} \approx 6$). On the other hand, aqueous Gln is known to be prone to the formation of Gln$\cdots$Gln aggregates. Two neutron diffraction studies coupled with computational modeling by Rhys *et al.* [221, 222] revealed that a rather large fraction of up to $\sim 20\,\%$ of Gln zwitterions are participating in Gln$\cdots$Gln-clusters (*via* backbone–backbone, backbone–side-chain and side-chain–side-chain interactions) in a $\sim 0.2\,\text{M}$ solution, with the major fraction being Gln$\cdots$Gln dimers ($\sim 10\,\%$). Similarly to glutamate, no direct indications of such long-lived aggregates could be observed in the DR spectra, but an increase of the effective dipole moment of Gln through a preferential parallel arrangement of Gln molecules among each other is certainly conceivable. It is interesting to note that for glycine [226], ectoine [152] or proline [162], which do not possess H-bond acceptor or donor groups at the side-chain, no effective enhancement of the dipole moment due to parallel alignment of the solute molecules was observed.

3.2.6 Concluding Remarks

The complex permittivity spectra of NaGlu(aq) and Gln were satisfactorily fitted by combinations of three Debye equations. Contrary to NaGlu(aq), no slow-water contribution was describable in the DR spectra of Gln(aq). It was found that effectively ~ 6 water dipoles were tightly bound by the hydrophilic moieties of the Gln molecule, irrespective of the concentration, while the corresponding value of Glu^- dropped linearly from $Z_{\text{ib}}^0 \approx 5$ at infinite dilution to ~ 0 at $c(\text{NaGlu}) > 0.7\,\text{M}$. The slightly higher number of irrotationally bound water molecules of Gln(aq) compared to Glu^-(aq) in the respective concentration range ($\Delta Z_{\text{ib}} \approx 2$) was linked to the hydration of the carbamoyl group of the former. Cooperative hydration effects of the α-amino acid backbone were discussed to lead to the appearance of "frozen" water in the Glu^- solutions. Despite the lower Z_{ib}, the total amount of water molecules impeded in their dynamics around the Glu^- anion was significantly higher compared to Gln(aq). Extrapolation of the obtained hydration numbers of Glu^- to infinite dilution indicated that virtually all water molecules in the first hydration sheath are affected by the presence of the amino acid (~ 40). An increase of the solute concentration and thus increasing steric crowding leads to a rapid drop of these hydration numbers, which suggests that the hydration shell of Glu^- is rather fragile.
Analysis of DR spectra of HGlu solutions at different pH revealed that the number of moderately bound water molecules increases with increasing degree of protonation of HGlu. On the other hand, the obtained Z_{ib} values of the individual protonated/deprotonated HGlu forms suggested that besides short-range hydration effects, such as H-bonds, long-

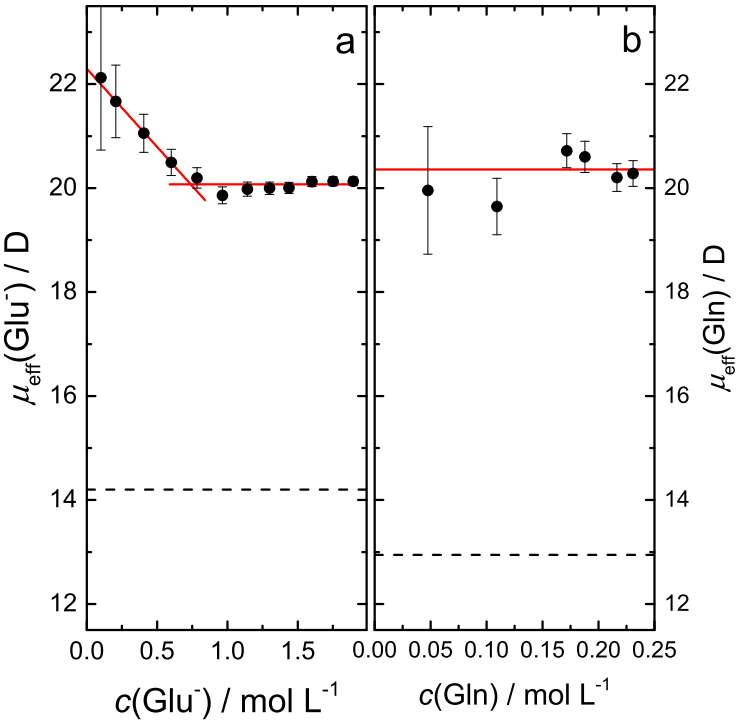

Figure 3.25: Effective dipole moments, μ_{eff}, of (a) Glu^- and (b) Gln as obtained from the DR spectra at 25°C. The symbols denote the experimental data, solid lines represent empirical weighted fits. The dashed lines indicate the the calculated (Gaussian 09, B3LYP/6-31++G(d,p) and B3LYP/6-31G(d,p) with the PCM solvation model) apparent dipole moments of the respective molecules.

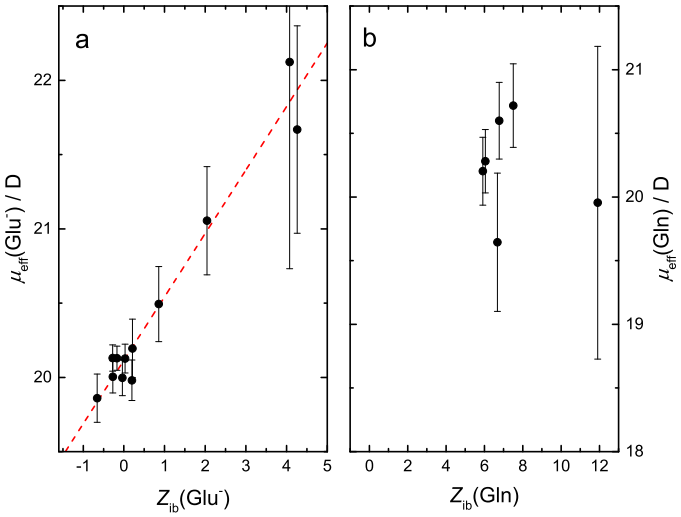

Figure 3.26: Effective dipole moments, μ_{eff}, of (a) Glu^- and (b) Gln as a function of Z_{ib}. The dashed line indicates a linear fit.

range (electrostatic) interactions are most probably decisive for the structure and dynamics of their hydration shells.

The experimental effective dipole moments of Glu^- and Gln were found to be markedly higher than the computed dipole moments of the "bare" amino acids. Neglecting possible conformational differences between the α-amino acids in solution and the calculated low-energy structures, this discrepancy was attributed to preferential parallel alignment of neighboring dipoles and the solute molecule. In hand with the fast loss of hydration water of Glu^-(aq), the obtained μ_{eff} of Glu^- indicated that dipolar solute-solute correlations most likely occur in the NaGlu(aq) solutions. Further, the observed fast decrease of the effective dipole moment of Glu^- at lower c could be correlated with the number of tightly bound H_2O molecules aligning their dipole moments on average parallel to the amino acid dipole direction.

Similar to Glu^-(aq), solute-solvent and solute-solute dipolar correlations could explain the high μ_{eff} of Gln. In particularly the presence of the latter correlations was consistent with the literature on aqueous Gln solutions. It was pointed out that Gln zwitterions in aqueous solution or as constituents of proteins are infamous for their tendency to form Gln$\cdots$Gln associates, which are currently linked to various degenerative human diseases. In hand with the comparably small total amount of hydration water, the solvation sheath of Gln is apparently not able to suppress the pronounced propensity of Gln towards aggregation, although the present DRS results suggested that no long-lived, but rather short-lived, Gln$\cdots$Gln aggregates are formed in the solution.

3.3 γ-Aminobutyric Acid, α-Aminobutyric Acid & n-Butylammonium Chloride

3.3.1 Introduction

The amino acid γ-aminobutyric acid (GABA) (Figure 3.27(a)) is the predominant inhibitory NT regulating the neural activities in the mammalian central nervous system [241]. The concentration of GABA in the brain was found to be extensively higher than those of classical monoamine NTs and more than one third of brain neurons use GABA for synaptic communication. A proper concentration of GABA in the organism is crucial for the mental and also physical health of humans [242]. Several distinct types of GABA receptors have been identified, namely GABA(A), GABA(B) and GABA(AOr) (GABA(C)) [243]. Malfunctions of GABA-metabolic and -anabolic cycles as well as disfunctions of the "GABAergic" receptors are linked to a large number of human diseases, such as anxiety and stress disorders, musculoskeletal and pain disorders, insomnia, drug-withdrawal syndromes, epilepsy, liver diseases and hepatic encephalopathy, learning and memory disorders, hormonal disorders and many other related conditions [242, 244, 245]. Similar to AcCh, the conformation of the zwitterionic GABA molecules was found to be decisive for the affinity to the different types of receptors and metabolic enzymes [243, 246, 247]. Furthermore, it was shown that GABA can potentially act as an osmolyte, a nitrogen storage and a pH regulating agent in living organisms [248]. Due to its significant pharmacological importance, the development of novel GABAergic drugs for potential GABA pharmacological studies is an active area of research in the fields of medicinal chemistry [242].

α-Aminobutyric acid (AABA), a structural isomer of GABA (Figure 3.27(b)) and a metabolite in isoleucine biosynthesis, is a non-proteogenic amino acid which can be found in the human kidney, in liver tissues, and in most biological fluids [249]. Despite some structural resemblance between GABA and AABA, the latter does not act as a neurotransmitter and is thus thought to be of minor pharmacological importance.

Clearly, deepening the knowledge on the behaviour of the two isomers in aqueous solution would be beneficial for the understanding of their different bioaction. Therefore, the hydration and dynamics of GABA and AABA in water was studied by DRS at 25 °C. The investigated solutions were studied in the concentration ranges of $0.2071 \leq c(\mathrm{GABA})/\mathrm{M} \leq 6.241$ and $0.09980 \leq c(\mathrm{AABA})/\mathrm{M} \leq 1.708$, respectively (note: solubility limits are $\sim 12.6\,\mathrm{mol\,kg^{-1}}$ for GABA(aq) and $\sim 2.2\,\mathrm{mol\,kg^{-1}}$ for AABA(aq)). To obtain information on the hydration of individual functional groups of the amino acids, DR measurements of aqueous solutions of the salt n-butylammonium chloride (BACl, n-butylamine hydrochloride) (figure 3.27(c)) were performed ($0.03584 \leq c(\mathrm{BACl})/\mathrm{M} \leq 1.190$) and the effect of protonation was studied by comparison of BACl with its unprotonated form (n-butylamine) [250]. In general terms, the n-butylammonium cation (BA, $\mathrm{BA^+}$) and n-butylamine can be considered as suitable models for basic side-chain moieties in proteins and the knowledge of the dynamics and hydration of the "simpler" $\mathrm{BA^+}$ and n-butylamine molecules might be transferred onto the biologically important substance group of bio-

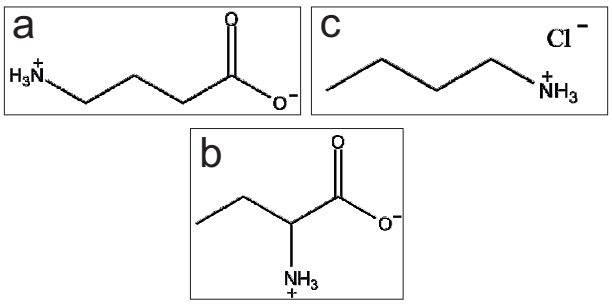

Figure 3.27: Chemical structures of (a) γ-aminobutyric acid, (b) α-aminobutyric acid and (c) n-butylammonium chloride.

genic amines. These compounds are usually produced by decarboxylation of amino-acids and some of the biogenic amines, such as the NTs dopamine, serotonin and histamine, are crucial for biological functions in humans and animals [251, 252]. As DRS detects all species with a permanent dipole moment $\neq 0$ and a life time comparable or larger than the rotational correlation time of the corresponding species, possible formation of alkylammonium chloride ion-aggregates, which are known to have a major influence on the molecular recognition of (mono)alkylammonium molecules [253, 254], was discussed for the exemplary BACl(aq) system.
This is the first systematic broadband dielectric study of GABA(aq), AABA(aq) and BACl(aq) over such wide frequency and concentration ranges, although some dielectric studies of aqueous solutions of GABA [41, 224, 255, 256], AABA [255, 257] and BACl [258] exist.
The data acquisition and the discussion of the applied fitting models of the DR spectra will be treated in the first part of this section. In the last and major part, the results of the evaluation of the dielectric spectra, namely the structure, dynamics and the hydration behaviour of the investigated solutes, will be discussed in detail.

3.3.2 Data Acquisition and Processing

The GABA(aq), AABA(aq) and BACl(aq) samples were prepared as described in Section 2.2. The densities, viscosities and electrical conductivities (only for BACl(aq)) were obtained following the procedures of Section 2.4 and are shown in Tables A.10, A.11 and A.12. Additionally, the pH-values of the amino acid samples were checked at room temperature with a pH-meter (pHenomenal PCL 1000, VWR, Germany). The glass electrode was calibrated with standard buffer solutions of pH = 4.0, 7.0 and 10.0 prior to measurement. The obtained pH-values of the GABA(aq) and AABA(aq) solutions were found to be 6.2-7.4 and 6-6.5, respectively (Tables A.10 and A.11). Considering the pKa values of both acidic groups of GABA and AABA, with pK_a(-COOH) = 4.23, pK_a(-NH_3^+) = 10.43 for GABA and pK_a(-COOH) = 2.55, pK_a(-NH_3^+) = 9.60 for AABA [259], the present pH-values confirm that the zwitterionic form was the clearly predominant species

in solution.
The permittivity spectra of the aqueous solutions were recorded at 25 °C in the frequency range 0.05-89 GHz using the dielectric probe kit VNA setup and the E-band interferometer (Section 2.3). Due to pronounced relaxation effects in the low-frequency region of the GABA(aq) spectra, measurements with the TDR cells connected to the VNA were additionally performed for the GABA samples, thus extending the covered frequency region down to 0.01 GHz. As mentioned previously (Section 3.1.2), in the case of $\kappa > 0$ the effective low-frequency limit might exceed the manufacturer limit. Accordingly, the $\nu_{\min}$ of BACl(aq) was in the range $0.05 \leq \nu_{\min}/\mathrm{GHz} \lesssim 0.2$, depending on the BACl(aq) concentration.

3.3.3 Choice of Relaxation Model and Assignment of Modes

GABA(aq) and AABA(aq). The measured dielectric spectra of GABA and AABA solutions at 25 °C are shown in Figure 3.28. Combinations of up to five HN-equations were tested to fit the experimental spectra. Evaluating the fits according to the criteria discussed in Section 2.3.3 and taking into account the results of the Zasetsky's analysis shown in Figures A.19 and A.20, a superposition of four Debye equations (D+D+D+D) was found to yield the best fit of the DR spectra of GABA(aq) over the whole concentration range and for AABA(aq) at $c(\mathrm{AABA}) \geq 0.6055$ M, while the D+D+D model provided a better description of the AABA(aq) spectra at lower concentrations. The best-fit parameters are summarized in Tables 3.10 and 3.11. Figure 3.29 shows the decomposition of exemplary dielectric loss spectra into the individual contributions of the various relaxation processes. The static permittivities increased with rising solute concentration for both amino acids (Tables 3.10 and 3.11, Figures A.22 and A.23), indicating the presence of highly dipolar solute-related species in the solution (Section 3.2). A similar behaviour was reported for solutions of various other zwitterionic compounds [162, 226–228] and GABA(aq) solutions [41]. This effect was more pronounced in the present GABA(aq) spectra, showing a higher $\mathrm{d}\varepsilon/\mathrm{d}c$ value compared to AABA(aq) ($46.3\,\mathrm{L\,mol^{-1}}$ *vs.* $22.9\,\mathrm{L\,mol^{-1}}$). Accordingly, the low-frequency mode $j = 1$, located between $\sim 0.1 - 2.6$ GHz ($\tau_1 \approx 60 - 1200$ ps), can be assigned to the reorientation of the zwitterionic amino acid dipoles. Its amplitude and relaxation time increased systematically with increasing solute concentration and for both systems, and in particularly for GABA(aq), it was the clearly dominating process at higher c (Tables 3.10 and 3.11, Figures A.22 and A.23).
The intermediate mode 2 appeared in the dielectric spectra upon addition of GABA to water and its amplitude increased with rising c. Based on its magnitude and location in the DR spectra, this mode can be assigned to the fraction of water moderately slowed down in its dynamics due to the presence of the solute, *i.e.*, slow-water [152, 154, 156–160, 162–164]. Consistent with Zasetsky's analysis (Figure A.20), the slow-water mode was not discernible in the DR spectra of AABA(aq) at low concentrations and could only be resolved for $c(\mathrm{AABA}) \geq 0.6055$ M. Interestingly, τ_2 of AABA(aq) solutions stayed fairly constant (~ 20 ps), while an increase of τ_2 with increasing c (~ 17 ps to ~ 110 ps) could be detected for GABA(aq) in the studied concentration range (Tables 3.10 and 3.11, Figures

A.22 and A.23). Thus, a constant retardation factor for water dynamics of $r = \frac{\tau_2}{\tau_3} \approx 2.1$ can be given for the AABA(aq) solutions, whereas a concentration-dependent r value, ranging between ~ 2.0 and ~ 13.4, was observed for GABA(aq).
At lower concentration, both sets of samples were dominated by mode $j = 3$, centered at $\sim 17-19$ GHz ($\sim 8.2-9.6$ ps). The amplitude, S_3, decreased systematically with increasing amino acid concentration. Judging by its intensity and location, mode 3 can unequivocally be assigned to cooperative reorientation of essentially unperturbed bulk-water molecules [22, 150]. Note that for AABA(aq) τ_3 showed some increase with increasing c, which indicates an effect of the solute on the "structure" of bulk-water, while for GABA(aq) the respective relaxation time stayed essentially constant. Also apparent from the GABA(aq) and AABA(aq) DR spectra (Figure 3.29) is the presence of small-amplitude contribution $j = 4$ located above the present upper-frequency limit at ~ 500 GHz ($\tau_4 \approx 0.3$ ps). The intensity and location is typical for the so-called fast-water process, which is currently thought to be associated with the fast switch of hydrogen-bond connections between neighboring water molecules and was also resolved in neat water [150]. Similar to the DR spectra of AcChCl(aq) (Section 3.1) and various aqueous electrolyte systems and solutions of small, biologically active molecules [55, 98, 151–153], the relaxation time of the fast-water mode, which is centered outside the accessible frequency range, was fixed to the neat water value to reduce scatter. Likewise, the infinite-frequency permittivity was assumed to be concentration-independent and was fixed to value of neat water, $\varepsilon_\infty = 3.52$ [154], during fitting.

BACl(aq). The experimental dielectric spectra of BACl(aq) (Figure 3.30(a)) were fitted on a test basis with up to five HN-equations. Assessing the quality of the fits by the criteria presented in Sec. 2.3.3 and Zasetsky's relaxation time distribution analysis (Figure A.21), the combination of three Debye modes or two Debye modes and one Cole-Cole mode, depending on the concentration respectively, (D+D+D(CC) model) was chosen as the best fitting model (Figure 3.30(b)). The fitting parameters of the D+D+D(CC) model are shown in Table 3.12.
Contrary to the solutions of the zwitterionic GABA and AABA, the static permittivity of BACl(aq) solutions decreased with rising c (Table 3.12, Figure A.24).
As typical for aqueous solutions, the intense mode $l = 3$ centered at $\sim 17 - 19$ GHz ($\bar{\tau}_3 \approx 9.4$ ps) can be readily assigned to the cooperative relaxation of the H-bond network of bulk-like water. The amplitude of the bulk-water mode decreased with increasing BACl(aq) concentration and its relaxation time showed a slight but noticeable increase with rising c (Table 3.12, Figure A.24). The latter shift might indicate the presence of a small contribution in the direct proximity of the bulk-water mode. The necessity to use the broader CC mode for c(BACl) ≥ 0.3785 M supports this picture. A low-amplitude slow-water process, which, however, could not be directly discerned in the DR spectra, with a relatively small retardation factor ($r \lesssim 2$) would certainly be an appropriate candidate for such a relaxation process. A previous dielectric study of BACl(aq) by Kaatze *et al.* [258] showed the presence of such a mode. Note that an acceptable description of the present spectra could also be achieved by the D+D(+D)+D model, where the alleged slow-water mode, located in the proximity of the bulk-water mode with a retardation factor of $r \approx 2$, was directly

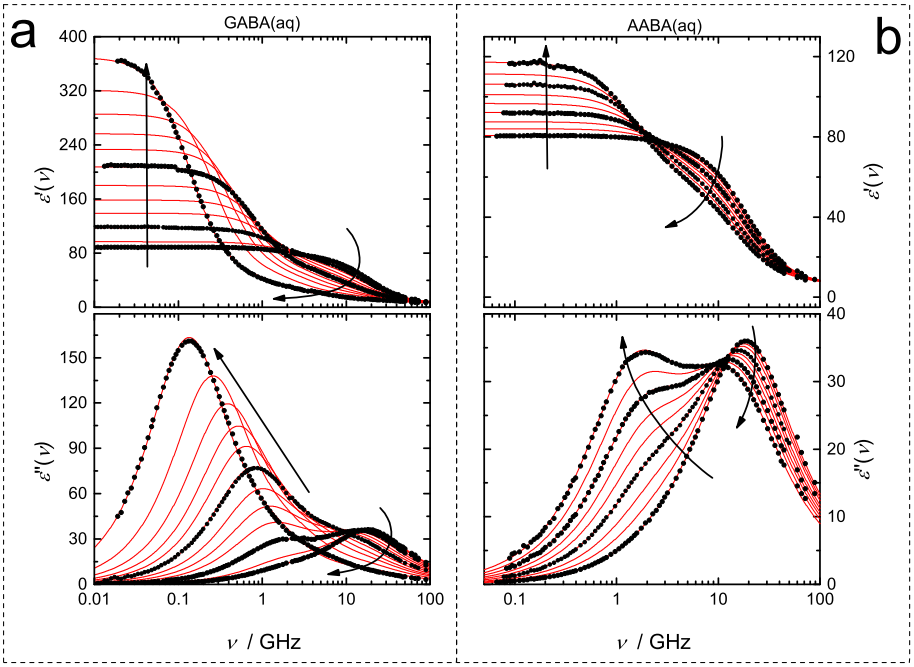

Figure 3.28: Relative permittivity, $\varepsilon'(\nu)$, and dielectric loss, $\varepsilon''(\nu)$, spectra of (a) GABA(aq) ($0.2071 \leq c/\mathrm{mol\,L^{-1}} \leq 6.241$) and (b) AABA(aq) ($0.09980 \leq c/\mathrm{mol\,L^{-1}} \leq 1.708$) at 25 °C. Symbols denote the experimental data. Solid lines represent the fits. For visual clarity data points are only shown for selected samples. Arrows indicate the trend with increasing solute concentration.

Table 3.10: Static permittivity, ε, relaxation amplitudes, S_j, relaxation times, τ_j ($j = 1, .., 4$), infinite frequency permittivity, ε_∞, of GABA(aq) at 25 °C and the reduced error function, χ_r^2, of the D+D+D+D fitting model.[a,b]

c	ε	S_1	τ_1	S_2	τ_2	S_3	τ_3	S_4	τ_4	ε_∞	χ_r^2
0[c]	78.37	–	–	–	–	72.42	8.35	2.43	0.278	3.52	0.0056
0.2071	88.8	13.3	79.0	0.539	17F	68.9	8.43	2.47	0.278F	3.52F	0.0221
0.3891	96.8	22.5	90.2	5.45	17.9	62.7	8.31	2.59	0.278F	3.52F	0.0373
0.8143	117	45.2	108	11.1	20.7	54.5	8.43	3.01	0.278F	3.52F	0.0717
1.250	139	69.7	128	12.8	24.5	49.6	8.71	3.45	0.278F	3.52F	0.4273
1.692	158	91.9	145	20.8	22.9	39.1	8.44	3.25	0.278F	3.52F	0.1340
2.157	180	116	169	22.6	24.4	33.9	8.55	3.54	0.278F	3.52F	0.1231
2.717	208	145	212	27.1	29.6	28.3	8.55	3.73	0.278F	3.52F	1.0743
3.280	233	173	260	28.3	34.6	24.3	8.84	3.88	0.278F	3.52F	1.2175
3.871	256	202	316	29.0	33.1	17.7	8.23	3.83	0.278F	3.52F	0.4692
4.460	286	232	422	30.6	45.1	16.3	8.2F	3.55	0.278F	3.52F	1.9120
5.227	321	269	628	30.7	62.2	13.8	8.2F	3.32	0.278F	3.52F	2.2497
6.241	369	321	1200	30.4	110	11.7	8.2F	2.77	0.278F	3.52F	2.5311

[a]Units: c in mol L^{-1}; τ_j in ps. [b]Parameter values followed by "F" were fixed during fitting; [c]taken from Ref. [97].

Table 3.11: Static permittivity, ε, relaxation amplitudes, S_j, relaxation times, τ_j ($j = 1, .., 4$), infinite frequency permittivity, ε_∞, of AABA(aq) at 25 °C and the reduced error function, χ_r^2, of the D+D(+D)+D fitting model.[a,b]

c	ε	S_1	τ_1	S_2	τ_2	S_3	τ_3	S_4	τ_4	ε_∞	χ_r^2
0[c]	78.37	–	–	–	–	72.42	8.35	2.43	0.278	3.52	0.0056
0.09980	80.6	3.94	56.6	–	–	70.7	8.44	2.44	0.278F	3.52F	0.0199
0.2508	84.1	9.62	59.8	–	–	68.2	8.60	2.70	0.278F	3.52F	0.0580
0.4033	87.6	15.2	64.3	–	–	66.1	8.77	2.73	0.278F	3.52F	0.0435
0.6055	92.1	21.6	71.8	1.21	25.2	62.7	9.06	3.08	0.278F	3.52F	0.0143
0.8069	96.7	28.5	77.0	3.24	18.8	58.4	9.11	3.04	0.278F	3.52F	0.0756
1.000	101	34.7	83.2	6.42	16.4	53.3	9.26	3.25	0.278F	3.52F	0.0402
1.226	106	41.5	91.3	10.3	18.1	47.8	9.16	3.25	0.278F	3.52F	0.1193
1.441	111	47.9	101	11.8	20.0	45.0	9.37	3.22	0.278F	3.52F	0.1538
1.708	117	56.0	111	14.5	19.5	39.8	9.56	3.43	0.278F	3.52F	0.0956

[a]Units: c in mol L^{-1}; τ_j in ps. [b]Parameter values followed by "F" were fixed during fitting; [c]taken from Ref. [97].

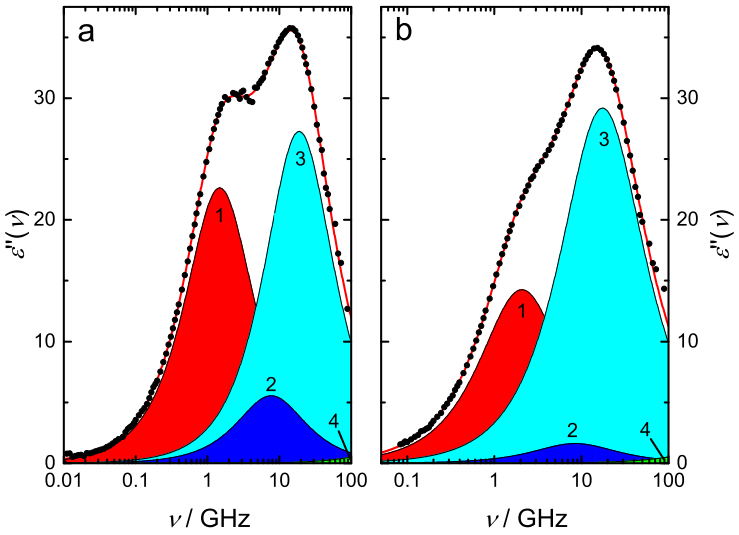

Figure 3.29: Dielectric loss spectrum of (a) 0.8143 M GABA(aq) and (b) 0.8069 M AABA(aq) at 25 °C. Symbols denote experimental data, lines indicate the fits. The shaded areas show the individual contributions of the D+D+D+D model.

resolved at higher BACl(aq) concentrations. However, the D+D(+D)+D model showed higher χ_r^2 values (up to $\sim$ 19 %) compared to the D+D+D(CC) model and the obtained evaluation parameters were physically less reasonable. Hence, the D+D(+D)+D approach was discarded.

In contrast to GABA(aq) and AABA(aq), the fast-water mode was not resolved for the BACl(aq) spectra. However, the comparably high infinite-frequency permittivity value of $\varepsilon_\infty \approx 6$ for BACl(aq) (3.52 for GABA(aq) and AABA(aq)) indicates that the fast-water contribution, which lies too far outside the investigated frequency range for BACl(aq), is automatically incorporated into ε_∞.

Upon addition of BACl to water, two additional processes in the lower frequency range appear: a less-intense mode located at a mean frequency of $\sim$ 0.3 GHz ($\bar{\tau}_1 \approx 460$ ps) and a faster processes centered between $\sim$ 1.1 and $\sim$ 3.7 GHz ($\tau_2 \approx 43 - 150$ ps). Whereas the latter process can be assigned to the reorientation of the dipolar BA^+ cations (note: the spherical Cl^- anion does not have a permanent dipole moment and, thus, does not contribute as such to the DR spectra), as suggested by its relaxation time values, the origin of mode $l = 1$ is not immediately obvious. Similarly to the case of CarCl(aq) already discussed previously (Section 3.1), an ion cloud contribution or a relaxation of dipolar ion-aggregates, *e.g.* BA^+-Cl^- IPs, or the combination of both, could lead to the observed dielectric response. At least for the case of ion-pairs, some quantitative analysis (although under fairly critical assumptions) is feasible and will be picked up in the following discussion.

Table 3.12: Static permittivity, ε, relaxation amplitudes, S_j, relaxation times, τ_l ($l = 1, .., 3$), width parameter, α_3, infinite frequency permittivity, ε_∞, of BACl(aq) at 25 °C and the reduced error function, χ_r^2, of the D+D+D(CC) fitting model.[a]

c	ε	S_1	τ_1	S_2	τ_2	S_3	α_3	τ_3	ε_∞	χ_r^2
0.03584	78.3	0.61	662	0.46	135	71.7	0	8.62	5.97	0.1384
0.07113	78.3	0.70	599	0.54	151	71.3	0	8.56	5.75	0.0925
0.1422	77.9	0.88	332	0.97	107	70.1	0	8.80	5.95	0.0895
0.2842	77.6	1.25	555	2.67	73.7	67.5	0	8.97	6.22	0.0799
0.3785	77.1	1.43	465	3.21	65.1	66.2	0.001	9.18	6.23	0.1680
0.5037	77.5	2.21	881	2.57	85.3	67.5	0.030	9.44	5.21	0.0956
0.6726	74.9	1.70	249	4.31	45.4	63.1	0.021	9.67	5.88	0.0603
0.8935	73.2	1.69	216	5.73	42.0	60.1	0.028	10.0	5.66	0.0732
1.190	70.9	1.88	157	5.28	42.7	58.3	0.048	10.9	5.48	0.0689

[a]Units: c in mol L^{-1}; τ_l in ps.

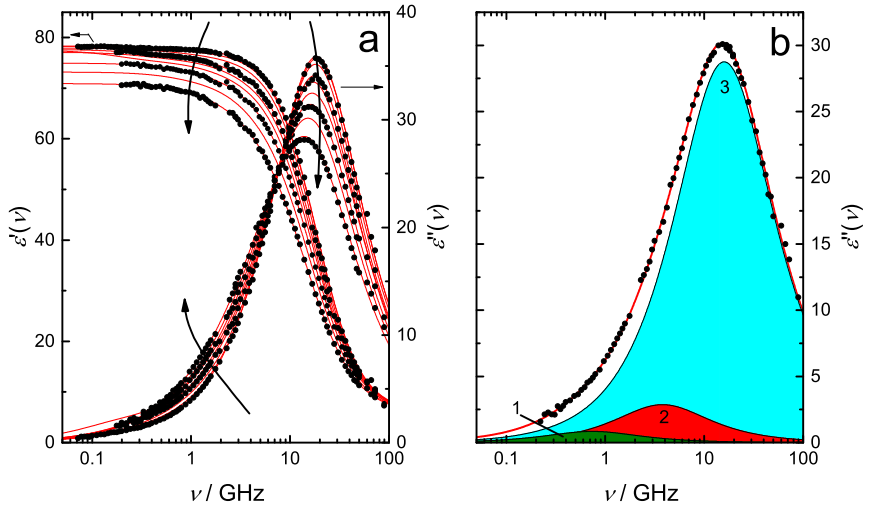

Figure 3.30: (a) Relative permittivity, $\varepsilon'(\nu)$, and dielectric loss, $\varepsilon''(\nu)$, spectra of BACl(aq) ($0.0358 \leq c/\text{mol L}^{-1} \leq 1.190$) at 25 °C. Symbols denote the experimental data. Solid lines represent the fits. For visual clarity data points are only shown for selected samples. Arrows indicate the trend with increasing solute concentration. (b) Dielectric loss, $\varepsilon''(\nu)$, spectrum of 0.8935 M BACl(aq). The shaded areas denote the individual relaxation modes of the D+D+D(CC) model.

3.3.4 Solute Relaxations

BACl(aq). Assuming that mode $l = 1$ in the BACl(aq) spectra originates solely from the relaxation of BA^+-Cl^--IPs, association constants for the IP formation, K_A, can be obtained from S_1 using Eq. 1.48. The acquired K_A values for the CIP and SIP species as a function of stoichiometric ionic strength, I ($= c$), are shown in Figure 3.31. Note that the values from DFT calculations (Gaussian 09, B3LYP/6-31++G(d,p) with PCM solvation model) were adopted for the dipole moments of the BA^+-Cl^--IPs in the above procedure (Figure A.25). The formation of 2SIPs was ruled out on the grounds of the moderate hydration of the involved alkylammonium cation [260, 261] (see below) and chloride anion [22]. The standard-state association constant, as obtained from the Guggenheim-type fit (Equation 3.2), were found to be $\lg K_A^\circ = 1.8 \pm 0.3$ and $\lg K_A^\circ = 1.4 \pm 0.2$ for the CIP and SIPs species, respectively. The present numbers would indicate that the association into IPs is very pronounced in BACl(aq) solutions, irrespective of the presumed IP species. Thus, for the more strongly associating CIP case, up to $\sim 70\,\%$ of the present ions would be bound into ion-pairs at low solute concentrations. These numbers are rather high considering that the extent of association of the chemically related NH_4^+, an unalkylated homologue of n-butylammonium cation, and Cl^- is still under debate. Whereas some studies reported the formation of CIPs [262] or SIPs [263] in aqueous solution, others found a negligible tendency of NH_4^+ and Cl^- towards IP formation [264]. A DRS study of NH_4Cl(aq) performed by Shaukat [265] revealed $\lg K_A^\circ = 1.7 \pm 0.3$ for the SIPs as the dominant species. This number is in good agreement with the present BACl(aq) value.

However, similarly to CarCl(aq) (Section 3.1) and as pointed out by Shaukat [265], the assumption of a negligible IC contribution to the presumed IP relaxation mode is certainly not valid for the present BACl(aq) solutions, despite of the smooth variation of the obtained association constants with I. Most likely, the IP relaxation contribution is swamped by the IC relaxation at lower c, as indicated by the high relaxation times in this concentration region (Table 3.12). Since the IC relaxation effect decays rather fast at high electrolyte concentrations [55], the sharp drop of τ_1 at c(BACl) > 0.5 M might indicate the domination of the IP relaxation in the higher concentration regime. Note that the estimated relaxation times for the CIP and SIP reorientation process were calculated to be $\sim 70 - 150$ ps and $\sim 150 - 300$ ps, depending on the hydrodynamic boundary conditions, respectively. The predicted SIP relaxation times are in good agreement with the observed τ_1 values at higher c (Table 3.12), which implies that the solvent-shared IP is more likely to be responsible for the dielectric response of mode 1 and is thus predominant in solution. Given the fact that appropriate theories for the separation of the IC contribution from the DR spectra are currently unavailable, a definite assignment of distinct IP species contributing to mode 1 should be taken with a grain of salt.

The amplitude of process $l = 2$ of the BACl(aq) spectra, which was assigned to the reorientation of the dipolar BA^+ cation, can be analyzed *via* Equation 1.48. The obtained effective dipole moments as a function of BACl concentration are shown in Figure 3.32(a). Additionally, the effective dipole moments of unprotonated BA^+ species, namely n-butylamine, are shown in Figure 3.32(b). The latter were retrieved from unpublished dielectric relaxation

measurements (in the frequency range 0.2 GHz - 2.5 THz) of aqueous n-butylamine/water mixtures ($1.5 \leq c$(n-butylamine)/M ≤ 10.0) from our laboratory [250]. The μ_{eff} values of the uncharged n-butylamine are generally lower compared to BA^+(aq) and, accordingly, the effective dipole moment extrapolated to infinite dilution of BA^+(aq) is almost twice as high as the respective n-butylamine value (11.3 D *vs* 6.0 D, Figure 3.32). For both species, the experimental dipole moment values are fairly comparable with the calculation results (Figure 3.32). However, in both cases a systematic decrease of μ_{eff} with increasing c can be observed. Neglecting possible conformational changes with varying c, the decrease in μ_{eff} can be attributed to a decrease of orientational correlations/interactions between the relaxing species and the surrounding dipoles with rising solute concentration. As can be seen in Figure 3.32(a), the effective dipole moment of BA^+(aq) coincides well with the calculated value at low c. At higher concentrations the experimental value falls below $\mu_{\text{ap}}^{\text{calc}}$. This trend might indicate increasing preferential anti-parallel orientation between the relaxing dipole and the neighbouring molecules ($g < 1$, Equation 1.52). Since no systematic effects on the calculated dipole moments could be observed when explicitly taking into account varying numbers of water molecules into the calculation of low-energy BA+x·H_2O structures ($x = 1, .., 6$, Figure A.25), a negative correlation between the hydration water and BA dipoles is less likely. On the other hand, the n-butylammonium molecule, comprising a charged head-group and a hydrophobic tail, has some amphiphilic properties. Although no clear aggregates, in particularly in the studied concentration range (cmc of n-pentylammonium chloride = 1.9 M [266]), should be expected [267], the formation of (short-lived) pre-aggregates, *e.g.* dimers, would be conceivable. As just on simple physico-chemical grounds the energetically favorable arrangement would involve a maximized -$NH_3^+ \cdots NH_3^+$- distance with their hydrophobic tails most likely joined together, a preferential anti-parallel orientation and thus a reduction of μ_{eff} with increasing BA^+ concentration would be conceivable.

Besides the possibility of preferential negative correlations of the BA^+ dipoles, potential long-lived aggregates could lead to a similar effect. If the life-time of such aggregates ($\mu \neq 0$) was at least comparable with their reorientation correlation, a separate relaxation process should be discernible in the DR spectra. A relaxation time of $\sim 60 - 200$ ps would be expected for dimers, as obtained from the estimation *via* Equation 1.59. Accordingly, even higher relaxation times would be observed for larger aggregates. Thus, some rather weak relaxation processes (μ is anticipated to be small) linked to these species could be "hidden" under mode $l = 1$ and $l = 2$, respectively. At least for mode 2, this could explain the drop of $\mu_{\text{eff}}(BA^+)$ at higher c as the concentration of the "free" BA^+(aq) molecules is set equal to the analytical BACl(aq) concentration during the calculation of $\mu_{\text{eff}}(BA^+)$. In the not so unlikely case that the dipole moment of these species is zero, these aggregates would be invisible in the dielectric spectra, which, then again, would result in an effective decrease of the experimental BA^+ dipole moments with rising c. Either the aggregates are long lived or the dipoles are only preferentially aligned in opposite directions, both effects would lead to a decrease in the experimental $\mu_{\text{eff}}(BA^+)$ obtained from S_2. Similarly, the insertion of the stoichiometric BA^+ in the calculation of the effective dipole moment also implies that the formation of $BA^+ \cdots Cl^-$-IPs discussed above could lead (or at least

contribute) to the observed decline of $\mu_{\text{eff}}(\text{BA}^+)$.
The relaxation time of the BA^+ reorientation process, τ_2, decreased with increasing BACl concentration (Table 3.12, Figure A.24). Using the geometry obtained from DFT calculations (Figure A.25(a)), a relaxation time between $\sim 30 - 120$ ps would be predicted for the reorientation of the bare BA cation. The observed τ_2 values are within the hydrodynamic limits, apart from the low-concentrated samples at $c(\text{BACl}) < 0.1422$ M (Table 3.12), which might be traced back to experimental problems of resolving such low-intense modes in this concentration region. The decrease of τ_2 might originate from changes in the conformation (note that possible conformational changes were entirely neglected in the above discussion of the effective dipole moment) and thus the volume of the rotating species, or, in line with the above discussion of μ_{eff}, from the increase of anti-parallel interactions of the BA^+ cations with neighbouring cations. Using the Madden and Kivelson equation (Eq. 1.68), which connects the microscopic rotational correlation time with the corresponding relaxation time, while accounting for dipole-dipole interactions, the extent of anti-parallel alignment can be estimated. Under the assumption that the relaxation time of ~ 107 ps at $c(\text{BACl}) = 0.1422$ M (Table 3.12) represents the reorientation of the "uncorrelated" dipole, values of the Kirkwood correlation factor, g_{K}, can be obtained. The g_{K} values decreased from ~ 0.8 to ~ 0.4 with increasing solute concentration. Despite the neglect of a possible variation of the effective volume of the dipole (Equation 1.60), these values compare fairly well with the g values ($g \approx 1 - 0.5$) obtained from μ_{eff} and Equation 1.52, assuming that the experimental infinite dilution dipole moment value corresponds to the apparent dipole moment of BA^+(aq) (Figure 3.32(a)).
The behaviour of n-butylamine in water is somewhat different from its protonated form. As shown in Figure 3.32(b), the effective dipole moment of n-butylamine is significantly increased at lower concentrations, while at higher c the theoretical dipole moment value is approached (within the error bars). A MD simulation study of Kusalik *et al.* [268] on pure liquid methylamine and aqueous methylamine solutions revealed some degree of association of the methylamine molecules forming H-bonds between the amine groups. This aggregation process was discussed to be additionally driven by the hydrophobic effect associated with the nonpolar methyl moieties. Keeping in mind that the hydrophobic effect is even more pronounced for the n-butylamine molecule, a comparable picture could also apply to for the present solutions. Contrary to the discussion of the possible formation of anti-parallel orientation of the butylammonium cations in BACl(aq) solutions, a parallel alignment of dipole in the n-butylamine aggregates, which break down with increasing solute concentration, would lead to the observed features of μ_{eff}(n-butylamine) (Figure 3.32(b)). On the other hand, parallel alignment of hydrating water dipoles with respect to the n-butylamine dipole would result to a similar effect. Due to the lack of any further information, this is as far as μ_{eff}(n-butylamine) can be discussed. Further investigations, such as statistical mechanical calculations, MD simulations or diffraction experiments, would certainly give a clearer microscopic picture and surely help to clarify this issue.
GABA(aq) and AABA(aq). The effective dipole moments of GABA(aq) and AABA(aq), obtained from the amplitude of the solute relaxation mode $j = 1$ using Equation 1.48, are shown in Figure 3.33. The effective dipole moments of both amino acids decrease

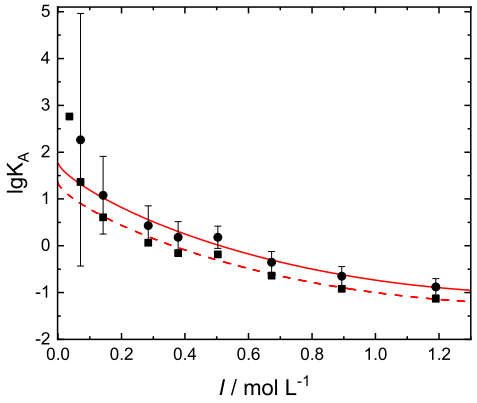

Figure 3.31: Association constant, K_A (in M^{-1}), for the formation of CIPs (●) and SIPs (■) of BACl(aq) as a function of ionic strength, I, at 25°C. The Guggenheim-type fit is denoted as a solid line and dashed line, respectively. The error bars are not shown for the K_A values of the SIP species for the sake of clarity.

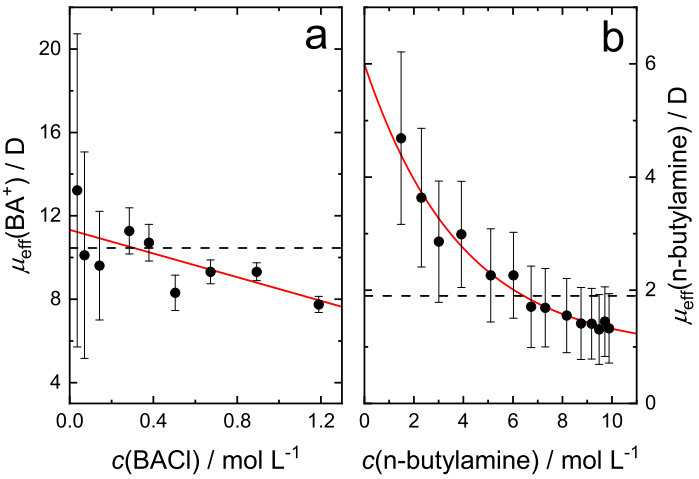

Figure 3.32: Effective dipole moments, μ_{eff}, of (a) BA^+ and (b) n-butylamine [250] as obtained from the DR spectra at 25°C. The symbols denote the experimental data, solid lines represent empirical weighted fits. The dashed line indicates the the calculated (Gaussian 09, B3LYP/6-31G(d,p) and B3LYP/6-31++G(d,p) with the PCM solvation model) apparent dipole moments of the respective molecules.

systematically with increasing solute concentration. At higher c(GABA), μ_{eff}(GABA) seems to be converge against a plateau value of $\sim$ 25.6 D (Figure 3.33(a)). Note that μ_{eff}(AABA) decreases much faster than the GABA value in the respective concentration range ($\mathrm{d}\mu_{\text{eff}}/\mathrm{d}c \approx 1.4\,\mathrm{L\,D\,mol^{-1}}$ for AABA(aq) and $\approx 0.5\,\mathrm{L\,D\,mol^{-1}}$ for GABA(aq)). The trend of μ_{eff} of GABA differs from the observations made by Kaatze *at al.* [255] using DRS, who reported a rather constant μ_{eff}(GABA) value over a similar concentration range. As would expected from the greater distance of the charged moieties, μ_{eff} of GABA(aq) is higher than the corresponding AABA(aq) value. Extrapolation to $c = 0$ yields infinite-dilution dipole moment values of 27.2 D and 22.1 D for GABA and AABA, respectively. These values are relatively large considering the small size of these molecules and higher than the respective values of $\sim$ 20 D and $\sim$ 15 D reported by Kaatze *et al.* [255]. The computed dipole moment values, obtained from low-energy structures using Gaussian 09, B3LYP/6-31G(d,p) and B3LYP/6-31++G(d,p) with the PCM solvation model, are visibly lower than the experimental values (Figure 3.33). This observation might indicate that the calculated lowest-energy conformations do not well represent the geometrical structures of GABA and AABA in a real solution. As already discussed in Sec. 3.1, taking into account the conformational flexibility of molecules containing several rotational centers in the discussion of the experimental dipole moments is not straightforward, and a full-scale (but fairly time-consuming) conformational analysis of each molecule, rather than considering only one geometrical structure (Figures A.26 and A.27), would certainly be necessary to fully unravel the extent of the conformational effect. In contrast to AABA, many studies on the conformation of the neurotransmitter GABA exist in literature. Whereas some studies indicated rather low energy barriers between the various GABA conformers and thus high conformational flexibility [269–272], others reported prevalence of either the unfolded (linear, extended) form [41, 273] or the folded ("proline-like" [248]) conformer [274]. The latter form was discussed to be stabilized by intramolecular H-bonds between the ammonium and carboxylate moieties and n-π^* interactions [270, 271]. Crittenden *et al.* [270] calculated values of $\sim$ 25 D for the linear GABA conformer, while a lower value of $\sim$ 16.5 D was obtained for the folded form. Sharma and Chandra [272] obtained dipole moments of $\sim$ 18 D for the folded conformers and $\sim$ 25 − 29 D for the linear form by theoretical calculations, while *ab initio* calculations performed by Odai *et al.* [273] found a value of 31.3 D for the unfolded form. By simple comparison of the the present dipole moment values ($\sim 27-26$ D) of GABA(aq) with the literature data and neglecting possible dipolar correlations of the solute with neighbouring molecules (Equation 1.52), the DRS results would indicate that the linear form of GABA predominates in aqueous solution, while the folded conformer is of minor importance. Similarly, a DRS study combined with fs-IR by Ottosson *et al.* [41] reported an experimental value of $\sim$ 26 D for GABA in water, which is in very good agreement with the present results. Further, similar to the present findings although not as strongly pronounced, a systematic decrease of μ_{eff}(GABA) with rising c could be observed in the latter study. The applied fitting model and the observed relaxation times are in very good agreement with the present results. The optimized geometries of the bare amino acids, whose dipole moments are denoted in Figure 3.33, do not correspond to the dominant linear conformer but rather show a slight degree of folding

(Figures A.26(a) and A.27(a)), which would explain the lower computed dipole moment values. Interestingly, the effective dipole moment of BA^+ at $c \to 0$ (Figure 3.32(a)) is by a factor of $\sim 1/2$ lower than the respective GABA value. This value would indeed be expected on simple electrostatic grounds if one of the charges at GABA was simply switched off, which on the other hand underlines the consistency of the present DR experiments.
Similar literature data on the conformation of AABA in aqueous solution is rather sparse. However, given the structural resemblance, it is reasonable to assume an analogous situation might also apply for AABA(aq). Rodrigo *et al.* found evidence for the predominance of the extended AABA conformer in aqueous solution from diffusion coefficient and NMR measurements [275]. However, further investigations of the conformation of AABA in aqueous solution would certainly be beneficial to give a definite answer.
Transforming the relaxation time of the GABA/AABA reorientation modes, τ_1, into the corresponding rotational correlation time (Section 1.3.6), the modified Stokes-Einstein-Debye equation (Equation 1.59) can be used to obtain the effective volumes of the rotating species, V_{eff}. As can be seen in Figure 3.34, the experimental rotational correlation times can be well fitted by Eq. 1.59, which indicates a constant V_{eff} (determines the slope in Figure 3.34) over the whole concentration range. Accordingly, neither the hydrodynamics friction coefficient, C, nor the molecular volume of the rotating species, V_{m}, change with increasing c (Equation 1.60). The latter indicates that the aforementioned systematic decrease of μ_{eff} cannot be linked to systemic changes of the conformation of the amino acids, as the geometries of the relaxing species stay essentially unperturbed. Using the molecular volume from the DFT-geometries (Figures A.26(a) and A.27(a)) as a first approximation for V_{m}, friction coefficients of $C(\text{GABA}) = 0.26$ and $C(\text{AABA}) = 0.39$ can be obtained. These values are within the theoretical boundary conditions, *stick* ($C = 1$) and *slip* ($C = 0.18$ for GABA and $C = 0.11$ for AABA), for both amino acids. The higher C value of AABA(aq) and thus a stronger coupling to the surrounding medium might reflect the different position of the amine group and the associated differences in the solvent-solute interactions (see below).
As can be seen in Figs. A.26 and A.27, the dipole moments of GABA and AABA hydrates (GABA/AABA·$x$$H_2O$), estimated from the geometry optimization at the B3LYP/6-31G(d,p) and B3LYP/6-31++G(d,p) level of theory with the PCM solvation model, are increased compared to the bare zwitterions. This means that the dipoles of hydrating water molecules tend to arrange themselves preferentially parallel with respect to the solute dipoles, which might lead to an effective enhancement of the detected μ_{eff} of the amino acids. A gradual break-down of this orientational correlation with rising c, *e.g.* by dehydration, might explain the observed decreasing behaviour of μ_{eff}. It should be noted that increasing anti-parallel orientation solute-solute dipoles, similarly to BACl(aq), would lead an equivalent effect, although a DRS study of Rodríguez-Arteche *et al.* found that the tendency to dipolar alignment of the zitterions in various aqueous amino acid solutions is very weak [228]. It should also be pointed out that the latter picture implies that the above discussion of the assignment of a specific conformer as the predominant form in aqueous solution, simply based on the magnitude of the dipole moment value, is not entirely permissible, as dipolar correlations most likely also have a non-insignificant contribution.

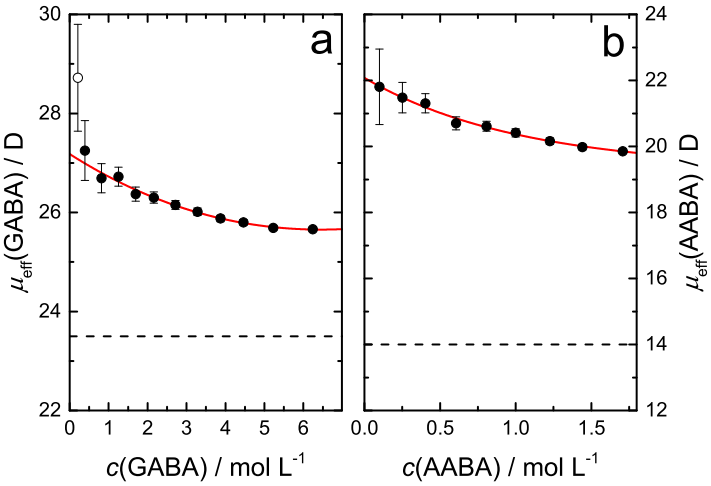

Figure 3.33: Effective dipole moments, μ_{eff}, of (a) GABA and (b) AABA as obtained from the DR spectra at 25°C. The symbols denote the experimental data, solid lines represent empirical weighted fits. Hollow symbols were excluded from the fits. The dashed lines indicate the the calculated (Gaussian 09, B3LYP/6-31G(d,p) and B3LYP/6-31++G(d,p) with the PCM solvation model) apparent dipole moments of the respective molecules.

However, in order to resolve the extent of both effects, the hydration of the solute, which is inevitably linked to the solute structure and its dynamics, has to be analyzed.

3.3.5 Solvent Relaxations - Hydration of GABA, AABA and BACl

BACl(aq). Following the procedure described in 3.1.6, the numbers of irrotationally bound water molecules, Z_{ib}, of the BA^+(aq) cation were obtained from the bulk-water relaxation mode $l = 3$ (Figure 3.35(a)). As a slow-water process could not be resolved in the BACl(aq) DR spectra, the Z_{ib} numbers equal the total effective hydration numbers of the solute. The corresponding hydration numbers of the unprotonated n-butylamine [250] are shown for comparison in Figure 3.35(b). The Z_{ib} values of both species decrease continously with increasign c, as would be expected from the decreasing solvent-to-solute number ratio and the increasing hydration shell overlap [22]. Extrapolation to $c \to 0$ yielded infinite dilution hydration numbers of $Z^0_{\text{ib}} = 3.9 \pm 0.4$ and $Z^0_{\text{ib}} = 1.7 \pm 0.1$ for BA^+(aq) and n-butylamine(aq), respectively. These numbers are markedly lower than the total number of first neighbour solvent molecules around BA^+ ($\sim$ 34) and n-butylamine ($\sim$ 33), as estimated from the solvent accessible surface area of the computed geometries in Figure A.25. As irrotational bonding is commonly associated with the hydration of polar moieties, rather than hydrophobic hydration of non-polar groups [22, 237], the present Z_{ib} values can readily be assigned to -NH_3^+/-$NH_2 \cdots H_2O$ interactions. Literature data on hydration of BA^+ and n-butylamine is rather sparse. However, information on the hydration of

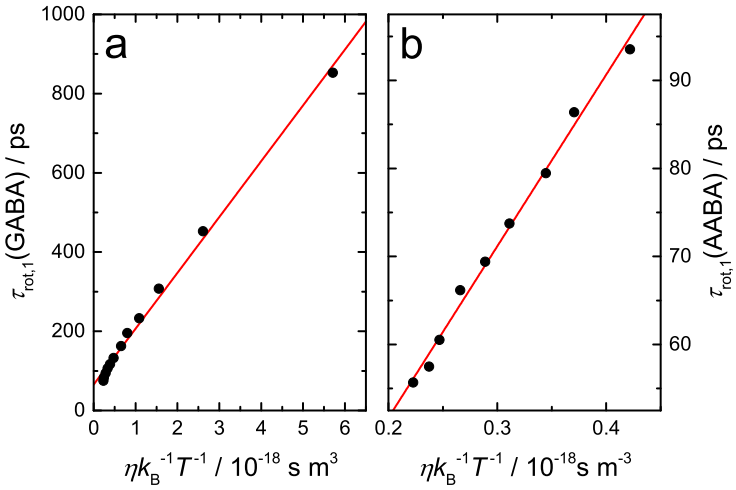

Figure 3.34: Rotational correlation time of the (a) GABA(aq) and (b) AABA(aq) reorientation as a function of $\eta k_B^{-1} T^{-1}$. Linear line denotes the fit to the modified Stokes-Einstein-Debye equation (Eq. 1.59).

the shorter homologues, *e.g.* methylammonium/methylamine, is more common and the hydration structure of the head-group would not be expected to strongly differ among the n-alkylamines, as long as the alkyl chain is not too long so that aggregates (*e.g.* micelles) start to form.

Theoretical studies of the unprotonated methylamine in aqueous solution reported ~ 3 water molecules to be strongly bound by the -NH_2 group [236, 276]. The RISM calculations of Fedotova and Kruchinin revealed a coordination number of $CN_1 \approx 7$ [17]. In contrast to BA^+, which posses only H-bond-donor capabilities, n-butylamine can also accept one hydrogen bond from the solvating water molecules [277]. The n-butylamine molecules are known to form $\sim$2 H-bonds with the hydrating water in total [17, 276]. This number coincides well with the observed infinite dilution hydration number of $Z^0_{ib} = 1.7$ observed by DRS for n-butylamine in water (Figure 3.35(b)). One of these two bonds corresponds to a -$H_2N\cdots$H-OH proton acceptor bond, while the two H-bond donating sites at -NH_2 lead to the formation of effectively one H-bond with water in total [236, 268, 276]. The water molecules coordinated at the amine hydrogens were reported to undergo a comparably fast exchange, implying a weaker interaction strength compared to the strong proton acceptor bond [236].

The coordination numbers of the ammonium group at the methylammonium cation reported in literature vary in the range $CN_1 \approx 3 - 8$ [234, 261, 278, 279]. Similarly to the unalkylated ammonium ion, NH_4^+ [170, 231–233], the hydration shells of alkylammonium cations are often classified as labile [234, 261]. The mobility of water molecules in the vicinity of the ammonium moiety was reported to be unchanged compared to the bulk and a high flexibility of the hydration shell was observed by MD simulation of Chaiyasit

et al [261]. On the other hand, some simulation studies found evidence for a rather stable solvation sheath around the onium cation [235, 236]. Hesske and Gloe [236] reported markedly higher residence times for water at the onium moiety compared to the unprotonated molecule and 4.2 H_2O molecules were found to be located in the first hydration layer around the -NH_3^+ group of the methylammonium cation. For glutamate $\sim$ 5 water molecules were found to be irrotationally bound at infinite dilution and the presence of such strongly bound water was discussed to be linked to the onium group (Section 3.2). Kuntz [280] measured a hydration number of 4.5 for the sidechain of lysine by NMR experiments of frozen polypeptide solutions. All these numbers agree exceptionally well with $Z_{\mathrm{ib}}^0 \approx 4$ obtained for n-butylammonium by DRS. A higher infinite dilution hydration number of ~ 8 for BA^+ (~ 5 for n-butylamine) was obtained from acoustic measurements by Burakowski and Gliński [281]. Note that although the number of strongly bound water molecules of the BA cation is higher compared to the uncharged n-butylamine ($\Delta Z_{\mathrm{ib}}^0 \approx 2$), the hydration of the former breaks down much faster with increasing c ($\mathrm{d}Z_{\mathrm{ib}}/\mathrm{d}c \approx$ -1.8 L mol^{-1} *vs* -0.18 L mol^{-1}), which suggest that, in spite of the relatively higher number of water molecules effectively "frozen" on the DRS timescale at the onium group, its hydration sheath crumbles very fast when steric stress is increased. This observation of a relatively strong hydration at low c but a fast break-down of the solvation sheath as the concentration is increased might explain the discrepancy of the literature data of whether the hydration structure of the alkylammonium ion can be classified as flexible or rather stable. Note that a similar behaviour was observed for glutamate (Section 3.2), for which $Z_{\mathrm{ib}}(\mathrm{Glu}^-)$ declines fast with solute concentration.

At this stage, it is instructive to compare the present results to the hydration of butanoate, as investigated by DRS [237]. In contrast to BACl(aq), no irrotationally bound water could be detected for the butanoate solutions. On the other hand, an intense slow-water mode was clearly discernible in the DR specta, revealing an infinite dilution hydration number of $Z_{\mathrm{s}}^0 \approx 33$. At higher concentration, a value of $Z_{\mathrm{s}}(c \to \infty) \approx 6$ was systematically approached. The latter value was attributed to the number of water molecules impeded in their dynamics by hydrophilic hydration of the carboxylate moiety [160]. The difference, $Z_{\mathrm{s}}^0 - 6 \approx 27$, could thus be readily assigned to the hydrophobic hydration of the alkyl chain. The hydration butanoate is distinctly different from BA^+ and, given their structural similarity (both contain a linear alkylchain and a charged headgroup), quite surprising. However, it should be kept in mind that the sign of charged entities, and thus the differences in their polarizabilities, play a major role in the solvation strength and structure [34, 282]. A Monte-Carlo simulation study of acetate and methylammonium in aqueous solution by Alagona *et al.* [234] showed that, in contrast to acetate anion, the methyl group of the methylammonium cation is partly charged by the onium moiety, which results in stronger (less hydrophobic) -CH_3–H_2O interactions. A similar effect was found by Meng and Kollman using MD simulations [279]. A smearing-out of the positive charge even beyond the first methylene group was reported by James Port and Pullman [283] for tetraethylammonium cations and Davis *et al.* [284] confirmed in an experimental Raman spectroscopy study that alkyl chains at onium cations are markedly less hydrophobic due to charge delocalization compared to alkylcarboxylates. Although some contribution of

dynamically slowed down water could be at least indirectly observed in the DR spectra of BACl(aq) in the form of the broadening parameter, α_3, and the increasing behaviour of the bulk-water relaxation time, τ_3 (Table 3.12), a resolution of this solvent mode was not possible. Thus, a similar polarization effect of the linear butyl chain might be conceivable for the studied BA^+ cation, which could explain the virtual absence of hydrophobically impeded water fraction in the BA^+(aq) solutions. Interestingly, a slow-water mode could be resolved and assigned to the hydrophobic hydration of the alkyl moieties for Me_4N^+(aq) (Section 4.2), as well as $AcCh^+$(aq) and Car^+(aq) (Section 3.1), which would imply that such a charge delocalization effect is more pronounced in monoalkylammonium molecules compared to tetrasubstituted cations.
Furthermore, cooperative hydrophobic-hydrophilic hydration effects at the alkylcarboxylate, similarly to the results of Reference [230], might also lead to markedly different hydration structures of BA^+ and butanoate. In the cited Car-Parrinello study, the hydration 1-ethyl-3-methyl-imidazolium chloride was investigated and it was found that that hydrating water at the imidazolium-chloride IPs aligns itself in such a ways that hydrophilic as well as hydrophobic hydration patterns are adopted at the same time, without any orientational mismatch in the region between the polar and unpolar groups. Thus, higher hydration numbers would be expected for species with such a feature. A similar effect might apply for butanoate, for which much higher Z_t values compared to BA^+(aq) are observed.
Although there are strong hints that these effects might be present for the two systems, a clear evidence cannot be given here, since DRS only provides a macroscopic rather than microscopic picture on the solute hydration. Further investigations, such as MD simulations, which have the ability to scan the water dynamics and orientation around the solute, would certainly shed some light on this issue.
GABA(aq) and AABA(aq). The effective hydration numbers of GABA and AABA, obtained from the solvent-related modes of the dielectric spectra, are shown in Figure 3.36. The respective infinite dilution values of both solutes are listed in Table 3.13. Despite the comparable overall magnitude of the hydration numbers and fairly comparable Z^0_{ib} values, the hydration of the two amino acids differs noticeably. The total hydration number of GABA(aq) solutions decrease continuously with c, while a rather constant value $Z_t(c) \approx Z^0_t = 9.4 \pm 0.8$ can be observed for AABA(aq) over the studied concentration range. Here, it should be kept in mind that the covered concentration range was significantly smaller for AABA(aq) solution due to solubility limits. The slow-water mode could not be resolved in the AABA(aq) spectra at low concentrations, resulting in vanishing Z_s values at $c(\text{AABA}) \leq 0.4033\,\text{M}$. At $c(\text{AABA}) > 0.4033\,\text{M}$, a slow-water mode appeared and its amplitude increased continuously with c (Table 3.11, Figure A.23). The thus obtained Z_s values increase with increasing AABA concentration (Figure 3.36(b)) and a plateau value of ~ 6 is approached as c(AABA) is reaching the solubility limit. The Z_s values of GABA(aq), for which the slow-water mode was describable over the complete concentration range, decrease steadily from $Z^0_s = 10$ to ~ 2 a high c. The Z_{ib} values decline systematically with rising solute concentration for both amino acids. However, the deduced infinite dilution numbers of irrotationally bound water are markedly higher for AABA (Table 3.13). The

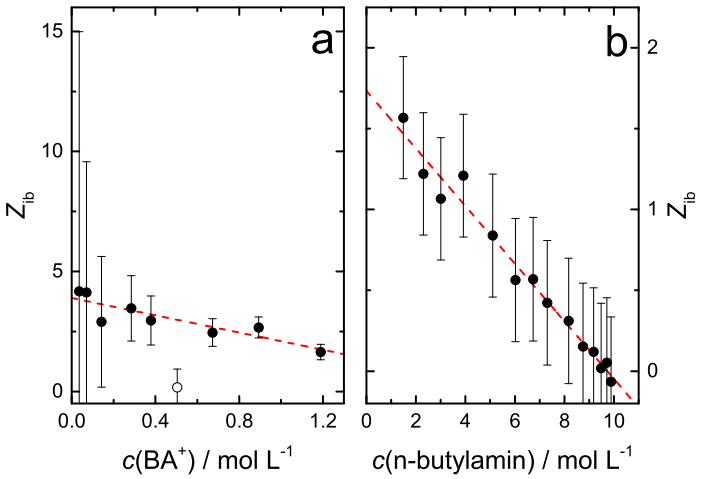

Figure 3.35: Numbers of irrotationally bound solvent molecules, Z_{ib}, of (a) BA^+ and (b) n-butylamine at 25 °C. Dashed lines denote linear weighted fits.

Z_{ib} values of AABA(aq) decrease from 9.4 at $c \to 0$ to ~ 3 at the highest concentration. The respective value of GABA(aq) decline from ~ 2 at infinite dilution to $Z_{ib} \approx 0$ at high GABA concentrations. Note that the unphysical $Z_{ib} < 0$ values at c(GABA) $\geq$ 4.460 M can regarded as ~ 0 within the error limits (Figure 3.36(a)). Despite the higher Z_{ib} values, a steeper overall decrease with rising solute concentration can be observed for AABA(aq) ($dZ_{ib}/dc \approx$ -4 L mol^{-1}) compared to GABA(aq) ($dZ_{ib}/dc \approx$ -1 L mol^{-1}). Note that in Section 3.2 a similarly fast dehydration ($dZ_{ib}/dc \approx -5$ L mol^{-1}, Figure 3.21) was observed for Glu^-, whose chemical structure differs from AABA only by the presence of a -COO^- at the γ-carbon.
Clearly, the hydration water dynamics of the two amino acids, which only differ in the position of one functional group, is significantly different. Note that similar numbers of ~ 35 and ~ 34 water molecules can be packed into the first shell around the GABA and AABA molecules, respectively, as retrieved from solvent accessible surface area calculation of the structures in Figure A.26(a) and A.27(a). However, given that the hydration is governed by short-range interactions, there is no necessary reason why the hydration structure should be the same for the two isomers, although it seems intuitively sensible at first. The concentration-behaviour of the hydration numbers of GABA(aq), for which the charged groups are relatively far away, is at least qualitatively comparable to the hydration of its functional components: the existence of a pronounced slow-water fraction and the decline of the Z_s values with increasing c is consistent with the hydration properties of the butanoate anion [237]. As no slow-water could be found in the DR spectra of BA^+(aq) (see above), it might be assumed that the slow-water fraction is most likely associated with the hydrophilic and hydrophobic hydration of the alkylcarboxylate moiety. Note that the Z_s values observed for GABA(aq) are markedly lower compared to butanoate [237]

($Z_s^0 \approx 10$ for GABA vs $Z_s^0 \approx 33$ for butanoate). This difference might be due to the hydrophobicity diminishing effects of the alkyl chain imposed by the onium group, as discussed above. Keeping in mind that the major proportion of the Z_s of butanoate is linked to the hydrophobic hydration of the hydrocarbon chain, a lower Z_s would be expected for GABA(aq). In accordance with this view, Pottel *et al.* [256] reported a higher number of slowed down water molecules, $\sim 18-12$, for the deprotonated GABA molecule in a 1 M solution compared to the (protonated) zitterionic form ($\sim 9-11$). The deceleration of the water dynamics at the carboxylate group was reported to be not strong enough to "freeze" the water molecules on the DRS timescale [237]. Thus, the observed Z_{ib} values of GABA(aq) can be attributed to the hydration of the protonated amine moiety and the derived Z_{ib}^0 value of ~ 2 is rather close to the BA^+(aq) value of ~ 4 (Figure 3.35).
On the other hand, the close proximity of the charged onium and carboxylate moities in AABA completely annihilates the possibility of predictability of its hydration pattern on the basis of the hydration of the individual functional groups. The higher infinite dilution number of strongly bound water molecules of AABA(aq) might be associated with the closer location of the two oppositely charged groups, which might lead to a stronger, presumably cooperative, binding of the water dipoles at the charged moieties. Similar to present results, a higher number of strongly bound water molecules was found for the α-alanine compared to the β-isomer [228]. A similar situation might also apply for Glu^- studied in Section 3.2. Note that the higher Z_{ib} values of AABA compared to GABA are consistent with the higher hydrodynamic friction coefficient values for AABA for the reorientation of zwitterions in solution (Section 3.3.4). As the total number of dynamically affected water molecules stays fairly constant for AABA(aq), it can be assumed that the solvent molecules, which are initially "frozen", regain some of their mobility with rising c such as they contribute as slow-water to the DR spectra. Interestingly, the plateau values of $Z_s \approx 6$ coincides with the number of water molecules bound to the carboxylate group of an alkylcarboxylate anion [16, 160, 234, 237, 280].
The present total hydration number of AABA are generally higher than the observed literature values. Adiabatic compressibility and viscosity measurements [281, 285] revealed an infinite-dilution hydration number of ~ 3. Suzuki *et al.* [257] reported ~ 7 water molecules being impeded dynamically by the AABA molecule by using DRS in a 0.2 M solution at 20 °C. A THz-spectroscopy study of an aqueous ~ 0.5 M AABA solutions at 26.85 °C suggested a hydration number of ~ 6 [286]. It should be mentioned that in the latter study the hydration number was derived from the bulk-water relaxation mode centered at 19 GHz, while the studied frequency ranges was limited to $200-12000$ GHz [286]. The resolution of a mode located far outside the scanned frequency range is usually not unproblematic and higher errors in the amplitude would be expected. Thus, the comparison of the present results with the THz data of Ref. [286], which were also measured at slightly higher temperatures, should be taken with care. The Z_{ib}^0 value of the structurally-related Glu^- of ~ 5 is markedly lower than the present AABA value. Analogous to the latter, this "frozen" water fraction was discussed to originate (most likely) from the hydration of the backbone of the α-amino acid (Section 3.2).
The dielectric relaxation study of Pottel *et al.* of 1 M GABA(aq) solutions at 25 °C yielded

$\sim 9-11$ slowed-down molecules [256], which coincides exceptionally well with the present results ($Z_s(1\,\mathrm{M}) \approx 9$, Figure 3.36). A more recent dielectric/fs-IR study of GABA(aq) by Ottosson *et al.* [41] showed comparable but slightly higher Z_{ib} and Z_s values over a similar concentration range. The reported Z_{ib} values of GABA decreased from ~ 4 to ~ 1 in the concentration range $1 \leq c(\mathrm{GABA})/\mathrm{M} \leq 6$. Analogously, the Z_s values declined from ~ 14 to ~ 6. Acoustic measurements of aqueous GABA solution revealed a hydration number of 7.2 at infinite dilution [281] and a theoretical study by Ramek and Nagy [287] indicated that GABA forms in total $\sim 6.5-8$ stable H-bonds with water. Assuming that $Z_s(\text{-}\mathrm{COO}^-) \approx 6$ water molecules are slowed down in the vicinity of the carboxylate group [237], the latter literature values are in good agreement with the number of water molecules bound by the hydrophilic moieties, $Z_{ib}^0 + Z_s(\text{-}\mathrm{COO}^-) \approx 8$.
At this stage, it is instructive to try to relate the hydration results to the obtained dipole moments of the respective molecules. As discussed in the previous section (Section 3.3.4), the behaviour of the experimental dipole moments of GABA(aq) and AABA(aq) might be associated to its interaction with the surrounding solvent molecules. In Figure 3.37 the effective dipole moments of the two amino acids are plotted against the number of strongly bound water molecules. As can be seen, μ_{eff} of both molecules show a marked linear dependence on Z_{ib}. The positive slope implies that the strongly bound water dipoles align themselves preferentially parallely with respect to the solute dipoles. As the solute concentration increases, a decrease in Z_{ib} is observed (Figure 3.36) and as consequence thereof the dipolar correlations break down. Interestingly, the slope of the linear fit in Figure 3.37 was identical for the two zwitterions ($\mathrm{d}\mu_{eff}/Z_{ib} \approx 0.4\,\mathrm{D}$), indicating a similar mechanism of dipolar coupling of the two structurally related molecules. Extrapolation of the curves in Figure 3.37 to $Z_{ib} \to 0$ yields the effective dipole moments of the essentially bare zwitterions. For GABA(aq) $\mu_{eff}^{Z_{ib}\to 0} = 23\,\mathrm{D}$ is thus obtained, while a value of $\mu_{eff}^{Z_{ib}\to 0} = 19\,\mathrm{D}$ is found for AABA(aq). The latter value is higher than the computed dipole moment of the bare AABA zwitterion (14.0 D; Figure A.27(a)). The obtained dipole moment of the non-strongly hydrated GABA molecule agrees well with $\mu_{ap}^{calc} = 23.5\,\mathrm{D}$ obtained from DFT calculations (Figure A.26(a)) and, to take up the discussion of the GABA conformation of the previous section, the relatively high $\mu_{eff}^{Z_{ib}\to 0}$ value confirms that the folded, "proline-like" conformer is most probably less stable than the (at least partly) elongated form in aqueous solution.

3.3.6 Concluding Remarks

The dielectric spectra of BACl(aq) were fitted by two Debye and one Cole-Cole equation. A distinct slow-water process was not discernible in the present spectra over the studied concentration range. The low-frequency process in the DR spectra of BACl(aq) was assigned to a possible IP relaxation. Since the association constants retrieved from the latter mode were found to be too high, a non-negligible IC contribution was suggested to contribute significantly to the low-frequency mode of the BACl(aq) spectra, masking the IP response. The obtained effective dipole moments of BA^+(aq) and n-butylamine decreased systematically with increasing concentration. Besides possible concentration-induced conformational

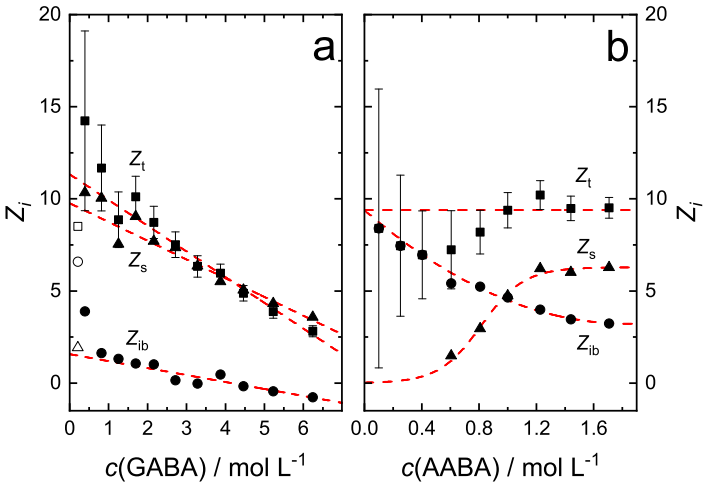

Figure 3.36: Total effective hydration numbers, Z_t(■), and the numbers of moderately retarded, Z_s(▲), and irrotationally bound water, Z_{ib}(●), of (a) GABA(aq) and (b) AABA(aq) as a function of concentration at 25 °C. Dashed lines denote weighted empirical fits. The intercept of $Z_{ib}(c)$ of AABA(aq), was fixed to $Z_t^0 - Z_s^0$. Error bars of Z_s and Z_{ib} were omitted for the sake of clarity. Unfilled symbols were not included in the fits.

Table 3.13: Infinite dilution hydration numbers, Z_t^0, Z_s^0 and Z_{ib}^0 of GABA(aq) and AABA(aq) at 25 C. The errors were obtained from the standard errors of the empirical fits.

	Z_t^0	Z_s^0	Z_{ib}^0
GABA(aq)	11.3 ± 0.7	9.8 ± 0.3	1.6 ± 1
AABA(aq)	9.4 ± 0.8^a	0 ± 0.4	9.4 ± 1.2^b

[a]Slope of the linear fit was fixed to 0; [b]Z_{ib}^0 were calculated from the extrapolated Z_t^0 and Z_s^0 values according to $Z_{ib}^0 = Z_t^0$ - Z_s^0

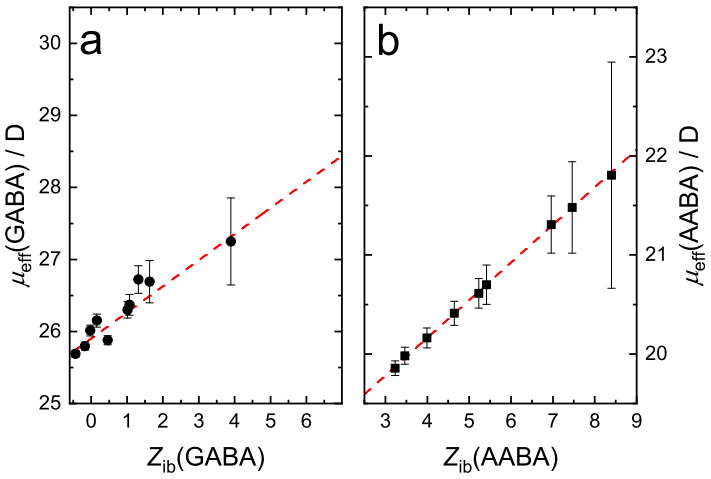

Figure 3.37: Effective dipole moments, μ_{eff}, of (a) GABA and (b) AABA as a function of Z_{ib}. The dashed line indicates a linear fit.

changes, potential dipolar solute-solute correlations were discussed to be responsible this effect. The analysis of the solvent-related mode revealed ~ 4 and ~ 2 irrotationally bound water molecules at the the onium and amine moiety, respectively. The obtained hydration numbers suggested a markedly different hydration pattern of BA^+(aq) compared to its couterpart, the butanoate anion. The inability to resolve a slow-water mode in BACl(aq) spectra was discussed to be associated with hydrophobicity-diminishing effects of the onium group.

The dielectric spectra of GABA(aq) were successfully fitted by a combination of four Debye equations. A three Debye model had to be used at lower concentrations of AABA(aq), while at higher AABA(aq) concentrations four Debye equations described the spectra satisfactorily. Whereas the total hydration numbers at infinite dilution were comparable for both zwitterions, significantly higher Z_{ib}^0 value were observed for AABA(aq) and the trends of Z_{s} were crucially different for both amino acids. These discrepancies were discussed to be linked to the different locations of the onium moiety and the associated effects on the hydration structure. It was found that the solvation structure and dynamics of GABA(aq) could be fairly well modeled by considering the hydration characteristics of the individual functional groups, while the close location of the charged groups prohibited such a simplified approach for AABA(aq). The obtained effective dipole moments of GABA(aq) and AABA(aq) were found to decrease with increasing solute concentration for both molecules. Consistent with the observed hydration numbers, this decline was argued to be linked to the gradual loss of preferentially parallely aligned and tightly bound water dipoles at the zwitterions with increasing c. The magnitude of the dipole moment values of GABA(aq) suggested that the folded (ring- or proline-like) conformer is most likely of minor importance in aqueous solution.

The latter results underline that the dissimilar bioaction of GABA and AABA may not only be linked to their differing spatial structures, in the sense of molecular recognition, but there a also marked differences regarding their interaction with the surrounding medium, *i.e.*, water, which could be clearly observed in this dielectric study and which should equally be taken into account when discussing the biological behaviour of the two compounds.

Chapter 4

Inorganic Salt Solutions

The materials presented in this chapter form the basis for the paper:

Friesen, S.; Hefter, G.; Buchner, R. Cation Hydration and Ion Pairing in Aqueous Solutions of $MgCl_2$ and $CaCl_2$. *J. Phys. Chem. B* **2019**, *123*, 891–900.

The following first section closely follows the publication.

The chemical, and hence biological, behaviour of ions in aqueous solution is governed by a subtle interplay between their level of hydration and their interactions with other ions, especially those of opposite charge [282, 288]. In more general terms, their chemical characteristics are reflected in a subtle balance between solute-solvent and solute-solute interactions: relatively minor changes in either can result in dramatic differences in behaviour and function [26].
However, before the effect of the ions on the structure and dynamics of biomolecules can be studied, the properties of the salts in water have to be analyzed, in order to disentangle the specific ion-solvent and ion-biomolecule effects. In the following, $MgCl_2$(aq), $CaCl_2$(aq) and NH_4NCl(aq) solutions will be discussed.
As LiCl(aq) [289], NaCl(aq) [55, 186], KF(aq) [290, 291] and KCl(aq) [292] were already studied and, for the most part, published in previous works, it was refrained from remeasuring or discussing these binary systems in detail in the framework of this thesis.

4.1 Magnesium Chloride and Calcium Chloride

The alkaline earth metal ions magnesium(II) and calcium(II) are omnipresent in nature [225]. For instance, Mg^{2+} is the second most common cation in seawater [293] (and most natural water bodies [294]), while Ca^{2+} is the most abundant metal cation in the human body (mostly in bones and teeth) [288]. Both ions have profound biological importance. Thus, Mg^{2+} is essential for stabilization of proteins, polysaccharides, lipids and DNA/RNA

molecules. Its concentration is in the mM range inside and outside the human cells. The calcium ion is critical for bone formation, blood coagulation, enzymatic reactions and it plays a key role in signal transduction processes [288]. The resting Ca^{2+} concentration inside human cells lies in the region $\sim 0.01 - 0.05\,\mu$M (can increase up to 1 mM upon stimulation) and ~ 3 mM in the extracellular fluid [295].

The significance of both ions in anorganic chemistry and biology is indisputable. Accordingly, aqueous solutions of $MgCl_2$ and $CaCl_2$ have been studied extensively by traditional techniques such as conductometry and potentiometry [296, 297] and using modern instrumental methods such as X-ray [42, 46, 298, 299] and neutron diffraction [300, 301], extended X-ray absorption fine structure (EXAFS) spectroscopy [45, 302, 303], and by computer simulations [300, 301, 304–310]. Much has been learnt from these studies regarding the structure and the dynamics of these solutions. With regards to hydration there is a general consensus that Mg^{2+}(aq) is surrounded by two well-formed layers of water molecules whose dynamics differ considerably from those of bulk water. The character of the hydration of Ca^{2+}(aq) is still a hotly debated topic even though most investigations conclude that it is somewhat less strongly hydrated than Mg^{2+}(aq).

Both $MgCl_2$(aq) and $CaCl_2$(aq) have commonly been considered archetypal strong 2:1 electrolytes [297]. Nevertheless there is some evidence, primarily from traditional methods, of a small amount of ion association [311]. It is highly important to resolve this issue, as even small ion-pairing (formation) constants can significantly alter chemical speciation at moderately concentrated solutions.

Besides the ability to analyze the hydration structures and its dynamics, DRS is a very sensitive, albeit not the most accurate, probe of ion pairing in electrolyte solutions, with a unique ability to detect different kinds of IPs with the sensitivity: 2SIP > SIP > CIP [312].

The present study reports a detailed investigation of the dielectric spectra of aqueous solutions of $MgCl_2$ and $CaCl_2$ at 25 °C and concentrations up to $\sim 1.8\,\mathrm{mol\,L^{-1}}$. Apart from two rather old studies [44, 313] made over more limited frequency ranges, this is the first broadband DRS study of the aqueous solutions of these two important salts.

4.1.1 Data Acquisition and Processing

The sample preparation and handling was carried out according to procedures in Sections 2.1 and 2.2. The measured densities, viscosities and conductivities (Section 2.4) of the $MgCl_2$(aq) and $CaCl_2$(aq) solutions are summarized in Tables A.13 and A.14, respectively. The dielectric spectra were recorded in the frequency range 0.05 - 89 GHz at 25 °C (Dielectric probe kit VNA setup + E-band interferometer, Section 2.3). As pointed out in Section 1.1.2, the lowest accessible frequency, ν_{min}, increases with increasing conductivity, that is, with increasing salt concentrations. Accordingly, ν_{min} was always $0.07 \leq \nu/\mathrm{GHz} \leq 0.66$ for the highly conductive $MgCl_2$(aq) and $CaCl_2$(aq) solutions (Tables A.13 and A.14).

4.1.2 Fitting Models and Assignment of Modes

Combinations of up to five HN-equations (equation 1.41) were tested to fit the dielectric relaxation spectra. Consistent with the Zasetsky plots (Figures A.28 and A.29), a sum of up to four Debye processes (D+D+D+D model) for $MgCl_2$(aq) and up to five (D+D+D+D+D model) for $CaCl_2$(aq) solutions provided the best description of the recorded spectra. The parameters obtained from these fits are shown in Tables 4.1 and 4.2. As usual, modes are numbered from lower to higher frequencies. For clarity in the following discussion j will be used to identify only $MgCl_2$(aq) modes; modes in $CaCl_2$(aq) solutions will be designated as l. Further, for reasons that will become obvious, the lowest frequency process observed for $CaCl_2$(aq) solutions will be defined as the $l = 0$ mode.

The dielectric spectra and their evolution with rising salt concentration are shown in Figure 4.1. The dominant mode ($j, l = 3$) in the spectra, centered at ∼19-26 GHz, can be unambiguously assigned, on the basis of its location and intensity, to the cooperative reorientation of bulk water molecules [22, 150]. The amplitude of this mode, S_3, decreased systematically with increasing solute concentration for both systems (Figures A.30 and A.31). Also apparent in the spectra (Figure 4.2) is a low intensity mode ($j, l = 4$) centered well above the present upper-frequency limit. This mode can be attributed to the fast switch of H-bond connections between adjacent H_2O molecules *via* a triangular transition state as mentioned previously (Section 3.1). Since the present spectra were limited to $\nu \leq 89$ GHz it was not possible to resolve this process completely, as has been also found for various electrolyte systems [55, 98, 151]. Accordingly, its relaxation time, τ_4, was fixed at the neat water value of 0.278 ps [154] (except for $c(CaCl_2) \leq 0.085$ M; Table 4.2).

The lower-frequency modes ($j, l \leq 2$) in the present spectra appear upon addition of salt and are thus solute-related. For $MgCl_2$(aq), two solute-modes ($j = 1, 2$), whose amplitudes varied with c, were observed (Table 4.1, Figure A.30). All of the ions present in these solutions are symmetrical, consequently, they do not have permanent dipole moments and thus do not contribute (directly) to the DR spectra. It is therefore reasonable, given their locations and intensities, to assign both of these modes to ion pairs, having lifetimes at least similar to their rotational correlation times.

Similarly, modes ($l = 1, 2$) observed in the $CaCl_2$(aq) DR spectra (Table 4.2, Figure A.31) can reasonably be attributed to (solvated) ion-pairs. However, an additional slow process, which was labeled $l = 0$ for convenience, variably centered at 15-270 MHz (∼1100-600 ps), was also detected at least in some spectra. While this mode might also be related to ionic aggregates, the long relaxation time, the increase and subsequent decrease of its amplitude, S_0, at low c, followed by its disappearance altogether from the spectra at $c \gtrsim 0.45$ M, are more consistent with an ion-cloud relaxation rather than ion pairs [55, 166]. The absence of a similar effect for $MgCl_2$(aq) may reflect the more tightly bound hydration shell of Mg^{2+} *cf.* Ca^{2+} (see below), or that the IC mode may have shifted to $\nu < \nu_{min}$ since the IC relaxation time varies with $\sim 1/\kappa$ [54]. Alternatively, it may simply reflect the accumulation of experimental errors in the DRS measurements at low ν of strongly conducting systems.

Table 4.1: Static permittivity, ε, relaxation amplitudes, S_j, relaxation times, τ_j ($j = 1, ..., 4$), infinite frequency permittivity, ε_∞, and the reduced error function, χ^2_r, of the D+D+D+D model fitted to the DR spectra of $MgCl_2$(aq) at 25 °C.[a,b]

c	ε	S_1	τ_1	S_2	τ_2	S_3	τ_3	S_4	τ_4	ε_∞	χ^2_r
0[c]	78.37	–	–	–	–	72.42	8.35	2.43	0.278	3.52	0.0056
0.03094	78.5	1.77	487	0.7F	18.0F	70.3	8.20	2.20	0.278F	3.52F	0.0295
0.07636	78.1	2.58	279	0.9F	18.0F	68.8	8.20	2.31	0.278F	3.52F	0.0543
0.1513	76.0	2.88	165	1.22	17.5	65.9	8.12	2.47	0.278F	3.52F	0.0609
0.3064	71.6	2.55	145	1.8F	18.0F	60.7	8.10	2.99	0.278F	3.52F	0.105
0.4105	69.7	2.38	113	2.05	16.8	58.7	8.14	3.01	0.278F	3.52F	0.106
0.5180	66.3	1.48	128	2.98	21.0	55.0	8.08	3.33	0.278F	3.52F	0.155
0.6270	63.2	0.510	82.4	4.7F	23.6	51.5	7.93	2.89	0.278F	3.59	0.145
0.8481	58.8	0.450	94.5	7.66	16.9	44.0	7.52	3.15	0.278F	3.52F	0.102
1.079	53.6	–	–	8.72	16.2	37.9	7.40	3.53	0.278F	3.52F	0.0926
1.371	49.6	–	–	11.4	14.3	31.1	7.00	3.50	0.278F	3.52F	0.0980
1.642	45.3	–	–	12.5	13.8	25.4	6.74	3.85	0.278F	3.52F	0.0887

[a]Units: c in mol L^{-1}; τ_j in ps. [b]parameter values followed by "F" were fixed. [c]taken from Ref. [97].

Table 4.2: Static permittivity, ε, relaxation amplitudes, S_l, relaxation times, τ_l ($l = 0, ..., 4$), and infinite frequency permittivity, ε_∞, of the D+D+D+D+D model fitted to the DR spectra of $CaCl_2$(aq) at 25 °C. [a,b]

c	ε	S_0	τ_0	S_1	τ_1	S_2	τ_2	S_3	τ_3	S_4	τ_4	ε_∞	χ^2_r
0[c]	78.37	–	–	–	–	–	–	72.42	8.35	2.43	0.278	3.52	0.0056
0.04865	80.7	2.55	1124	1.61	241	–	–	70.5	8.30	2.65	0.702	3.45	0.0315
0.08515	78.2	3.07	982	1.98	167	0.248	20.0F	66.7	8.08	2.65	1.11	3.52F	0.0950
0.2173	76.4	2.15	900F	2.79	137	2.44	20.6	62.8	7.85	2.65	0.278F	3.52F	0.0777
0.4349	69.7	1.18	600F	2.70	97.7	3.25	18.2	56.3	7.61	2.78	0.278F	3.52F	0.105
0.6106	64.3	–	–	1.27	132	4.04	22.0	52.3	7.58	3.18	0.278F	3.52F	0.105
0.7849	60.4	–	–	1.26	182	5.03	20.0F	47.6	7.30	3.02	0.278F	3.52F	0.108
0.8726	57.8	–	–	–	–	5.75	22.4	45.3	7.21	3.22	0.278F	3.52F	0.114
1.050	54.0	–	–	–	–	7.06	17.8	39.8	6.96	3.56	0.278F	3.52F	0.117
1.225	50.6	–	–	–	–	7.85	19.0F	35.5	6.56	3.64	0.278F	3.52F	0.158
1.786	44.8	–	–	–	–	8.76	17.7	28.4	6.07	4.12	0.278F	3.52F	0.146

[a]Units: c in mol L^{-1}; [b]τ_j in ps. parameter values followed by "F" were fixed. [c]taken from Ref. [97].

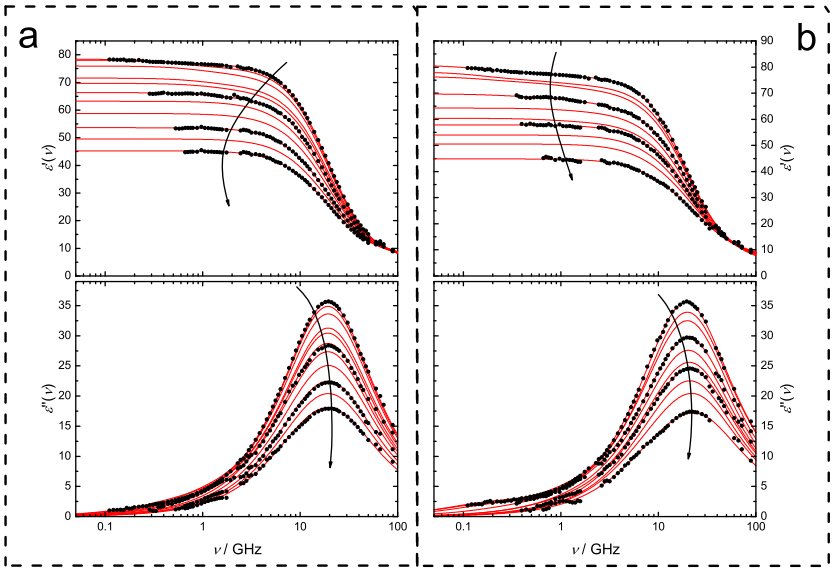

Figure 4.1: Relative permittivity, $\varepsilon'(\nu)$, and dielectric loss, $\varepsilon''(\nu)$, spectra of (a) $MgCl_2$(aq) ($0.03094 \leq c/\mathrm{mol\,L^{-1}} \leq 1.642$) and (b) $CaCl_2$(aq) ($0.04865 \leq c/\mathrm{mol\,L^{-1}} \leq 1.786$) at 25 °C. Symbols denote the experimental data. Solid lines represent the fits. For visual clarity data points are only shown for selected samples. Arrows indicate the trend with increasing electrolyte concentration.

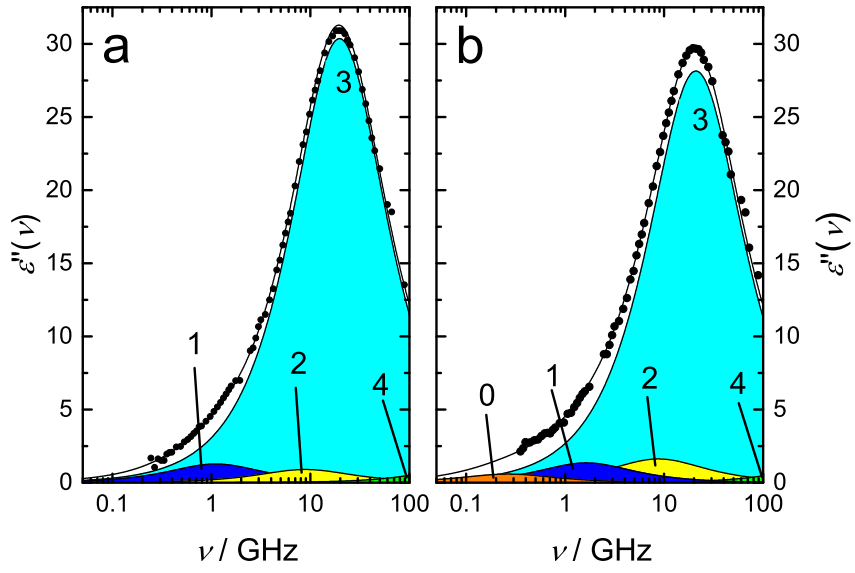

Figure 4.2: Dielectric loss spectrum, $\varepsilon''(\nu)$, of (a) 0.3064 M $MgCl_2$(aq) and (b) 0.4349 M $CaCl_2$(aq) at 25 °C. Experimental values are denoted by symbols, the solid line represents the overall fit. Shaded areas indicate the contributions to the spectrum from the various D modes.

4.1.3 Solute Relaxations- Ion Pairing

Although $MgCl_2$ and $CaCl_2$ have long been considered as archetypal strong 2:1 electrolytes, the appearance of solute-dependent modes at low frequencies in the DR spectra can be considered as evidence for at least some degree of ion pairing, if the following conditions are fulfilled. First, all free ions present in the solutions must be fully symmetrical and thus not contribute to the spectra ($\mu_{\text{ion}} = 0$). Second, while ion-cloud relaxation undoubtedly contributes to the spectra at low ν its contribution should become small and negligible at higher ν and higher c. Third, no distinct slow-water or other plausible modes should contribute significantly to the spectra in the region of the resolved solute modes. As all of these criteria have been met, it is safe to conclude that the finite amplitudes of modes 1 and 2 indicate the presence of small amounts of ion pairs.
Ion pairing in electrolyte solutions can be best described by the well-established Eigen-Tamm mechanism [314, 315]. According to this model, free solvated ions initially associate, with their first hydration shells intact, to form double-solvent-separated ion pairs (2SIPs). These may then lose their intervening water molecules, forming successively solvent-shared (SIPs) and contact ion pairs (CIPs). Assuming that only 1:1 IPs are formed, the process of the present system can be written as

$$\underset{\text{free ions}}{M^{2+}(aq) + Cl^-(aq)} \overset{K_{2SIP}}{\rightleftharpoons} \underset{2SIP}{\left[M^{2+}(OH_2)(OH_2)Cl^-\right](aq)} \overset{K_{SIP}}{\rightleftharpoons} \underset{SIP}{\left[M^{2+}(OH_2)Cl^-\right](aq)} \overset{K_{CIP}}{\rightleftharpoons} \underset{CIP}{\left[M^{2+}Cl^-\right](aq)} \tag{4.1}$$

Note that the above mechanism does not necessarily mean all three types of IPs should always be detectable in solution. Depending on the stability of the IP species, only one or two kinds of the above proposed IPs might be present.
The overall ion-association equilibrium constant, K_A, which is directly measured by thermodynamic techniques and by conductometry, is related to the above equilibrium constants *via*

$$K_A = \frac{c_{IP}}{c_+ c_-} = K_{2SIP} + K_{2SIP}K_{SIP} + K_{2SIP}K_{SIP}K_{CIP} \tag{4.2}$$

where $c_{IP}(= c_{2SIP} + c_{SIP} + c_{CIP})$ is the total concentration of all IPs formed and $c_\pm$ is the concentration of the free cations and anions, respectively.
Concentrations of detected IPs were obtained from observed amplitudes S_1 and S_2 using equation 1.48. The effective dipole moments of the different species, $\mu_{\text{eff,IP}}$, and the corresponding field factors, A_{IP} and f_{IP}, were derived using the procedure of Barthel *et al.* [72]. Polarizabilities of the IPs were calculated as: $\alpha_{IP} = \alpha_+ + \alpha_- + m \cdot \alpha_{H_2O}$, where $m = 0$, 1 or 2 for CIPs, SIPs and 2SIPs, respectively. Polarizabilities of the bare ions [316, 317] were taken to be $7.13 \cdot 10^{-32}$ Å^3 for Mg^{2+}, $6.3 \cdot 10^{-31}$ Å^3 for Ca^{2+}, $3.42 \cdot 10^{-30}$ Å^3 for Cl^- and $1.44 \cdot 10^{-30}$ Å^3 for H_2O [318]. The permanent dipole moments of the IPs, μ_{IP}, were calculated using the center of hydrodynamic stress (CHS) as the pivot. This requires detailed knowledge of the size and shape of the IPs, which are unknown for the present $MCl^+(aq)$ species. However, the CHS can be estimated approximately using the approach of Dote

and Kivelson [75]. The calculated values of $\mu_{\text{eff, IP}}$ for all the 1:1 species are given in Table A.15.

The K_A values obtained from eqs. 1.48 and 4.2 were fitted as a function of the stoichiometric ionic strength, $I(= 3c)$, to obtain the standard state (infinite dilution) quantity, K_A°, using an extended Guggenheim-type equation (equation 3.2). The fits are shown in Figure 4.3. Note that similar results (not shown) were obtained using the less-realistic center of mass as the rotational pivot, and were found to have only minor effects on the calculated equilibrium constants. Such calculations were therefore not further considered.

It should be noted that the relaxation process located at ~ 1.1 GHz could not be resolved at higher c for either system due to its decreasing intensity (Figures A.30 and A.30; Tables 4.1 and 4.2). Values of S_1 under such conditions were therefore extrapolated using an empirical exponential fit of the amplitudes at lower c. The initial rise and subsequent decay of S_1 with increasing c is fully consistent with the sequential formation of IP species (eq. 4.1) [319]. Likewise, the value of S_2 at the lowest $c(CaCl_2)$ was obtained *via* a simple polynomial fit of $S_2(c)$ at higher c (Table 4.2).

Judging by their relaxation times, modes 1 and 2 could be assigned to the presence of 2SIPs and SIPs, respectively. This assignment is consistent with the strong hydration of the cations discussed further below and by the physical plausibility of the derived K_A values. The formation of SIPs only involves the loss of a water molecule (equation 4.1) and so was described by an empirical linear regression: $K_{SIP}(I) = K_{SIP}^\circ + D{\cdot}I$ (Figure 4.3). The values of K_{2SIP} were fitted with equation 3.2 and, since no evidence for significant CIP formation was found, K_{2SIP}° was fixed in this fit to the value of $K_{2SIP}^\circ = K_A^\circ/(1 - K_{SIP}^\circ)$ (equation 4.2).

The obtained standard state association constants are shown together with the literature values in Table 4.3. As expected from their status as classical strong electrolytes, the overall ion association constant, K_A°, for both salts is rather small. The absence of a difference between the K_A° values for $MgCl^+$(aq) and $CaCl^+$(aq), which would be expected on electrostatic grounds, reflects the attenuation of such effects by solvation (see below).

Given the general difficulties of quantifying weak complexation [325] and the limits in the accuracy of the DRS experiment, it is important not to over-interpret the present results. Nevertheless, the obtained association constants agree broadly with the fairly scattered values obtained from potentiometry [321–324, 326] and MD simulations [320] (Table 4.3). The slightly higher present results compared to the literature constants might reflect the presence of unresolved (small) IC contributions to the IP modes. Accordingly, the constants reported here should be regarded as upper limits.

At this stage, it is instructive to discuss the possibility of other relaxation processes, besides IP and ion-cloud relaxation, which might contribute to the DR spectra in the low-frequency region. In the view of the weakness of the 1:1 IPs (Table 4.3), significant formation of higher order species such as triple ions, MCl_2^0(aq), can be ruled out, at least over the present concentration range. At much higher salt concentrations, packing effects and dehydration dominate and the concept of specific individual species becomes less clear-cut.

No CIP relaxation processes were found in either system. Although the relatively short relaxation time of mode 2 ($\tau_2 \approx 19$ ps) might be consistent with the formation of CIPs,

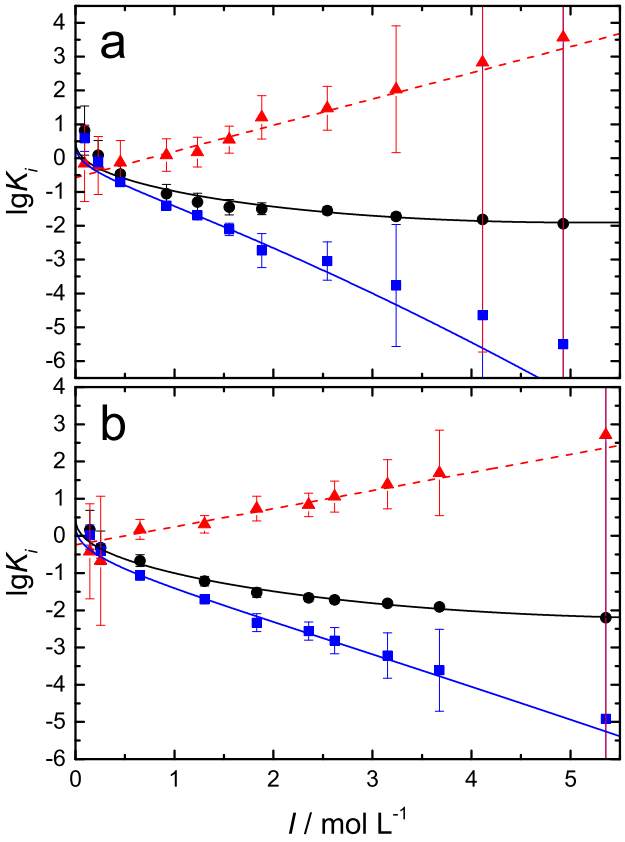

Figure 4.3: Overall association constant, K_A (●), and step-wise association constants, K_{2SIP} (■) and K_{SIP} (▲), for the formation of 1:1 IPs for: (a) $MgCl_2$(aq) and (b) $CaCl_2$(aq) at 25 ℃ as functions of the stoichiometric ionic strength, I. The solid lines indicate the fit to equation 3.2; the dashed lines represent empirical linear fits.

Table 4.3: Standard-state formation constants, K°_A, K°_{2SIP} and K°_{SIP}, for 1:1 IPs in $MgCl_2$(aq) and $CaCl_2$(aq) at 25 ℃.[a]

	$MgCl^+$(aq)		$CaCl^+$(aq)	
	present work	literatur	present work	literature
$\log K^\circ_A$	0.5 ± 0.2	-0.19 [320]; -0.13[b] [321]; 0.28[c] [322]; 0.57 [323]	0.5 ± 0.1	-0.292 [324]; -0.17[b] [321]; ∼0[d] [320]; 0.39[c] [322]; 0.4 [323]; 0.43 [323]
$\log K^\circ_{2SIP}$	0.4 ± 0.2	–	0.3 ± 0.1	–
$\log K^\circ_{SIP}$	-0.6 ± 0.1	–	-0.2 ± 0.1	–

[a] K°_A and K°_{2SIP} in L mol^{-1}; K°_{2SIP} was calculated from K°_A and K°_{SIP} and was fixed during fitting; [b] $\log K_A$ in 1 M $NaNO_3$(aq); [c] $\log K_A$ at $I = 0.4$ M; [d] Values varied between -0.1 and 0.15.

their inclusion produced unrealistic K_A values. Regarding the $MgCl_2$(aq) solutions, the absence of CIPs is consistent with the strong hydration (see below) of Mg^{2+}(aq) and a variety of experimental [42, 299, 300, 307] and computational studies [43, 327]. For $CaCl_2$(aq) the situation is less straightforward: some studies [43, 46, 47, 305, 306] claim the presence of CIPs, at least at higher concentrations ($c \gtrsim 4$ M), while many others [45, 298, 302, 303, 328] report negligible formation. The latter is consistent with present results and the pronounced hydration of Ca^{2+}(aq) (see below).
Furthermore, the existence, or not, of a slow water mode must also be considered. As such contributions are usually located at about 15 – 30 ps in the DR spectrum [22], they might be associated with mode 2. While some slow water can not be ruled out in MCl_2(aq) solutions, the current precision of DR spectra is insufficient to resolve this mode for the present electrolyte solutions. All that can be said at this stage is that the intensity of mode 2 is mostly due to SIPs, with some small contribution from slow water and, probably, very minor contributions from IC relaxation and CIPs.

4.1.4 Solvent Relaxations - Ion Hydration

Using equations 1.48 and 3.4, the effective total hydration numbers, Z_t, can be determined from the kinetic depolarization-corrected (Chapter B of the Appendix) sum of the solvent amplitudes, S_3 and S_4 (equation 3.3). Since no slow-water mode was discernible in the present DR spectra, Z_t is equal to the number of irrotationally bound water molecules, Z_{ib}. Furthermore, it is known that $Z_{ib}(Cl^-) \approx 0$ [22, 156] and therefore the obtained Z_{ib} values refer to the cations only.
The values of $Z_{ib}(M^{2+})$ obtained for the two cations are shown as functions of concentration in Figure 4.4. Their magnitudes and variation with c are remarkably similar. Note that differences between Na^+(aq) and K^+(aq), for example, are much greater [55, 154].

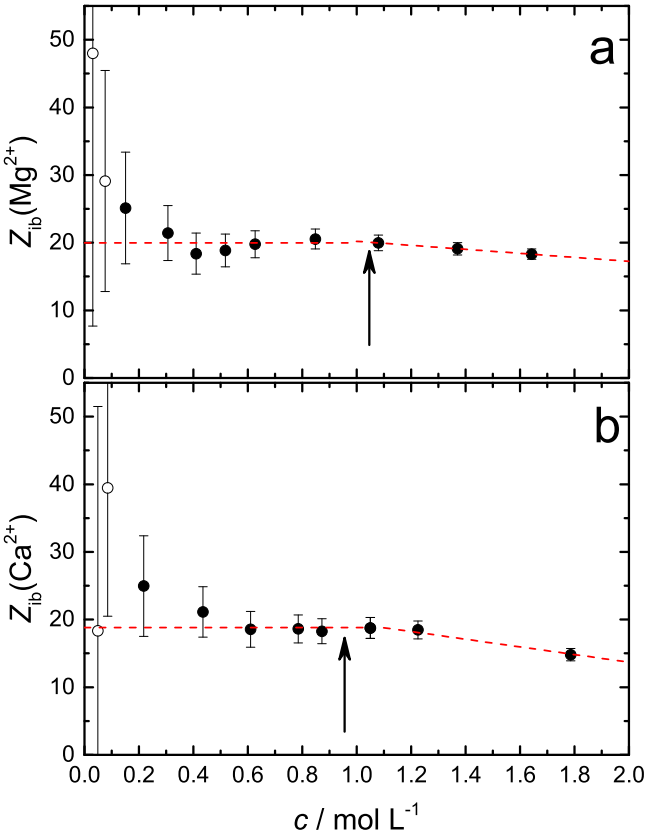

Figure 4.4: Effective hydration numbers, Z_{ib}, of (a) Mg^{2+} and (b) Ca^{2+} at 25 °C. The dashed lines are linear fits. The arrows indicate the estimated overlap-onset concentration, c^*, of the overlap of the second hydration shells of the cations. Unfilled symbols denote data points omitted in the fitting procedure.

Table 4.4: Overlap-onset concentrations, c^* in $\mathrm{mol\,L^{-1}}$, for $MgCl_2$(aq) and $CaCl_2$(aq) as a function of the number of hydration shells around the cation, n_+.

n_+	$c^*(MgCl_2)$	$c^*(CaCl_2)$
1	3.75	3.22
2	1.05	0.95
3	0.43	0.40

The values of $Z_{\mathrm{ib}}(c)$ for Mg^{2+} and Ca^{2+} were almost independent of concentration at $c \lesssim 1\,\mathrm{M}$ (Figure 4.4). Extrapolation of these values using a weighted least squares linear fit yielded infinite dilution hydration numbers, $Z^0_{\mathrm{ib}}(Mg^{2+}) = 20 \pm 1$ and $Z^0_{\mathrm{ib}}(Ca^{2+}) = 19 \pm 1$. Given that true uncertainties are likely to be greater than the regression values *, these two results are in essence identical. At $c \approx 1\,\mathrm{M}$, a small but discernible change in $Z_{\mathrm{ib}}(c)$ can be observed for both cations (Figure 4.4), showing a linear decrease at higher c. Similar trends in Z_{ib} have been reported in other electrolyte solutions [55, 98, 154, 319] and are commonly attributed to hydration-sheath overlap. The onset concentration of such an overlap can be estimated on simple geometrical grounds. The minimum distance required to prevent overlap of ion hydration shells is generally given as

$$d_{\min} = [r_+ + (n_+ \cdot d_{\mathrm{w}})] + [r_- + (n_- \cdot d_{\mathrm{w}})] \tag{4.3}$$

where $r_\pm$ is the (crystallographic) radius of a bare ion (= 0.72, 1.00 and 1.81 Å for Mg^{2+}, Ca^{2+} and Cl^-, respectively) [317], $d_{\mathrm{w}} = 2.85\,\text{Å}$ is the diameter of a water molecule [329] and $n_\pm$ denotes the presumed number of hydration layers around the cation or anion. $n_- = 0$ was assumed throughout for the weakly hydrated Cl^-(aq). The thus obtained overlap-onset concentrations for various values of n_+ are listed in Table 4.4.

The concentration at which the primary hydration layer ($n_+ = 1$) of both cations begins to overlap ($c^* > 3\,\mathrm{M}$) is outside the present concentration range. On the other hand, the values of c^* at $n_+ = 2$, corresponding to overlap-onset of second hydration shells, agree reasonably well with the break in the $Z_{\mathrm{ib}}(c)$ curves at $c \approx 1\,\mathrm{M}$ (Figure 4.4). Consistent with the weaker hydration of Ca^{2+} (see later), the slope at $c > 1\,\mathrm{M}$ is more negative for Ca^{2+} ($-5.7\,\mathrm{M^{-1}}$) than Mg^{2+} ($-3.0\,\mathrm{M^{-1}}$). The apparent decrease in $Z_{\mathrm{ib}}(M^{2+})$ in the region $0.2 \lesssim c/\mathrm{M} \lesssim 0.5$ (Figure 4.4) might indicate the overlap of a 3rd shell (Table 4.4). However, given the likely uncertainties, this should be rather considered an experimental artifact.

Table 4.5 shows the present Z^0_{ib} values for Mg^{2+}(aq) and Ca^{2+}(aq) along with the corresponding DRS results for comparable (divalent) cations. The present values are slightly higher than those of the other divalent cations. It should be noted that the latter were mainly obtained from measurements of more strongly associated (mostly sulfate) salts and,

*Since the "real" errors of the measurement and subsequent fitting were unknown, the error bars in Figure 4.4 were calculated from the deviation of $S^{\mathrm{ap}}_{\mathrm{b}}$ from an empirical polynomial of the form $S^{\mathrm{ap}}_{\mathrm{b}}(c) = S^{\mathrm{ap}}_{\mathrm{b}}(0) + a \cdot c + b \cdot c^{1.5} + d \cdot c^2$.

Table 4.5: Ionic radii, r_+, and effective hydration numbers at infinite dilution, Z^0_{ib}, determined by DRS for divalent cations.

Cation	r_+/pm[a]	$Z^0_{\mathrm{ib}}(\mathrm{M}^{2+})$		salt
		present work	literature	
Ca^{2+}	100	19	–	Cl^-
Cd^{2+}	95	–	12 [44]	Cl^-
Co^{2+}	75	–	17 [22]	SO_4^{2-}
Cu^{2+}	73	–	19 [22, 44]	Cl^-, SO_4^{2-}
Mg^{2+}	72	20	14 [319];15 [44]	Cl^-, SO_4^{2-}
Ni^{2+}	69	–	17 [22]	SO_4^{2-}

[a] From Marcus [317]

as such, are probably under-estimates. As would be expected, the values of $Z^0_{\mathrm{ib}}(\mathrm{M}^{2+})$ are much larger than those of monovalent cations, for which $Z^0_{\mathrm{ib}}(\mathrm{M}^{+}) \approx 0$ to 6 [22] is usually observed. Values of $Z^0_{\mathrm{ib}}(\mathrm{M}^{3+})$ for trivalent cations are sparse and show more scatter but are mostly considerably higher than those for M^{2+}(aq), being located within the range 18 to 44 [22, 98].

As extensively studied by X-ray [170, 299], neutron [300] and Raman scattering [307] investigations, and MD simulations [42, 307, 309], the magnesium cation has a primary coordination number of $CN_1 = 6$, with a strictly octahedral geometry [170]. X-ray diffraction and MD simulation studies have also reported a second hydration shell with $CN_2 = 12$ [170]. Consistent with these findings, the present value of $Z^0_{\mathrm{ib}}(\mathrm{Mg}^{2+}) \approx 20$ also suggest the formation of a well-defined, strongly-bound second hydration shell and possibly even a small amount of ordering of water molecules beyond that shell ($CN_1 + CN_2 < Z^0_{\mathrm{ib}}(\mathrm{Mg}^{2+})$).

The hydration structure of Ca^{2+} is less clear-cut. Reported values of the primary coordination number vary over the range: $6 \leq CN_1 \leq 10$ [170]. The larger values compared to Mg^{2+} presumably reflect the greater size and surface area of the bare calcium ion, which enables more "nearest neighbours" to be packed into the first coordination sphere. Literature data regarding the second hydration shell of Ca^{2+} are, surprisingly, in good agreement. A combined EXAFS, X-ray scattering and MD study by Jalilehvand *et al.* [303] found $CN_2 = 16 - 18$. Badyal *et al.* [328] reported $CN_2 = 19 - 20$ from neutron diffraction measurements, while Hofer *et al.* [308] estimated $CN_2 = 19$ using MD simulations. Given the differences observed for CN_1, at least some of this agreement must be accidental. Nevertheless, taking their average gives a total ($= CN_1 + CN_2$) of 24 to 28 H_2O molecules collectively located within the first two hydration sheaths of Ca^{2+}(aq). These numbers are somewhat larger than the present result of $Z^0_{\mathrm{ib}}(\mathrm{Ca}^{2+}) \approx 19$. However, it must be kept in mind that the hydration numbers obtained by DRS are a measure of water dynamics not geometry. It can be speculated that the CN_1 values of Ca^{2+} might result in a much less strongly bound second shell, thereby causing Z_{ib} to be less than the maximum ex-

pected from electronic considerations alone. The weaker hydration of Ca^{2+} compared to Mg^{2+} is also evident from the comparison of the differences in the the Gibbs energies of hydration: $\Delta_{hyd}G^{\circ} = -1527\,kJ\,mol^{-1}$ (Ca^{2+}) *vs.* $-1837\,kJ\,mol^{-1}$ (Mg^{2+}) [282]. Accordingly, the residence times of H_2O molecules in the first hydration layer vary significantly between the two cations. For Ca^{2+}, the mean residence time is on the sub-nanosecond timescale [170, 304–306, 320, 330–332] (with a slightly higher rate of exchange between the first and second shells) [310, 332], whereas that for Mg^{2+}(aq) is in the microsecond regime [170, 307, 320, 333].

The bulk-water relaxation time, τ_3, replotted on a more usable scale in Figure 4.5, decreased approximately linearly with rising salt concentration for the two electrolyte systems. Such a decline, albeit generally not linear, appears to be characteristic for inorganic salts [98, 151, 334–336]. Considering that water dynamics are essentially decoupled from viscosity in aqueous electrolyte solutions [22, 169], the decrease in τ_3 with increasing salt concentration (Figure 4.5) most likely reflects a slight disruption of the bulk water structure by the presence of the hydrated ions. That the slope of $\tau_3(c)$ in Figure 4.5 is more negative for the calcium salt: $-1.24\,ps\,L\,mol^{-1}$ *vs.* $-0.94\,ps\,L\,mol^{-1}$ for $MgCl_2$(aq), may simply reflects the greater size of Ca^{2+}(aq) compared to Mg^{2+}(aq). The rotational correlation time of water molecules around Ca^{2+} obtained from NMR measurements is ∼7-9 ps, which significantly higher than the 2.5 ps of neat water, but lower than the 13 ps observed for Mg^{2+}(aq) [170]. Interestingly, the ratio of the slopes of the two curves in Fig. 4.5 is approximately equal to the inverse of the ratio of the rotational correlation times for the two cations. However, it should be kept in mind that NMR and DRS probe two different ranks of the time-correlation function of the anisotropic water rotation (Section 1.3.5) in the hydration layer and thus these numbers should be used for a qualitative comparison only. Since the electric field of the present cations impedes the dynamics of the solvent in the second hydration shell, it would also make sense to compare the respective quantities for hydration layers beyond the first shell, which, however, are not available in literature.

4.1.5 Concluding Remarks

The DR spectra of $MgCl_2$(aq) and $CaCl_2$(aq) could be satisfactorily fitted by combinations of up to four Debye and up to five Debye equations, respectively. The analysis of the spectra indicates that both Mg^{2+} and Ca^{2+} are strongly hydrated, with each possessing two well-defined hydration shells. Approximately 20 water molecules were immobilized on the DRS timescale at infinite dilution for both cations, but no evidence was found for the existence of a slow-water fraction. Evidence for a slightly weaker hydration of Ca^{2+} *cf.* Mg^{2+} were found. The two solute-dependent modes at low frequencies were assigned to the formation of ion pairs in these classical strong electrolyte solutions. Detailed analysis of these modes indicated that they could be assigned to double-solvent-separated and solvent-shared IPs, which was consistent with the strong hydration of the two cations. The overall IP formation constants calculated from the DR spectra were in reasonable agreement with literature data. The formation of contact ion pairs was not observed in the DR spectra.

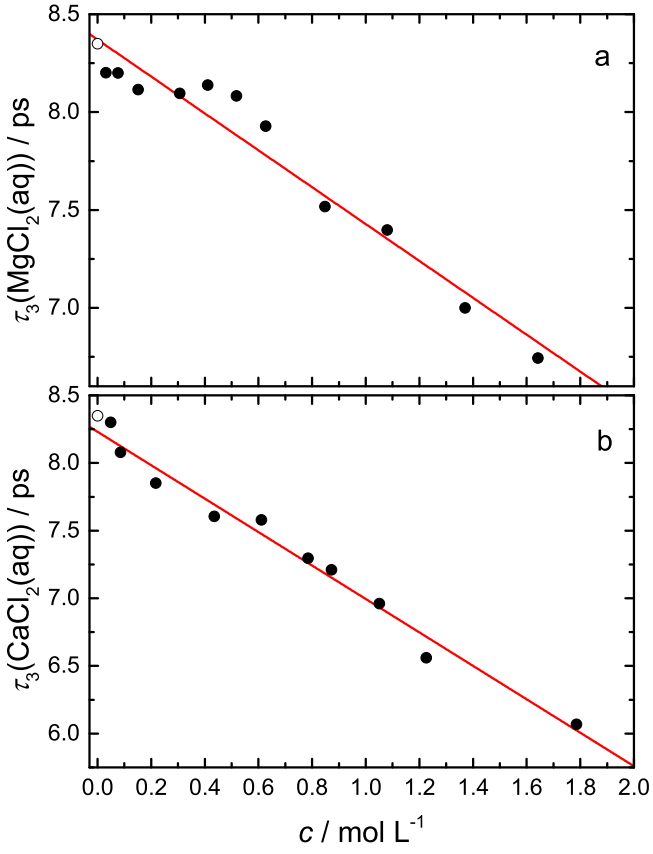

Figure 4.5: Linear regressions (lines) of the dominant bulk water relaxation time, τ_3, as a function of the total salt concentration, c, in (a) $MgCl_2$(aq) and (b) $CaCl_2$(aq). The open symbol is for pure water.

4.2 Tetramethylammonium Chloride

4.2.1 Introduction

Aqueous solutions of (symmetrical) tetra-n-alkylammonium (TAA) salts belong to some of the most extensively studied systems during the last few decades [14, 48, 49, 199, 200, 278, 337–352]. The reason for this is its unique structure, which comprises a net positive core charge and (tunable) non-polar alkyl tails. This combination makes TTA cations a prominent target for the investigation of the interplay of the hydrophobic and hydrophilic interactions and the effects of the hydrophobicity on the structure and dynamics of the solvent molecules. Frank and Evans used TAA salts in their famous study in which they claimed so-called "microscopic iceberg" formation around hydrophobic solutes [351], which however was challenged since then [48, 346].

Especially for the shortest homologue, *i.e.* tetramethylammonium (TMA, TMA^+, Me_4N^+), conclusions on whether it behaves as an apolar species or a classical ion in water are still controversial and a coherent picture is lacking. Its properties in solution can most appropriately be described as intermediate between alkali and larger, hydrophobic TAA cations. While some studies claim that the hydration of TMA is predominantly of hydrophilic (ionic) nature [348–350] the majority of investigations report a well-defined hydration shell of hydrophobic character [14, 48, 49, 199, 200, 347]. The latter is characterized by a preferential tangential alignment of the H_2O molecules with respect the TMA sphere and thus a maximization of H-bonding with the surrounding solvent molecules [48], resulting in a slow down of the reorientation dynamics of the water molecules compared to bulk-water [200, 352].

Besides the special combination of charge and hydrophobic groups, the systems necessarily include couterions. It could be shown that the (thermodynamic) properties of (short-chained) TAA salt solutions strongly depend on the present counterion [199, 344] and some degree of association into IPs with halide counterions was detected by theoretical [49, 338, 341] and experimental studies [156, 176, 177, 341, 353].

Unraveling the hydration features of such solutes would be a great step in understanding many important biological processes, such as self-assembly and molecular recognition [354, 355]. In particular, trimethylammonium groups are a component of the many biologically important compounds, such as lipids or the previously discussed NTs carbachol and acetylcholine (Section 3.1). Thus, knowledge of the nature and strength of the solute-solvent and solute-solute interactions of TMA^+ would certainly help to shed some light on the properties of those more complex molecules.

In this work, the structure and dynamics of TMACl(aq) solutions was studied by the means of DRS. The dielectric spectra were recorded in the frequency region $0.05 \leq \nu/\mathrm{GHz} \leq 89$ and concentration range of $0.09600 \leq c/\mathrm{M} \leq 1.495$ at 25 °C. In the following, detailed information on the hydration of the TMA cation and the extent of $Me_4N^+ \cdots Cl^-$-IP formation, deduced from the evaluation of the DR spectra, will be presented and discussed.

4.2.2 Data Acquisition and Processing

The TMACl(aq) sample were prepared according to procedures in Sections 2.1 and 2.2. The densities, viscosities and conductivities (Section 2.4) are listed in Table A.16. The dielectric spectra were recorded in the frequency range $0.05 \leq \nu/\mathrm{GHz} \leq 89$ and at 25 °C (Dielectric probe kit VNA setup + E-band interferometer, Section 2.3). Due to the electrical conductivity of the TMACl(aq) solutions (Table A.16, the effective accessible low-frequency limit, ν_{min} (Section 1.1.2), was in the region of $0.1 \leq \nu/\mathrm{GHZ} \leq 0.4$, depending on the electrolyte concentration.

4.2.3 Fitting Models and Assignment of Modes

The acquired complex permittivity spectra of TMACl(aq) are shown in Figure 4.6. For the formal description of the dielectric spectra various conceivable combinations of up to five individual relaxation processes in the form of HN equations (equation 1.41) were tested. Evaluation of the fits according to the criteria presented in Section 2.3.3 revealed that combinations of four Debye equations at low concentrations (c(TMACl) ≤ 0.1986) and three Debye relaxations at higher c (c(TMACl) ≥ 0.4143) yielded the best fits for the present spectra. The parameters of this fitting model, in the following abbreviated as (D+)D+D+D, are summarized in Table 4.6. The relaxation modes $l = 0, .., 4$ are numbered from lower to higher frequencies.
The static permittivities, ε, of the TMACl(aq) solutions decreased with increasing salt concentration (Table 4.6, Figure A.33). This dielectric decrement is to be expected on grounds of the finite, non-polar cations and anions reducing the concentration of the dipolar solvent molecules, kinetic depolarization (Chapter B of the Appendix) and hydration effects (see further below).
As also indicated in the Zasetsky's relaxation time distribution analysis (Figure A.32), the spectra were dominated by high-intensity mode $l = 3$ located at $\sim 17 - 19\,\mathrm{GHZ}$ (Figure 4.7), which can unambiguously be assigned to the cooperative relaxation of the H-bond network of bulk-like water [22]. Its amplitude decreased with rising c, as would be expected for the same reasons already mentioned above for the decline of ε. The relaxation time, τ_3, increased continuously from 8.4 to 9.76 ps with increasing electrolyte concentration (Table 4.6). A similar increase of the bulk-like water relaxation time was observed in the DR spectra of TMABr(aq) [156]. A fast-water process, which is often found in the spectra of aqueous solutions but is located far outside the accessible frequency range [150], was not discernible in the present DR spectra, in contrast to spectra of AcChCl(aq) (Section 3.1) and TMABr(aq) [156]. However, the high value of $\varepsilon_\infty \approx 6$ (value of neat water $\varepsilon_\infty = 3.52$ [154]) indicates that the fast-water contribution is incorporated into ε_∞.
The amplitude of mode $l = 2$, centered at $\sim 8\,\mathrm{GHz}$ ($\sim 19\,\mathrm{ps}$), increased systematically with increasing TMACl concentration. Based on its magnitude and relaxation time, this process was assigned to the relaxation of moderately bound water molecules, *i.e.* slow-water [152, 154, 156–160, 162, 163]. The slow-water process with a comparable retardation factor could also be resolved for solutions of AcChCl and CarCl and its presence was assigned

Table 4.6: Static permittivity, ε, relaxation amplitudes, S_l, relaxation times, τ_l ($l = 0, .., 3$), infinite frequency permittivity, ε_∞, of TMACl at 25 °C and the reduced error function, χ_r^2, of the (D+)D+D+D fitting model.[a]

c	ε	S_0	τ_0	S_1	τ_1	S_2	τ_2	S_3	τ_3	ε_∞	χ_r^2
0.09600	78.3	1.37	592	0.359	121	0.226	16.2	70.7	8.40	5.70	0.0934
0.1986	77.2	1.25	506	0.965	123	0.748	18.3	68.3	8.47	5.96	0.0541
0.4143	74.1	–	–	1.76	173	2.85	20.5	63.7	8.51	5.72	0.0565
0.6250	71.3	–	–	1.61	149	3.71	20.2	60.1	8.73	5.83	0.0805
0.8038	68.8	–	–	1.38	125	4.59	16.8	56.7	9.03	6.16	0.0810
0.9885	66.4	–	–	0.910	157	6.27	18.3	53.1	9.05	6.08	0.0740
1.197	63.8	–	–	0.642	233	6.97	19.4	49.8	9.36	6.32	0.144
1.495	60.0	–	–	0.123	251	7.17	18.9	46.5	9.76	6.19	0.0562

[a]Units: c in mol L^{-1}; τ_j in ps.

mainly to the water molecules hydrating the trimethylammonium functional group, as discussed previously in Section 3.1.
A low-intensity mode $l = 1$ located at a mean relaxation frequency of ~ 1 GHz (~ 170 ps) appeared in the DR spectra upon addition of the salt into water. Its amplitude went through a maximum with rising c, while its relaxation time showed some scatter. Since the present ions are symmetrical, they do not have a permanent dipole moment and thus do not contribute to the DR spectra. Consequently, judging by its location and intensity, mode $l = 1$ was assigned to relaxation of dipolar TMA^+-Cl^- 1:1 IPs with a lifetime which is at least comparable to the rotational correlation time. Furthermore, an additional mode $l = 0$ could be resolved at low concentrations, which disappeared at higher c (Table 4.6). Although relaxation of some kind of dipolar ionic aggregates, which form at low c and dissociate at higher concentrations, would be conceivable for such a process, it is more reasonable to ascribe this mode to IC relaxation in the basis of its amplitude and relaxation time and its disappearing behaviour at higher ionic strengths [55, 166]. As currently no in-depth theory on the extent of the IC contribution to the DR spectra exist and the IC mode was only discernible for a limited number of spectra (only for the lowest concentrated samples), it will be abstained from the analysis of this mode in the following.

4.2.4 Solute Relaxation - Ion Pairing

Despite the reputation of TTA salts as non-interacting electrolytes, which are commonly used as a background in potentiometric measurements [356], some degree of association into IP could be deduced from the DR spectra of TMACl(aq).
Following the Eigen-Tamm theory (equation 4.1), one of three possible 1:1-IP species, with

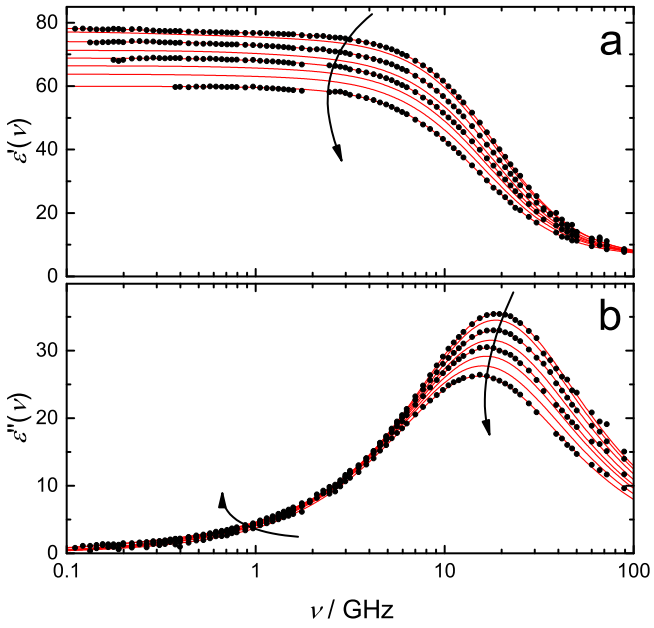

Figure 4.6: (a) Relative permittivity, $\varepsilon'(\nu)$, and (b) dielectric loss, $\varepsilon''(\nu)$, spectra of TMACl(aq) ($0.09600 \leq c/\mathrm{mol\,L^{-1}} \leq 1.495$) at 25 °C. Symbols denote the experimental data. Solid lines represent the fits. For visual clarity data points are only shown for selected samples. Arrows indicate the trend with increasing electrolyte concentration.

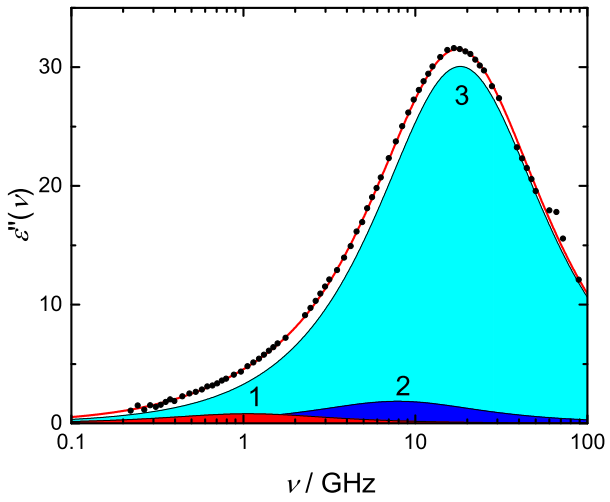

Figure 4.7: Dielectric loss spectrum of 0.6250 M TMACl(aq) at 25 °C. Symbols denote experimental data, lines indicate the fits. The shaded areas show the individual contributions of the fitting model.

varying degree of solvation (2SIP, SIP, CIP), could be assigned to the relaxation process $l = 1$. Based on the magnitude of the relaxation time τ_1, both, 2SIPs and SIPs, would be conceivable for this process, while the CIPs could be ruled out since the estimated relaxation time for rotational diffusion of CIPs ($\tau_{\mathrm{CIP}}^{stick} \approx 110\,\mathrm{ps}$ and $\tau_{\mathrm{CIP}}^{stick} \approx 17\,\mathrm{ps}$) is clearly smaller than τ_1. Neither the chloride anion nor the TMA cation are known to be strongly hydrated (see above and discussion of hydration below). Thus, the formation of long-lived 2SIPs was assumed be less likely. Previous simulation [49, 338] and neutron diffraction [14] studies of TMACl(aq) solutions, which have reported the presence of SIPs without any indication on formation of 2SIPs, corroborate the latter assignment of the relaxation mode $l = 1$ to SIPs.

The association constant, $K_{\mathrm{A}} = K_{\mathrm{SIP}} = \frac{c(\mathrm{SIP})}{(c(\mathrm{TMACl}) - c(\mathrm{SIP}))^2}$, as a function of the stoichiometric ionic strength, I, is shown in Figure 4.8. The concentrations of the IPs were obtained from the amplitudes S_1 using equation 1.48. The effective dipole moment of the SIP and the corresponding field factors, A_{SIP} and f_{SIP}, were calculated as described previously [72]. The polarizability was taken to be $\alpha_{\mathrm{SIP}} = \alpha_+ + \alpha_- + \alpha_{\mathrm{H_2O}}$. The bare ion polarizabilities were taken from Ref. [317] ($9.08 \cdot 10^{-30}\,\mathrm{Å}^3$ for Me_4N^+ and $3.42 \cdot 10^{-30}\,\mathrm{Å}^3$ for Cl^-) and for water the value $1.44 \cdot 10^{-30}\,\mathrm{Å}^3$ was inserted [318].

The obtained K_{A} values could be fitted with an extended Guggenheim-type equation (equation 3.2) to give the standard state value of $K_{\mathrm{A}}^{\circ} = 1 \pm 0.1\,\mathrm{M}^{-1}$. The present value coincides fairly well with $K_{\mathrm{A}}^{\circ} = 0.8 \pm 0.2\,\mathrm{M}^{-1}$ obtained from conductivity measurements [177]. Buckner and Jorgensen calculated $K_{\mathrm{A}} = 0.3\,\mathrm{M}^{-1}$ at $c(\mathrm{TMACl}) \approx 0.2\,\mathrm{M}$

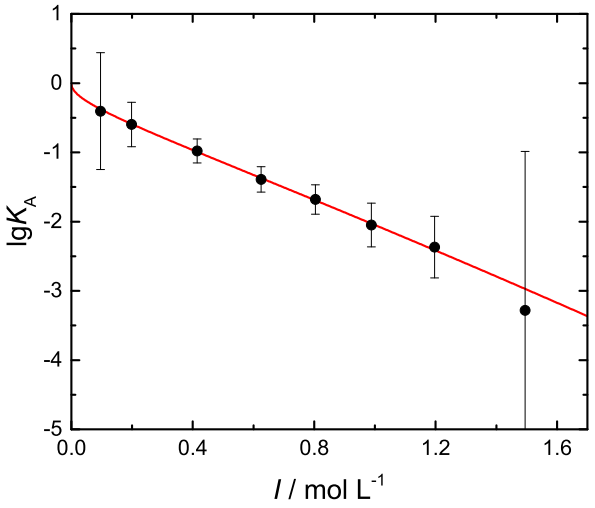

Figure 4.8: Association constant, K_A (in M^{-1}), for the formation of SIPs (●) of TMACl(aq) as a function of ionic strength, I, at 25°C. The Guggeheim-type fit is denoted as a solid line.

in a simulation study [338], which agrees exceptionally well the present DRS value of $K_A(0.1986\,M) = 0.3 \pm 0.1\,M^{-1}$. Heyda *et al.* [341] reported a slightly higher value of $K_A = 1.3\,M^{-1}$ at c(TMACl) = 0.25 M and dilute-conductivity measurements by Bešter-Rogač *et al.* [176] found a standard-state formation constant value of $K_A^\circ = 2.17\,M^{-1}$, which is by a factor of ~ 2 higher than the DRS values. Nevertheless, the present results are generally in rather good agreement with the literature data, despite the fact that DRS is not the most sensitive tool for studying the extent of ion-pairing. As already mentioned above, the great strength of DRS is rather the ability to distinguish the different kinds of IPs in solution [325].

At this stage, the possible formation of CIPs should be shortly discussed. The presence of both SIPs and CIPs was claimed in literature [14, 338]. Note that association into CIPs was also reported in the DR spectra of TMABr(aq) [156]. As indicated by its predicted relaxation time (see above), mode $l = 2$ would also be conceivable for the relaxation of CIPs (Table 4.6). However, treating mode $l = 2$ as an IP mode would lead to too high association constant values. Thus, a standard-state formation constant of $4.5 \pm 0.8\,M^{-1}$ would be obtained, which is significantly higher the literature values (see above). Although some contribution of CIPs to mode $l = 2$ cannot be ruled out, it was therefore concluded that mode 2, which will be the subject of discussion in the subsequent section, is most likely due to the relaxation of slowed-down solvent molecules rather than IPs.

4.2.5 Solvent Relaxations - Ion Hydration

Remembering that $Z_t(Cl^-) = 0$, the effective hydration numbers of the TMA^+ cation can be directly obtained from the solvent amplitudes, S_2 and S_3, using equations 1.48 and 3.4 - 3.6. As can be seen in Figure 4.9, irrotationally bound water is virtually absent in the TMACl(aq) solutions, making $Z_t(TMA^+) \approx Z_s(TMA^+)$. Since no strong coulombic interactions between the rather large TMA^+ ($r(TMA^+) > r(Cs^+)$ [317]) and the hydrating water dipoles would be expected, the lack of "frozen" water dipoles is physically reasonable [156, 357].

The Z_s values, originating from the hydration of the TMA cation, decreased with increasing TMA concentration (Figure 4.9). The decline of hydration numbers with increasing solute concentration is commonly explained by increasing overlap of hydration shells of the solute molecules [152, 186]. Extrapolation of $Z_s(c)$ to $c = 0$ yielded the infinite dilution value of $Z_s^0 = 5.6 \pm 0.5$ and at the higher end of the studied concentration range the value of ~ 3.5 was observed (Figure 4.9). The number of water molecules in the first hydration layer, CN_1, of the TMA cation reported in computer simulation [49, 200, 278, 338, 347] and experimental (NMR [337] and neutron diffraction [358]) studies varies in the region $CN_1 \approx 20 - 26$. Whatever the exact CN_1 value might be, the present Z_s values are markedly smaller than the number of H_2O molecules in the first hydration shell, indicating that effectively only a small fraction of the hydration water is impeded in its dynamics. Considering the structure of the hydration sheath, there seems to be consensus that water molecules in the primary hydration shell of TMA^+ align in such way that their dipole moments are preferentially tangential to the ion sphere [14, 48, 49, 199, 200, 347], similarly to the hydration of the onium group of $AcCh^+$ and Car^+ (Section 3.1). Analogous to the TMA moiety at the $AcCh^+$, the water molecules were found to be preferably located in the voids between the methyl groups [199, 347]. García-Tarrés and Guàrdia [200] deduced a retardation factor of ~ 1.5 of water in the first hydration layer compared to the bulk by means of a MD simulation of aqueous TMA solutions, which is in reasonable agreement with the present DRS results (retardation factor: $r = \tau_2/\tau_3 \approx 2$ (Table 4.6)). Interestingly, no slow-water mode could be resolved in the DR spectra of TMABr(aq) in a previous DRS study [156]. However, it should be noted that the observed retardation factor of ~ 2 for TMACl(aq) is rather small. A proper separation of the high-intensity bulk-water mode and the weak slow-water process with such a small retardation factor (Figure 4.7) is often hard to achieve and, from experience, $r \approx 2$ might be considered as an approximate resolution limit for a classical slow-water process. As the presence/absence of the slow-water fraction is rather unlikely to be linked to the differences in the hydration of the two halide anions [156], the inability to resolve a slow-water mode in the DR spectra of TMABr(aq) might be connected to the limited accuracy of the experiment.

In contrast to the most solutions of classical inorganic salts [98, 99, 151, 334–336], an increase of the bulk-water relaxation time with rising c(TMACl) was observed in the present DR spectra (Table 4.6). A similar trend was found for various TTA salts (TMA, tetraethyl-, tetrapropyl- and tetrabutylammonium salts) in aqueous solution [156]. Although the increase in τ_3 is rather moderate, it may be concluded that, besides the direct impedance

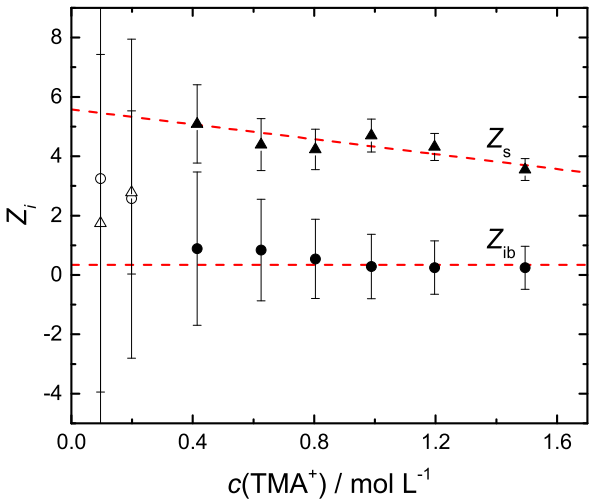

Figure 4.9: Number of irrotationally bound, Z_{ib}(●), and the numbers of moderately retarded water molecules, Z_{s}(▲), of TMA^+(aq) as a function of concentration at 25 C. Dashed lines denote weighted linear fits. Unfilled symbols were not included in the fits.

of the dynamics of hydration water, some effect on the bulk-water structure induced by the presence of the fairly large, nonpolar TMA surfaces is present. In terms of the extended jump model (EJM) for water relaxation of Laage [82] (Section 1.3.5) this would imply that either the characteristic time for the frame relaxation, τ^{frame}, which mainly comprises spatial effects, or the jump-reorientation time, τ^{jump}, which is connected to the H-bond strength between the water molecules, is increased compared to neat water. As the bulk H_2O-H_2O pair distribution functions were found to be essentially unperturbed by the presence of TMA^+ [49, 199], an enhancement of the bulk-water H-bond strength can be ruled out. On the other hand this implies that, most probably, steric effects imposed by the apolar cations lead to an overall hindrance of the reorganization of the water-frame around a reorienting H_2O dipole in the bulk, which results in an gradual increase of τ_{bulk} as observed in the DR experiments.

4.2.6 Conclusion

The DR spectra of aqueous TMACl solutions were fitted by a combination of up to four Debye equations. The analysis of the solvent related modes revealed that effectively ~ 6 H_2O molecules are dynamically impeded in the apolar hydration sheath of the TMA cation. As would be expected from the rather low charge density of the TMA cation, virtually no irrotationally bound water was found. The continuous increase of the bulk-water relaxation time with rising salt concentration was interpreted to result from a steric hindrance of the

TMA^+ ions on the bulk-water relaxation process.
The evaluation of the solute mode showed that the degree of TMA^+-Cl^--IP formation is low, but still detectable. Based on the rather weak hydration of the TMA cations and Cl^- anions and the observed relaxation time of the IP process, long-lived solvent-shared IPs were discussed to be the predominant species responsible for the IP relaxation process in the DR spectra of TMACl(aq). The obtained association constants were in good agreement with literature data. In hand with previous studies [14, 49, 199, 338], no indications for cation-cation aggregation of TMA, which was reported for higher (more hydrophobic) TAA homologues [22, 343, 359], could be detected in the DR spectra.

Chapter 5

Ternary Systems - Effect of Salts on the Neurotransmitter Solutions

5.1 Introduction

The binary solutions of the biologically active molecules studied in Chapter 3 provide some insight into their behaviour in aqueous media. However, from a biological standpoint binary systems are a very crude simplification of the real situation in living organisms. Chemistry in biological systems is mainly conducted in aqueous solution, involving many different kinds of dissolved ions, which may influence the activity of the biomolecules [288]. In particular for NTs, these interactions could even alter signaling abilities, as to reach the receptors the neurotransmitters have to diffuse across the synaptic cleft, where they may come in contact with other solvated molecules and ions.

Since the pioneering work of Hofmeister [24, 25], many attempts of predicting ion specific effects have been made. The famous concept of "matching water affinities" by Collins is one of the most successful approaches, as it takes into account electrostatics and hydration effects. This concept is deduced from a correlation of the standard heat of solution of a crystalline salt at infinite dilution with the difference between the absolute heats of hydration of the corresponding individual anion and cation in the gas phase [360]. The Collins' rule can often be applied as a guide to explain association phenomena in aqueous solutions. For instance, it could be utilized to explain trends of activity coefficients of ions [30], electrophoretic mobilities [31] and counterion binding of proteins [360].

However, it should be pointed out that the latter concept has also its limitations. For instance, binding of ions to uncharged surfaces cannot be explained by Collins' rule. Salis and Ninham [29] argued that inclusion of dispersion forces into the Collins' concept could even further improve its applicability and, at the same time, it would provide a justification for Collins' rule to be described as a "theory" rather than "an empirical rule based on phenomenological observations" [29].

Until today, no such concepts exist. Clearly, all these effects (electrostatics, dispersion, local hydration,...) have to be taken into consideration when studying the properties of

solutions containing electrolytes.
The following chapter makes an attempt to disentangle these rather specific effects of inorganic salts on the biomolecule solutions by means of dielectric relaxation spectroscopy ($0.05 \leq \nu/\mathrm{GHz} \leq 89$; at 25 °C). This chapter encompasses the study of the effects of KCl and KF on AcChCl(aq) at varying inorganic salt : NT ratios. Further, the influence of various chloride salts (LiCl, NaCl, $MgCl_2$ and $CaCl_2$) on NaGlu(aq) and Gln(aq) solutions was investigated.
The ions Na^+, K^+, Mg^{2+}, Ca^{2+} and Cl^- are some of the most common in living organisms and are essential for various biological functions, *e.g.* signal transduction, osmotic control, and stability of proteins, DNA, and membranes. Lithium is nonessential in biological systems but is considered to have a high therapeutic value. Despite its high importance for bio-mineralization of bone and teeth, free F^- anions as such are present at very low concentrations in living organisms [288]. However, from a physico-chemical point of view, a study of the effect of anions of high charge density, such as F^-, on the dynamics and structure of $AcCh^+$(aq) solutions is of significant interest.

5.2 Acetylcholine Chloride(aq) with Inorganic Salts

5.2.1 Data Acquisition and Processing

The densities, viscosities and electrical conductivities (Section 2.4) of the AcChCl+KCl(aq) and AcChCl+KF(aq) solutions, which were prepared by systematic addition of the respective salt to a ~ 0.25 M AcChCl(aq) solution, are shown in Tables A.17 and A.18. The permittivity spectra were recorded in the frequency range $0.05 \leq \nu/\mathrm{GHz} \leq 89$ (Dielectric probe kit VNA setup + E-band interferometer, Section 2.3) at 25 °C. However, due to the rather high electrical conductivity of both sets of samples the noisy dielectric data at frequencies below $0.2 - 0.4$ GHz, depending on the concentration of the inorganic salt, were discarded in the fitting of the spectra (Section 3.1).

5.2.2 Fitting of the Spectra and Relaxation Models

Various combinations of up to five HN-equations were tested to model the obtained DR spectra of AcChCl+KCl(aq) and AcChCl+KF(aq). Taking into account the results of Zasetsky's analysis (Figures A.34 and A.35) and the evaluation criteria of Section 2.3.3, both sets of spectra could be best fitted by a combination of four Debye equations (D+D+D+D), in parallel to the fitting model applied for the binary AcChCl(aq) solutions 3.1. The permittivity spectra and their corresponding fits are shown in Figure 5.1. As for binary AcChCl(aq), the three faster relaxation processes ($j = 2, 3, 4$, Tables 5.1 and 5.2) could be readily assigned to the relaxation of the solvent molecules, with process $j = 2$ being due to the reorientation of moderately bound water molecules and processes $j = 3, 4$ corresponding to the relaxation of essentially bulk-like water (Section 3.1). By the same token, process $j = 1$ located at ~ 1.6 GHz ($\tau_1 \approx 100$ ps) could be attributed to the reorientation of

the $AcCh^+$ dipole. Note that although some formation $AcCh^+ \cdots Cl^-$-IPs was detected by dilute conductivity measurements (Section 3.1), a separate IP mode was not discernible in the DR spectra of the binary AcChCl(aq) solutions as well as the present ternary systems. The static permittivity, ε, and the dominant bulk-water mode, S_3, decreased with increasing salt concentration (Tables 5.1 and 5.2; Figure A.36), reflecting the continuous replacement of solvent dipoles by non-polar ions and increasing hydration effects (see below). Similar to the binary AcChCl(aq) solutions (Section 3.1), the relaxation time of the fast-water process, τ_4, and the infinite-frequency permittivity, ε_∞, had to be fixed to the neat-water values during the fitting of the spectra to achieve consistent fits. The amplitudes of the slow-water modes, S_2, showed a rather peculiar behaviour with rising concentrations of the potassium salts. For AcChCl+KCl(aq) S_2 stayed fairly constant up to $c(\mathrm{KCl}) \approx 0.3\,\mathrm{M}$. Above this threshold an increase of the amplitude could be observed (Tables 5.1; Figure A.36(a)). The corresponding amplitude for AcChCl+KF(aq) showed a similar trend. However, after reaching a maximum at $c(\mathrm{KF}) \approx 0.6\,\mathrm{M}$, S_2 dropped again (Tables 5.2; Figure A.36(b)). A possible explanation of this behaviour will be given further below.

The $AcCh^+$ relaxation amplitudes, S_1, showed some scatter for both systems. An overall decrease with rising salt concentration could be observed (Tables 5.1 and 5.2; Figure A.36). Note that in contrast to KCl(aq) [292], a relaxation process with a relaxation time very close to τ_1 of the $AcCh^+$ reorientation mode could be detected in the DR spectra of binary KF(aq) solutions [291]. This mode most likely is a composite process, comprising a very weak $K^+ \cdots F^-$-IP relaxation and a somewhat stronger IC contribution. However, since the amplitude of this mode is very low ($S \lesssim 1$) and it incorporates an inseparable IC relaxation part, it was abstained from correcting the AcChCl+KF(aq) spectra for the presence of this KF solute relaxation (Chapter C of the Appendix). However, it should be kept in mind that such additional contributions might exist when analyzing the relaxation parameters of mode $j = 1$ of the present ternary solutions.

5.2.3 Effects of the Background Electrolyte

Effects on the hydration. Before the effects of the electrolytes on the NTs will be disentangled, it is instructive to say a few words about the properties of the inorganic salts in solution themselves. It is known that the larger K^+ ions (compared to Li^+ and Na^+) in aqueous solution are not able to "freeze" water molecules in their hydration shells on the DRS timescale. Instead these moderate $K^+ \cdots H_2O$ interactions result in the appearance a slow-water fraction in the DRS spectra of solutions containing potassium ions. Recent dielectric measurements of salt solutions containing K^+ indicate that 6.6 H_2O molecules are effectively retarded by the K^+ cation [154]. Neutron diffraction experiments [13, 361] and molecular dynamics simulation [362–364] of potassium salts in aqueous solution reported 1^{st}-shell coordination numbers of $CN_1(K^+) \approx 6 - 10$ and the hydration shell around K^+ was characterized as well defined but yet not very rigid [362, 363]. This agreement between the DR results and the average coordination number of K^+ corroborates that virtually all water molecules in the first hydration shell are dynamically affected by the electric field of

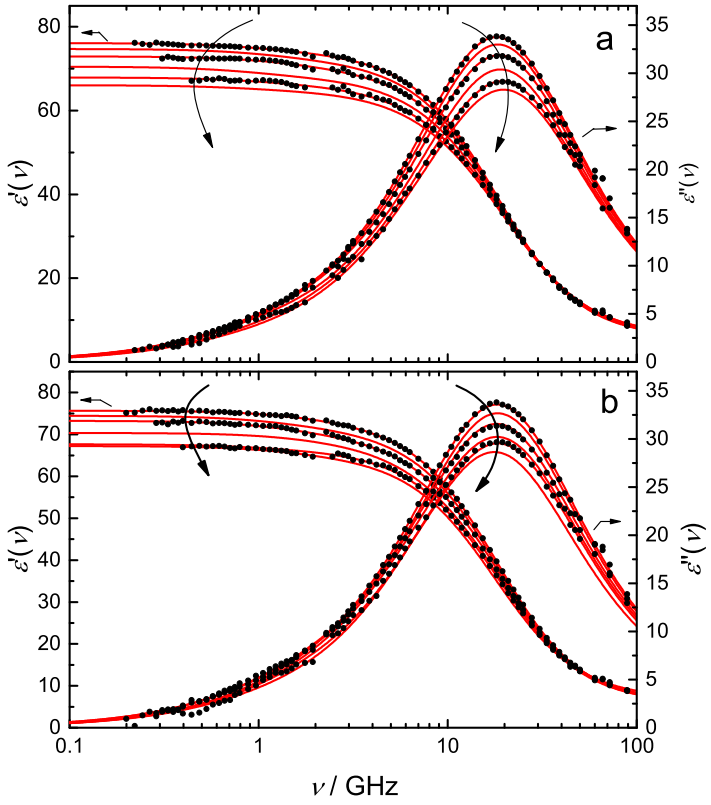

Figure 5.1: Relative permittivity, $\varepsilon'(\nu)$, and dielectric loss, $\varepsilon''(\nu)$, spectra of (a) AcChCl+KCl(aq) (c(AcChCl) $\approx$ 0.25 M; $0 \leq c(\mathrm{KCl})/\mathrm{mol\,L^{-1}} \leq 1.015$) and (b) AcChCl+KF(aq) (c(AcChCl) $\approx$ 0.25 M; $0 \leq c(\mathrm{KF})/\mathrm{mol\,L^{-1}} \leq 1.054$) at 25 °C. Symbols denote the experimental data. Solid lines represent the fits. For visual clarity data points are only shown for selected samples. Arrows indicate the trend with increasing solute concentration.

Table 5.1: Static permittivity, ε, relaxation amplitudes, S_j, relaxation times, τ_j ($j = 1, .., 4$), and the infinite frequency permittivity, ε_∞, obtained from the D+D+D+D model fit of dielectric spectra of AcChCl+KCl(aq) solutions at 25 °C.[a,b]

c(KCl)	c(AcChCl)	ε	S_1	τ_1	S_2	τ_2	S_3	τ_3	S_4	τ_4	ε_∞	χ^2_r
0	0.2507	76.0	2.41	121	2.67	17.8	64.9	8.58	2.50	0.278	3.52	0.0656
0.1521	0.2497	74.7	2.95	116	1.95	19.5	64.4	8.48	2.37	0.278	3.52	0.0702
0.3039	0.2486	72.9	3.01	99.5	2.51	18.8	61.2	8.33	2.71	0.278	3.52	0.1128
0.6185	0.2462	70.5	2.70	156	4.19	18.8	57.2	8.05	2.85	0.278	3.52	0.0988
0.8325	0.2447	67.9	1.93	133	5.68	18.6	53.8	7.78	2.99	0.278	3.52	0.0859
1.054	0.2429	66.1	1.39	171	6.84	18.8	51.4	7.55	2.90	0.278	3.52	0.0144

[a] c in mol L^{-1}, τ_j in ps; [b] parameter values followed by "F" were fixed during fitting.

Table 5.2: Static permittivity, ε, relaxation amplitudes, S_j, relaxation times, τ_j ($j = 1, .., 4$), and the infinite frequency permittivity, ε_∞, obtained from the D+D+D+D model fit of dielectric spectra of AcChCl+KF(aq) solutions at 25 °C.[a,b]

c(KF)	c(AcChCl)	ε	S_1	τ_1	S_2	τ_2	S_3	τ_3	S_4	τ_4	ε_∞	χ^2_r
0	0.2510	75.7	2.64	83.8	2.43	19.2	64.6	8.51	2.42	0.278F	3.52F	0.1685
0.1688	0.2506	74.5	2.95	114	2.07	27.2	63.6	8.49	2.35	0.278F	3.52F	0.0576
0.3281	0.2502	73.2	3.60	100	3.77	19.0	59.5	8.44	2.85	0.278F	3.52F	0.1095
0.6053	0.2494	70.4	2.41	81.3	7.41	18.9	54.3	8.10	2.76	0.278F	3.52F	0.2246
0.7840	0.2490	67.7	1.49	142	6.51	17.2	53.6	8.15	2.52	0.278F	3.52F	0.1604
1.015	0.2483	67.2	2.65	95.8	5.56	16.0	51.9	8.56	3.62	0.278F	3.52F	0.4110

[a] c in mol L^{-1}, τ_j in ps; [b] parameter values followed by "F" were fixed during fitting.

the potassium cation.
In contrast to Cl^-, for which the dynamics of its hydration water is similar to bulk-like water ($Z_t(Cl^-) \approx 0$) [22], the first solvation shell of F^- was reported to be more compact [365, 366]. Accordingly, dielectric spectra of KF in aqueous solution at 25 °C [291] indicate that ~ 16 water molecules are moderately bound by both ions at infinite dilution, while $Z^0_{ib}(KF) \approx 0$ [291]. The coordination number, $CN_1(F^-)$, obtained from neutron diffraction [13] and MD simulation studies [366–368] ranges from 6.0 to 6.9. Note that $Z^0_t(KF) = 16.4$ is in reasonable agreement with the sum $CN_1(K^+) + CN_1(F^-) \approx 12 - 17$.
From the point of view of the dielectric experiment, the presence of additional species affecting the water structure and dynamics makes the analysis of the hydration of the NT more complicated, as the hydration numbers calculated from the solvent-amplitudes using Eqs. 3.4-3.6 incorporate both, the contribution from the solvation of the NT *and* the electrolyte. Thus, appropriate allowances for the hydration numbers of the inorganic salts have to be made in order to disentangle the neurotransmitter-specific information from the overall hydration numbers.
The overall numbers of water molecules impeded in their dynamics and normalized by the AcChCl concentration in AcChCl+KCl(aq) are shown in Figure 5.2. The addition of KCl to AcChCl(aq) has hardly any effect on the number of irrotationally bound water molecules per equivalent of $AcCh^+$ within their large error bars and all Z_{ib} values are fairly low, whereas an increase of Z_s can be observed at $c(KCl) > 0.3\,M$ (Figure 5.2(a)). The latter increase with $c(KCl)$ is reasonable considering that the concentration of K^+ and thus the amount of slow-water increases continuously. The hollow symbols in 5.2(b) indicate $Z_t(AcCh^+)$ after correction of the overall Z_t for $Z_t(K^+) = 6.6 \pm 1.0$ [154]. Note that in this approach $Z_t(K^+)$ was assumed to be concentration-independent. This assumption is supported by neutron diffraction measurements on KCl(aq) solutions up to its saturation limit [369], which reported only a very weak dependence of the hydration structure of K^+ on the salt concentration. Upon addition of KCl, $Z_t(AcCh^+)$ drops continuously from ~ 10 at $c(KCl) = 0$ down to negative numbers at high $c(KCl)$ (~ -5 at $c(KCl) \approx 1.1\,M$). Negative hydration numbers are obviously unphysical, but within the (fairly large) error bars $Z_t(AcCh^+)$ can be approximated as ~ 0 in the higher $c(KCl)$ region (Figure 5.2(b)).
The present results indicate that systematic addition of KCl to AcChCl(aq) results in a fast dehydration of $AcCh^+$, in the sense that retarded water molecules regain their mobility, which eventually leads to a complete disappearance of dynamically impeded water molecules in the vicinity of $AcCh^+$ at $c(KCl) \approx 0.4\,M$. Estimations of the onset of the hydration shell overlap between the present ions suggest that at $c(KX) \approx 0.3\,M$ the first hydration layers of the $AcCh^+$ cations and neighboring ions start to overlap. Although the overlap of the hydration shells certainly is the major contribution to the drop in $Z_t(AcCh^+)$, the observed decrease of $Z_t(AcCh^+)$ below onset concentration for the overlap of the 1st hydration sheaths indicates that the "simple" crowding effects can not completely explain the observed trend. Possibly ion-ion interactions, *i.e.*, $AcCh^+$-Cl^-/K^+, are also present and decisive for the hydration structure and dynamics of acetylcholine.
The corresponding plot of the hydration numbers of AcChCl+KF(aq) is shown in Figure 5.3. Similar to AcChCl+KCl(aq), the addition of KF leads to a fast drop of the over-

all hydration number of $AcCh^+$ (onset of 1st hydration shell overlap at $c(KF) \approx 0.3\,M$). However, the Z_{ib} values increase with increasing $c(KF)$, in contrast to AcChCl+KCl(aq) (Figure 5.2(a)). Simultaneously, the overall Z_s values in AcChCl+KF(aq) do not show a simple increase with increasing $c(KF)$ but go through a maximum at $c(KF) \approx 0.7\,M$. This behaviour of Z_s with rising $c(KF)$ is rather surprising given that $Z_t^0(KCl) = Z_s^0(KCl) \approx 16$ [291]. Since the total hydration number after the correction for $Z_t(KF)$ [291] (Figure 5.3(b)), is virtually zero at high $c(KF)$, the observed trends for Z_s and Z_{ib} in the AcChCl+KF(aq) solutions indicate that some of the moderately bound water at the present ions must become increasingly decelerated in its dynamics in such ways that it can not be detected in the DR spectra. In other words, the initially moderately retarded water becomes more tightly bound with rising $c(KF)$ and thus increasing crowding of the ions. The exact location (which ions are involved) and the precise origin of these effect cannot be given here, as DRS only provides a macroscopic view on this issue. On the other hand, no such "shifts of dynamics" could be observed for AcChCl+KCl(aq), which might suggest that the intrinsic nature of the F^- ion must be responsible for this effect. Note that the constant plateau values of Z_s and also Z_t at low salt concentrations in both systems (Figures 5.2 and 5.3) most probably reflects the interplay between dehydration, which reduces the amount of dynamically retarded water, and the continuous addition of salt, which increases the fraction of impeded water dipoles.

Effect on the dipole moment. At this stage, the question arises whether the above discussed hydration properties of $AcCh^+$ in the presence of KCl(aq) and KF(aq) can be correlated with the experimental effective dipole moments of the NT and/or if other effects, such as ion-pairing, can be deduced from the latter. The effective dipoles moments of $AcCh^+$, obtained from the amplitude S_1 *via* equation 1.48, are shown in Figure 5.4. The estimated errors of μ_{eff} are fairly large, which makes a quantitative analysis quite challenging. However, some interesting trends could still be observed. After a slight initial rise of μ_{eff} at low potassium salt concentrations in both systems, $\mu_{eff}(AcCh^+)$ of AcChCl+KCl(aq) starts to decrease at $c(KCl) > 0.4\,M$ (Figure 5.4(a)), while the $\mu_{eff}(AcCh^+)$ values of AcChCl+KF(aq) show some scatter in the corresponding concentration region (Figure 5.4(b)). It is interesting to note that $\mu_{eff}(AcCh^+)$, which was discussed to scale with the number water molecules tightly bound to $AcCh^+$ (Section 3.1), decreases in AcChCl+KCl(aq) in hand with the observed dehydration of the NT, while no such trend of μ_{eff} was detectable in AcChCl+KF(aq), consistent with the higher overall Z_{ib} at high $c(KF)$ (Figures 5.2 and 5.3).

Unfortunately, there is not much quantitative information on ion association between F^- and trimethylammonium compounds, let alone $AcCh^+$, in aqueous solution. DFT and *ab initio* calculation of $F^- \cdots AcCh^+$ and $Cl^- \cdots AcCh^+$ clusters by Davies *et al.* [370] suggested that the interaction with the trimethylammonium moiety is slightly more favorable for the fluoride anion compared to Cl^-. However, the cited study treated water as a continuum and thus neglected specific interactions between H_2O and the involved ions, which might have a significant influence on the derived binding energies. Following the observed trends of the association constant of Me_4NX salts in water [176], with X^- representing the halide anions Cl^-, Br^- and I^-, the tendency for the formation of $Me_4N^+ \cdots F^-$-IPs would

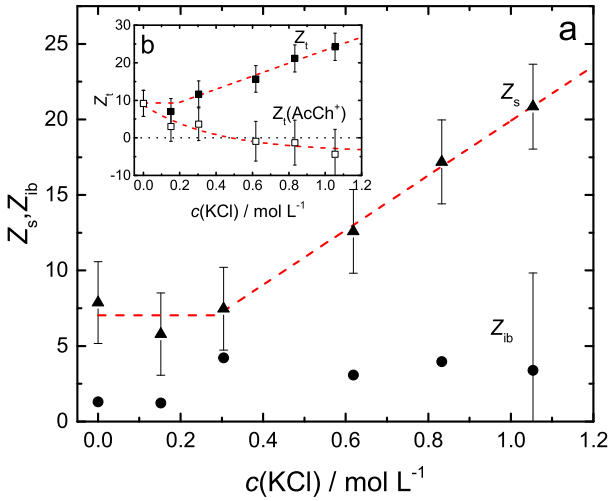

Figure 5.2: (a) The number of moderately retarded, Z_s (▲), and irrotationally bound water, Z_{ib} (●), per equivalent of $AcCh^+$ in AcChCl+KCl(aq) at c(AcChCl) ≈ 0.25 M and as a function of KCl concentration, c(KCl). (b) Total number of impeded water molecules normalized by the concentration of AcChCl, Z_t (■), and resulting values for the $AcCh^+$, $Z_t(AcCh^+)$ (□), after the correction for $Z_t(K^+)$ as a function of c(KCl). Dashed lines show empirical fits. For clarity the estimated error bars of Z_{ib} are only shown for one data point. The uncertainties of the remaining points are of similar magnitude.

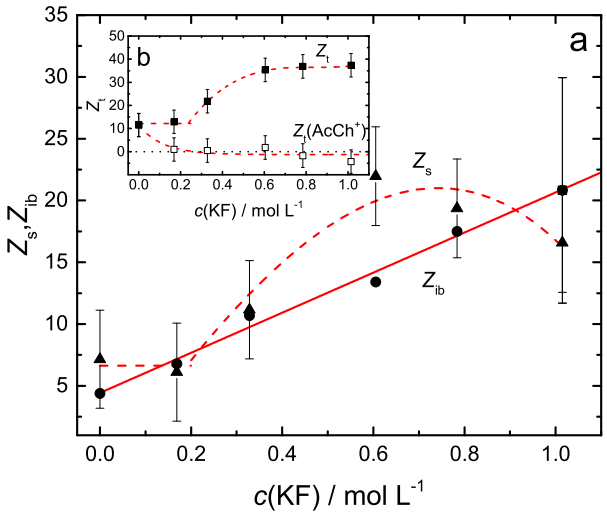

Figure 5.3: (a) The number of moderately retarded, Z_s (▲), and irrotationally bound water, Z_{ib} (●), per equivalent of $AcCh^+$ in AcChCl+KF(aq) at c(AcChCl) ≈ 0.25 M and as a function of KF concentration, c(KF). (b) Total number of impeded water molecules normalized by the concentration of AcChCl, Z_t (■), and resulting values for the $AcCh^+$, $Z_t(AcCh^+)$ (□), after the correction for Z_t(KF) as a function of c(KF). Dashed and solid lines show empirical fits. For clarity the estimated error bars of Z_{ib} are only shown for one data point. The uncertainties of the remaining points are of similar magnitude.

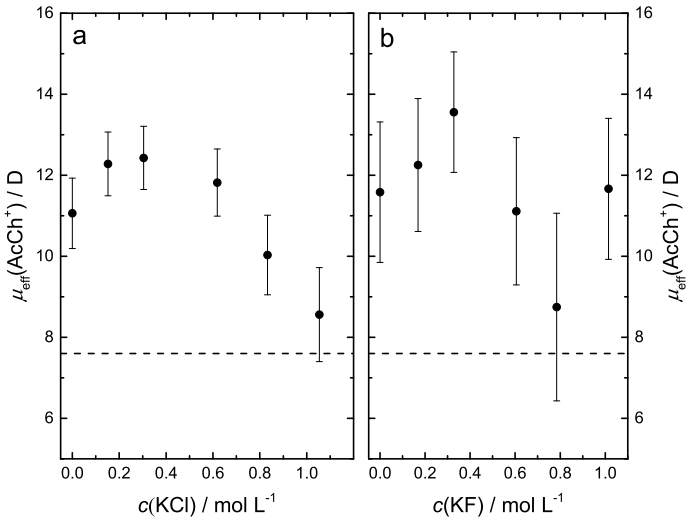

Figure 5.4: Effective dipole moments, μ_{eff}, of $AcCh^+$(aq) at c(AcChCl) $\approx$ 0.25 M upon addition of (a) KCl and (b) KF as obtained from the DR spectra at 25 °C. The dashed line indicates the the calculated (Gaussian 09, B3LYP/6-31G(d,p) with the PCM solvation model) apparent dipole moments of the "bare" $AcCh^+$ ion.

not be expected to be stronger than for $Me_4N^+ \cdots Cl^-$, simply judging by the sizes and the free energies of solvation of the present ions [282]. A similar trend might be expected for the ion binding abilities of the chemically related $AcCh^+$ [370].

Accordingly, the observed small initial increase of $\mu_{\text{eff}}(AcCh^+)$ in Figure 5.4 at low potassium salt concentrations ($c < 0.4$ M) might indicate the formation of highly dipolar $AcCh^+ \cdots Cl^-$ and $AcCh^+ \cdots F^-$-aggregates (Figure A.37), which have a similar relaxation time as the $AcCh^+$ dipole and thus are "hidden" under mode $j = 1$. It should be pointed out that, generally speaking, the relaxation time of IPs, τ_{IP}, is not only governed by the IP-reorientation time, $\tau_{\text{IP}}^{\text{reor}}$, which is connected to the size of the IP, but also by the ion-pairing kinetics, $\tau_{\text{IP}}^{\text{kin}}$. The observed relaxation time is given as $\tau_{\text{IP}}^{-1} = \tau_{\text{IP}}^{\text{reor}\,-1} + \tau_{\text{IP}}^{\text{kin}\,-1}$ [371]. Thus, IP modes might appear at higher relaxation frequencies compared to what would be expected from the IP size alone.

If these aggregates are indeed formed in the solution, the present decreasing trend of μ_{eff} would imply that these IPs most likely dissociate at higher salt concentrations. However, given the large error bars of μ_{eff} this is just speculation. "Simple" dipolar correlations of $AcCh^+$ and neighbouring dipoles would certainly result in a similar effect. Without any further (microscopic) information a definite answer for all these effects can unfortunately not be given here.

5.2.4 Concluding Remarks

The dielectric spectra of ternary AcChCl+KCl(aq) and AcChCl+KF(aq) solutions at 25 °C and a frequency range $\sim 0.2 \leq \nu/\mathrm{GHz} \leq 89$ were successfully fitted by a sum of four Debye equations. Similarly to the binary AcChCl(aq) solutions, no separate IP processes could be resolved in the permittivity spectra of bot sets of samples. The effect of increasing background electrolyte concentration on the hydration of $AcCh^+$ was investigated by the analysis of the amplitude of solvent-related relaxation modes. It was found that the addition of KCl as well as KF leads to a fast dehydration of the NT. Further, some changes in the overall hydration dynamics of water molecules, most likely associated with F^-, could be observed as the concentration of KF increased. Unfortunately, the origin of this effect can not be found by macroscopic techniques, such as DRS. Certainly, MD simulations, neutron diffraction or time-resolved IR experiments of aqueous AcChCl+KF solutions could give valuable insights into the mechanism behind this ion effect, which might generally be interesting from a biochemical standpoint.
A quantitative analysis of μ_{eff} of $AcCh^+$ was hampered by the scatter of the data and relatively large error bars of μ_{eff}, but, in particularly for AcChCl+KCl(aq), some indications of possible IP formation and correlations with the hydration structure were found.
Further, investigations of the present systems over wider concentration range would certainly give a more consistent picture. However, DRS is restricted in its applicability to systems having a relatively low electrical conductivity due to the undesirable conductivity contribution to the DR spectra (equation 1.20). Thus, spectra of samples with $\kappa \gtrsim 15\,\mathrm{S\,m^{-1}}$ are usually swamped by the conductivity in such ways that proper analysis become impossible. Nevertheless, despite all these limitations, the results obtained from these rather complex systems (at least in the view of dielectric spectroscopy) seem to be consistent.
As was argued by Bartoli and Roelens [372], the effect of the counterios on the binding of the $AcCh^+$ NT to its receptors is damped, but generally not negligible in biological systems. Thus, the present results might constitute a further step in the understanding of the ion-solvent and ion-ion interaction in such systems.

5.3 Sodium Glutamate(aq) with Inorganic Salts

5.3.1 Data Acquisition and Processing

The NaGlu+LiCl(aq), NaGlu+NaCl(aq), NaGlu+$MgCl_2$(aq) and NaGlu+$CaCl_2$(aq) solutions were prepared gravimetrically by addition of the respective salt to a $\sim$ 0.4 M NaGlu(aq) solution. The densities, viscosities and electrical conductivities of the present samples were determined according to procedures presented in Section 2.4. The corresponding data are shown in Table A.19. The complex permittivity spectra were recorded in the frequency range $0.05 \leq \nu/\mathrm{GHz} \leq 89$ (Dielectric probe kit VNA setup + E-band interferometer, Section 2.3) at 25 °C. However, due to the rather high electrical conductivity of the electrolyte solutions the effective low frequency limit was in the range $0.1 \leq \nu_{\mathrm{min}}/\mathrm{GHz} \leq 0.44$, depending on the added salt and its concentration (Section 3.1).

5.3.2 Choice of Relaxation Model and Assignment of Modes

The appropriate fit models for the spectra of the present solutions were primarily chosen by testing various models with sums of up to six HN-equations (equation 1.41) and assessing the quality of the fit by criteria discussed in Section 2.3.3. Consistent with Zasetsky's analysis (Figures A.38-A.41) combinations of three to five Debye equations yielded the best discription of the present DR spectra, depending on the background electrolyte and the concentration (Figure A.42). The parameters of the best-fit models of the studied solutions are summarized in Tables 5.3-5.6 .

Note that prior to fitting of the spectra of NaGlu+$MgCl_2$(aq) and NaGlu+$CaCl_2$(aq), the raw spectra had to be corrected for the significant amount of $MgCl^+$ and $CaCl^+$ ion pairs, which contributed significantly to the spectra in the lower frequency regime (Section 4.1). Details on this new approach of removing electrolyte-dependent IP modes from the DR spectra, and thus allowing to extract biomolecule-specific information, are given in Chapter C of the Appendix.

As would be expected, all spectra exhibit a mode $k = 3$ centered at $\sim 19\,\mathrm{GHz}$ ($\tau_3 \approx 8\,\mathrm{ps}$), which can unambiguously be assigned to the cooperative relaxation of the H-bond network of bulk-like water [22]. With increasing salt concentration this mode decreases significantly in intensity (Figures A.43, A.44, A.45 and A.46). Similar to binary NaGlu(aq) solutions (Section 3.2), a fast-water contribution could not be resolved for NaGlu+LiCl(aq) and NaGlu+NaCl(aq). However, its presence is obvious from the large ε_∞ values (Table 5.3 and 5.4). In the case of NaGlu(aq)+$MgCl_2$ and NaGlu(aq)+$CaCl_2$ fast-water could be resolved as mode $k = 4$ in the spectra, albeit with considerably scattering S_4 and τ_4 values (Tables 5.5 and 5.5). Accordingly, $\tau_4(c) \equiv \tau_4(0) = 0.278\,\mathrm{ps}$ and $\varepsilon_\infty(c) \equiv \varepsilon_\infty(0) = 3.52$ [154] were fixed in the final fit. The inability to resolve the fast-water contribution for the former two systems suggests a displacement of its relaxation time to higher frequencies. Most likely this shift is connected to the presence of monovalent cations (Li^+, Na^+), since for the present solutions alkaline earth cations (Mg^{2+} and Ca^{2+}) the fast-water mode becomes discernible upon addition of the respective salt. Similarly, the fast-water process was also resolved for binary $MgCl_2$ and $CaCl_2$ solutions in Section 4.1.

Besides the two modes associated with bulk water, the contribution at $\sim 9\,\mathrm{GHz}$ ($\tau_2 \approx 18\,\mathrm{ps}$), appearing for all NaGlu+salt systems (and the binary NaGlu(aq) solution, Section 3.2), must also be assigned to the solvent. As already discussed for NaGlu in water (Section 3.2), this slow-water mode 2 is typical for hydrophobic and weakly hydrophilic solutes and it arises from the slowed-down reorientation of H_2O molecules hydrating the solute.

Based on the previous discussion of the DR spectra of binary NaGlu(aq) solutions (Section 3.2), mode $k = 1$ can readily be assigned to the reorientation of the dipolar Glu^- anion. Naturally, this mode was also found for the salt-containing systems studied but interestingly, with its amplitude, S_1, decreasing with rising electrolyte content (Figures A.43, A.44, A.45 and A.46).

For all four salts studied their addition to $\sim 0.4\,\mathrm{M}$ NaGlu solution led to the emergence of a mode $k = 0$ at $\lesssim 0.8\,\mathrm{GHz}$ ($\tau_0 \lesssim 200\,\mathrm{ps}$). Its relaxation time, τ_0, scatters somewhat but the mean value clearly depends on the type of background electrolyte (Tables 5.3, 5.4, 5.5,

Table 5.3: Static permittivity, ε, relaxation amplitudes, S_k, and relaxation times, τ_k of the resolved modes $k = 0 \ldots 3$, infinite-frequency permittivity, ε_∞, and value of the reduced error function, χ^2_r, obtained from the (D+)D+D+D model fit of dielectric spectra of NaGlu+LiCl(aq) at 25 °C. [a,b]

c(LiCl)	c(GluNa)	ε	S_0	τ_0	S_1	τ_1	S_2	τ_2	S_3	τ_3	ε_∞	χ^2_r
0	0.394	84.9	–	–	13.9	94.9	4.58	19.0	60.3	8.15	6.12	0.0857
0.1013	0.393	83.9	2.32	204	12.5	89.7	8.33	15.3	54.8	7.77	6.02	0.0562
0.2866	0.391	82.0	2.68	171	12.0	96.4	6.31	16.2	54.7	8.01	6.24	0.110
0.5686	0.389	78.4	2.02	185	11.6	111	7.85	18.3	50.7	7.79	6.24	0.119
0.9469	0.386	73.7	2.62	191	10.2	118	7.48	19.4	47.1	7.75	6.45	0.124
1.508	0.382	66.0	–	–	9.80	133	10.9	19F	39.0	6.92	6.25	0.122

[a] c in mol L^{-1}, τ_k in ps; [b] parameter values followed by "F" were fixed during fitting.

Table 5.4: Static permittivity, ε, relaxation amplitudes, S_k, and relaxation times, τ_k of the resolved modes $k = 0 \ldots 3$, infinite-frequency permittivity, ε_∞, and value of the reduced error function, χ^2_r, obtained from the (D+)D+D+D model fit of dielectric spectra of NaGlu+NaCl(aq) at 25 °C. [a]

c(NaCl)	c(GluNa)	ε	S_0	τ_0	S_1	τ_1	S_2	τ_2	S_3	τ_3	ε_∞	χ^2_r
0	0.424	86.3	–	–	15.36	105	6.60	20.8	58.3	8.00	6.00	0.0914
0.1103	0.423	85.0	1.03	624	15.1	116	5.17	26.4	58.7	8.13	6.11	0.0671
0.2518	0.422	85.1	2.94	401	15.3	119	9.10	18.5	51.7	7.68	6.08	0.101
0.5059	0.419	82.2	1.59	495	15.4	113	11.0	15.3	47.9	7.47	6.35	0.138
0.8046	0.417	78.3	0.611	359	14.8	123	11.7	16.0	44.7	7.29	6.46	0.113
0.9994	0.415	75.1	–	–	14.08	119	12.3	15.0	42.1	7.11	6.72	0.109

[a] c in mol L^{-1}, τ_k in ps.

Table 5.5: Static permittivity, ε, relaxation amplitudes, S_k, and relaxation times, τ_k of the resolved modes $k = 0 \ldots 4$, infinite-frequency permittivity, ε_∞, and value of the reduced error function, χ^2_r, obtained from the D+D+D+D+D model fit of dielectric spectra of NaGlu+$MgCl_2$(aq) at 25 °C.[a,b]

$c(MgCl_2)$	c(GluNa)	ε	S_0	τ_0	S_1	τ_1	S_2	τ_2	S_3	τ_3	S_4	τ_4	ε_∞	χ^2_r
0	0.424	86.3	–	–	15.4	105	6.60	20.8	58.3	8.00	–	–	6.00	0.0914
0.0674	0.408	85.2	1.81	375	14.6	104	5.78	17.5	56.9	8.12	2.63	0.278F	3.52F	0.0635
0.1594	0.402	83.2	3.20	453	13.8	111	7.21	16.8	52.7	7.95	2.80	0.278F	3.52F	0.0675
0.3162	0.393	78.5	4.93	453	11.7	123	7.10	18.5	48.3	7.77	3.00	0.278F	3.52F	0.0828
0.4865	0.381	71.5	6.49	321	9.27	105	4.08	14.8	44.9	7.87	3.29	0.278F	3.52F	0.0620
0.8358	0.357	63.2	7.89	742	9.11	136	3.91	16.3	35.2	7.39	3.53	0.278F	3.52F	0.0474

[a] c in mol L^{-1}, τ_k in ps; [b] parameter values followed by "F" were fixed during fitting.

Table 5.6: Static permittivity, ε, relaxation amplitudes, S_k, and relaxation times, τ_k of the resolved modes $k = 0 \ldots 4$, infinite-frequency permittivity, ε_∞, and value of the reduced error function, χ^2_r, obtained from the D+D+D+D+D model fit of dielectric spectra of NaGlu+$CaCl_2$(aq) at 25 °C.[a,b]

$c(CaCl_2)$	c(GluNa)	ε	S_0	τ_0	S_1	τ_1	S_2	τ_2	S_3	τ_3	S_4	τ_4	ε_∞	χ^2_r
0	0.424	86.3	–	–	15.4	105	6.60	20.8	58.3	8.00	–	–	6.00	0.0914
0.1010	0.421	85.3	4.68	229	13.2	94.2	5.39	17.2	55.7	8.11	2.91	0.278F	3.52F	0.0347
0.2007	0.418	84.2	5.32	216	12.1	91.7	6.55	15.3	53.8	7.99	2.95	0.278F	3.52F	0.0875
0.2984	0.416	80.1	6.55	244	11.0	102	7.29	15.8	48.7	7.71	3.04	0.278F	3.52F	0.0463
0.4948	0.410	74.3	5.62	260	10.5	117	4.80	18.9	46.4	7.70	3.41	0.278F	3.52F	0.0418
0.7955	0.402	65.2	2.48	227	10.8	141	5.00	17.9	39.8	7.32	3.66	0.278F	3.52F	0.0728

[a] c in mol L^{-1}, τ_k in ps; [b] parameter values followed by "F" were fixed during fitting.

5.6). The corresponding amplitude, S_0, showed an initial rise with c(salt), followed by a drop off at higher salt concentrations of LiCl, NaCl and $CaCl_2$ (Figures A.43, A.44, A.45 and A.46). The series NaGlu(aq)+$MgCl_2$(aq) is an exception here as S_0 increased continuously over the entire concentration range (Figure A.45). Note that for NaGlu+LiCl(aq) and NaGlu+NaCl(aq) at a given salt concentration S_0 is significantly smaller than for the alkaline earth chlorides and this mode could not be resolved at the highest concentrations of LiCl and NaCl. This suggests that here mode 0 is dominated by IC relaxation (Section 3.1) although a weak ion-pair contribution is almost certainly present ofr NaGlu+LiCl(aq) for NaGlu+LiCl(aq), as discussed further below. On the other hand, for the studied 2:1 electrolytes the magnitude of S_0 suggests a significant contribution from $M^{2+} \cdots Glu^-$ ion pairs. Here, it should be pointed out again that the NaGlu+$MgCl_2$(aq) and NaGlu+$CaCl_2$(aq) spectra discussed here were already corrected for the contribution from $MgCl^+$ and $CaCl^+$ ion pairs, respectively (Chapter C of the Appendix).

5.3.3 Effects of the Background Electrolyte

Effects of salt addition on Glu^- hydration. To obtain the hydration number of Glu^- in the electrolyte-containing solutions, additivity of ionic hydration numbers was assumed. As usually, for the chloride anion $Z_t(Cl^-) = 0$ [156] was used whereas for Li^+ the single-ion hydration numbers of Ref. [289] at the given salt concentration were inserted. The corresponding Mg^{2+} and Ca^{2+} values were taken from Section 4.1. The thus obtained $Z_s(Glu^-)$ and $Z_{ib}(Glu^-)$ for ~ 0.4 M NaGlu(aq) in the presence of the electolytes are shown in Figure 5.5. Whilst for the 1:1 electrolytes $Z_{ib}(Glu^-) \approx 0$ and $Z_s(Glu^-)$ increased over the investigated range of salt concentrations (Figure 5.5(a),(b)), for the 2:1 electrolytes $Z_s(Glu^-)$ remained constant but $Z_{ib}(Glu^-)$ became increasingly negative for NaGlu+$CaCl_2$(aq) (Figure 5.5(c),(d)).

Obviously, negative $Z_{ib}(Glu^-)$ are unphysical. As will become clear in the discussion of solute relaxation below, it is argued that the divalent cations, $M^{2+} = Mg^{2+}$ & Ca^{2+}, form contact ion pairs (CIPs) of the type $\left[M^{2+} \cdots Glu^-\right]^+$(aq) with the glutamate anion, leading thus to a partial dehydration of the bound cations and thus decreasing Z_t values for the solutions. On the other hand, for $M^+ = Li^+$ & Na^+ the analysis of the solute relaxation suggests simultaneous binding of metal and chloride ions to aggregates of the type $\left[Cl^- \cdots M^+ \cdots Glu^-\right]^+$(aq), similar to aqueous ectoine [152] and L-proline [162] solutions upon NaCl addition.

Ion-pairing in Glu^- solutions. Although some MD simulations [15, 209] and neutron scattering studies [208] pointed out the existence of strong $Na^+ \cdots Glu^-$ interaction, no direct evidence for any kind of long-lived IPs could be observed without the addition of electrolytes to the NaGlu(aq) solution (Section 3.2).

Upon addition of salts, two different cases, depending on the type of cation, emerged: for NaCl and LiCl salt additions no separate IP mode could be resolved (mode $k = 0$ was attributed mainly to IC relaxation), while for bivalent salts a distinct IP process, also denoted as mode 0, was observed. To obtain IP concentrations from analysis of the IP mode in the latter solutions *via* equation 1.48, the value of the dipole moment of the

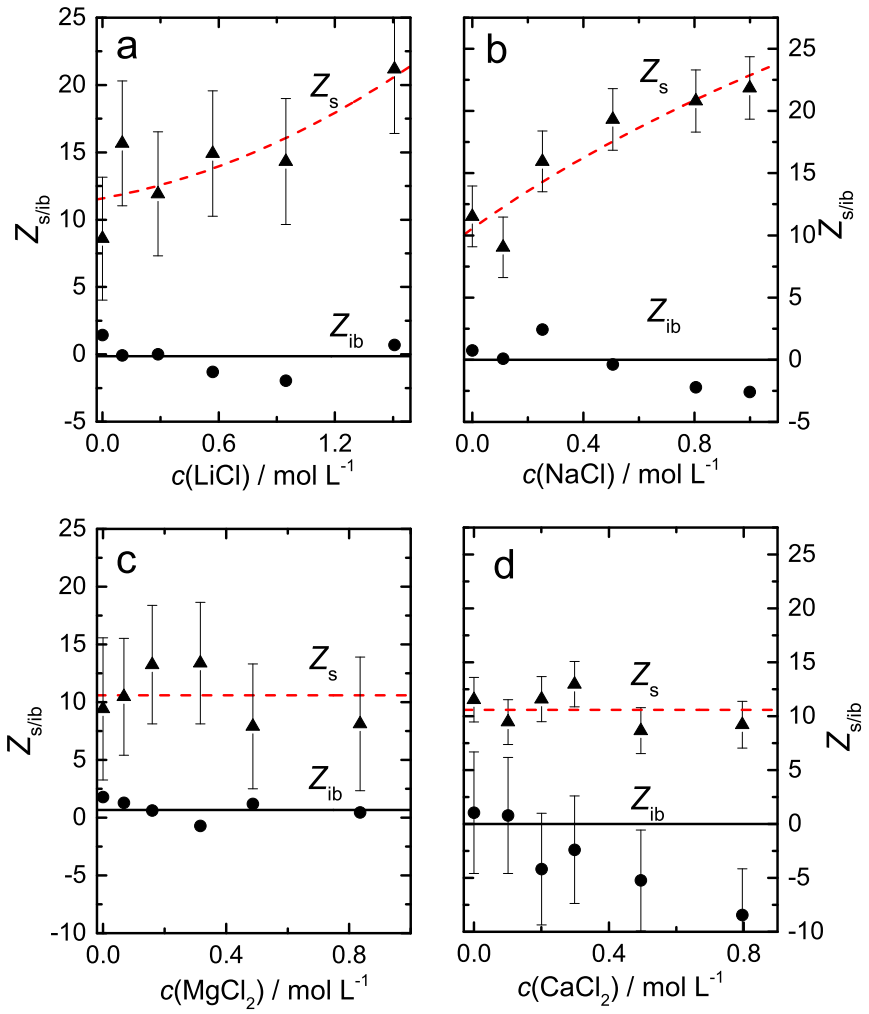

Figure 5.5: The number of moderately retarded, Z_s (▲), and irrotationally bound water, Z_{ib} (●), of Glu^- as a function of the concentration of (a) LiCl, (b) NaCl, (c) $MgCl_2$ and (d) $CaCl_2$ added to ∼0.4 M NaGlu(aq) solutions. Dashed lines as a guide to the eye; for clarity the error bars of Z_{ib} are only shown in (d).

Table 5.7: Infinite dilution binding constants, K_A°, of Glu^- with various ions as obtained by DRS at 25 °C.[a]

cation	most likely IP species	$\lg K_A^\circ$
Li^+	$[Li\cdots H_2O\cdots Cl\cdots OOCNH_3(CH_2)_2COO]^-$	1.1 ± 0.9
Na^+	$[Na\cdots H_2O\cdots Cl\cdots OOCNH_3(CH_2)_2COO]^-$	–
Mg^+	$[Mg\cdots OOC(CH_2)_2NH_3COO]^+$	1.0 ± 0.1
Ca^+	$[Ca\cdots OOC(CH_2)_2NH_3COO]^+$	1.5 ± 0.2

[a] K_A° in $L\,mol^{-1}$.

present IP species, $\mu_{eff}(IP)$, has to be used. This quantity is not known *a priori*, though. However, it should be kept in mind that the analytic glutamate concentration can be written as $c(IP) + c(Glu^-)$, where $c(IP)$ contributes to mode $k = 0$, while $c(Glu^-)$ governs the glutamate reorientation mode 1. Thus, $c(IP)$ can be obtained from the decrement of S_1 compared to its "ideal" value (S_1 in the case of no IP formation). Eventually, the association constant K_A (equation 4.2) can be obtained in this way.
However, this approach would only yield the extent of ion-pairing, but it would not give any molecular-level information on the present IP species. Therefore, geometries of various ion-glutamate aggregates embedded in water were obtained by DFT calculations (Gaussian 09 at the B3LYP/6-31++G(d,p) level with the PCM solvation model) and their predicted dipole moments were compared with the experimentally obtained $\mu_{eff}(IP)$ (Figure 5.6(c) and (d)). Note that in the analysis above the dipole-correlation factor of the IPs, g_{IP} (equation 1.52), was assumed to be unity (no parallel or anti-parallel alignment of neighbouring dipoles with respect to the IP) and only one specific ion-pair type was assumed to be responsible for the complete IP response.
Applying this procedure to NaGlu + $MgCl_2$(aq) and NaGlu + $CaCl_2$(aq), it was found that $\mu_{eff}(IP) \approx 29.7\,D$ and $\mu_{eff}(IP) \approx 28.1\,D$, respectively. For both salts the values compare well with the calculated dipole moments of ion-aggregates where Mg^{2+} and Ca^{2+} are bound directly to the sidechain -COO^- group, for which 29.7 D and 32.9 D were predicted by DFT calculations, respectively (Figures A.49(a) and A.50(a)). The tendency for the formation of CIPs is thus found to be higher than for the formation of solvent-shared IPs, despite the relatively strong hydration of both cations (Section 4.1). At least for calcium ions its tendency to preferentially form inner-sphere with carboxylate binding sites on proteins is known [288, 360] and the increased stability of CIPs of Ca^{2+}-carboxylates (formate/acetate) compared to the respective solvent-shared species was also proposed my Martinek *at el.* [301] in a recent MD simulation study in combination with neutron scattering experiments.
The association constant values were fitted to equation 3.2 as a function of ionic strength, I, to obtain the infinite dilution formation constant, K_A°, at $I \to 0$. Figure 5.7 shows the fit of $K_A(MgGlu^+)$ and $K_A(MgGlu^+)$ values. The obtained infinite dilution formation constants for $\left[Mg^{2+}\cdots Glu^-\right]^+$(aq) and $\left[Ca^{2+}\cdots Glu^-\right]^+$(aq) are listed in Table 5.7.
The binding constant of $\lg K_A(MgGlu^+) = 1.0 \pm 0.1$ and a somewhat higher value of

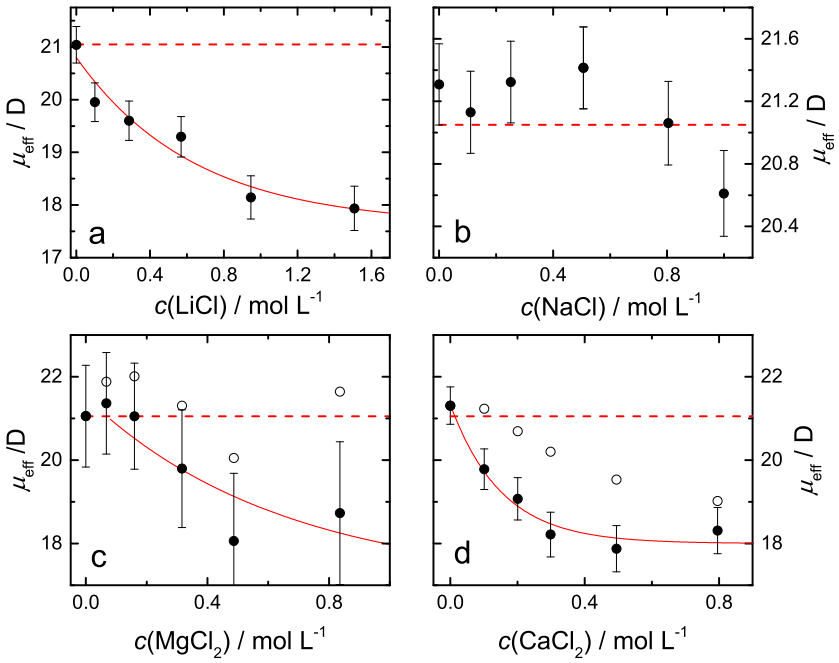

Figure 5.6: Effective dipole moment, μ_{eff} (●), of the species governing mode $k = 1$ in (a) 0.4 M NaGlu+LiCl(aq), (b) 0.4 M NaGlu+NaCl(aq), (c) 0.4 M NaGlu+$MgCl_2$(aq) and (d) 0.4 M NaGlu+$CaCl_2$(aq) solutions as a function of the concentration of added salt. The dashed line denotes the expected effective dipole moment in the case that mode $k = 1$ is due to Glu^- reorientation only and no IPs are formed; the solid lines in (a), (c) and (d) are guides to the eye. The hollow symbols in (c) and (d) denote the expected effective dipole moments after taking into account the formation of $M^{2+} \cdots Glu^-$-IPs.

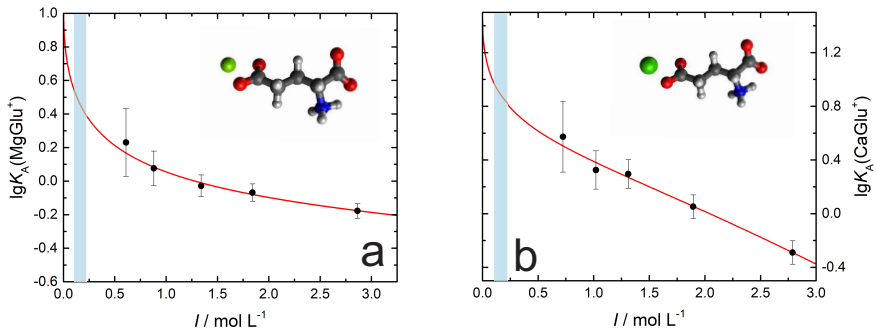

Figure 5.7: Formation constants, K_A (●), of (a) $MgGlu^+$ and (b) $CaGlu^+$ ion-pairs as a function of ionic strength, I, in NaGlu+$MgCl_2$ and NaGlu+$CaCl_2$ solutions (c(NaGlu) ≈ 0.4 M) and associated Guggenheim-type fits (lines). The inserts show the corresponding minimum-energy conformation of the $\left[M^{2+}\cdots Glu^-\right]^+$ aggregates from DFT calculations; the shaded areas indicate the physiologically relevant ionic strength range.

$\lg K_A(CaGlu^+) = 1.5 \pm 0.2$ indicate that ionpair formation between glutamate and the present divalent cations is pronounced in aqueous solution. Information on association constants of Glu^-(aq) with Mg^{2+} and Ca^{2+} is rather sparse in literature. Potentiometric measurements reported $\lg K_A \approx 1.8$ [373] and $\lg K_A \approx 1.9$ [374] at $I = 0.1$ M for the formation of $MgGlu^+$. Both values are in the same order of magnitude but higher than the formation constants obtained from the DR spectra. For $CaGlu^+$(aq) values of $\lg K_A \approx 1.4$ [373] and $\lg K_A \approx 0.8$ [375] were found at $I = 0.1$ M and $I = 0.16$ M, respectively. As $\lg K_A$ values usually decrease with increasing I, the former value is slightly higher than the association constant value at $I = 0.1$ M obtained by DRS. On the other hand, the latter value, which was measured in the physiologically relevant ionic strength of $I = 0.16$ M, agrees well with the value of $\lg K_A(CaGlu^+) \approx 0.9$ obtained from the extrapolation of the DR values to the corresponding ionic strength with the help of equation 3.2 (Figure 5.7(b)). The higher formation constants of $CaGlu^+$(aq) compared to $MgGlu^+$(aq) of the present study suggest a slightly higher affinity ofthe calcium ion towards glutamate. This trend is reversed in the potentiometric studies presented above, showing higher binding constants for Mg^{2+} complexes in comparison to $CaGlu^+$-IPs.

It interesting to note that for NaGlu+$MgCl_2$(aq) the effective dipole moment values corrected for the presence $\left[Mg^{2+}\cdots Glu^-\right]^+$-IPs (Figure 5.6(c)) now coincides well with the value of Glu^- in a "neat" NaGlu(aq) solution, while for NaGlu+$CaCl_2$(aq) the corresponding correction can not fully account for the decline of μ_{eff} (Figure 5.6(d)). The latter observation might indicate the existence some further effects, besides the formation of $\left[Ca^{2+}\cdots Glu^-\right]^+$-IPs, associated with the presence of $CaCl_2$ in NaGlu(aq). While specific dipolar correlations involving the solvent are always worth considering in solutions of small biologically active molecules (Sections 3.1, 3.2 and 3.3), the formation of higher order ionic

aggregates (*e.g.* $CaGlu_2$, $CaGlu_3^-$,...) cannot be ruled out. It should be pointed out that such species should not be directly observed in the DR spectra, since just by simple geometric considerations the dipole moment of such species should be very low or even zero. A computational study of Stevens and Rempe [376] deduced that the preferred number of $-COO^-$ ligands (formate/acetate) at Ca^{2+} in aqueous solution is two. Such triple ions of the form $\left[Glu^- \cdots Ca^{2+} \cdots Glu^-\right]$ would certainly explain the observed discrepancy in the corrected μ_{eff} values of NaGlu+$CaCl_2$(aq) (Figure 5.6(d)). Further, this could explain the obtained negative $Z_{\text{ib}}(Glu^-)$ at high $c(CaCl_2)$, since the hydration number of Ca^{2+} is such a complexes is certainly lowered compared to $Z_{\text{t}}(Ca^{2+})$ in the bulk, which is, however, used for the correction of the overall hydration numbers to obtain $Z_{\text{ib}}(Glu^-)$ in Figure 5.5(d). Simultaneously, this would also imply that no such higher order species are formed between smaller magnesium cation and glutamate. Assuming that $\left[Glu^- \cdots Ca^{2+} \cdots Glu^-\right]$ are formed exclusively [376], the corresponding triple ion concentration can be estimated from μ_{eff}, which are shown in Figure A.51. However, the latter results should be taken with a grain of salt, since many different steps with many different assumptions are involved in their derivation. They should rather be regarded as strong indications of the divergent nature of Mg^{2+} and Ca^{2+} ions. Consequently, it will be abstained from a further discussion.

Whereas for the divalent salt additions the IP-related mode 0 and mode 1 could be directly used to deduce the information on the extent and the most likely type of cation-glutamate IPs, for GluNa(aq) + LiCl/NaCl a different approach is required, as no distinct IP mode was observed in the DR spectra for the latter systems.

As can be seen in Figure 5.6(a,b), the obtained effective dipole moment values for NaGlu(aq) + LiCl are lower than expected effective dipole moment value of Glu^- at $\sim 0.4\,\text{M}$ Glu^- and they decrease continuously with c(LiCl), while for NaGlu(aq) + NaCl a slight drop below the expected $\mu_{\text{eff}}(Glu^-)$ can be observed only at higher c(NaCl). The latter quantity (dashed line in 5.6) was obtained under the assumption that mode $k = 1$ would only be governed by Glu^- reorientation only (no IP formation) and that the added salt does not break down the present dipolar correlations (Section 3.2). The drop of the effective dipole moment in the NaGlu(aq) + LiCl/NaCl solutions could be traced back to the replacement of the reorientating Glu^- dipoles by species which have a similar relaxation time but lower dipole moment compared to Glu^-(aq). $Li^+/Na^+ \cdots Glu^-$ IPs are suitable candidates for such a species. Evaluation of the dipole moments of the calculated structures in Figure A.47 for $Li^+ \cdots Glu^-$-cluster and Figure A.48 for $Na^+ \cdots Glu^-$-IPs reveals that only the species where cation is directly bound to the sidechain $-COO^-$ (Figures A.47(a) and A.48(a)) or aggregates with the cation and Cl^-, bridged by a water molecules, simultaneously bound to the backbone (Figures A.47(h) and A.48(h)) could be responsible for the observed effect. It is argued that the latter structure may explain the pronounced increase in Z_{s} (Figure 5.5(a) and 5.5(b)), as the amount of water molecules entrapped, and thus slowed down, in the quadrupolar $\left[Li^+ \cdots H_2O \cdots Cl^- \cdots Glu^-\right]^-$ structure increases with increasing salt content, similar to the case of L-proline and the reported formation of $\left[Na^+ \cdots H_2O \cdots Cl^- \cdots \text{proline}\right]$ aggregates [162]. In the following $\left[M^+ \cdots H_2O \cdots Cl^- \cdots Glu^-\right]^-$ aggregates will be designated as ion-pairs, although they

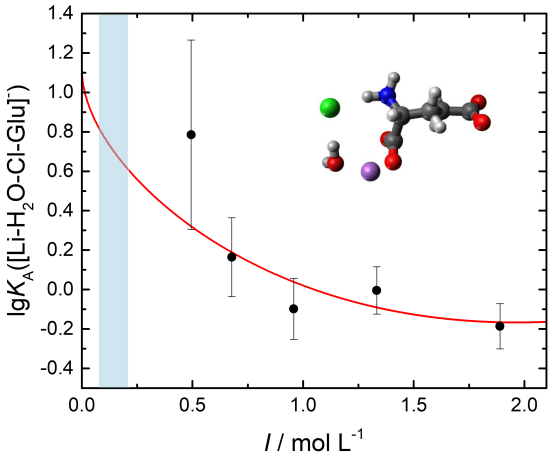

Figure 5.8: Formation constants, K_A (●), of ion-pairs between Li^+ and Glu^- as a function of ionic strength, I, in NaGlu+LiCl solutions (c(NaGlu) ≈ 0.4 M) and associated Guggenheim-type fit (lines). The insert shows the corresponding minimum-energy conformation of the $\left[Li^+ \cdots H_2O \cdots Cl^- \cdots Glu^-\right]^-$ aggregate from DFT calculations; the shaded area indicates the physiologically relevant ionic strength range.

are no classical ion-pairs in that sense. It should be also pointed out that the interaction of the cationic amine group of an α-amino acid with the chloride anion alone is rather weak [377–379] and thus the formation of double negatively charged $[Cl^- \cdots Glu^-]^{2-}$ aggregates is fairly unlikely. Therefore, no DFT calculation of such aggregates were performed.
Splitting up the amplitude $S_1 = S_{IP} + S_{Glu^-}$ and assuming a distinct, single IP species to be dominant, the concentration of the IPs, c(IP), and consequently the association constants (equation 4.2) can be obtained. In hand with the the trends in Z_s, this analysis assumes $\left[Li^+ \cdots H_2O \cdots Cl^- \cdots Glu^-\right]^-$ aggregates to be the only species present, although the formation of IPs with Li^+ bound to sidechain carboxylate cannot be ruled out completely. Either way, the calculated dipole moments of both species are quite similar (13.4 D vs. 13.8 D, Figure A.47), thus no significant changes to the formation constants would be expected. Figure 5.8 shows the obtained association constants of $\left[Li^+ \cdots H_2O \cdots Cl^- \cdots Glu^-\right]^-$ aggregates as a function of the ionic strength and the corresponding fit. The extrapolated formation constant value at infinite dilution of $\lg K_A^\circ = 1.1 \pm 0.9$ is comparable to $\lg K_A^\circ$ of $MgGlu^-$-IPs (Table 5.7). Note that the large error of ±0.9 might indicate that the found value might be overestimated.
Unfortunately, the extent of ion aggregation in NaGlu(aq) + NaCl solutions could not be quantified, as the effect of IP formation, if at all, could only be observed at c(NaCl) $\gtrsim$ 0.8 M, *i.e.*, $c(Na^+) : c(Glu^-) \approx 3{:}1$ (Figure 5.6). However, it may be concluded that sodium has a reduced tendency to bind to Glu^- compared to Li^- and that stable NaGlu-IPs, most probably in the form of $\left[Na^+ \cdots H_2O \cdots Cl^- \cdots Glu^-\right]^-$ aggregates, start to form as the

amount of Na^+ goes far beyond the equimolar concentration ratio between Na^+ and Glu^-. The higher propensity of Li^+ to bind to glutamate was also observed in the gas-phase by mass spectrometry experiments [380, 381].
Note that for NaGlu(aq) + $MgCl_2$ the formation of similar $\left[Mg^{2+}\cdots H_2O\cdots Cl^-\cdots Glu^-\right]$ aggregates ($\mu_{IP} = 29.7\,D$) would also be conceivable. Keeping in mind that no similar increase of Z_s with rising $c(MgCl_2)$ was observed (Figure 5.5) and that the formation of the corresponding $\left[Ca^{2+}\cdots H_2O\cdots Cl^-\cdots Glu^-\right]$ species ($\mu_{IP} = 42.6\,D$) for NaGlu(aq) + $CaCl_2$ could be excluded from the analysis of the dipole moments (Figure A.49), it can be inferred that binding of the present earth alkali metals to the sidechain rather than the backbone is more likely. It may be speculated that the strong repulsion between double positively charged cations and the onium moiety might be responsible for the present effect.

5.3.4 Concluding Remarks

The dielectric spectra of aqueous $\sim 0.4\,M$ NaGlu in the presence of different chloride salts (LiCl, NaCl, $MgCl_2$ and $CaCl_2$) at varying concentrations were recorded in the frequency range $0.05 \leq \nu/GHz \leq 89$ at $25\,°C$. It was found that combinations of up to four Debye modes yielded the best fits for DR spectra of NaGlu+LiCl(aq) and NaGlu+NaCl(aq), while five Debye modes were needed for NaGlu+$MgCl_2$(aq) and NaGlu+$CaCl_2$(aq). Mode $k = 0$ in the latter systems was assigned to the formation of IPs between the divalent cations and Glu^-. The evaluation of the alleged Glu^- reorientation mode $k = 1$ and comparisons with DFT-calculated IP structures revealed that ion-pair species with Mg^{2+} and Ca^{2+} directly bound to the sidechain carboxylates are the most likely candidates to be responsible for mode $k = 0$. Association constants were retrieved, respectively. In contrast to NaGlu+$MgCl_2$(aq) and NaGlu+$CaCl_2$(aq), the low-intensity mode 0 in the permittivity spectra of NaGlu+LiCl(aq) and NaGlu+NaCl(aq) was attributed to IC relaxation. Nevertheless, the trends in μ_{eff} were argued to be linked to the presence of Li^+/Na^+-Glu^- IPs. A detailed analysis of S_1 suggested that ion aggregates of the form $\left[M^+\cdots H_2O\cdots Cl^-\cdots Glu^-\right]^-$, where the binding occurs at the backbone, might be present in the solutions, similar to the previously reported case of L-proline+NaCl(aq) [162]. The corresponding association numbers could only be obtained for NaGlu+LiCl(aq), while no quantitative analysis was possible for NaGlu+NaCl(aq).
Hydration numbers of glutamate as a function of chloride salt concentrations were deduced from the amplitudes of the solvent-related relaxation modes. It was discussed that the increase of Z_s observed in NaGlu+LiCl(aq) and NaGlu+NaCl(aq) could be associated with the hydration of the quadrupolar $\left[M^+\cdots H_2O\cdots Cl^-\cdots Glu^-\right]^-$ species. The unphysical, negative Z_{ib} values obtained for NaGlu+$CaCl_2$(aq) were argued to result from a possible formation of higher order ionic aggregates, such as $\left[Glu^-\cdots Ca^{2+}\cdots Glu^-\right]$ triple ions. However, up to now this is just speculation and further experimental and computational approaches would certainly be necessary to clarify this issue.
Although some fairly bold assumptions were made in the analysis of the DR spectra, especially for the solute-related modes, the results appear to be consistent. For instance, the

dipolar correlations of Glu^- and the surrounding dipolar molecules were partly neglected or at least assumed to be of the same as in binary NaGlu(aq) solutions (Section 3.2), since the actual magnitude of these interactions was not known. Nevertheless, despite all this, a coherent picture on the interaction of Glu^- with other biologically important inorganic ions was obtained in the present DRS study and it might provide a deeper insight into some processes occurring in biological systems.

5.4 Glutamine(aq) with Inorganic Salts

5.4.1 Data Acquisition and Processing

The solutions of Gln+LiCl(aq), Gln+NaCl(aq), Gln+MgCl(aq) and Gln+CaCl(aq) were prepared from a $\sim 0.2\,\mathrm{M}$ Gln(aq) stock solution by systematic addition of the respective salts. The densities, viscosities and electrical conductivities (Section 2.4) of the solutions are shown in Table A.20. The dielectric spectra were measured at 25 °C and at a frequency range of $0.05 \leq \nu/\mathrm{GHz} \leq 89$ (Dielectric probe kit VNA setup + E-band interferometer, Section 2.3). Due to the increasing conductivity contribution to the DR spectra with increasing electrolyte content, noisy data points at the low frequency limit had to cut away for solutions of higher salt concentrations (Section 3.1). For the present solution the effective low-frequency limit was always $\leq 0.35\,\mathrm{GHz}$.

5.4.2 Choice of Relaxation Model and Assignment of Modes

The various fits (combination of up to six HN-equations) of the DR spectra of the solutions (Figure A.52) were evaluated according to the criteria presented in Section 2.3.3. For all four sets of samples combinations of four Debye modes (D+D+D+D model) yielded the best description.* The fitting parameters are shown in Tables 5.8-5.11.
Similar to "neat" Gln(aq) solutions (Section 3.2), a slow-water process (usually located at $\sim 30 - 18\,\mathrm{ps}$) was not resolved in the DR spectra of all four sets of samples, although the Zasetsky's analysis (Figures A.53-A.56) suggested the presence of such a mode in the Gln+LiCl(aq) and Gln(aq)+NaCl(aq) spectra. However, the inclusion of an additional mode at the corresponding frequency range led to unphysical fitting parameters. Thus, this fitting model was not further pursued.
The static permittivities of all solutions decreased with increasing salt concentration (Figures A.57, A.58, A.59 and A.60). Based on their relaxation time and intensity, and the previously discussed relaxation model of binary Gln(aq) solutions (Section 3.2), the three higher frequency modes could be readily assigned to the reorientation of the Gln dipoles (mode $k = 1$) centered at $\sim 2.3\,\mathrm{GHz}$ ($\tau_1 \approx 70\,\mathrm{ps}$), and relaxations of bulk-like water (modes $k = 2, 3$) at $\sim 19\,\mathrm{ps}$ ($\tau_2 \approx 8\,\mathrm{ps}$) and at $\sim 600\,\mathrm{GHz}$ ($\tau_3(c) = \tau_3(0) = 0.278\,\mathrm{ps}$), respectively. As would be expected, the bulk-like water amplitude, S_2, decreased with increasing chloride

*Note that the raw spectra of Gln+$MgCl_2$(aq) and Gln+$CaCl_2$(aq) were corrected for the contribution of $MgCl^+$(aq) and $CaCl^+$(aq)-IPs prior to fitting (Chapter C of the Appendix).

Table 5.8: Static permittivity, ε, relaxation amplitudes, S_k, and relaxation times, τ_k of the resolved modes $k = 0 \ldots 3$, infinite-frequency permittivity, ε_∞, and value of the reduced error function, χ^2_r, obtained from the D+D+D+D model fit of dielectric spectra of Gln+LiCl(aq) at 25 °C. [a,b]

c(LiCl)	c(Gln)	ε	S_0	τ_0	S_1	τ_1	S_2	τ_2	S_3	τ_3	ε_∞	χ^2_r
0	0.1991	82.3	–	–	6.82	66.8	69.2	8.50	2.68	0.278F	3.52F	0.0676
0.05155	0.1989	82.1	1.16	721	6.84	64.9	67.7	8.35	2.78F	0.278F	3.52F	0.1043
0.1010	0.1987	81.9	1.58	598	6.81	66.2	67.4	8.34	2.56	0.278F	3.52F	0.0803
0.2012	0.1984	80.8	1.95	505	6.78	72.6	66.1	8.35	2.39	0.278F	3.52F	0.0749
0.3990	0.1976	78.8	2.32	354	6.81	72.7	63.1	8.29	3.11	0.278F	3.52F	0.1693
0.6335	0.1967	76.7	2.91	341	6.84	70F	60.0	8.26	3.50	0.278F	3.52F	0.1988

[a] c in mol L^{-1}, τ_k in ps; [b] parameter values followed by "F" were fixed during fitting.

Table 5.9: Static permittivity, ε, relaxation amplitudes, S_k, and relaxation times, τ_k of the resolved modes $k = 0 \ldots 3$, infinite-frequency permittivity, ε_∞, and value of the reduced error function, χ^2_r, obtained from the D+D+D+D model fit of dielectric spectra of Gln+NaCl(aq) at 25 °C.[a,b]

c(NaCl)	c(Gln)	ε	S_0	τ_0	S_1	τ_1	S_2	τ_2	S_3	τ_3	ε_∞	χ^2_r
0	0.1991	82.3	–	–	6.82	66.8	69.2	8.50	2.68	0.278F	3.52F	0.0676
0.05826	0.1989	82.7	1.37	719	7.08	65.2	68.0	8.31	2.75	0.278F	3.52F	0.1506
0.1136	0.1987	82.3	1.74	587	7.05	66.7	67.5	8.28	2.45	0.278F	3.52F	0.0295
0.2078	0.1983	81.3	2.02	447	6.98	69.5	66.1	8.21	2.66	0.278F	3.52F	0.0824
0.4228	0.1975	78.8	2.37	315	6.77	70F	63.7	8.07	2.39	0.278F	3.52F	0.1231
0.6287	0.1968	76.6	2.67	314	6.75	70F	60.6	8.05	3.01	0.278F	3.52F	0.1273

[a] c in mol L^{-1}, τ_k in ps; [b] parameter values followed by "F" were fixed during fitting.

Table 5.10: Static permittivity, ε, relaxation amplitudes, S_k, and relaxation times, τ_k of the resolved modes $k = 0 \ldots 3$, infinite-frequency permittivity, ε_∞, and value of the reduced error function, χ^2_r, obtained from the D+D+D+D model fit of dielectric spectra of Gln+$MgCl_2$(aq) at 25 °C. [a,b]

$c(MgCl_2)$	c(Gln)	ε	S_0	τ_0	S_1	τ_1	S_2	τ_2	S_3	τ_3	ε_∞	χ^2_r
0	0.2016	82.4	–	–	6.84	70.6	69.3	8.46	2.71	0.278F	3.52F	0.0114
0.05073	0.2004	82.4	1.96	684	6.80	72.5	67.5	8.45	2.67	0.278F	3.52F	0.0519
0.08444	0.1995	81.8	2.50	787	7.33	67.5	65.8	8.35	2.64	0.278F	3.52F	0.0772
0.1515	0.1978	79.2	3.12	669	5.95	74.2	64.0	8.39	2.67	0.278F	3.52F	0.0727
0.3089	0.1937	72.2	2.62	453	4.61	85.4	58.4	8.33	3.02	0.278F	3.52F	0.0892
0.5640	0.1867	66.7	4.99	425	4.04	84.1	50.9	8.07	3.27	0.278F	3.52F	0.1301

[a] c in mol L^{-1}, τ_k in ps; [b] parameter values followed by "F" were fixed during fitting.

Table 5.11: Static permittivity, ε, relaxation amplitudes, S_k, and relaxation times, τ_k of the resolved modes $k = 0 \ldots 3$, infinite-frequency permittivity, ε_∞, and value of the reduced error function, χ^2_r, obtained from the D+D+D+D model fit of dielectric spectra of Gln+$CaCl_2$(aq) at 25 °C. [a,b]

$c(CaCl_2)$	c(Gln)	ε	S_0	τ_0	S_1	τ_1	S_2	τ_2	S_3	τ_3	ε_∞	χ^2_r
0	0.2016	82.4	–	–	6.84	70.6	69.3	8.46	2.71	0.278F	3.52F	0.0114
0.03936	0.2012	83.9	2.83	972	7.28	71.8	67.6	8.37	2.62	0.278F	3.52F	0.1887
0.0792	0.2007	83.5	3.87	955	7.06	75.2	66.2	8.36	2.79	0.278F	3.52F	0.2083
0.1748	0.1996	78.8	3.48	500F	6.12	72.6	62.7	8.28	2.94	0.278F	3.52F	0.1090
0.3071	0.1980	73.8	3.42	459	5.21	84.0	58.7	8.15	2.88	0.278F	3.52F	0.0956
0.5357	0.1952	68.6	5.21	541	4.68	83.4	51.8	7.86	3.43	0.278F	3.52F	0.2003

[a] c in mol L^{-1}, τ_k in ps; [b] parameter values followed by "F" were fixed during fitting.

salt concentrations. Whereas the amplitude of the Gln reorienation mode, S_1, was virtually independent of salt concentration for Gln+LiCl(aq) and Gln+NaCl(aq), a decrease of S_1 with $c(MCl_2)$ could be observed for the addition of earth alkali salts (Figures A.57, A.58, A.59 and A.60).
Beyond that, an additional mode, designated as $k = 0$, appeared at $\lesssim 0.5$ GHz ($\tau_0 \gtrsim 300$ ps) upon addition of salt to the Gln(aq) solution. Its average amplitude was smaller for the solutions containing monovalent cations compared to Mg^{2+} and Ca^{2+} containing solutions and it tendencially increased in magnitude with rising salt concentrations. The mean value of its relaxation time depended on the background electrolyte but for all four chloride salts τ_0 decreased with increasing salt concentration (Figures A.57, A.58, A.59 and A.60). Given its low intensity and location in the DR spectra, mode $k = 0$ was assigned to a composite processes comprising contributions from ion-cloud relaxation and relaxation of ion-Gln-complexes for all present systems. As the IC contribution is commonly more pronounced at low ionic strengths (Section 3.1), it might explain the fast initial rise of S_0 at low c, which eventually flattens out at moderate chloride salt concentrations (Figures A.57, A.58, A.59 and A.60. Further, its argued that at least at high earth alkali salt concentrations mode $k = 0$ is mainly governed by reorientation of $M^{2+} \cdots$ Gln-species. This assumption will be used a basis for some analysis of ion binding in Gln solutions further below.

5.4.3 Effects of the Background Electrolyte

Effects of salt addition on Gln hydration. Before the ion-binding abilities of Gln will be analyzed, the impact of the variuos salts on the hydration of glutamine was examined by the evaluation of the amplitudes of the solvent-related modes ($k = 2, 3$). Using the usual approach *via* equation 1.48 and taking into account the individual solvation numbers of the added salts (see above), effective hydration numbers of Gln could be obtained (Figure 5.9).
As can be seen in Figure 5.9(b), the addition of NaCl to Gln(aq) has virtually no effect on the hydration of Gln as $Z_t \approx 6$ stays constant over the whole concentration range within the estimated error bars. For Li^+ an increase of Z_t with c(LiCl) can be observed (Figure 5.9(a)), although the error bars are rather large and thus the corresponding values should be taken with a grain of salt.
The addition of earth alkali metal salts, MCl_2 ($M = Mg^{2+}$, Ca^{2+}), reveals a markedly different picture. At $c(MCl_2) \lesssim 0.1$ M Z_t stays fairly constant at ~ 5.5. Above this threshold the hydration numbers decrease linearly down to $Z_t \approx 0$ (within their uncertainties) at $c(MCl_2) \approx 0.55$ M. As the onset of the overlap of the 1^{st}-hydration shells of the present solutes can be estimated to occur at $c(MCl_2) \approx 0.3$ M, the observed dehydration is unlikely to originate only from steric effects. On the other hand, increasing $M^{2+} \cdots$ Gln interactions, *e.g.*, $MGln^{2+}$ complex formation, could lead to an enhanced desolvation of either of the two species, which would eventually result in the observed drop in Z_t.
Ion binding in Gln solutions. The effective dipole moment of Gln in the present solutions was calculated from the amplitude of mode $k = 1$.
Analogous to the constant Z_t in Gln+NaCl(aq), μ_{eff} is practically independent of the

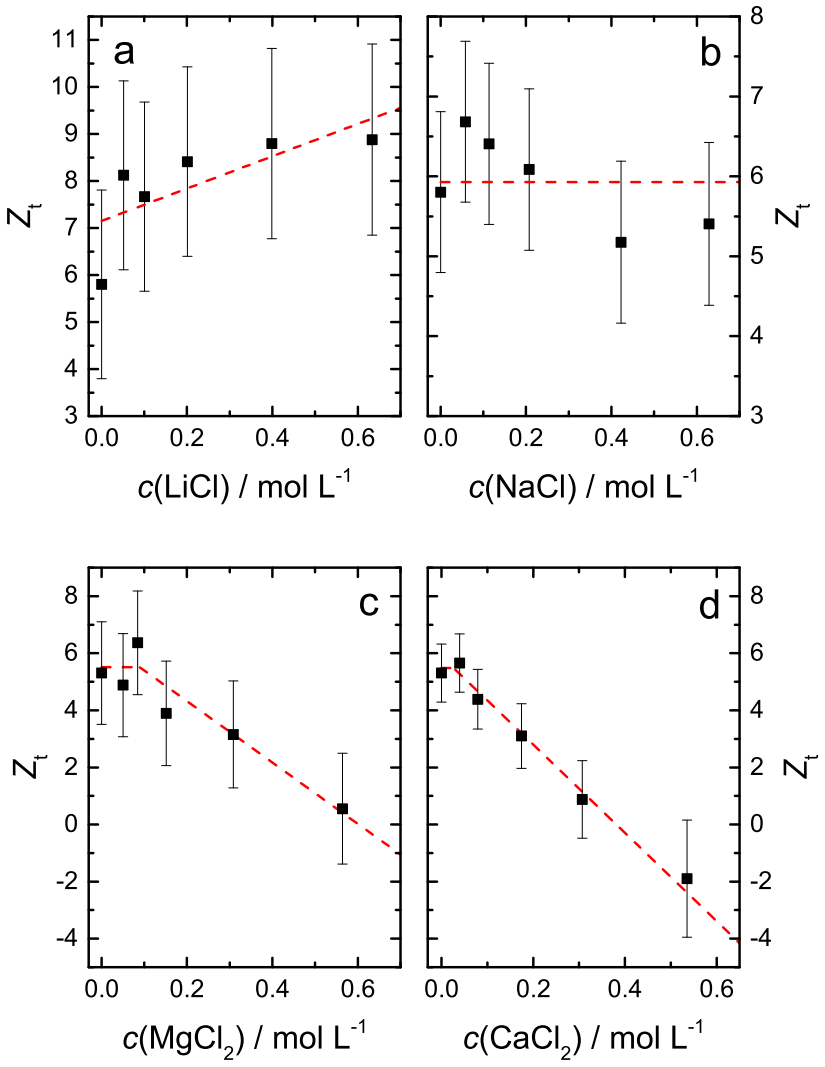

Figure 5.9: Total effective hydration number, Z_t (■) of Gln a function of the concentration of (a) LiCl, (b) NaCl, (c) $MgCl_2$ and (d) $CaCl_2$ added to ∼0.2 M Gln(aq) solutions. Dashed lines are guides to the eye.

amount of added NaCl (Figure 5.10(b)), which implies that neither sodium nor chloride ions in the present concentration range (c(NaCl) : c(Gln)≈ 3:1 at the highest concentrations) interact sufficiently with Gln so that its structure in the solution would be significantly affected.

For Gln+LiCl(aq) μ_{eff} meets the value of essentially "unperturbed" Gln dipoles at $c(\text{LiCl}) \lesssim 0.2\,\text{M}$. However, at higher concentrations (c(NaCl) : $c(Gln) > 1 : 1$) an increase can be observed. This increase is denoted only by two data points of μ_{eff}, making a quantitative analysis rather difficult (Figure 5.10(a)). Nevertheless, it implies that species with a higher effective dipole moment compared to a single Gln molecules in aqueous solution contribute significantly to mode $k = 1$. Note that the increase of Z_{t} in Gln+LiCl(aq) with rising salt concentration might be associated with the hydration of such structures, similar to the formation of $\left[\text{Li}^+ \cdots \text{H}_2\text{O} \cdots \text{Cl}^- \cdots \text{Glu}^-\right]^-$ in NaGlu+LiCl(aq) discussed further above.

The μ_{eff} values of Gln+$MgCl_2$(aq) and Gln+$CaCl_2$(aq) show different trends. Upon addition of salt, μ_{eff} stays virtually constant up to $c(\text{MCl}_2) \approx 0.1\,\text{M}$ ($c(\text{MCl}_2) : c(\text{Gln}) \approx 1 : 2$). An increase of the electrolyte concentration beyond this point results in a sudden drop of the effective dipole moment (Figure 5.10(c,d)). Similar to NaGlu+$MgCl_2$(aq) and NaGlu+$MgCl_2$(aq) in the previous section, this decrease was assigned to the formation of $\text{M}^{2+} \cdots$ Gln aggregates, which as such contribute to the low frequency mode $k = 0$ in the DR spectra. The latter assignment is supported by the estimation of relaxation times of the complexes *via* equation 1.59.[†].

Assuming that the dipolar correlations of the "unbound" Gln dipoles is essentially similar to Gln in binary glutamine solutions (Section 3.2) and that only 1:1 complexes are formed, the concentration of Gln complexes, $c(\text{MGln}^{2+})$, can be calculated from the observed μ_{eff} values. Figure 5.11 shows the obtained concentration values. Association constants, obtained from $c(\text{MGln}^{2+})$, lie in the region $\lg K_{\text{A}} \approx 0-0.3$ for MgGln^{2+} and $\lg K_{\text{A}} \approx 0$ for CaGln^{2+}, which is significantly lower than the observed formation constants of $\text{M}^{2+} \cdots \text{Glu}^-$-IPs ($\lg K^{\circ}_{\text{A}} = 1$ and $\lg K^{\circ}_{\text{A}} = 1.5$, respectively). According to this analysis, there is a somewhat higher tendency for Gln to associate with Mg^{2+} compared to Ca^{2+}. A comparison of μ_{eff}, the dipole moment of DFT-calculated structures (Figures A.61 and A.62) and the S_0 values at high c reveals that Mg^{2+} and Ca^{2+} bind preferentially to the backbone of Gln, forming $\left[\text{M}^{2+} \cdots \text{H}_2\text{O} \cdots \text{Cl}^- \cdots \text{Gln}\right]^+$ complexes, similar to the binding of Li^+ and Na^+ in Glu^- solutions (see above). However, this assignment should be treated with care as only three data points of μ_{eff} (which themselves bare relatively high uncertainties, Figure 5.10(c,d)) were used to derive the corresponding structure.

Nevertheless, the peculiar behaviour of μ_{eff} in Gln+$MgCl_2$(aq) and Gln+$CaCl_2$(aq) (Figure 5.10(c,d)) is consistent with the trends observed in Z_{t} in Figure 5.9(c,d). For the latter a similar abrupt change in its values was observed at $c(\text{MCl}_2) \approx 0.1\,\text{M}$, which supports the previously mentioned presumption that complex formation is responsible for the observed dehydration of the present solutes. Interestingly, the slope of the linear fit in at $c(\text{MgCl}_2) >$

[†]For the molecular volume of these species the volume of the low-energy conformations of $\text{M}^{2+} \cdots$ Gln aggregates (Gaussian 09 at the B3LYP/6-31G(d,p) level using the PCM solvation model) was used (Figures A.61 and A.62)

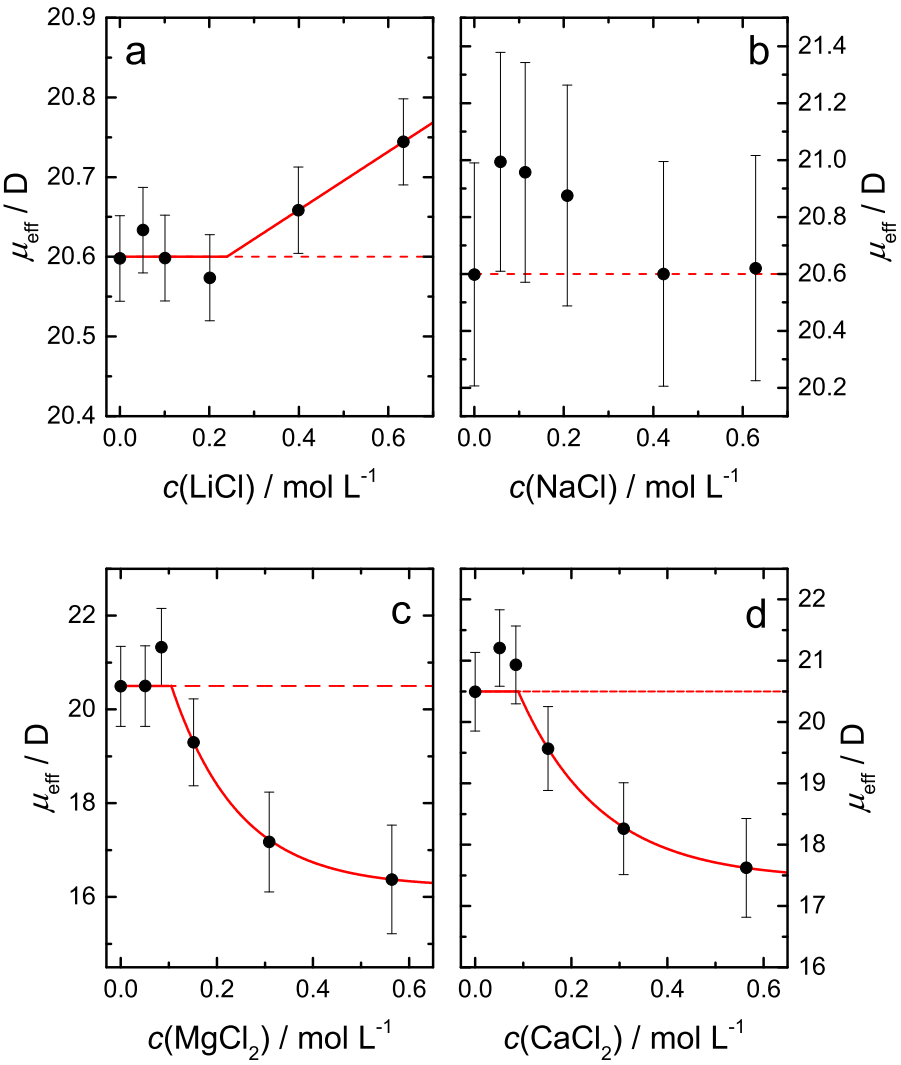

Figure 5.10: Effective dipole moment, μ_{eff} (●), of the species governing mode $k = 1$ in (a) 0.2 M Gln+LiCl(aq), (b) 0.2 M Gln+NaCl(aq), (c) 0.2 M Gln+$MgCl_2$(aq) and (d) 0.2 M Gln+$CaCl_2$(aq) solutions as a function of the concentration of added salt. The dashed line denotes the expected effective dipole moment in the case that mode $k = 1$ is due to Gln reorientation only and no IPs are formed; the solid lines in (a), (c) and (d) are guides to the eye.

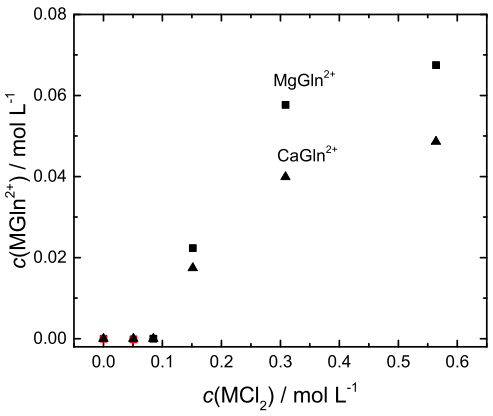

Figure 5.11: Concentration of 1:1 $M^{2+} \cdots$ Gln complexes ($M^{2+} = Mg^{2+}$ and Ca^{2+}) as a function of the salt concetration, $c(MCl_2)$, as estimated from the DR spectra of Gln+$MgCl_2$(aq) and Gln+$CaCl_2$(aq) (c(Gln) ≈ 0.2 M) at 25 °C.

0.1 M in Figure 5.9(c) is less negative than the corresponding $CaCl_2$ value (-10.8 L mol^{-1} *vs.* -15.8 L mol^{-1}) (Figure 5.9(d)), which is consistent with the slightly more labile hydration shell of Ca^{2+} as was found in Section 4.1.

5.4.4 Concluding Remarks

Dielectric spectra ($0.05 \leq \nu$/GHz ≤ 89 and at 25 °C) of ~ 0.2 M Gln(aq) solutions in the presence varying concentrations of LiCl, NaCl, $MgCl_2$ and $CaCl_2$ salts were measured and analyzed. For all four sets of samples combinations of four Debye equations provided the best fit of the complex permittivity spectra. The analysis of the solvent-related modes yielded hydration numbers of Gln in the ternary solutions, while the analysis of the Gln reorientation mode gave some information on the structure of the solutions.

It was found that in the presence of NaCl, Gln behaves essentially as in "neat" Gln(aq) solutions. The addition of LiCl led to some noticeable effects on the hydration and the effective dipole moment of Gln at high c(LiCl). However, a detailed analysis of these effects was not possible. Most likely, $Li^+ \cdots$ Gln aggregates are responsible for the observed trends in Z_t and μ_{eff} in the Gln+LiCl(aq) solutions. Studies of the Gln+LiCl(aq) system at higher concentrations and higher c(LiCl) : c(Gln) ratios would help to approve or disapprove this assumption.

For Gln+$MgCl_2$(aq) and Gln+$CaCl_2$(aq) a different picture emerged. It was argued that the observed trends in obtained effective dipole moments and hydration numbers of Gln can be interpreted as strong hits for the formation of $M^{2+} \cdots$ Gln ($M^{2+} = Mg^{2+}$ and Ca^{2+}) aggregates at $c(MCl_2) \gtrsim 0.1$ M. The concentration of these complexes were estimated under the assumption that only 1:1 species are formed. Further, it was hinted that the

present divalent cations most probably bind preferentially to the backbone of Gln, forming $\left[M^{2+}\cdots H_2O\cdots Cl^-\cdots Gln\right]^+$ species, in contrast to NaGlu+MCl_2 for which a coordination to the sidechain carboxylate was proposed further above. Apparently, for Gln(aq) the Mg^{2+} and Ca^{2+} ions are seemingly "forced" to bind to the backbone as there is no other appropriate alternative (besides, of course, not binding at all). The inclusion of a H_2O molecule and a Cl^- anion in this associate might provide some relief for the repulsive forces between the positively charged onium moiety and M^{2+}, but, all in all, the degree of this complex formation was found to be lower compared to the binding of the corresponding cations to the negatively charged sidechain of Glu^-. Unquestionably, further investigations which yield a molecular view of the solutions, such a neutron diffraction experiments, statistical mechanical calculations and MD simulations, would be helpful to complete or potentially correct the obtained picture of these ternary solutions.

Summary and Conclusion

This work reports detailed investigations of the structure and dynamics of aqueous solutions of biomolecules by the means of broadband dielectric relaxation spectroscopy (DRS). Various systems were investigated. First, binary solutions of neurotransmitters (acetylcholine chloride, carbamylcholine chloride, sodium glutamate, γ-aminobutyric acid) and chemically-related compounds (glutamine, α-aminobutyric acid, n-butylammonium chloride) were examined, which gave insight into the similarities and differences of their solvation and dynamics. Furthermore, aqueous solutions of different inorganic salts ($MgCl_2$, $CaCl_2$ and Me_4NCl) were studied. The results of the latter investigations were used to disentangle the effects of the different ions on the biomolecules in ternary solutions. Especially, these ternary systems could be regarded as a model for the situation in living organisms, where the biomolecules do not solely interact with the solvent but also with hydrated ions.

Binary Solutions of Neurotransmitters (NTs) and Chemically Related Compounds

The complex permittivity spectra at $0.05(0.01) \leq \nu/\mathrm{GHz} \leq 89$ provided unique information on the bahaviour of the investigated molecules in aqueous solution. Intensities and locations of the solvent-related relaxation modes yielded details of strength of solvation and dynamics of hydration water around the solutes. Hydration numbers could thus be obtained. In addition, the analysis of the solute relaxation processes, combined with the results of quantum chemical calculations, revealed distinctive information on specific solute-solvent and solute-solute interactions.

The evaluation of the NT reorientation modes in the solutions of acetylcholine chloride (AcChCl) and carbamylcholine chloride (CarCl) revealed a decline of the effective dipole moment of both NTs with increasing solute concentration. A comparison of the experimental values with the computed dipole moments of neurotransmitter-hydrates and the analysis of the relaxation times of the reorientation process suggested a dehydration effect to be responsible for this feature. In contrast to the spectra of AcChCl(aq), an ion pair/ion cloud composite mode could be resolved for CarCl(aq). However, as there is no theory available to separate the ion cloud contribution from the dielectric spectra, the obtained association constants of $\mathrm{Car}^+ \cdots \mathrm{Cl}^-$-ion pairs were too high compared to dilute-solution conductivity measurements. The latter indicate that IP formation is small but not negligible in aqueous

solution of NTs, with a slightly higher formation constant for CarCl compared to AcChCl. Consistent with the observed trends of the effective dipole moment, the effective numbers of slowed down (Z_s) and irrotationally-bound (Z_{ib}) H_2O molecules per equivalent of solute decreased with increasing solute concentration for both systems. A comparison between $AcCh^+$ and Car^+ revealed that the Z_{ib} values were virtually identical for both NTs, while a slightly higher number of slowed-down water dipoles could observed in the hydration sheath of Car^+. The latter was discussed to result from the replacement of the hydrophobic methyl group of $AcCh^+$ by a hydrophilic and H-bond forming -NH_2 moiety at the acyl carbon of Car^+. The evaluation of statistical mechanical 1D- and 3D-RISM calculations of AcChCl(aq) solution provided a molecular picture of the solvation of the NT. The results were in very good agreement with the DRS data. The alleged most striking structural feature of both neurotransmitters is the onium headgroup. The dehydration of this moiety prior to bonding to hydrophobic binding sites at the receptor proteins is decisive for its biological activity [145]. The dielectric results and in particular the RISM calculations showed strong features of hydrophobic hydration of the onium group in spite of its charge. The nitrogen atom is deeply buried inside a hydrophobic sheath. The calculation results indicate that water molecules in its 1^{st} hydration layer preferably interact among each other rather than with the onium group. Such a hydrophobic hydration pattern would certainly facilitate the desolvation process.

The analysis of the DR spectra of monosodium glutamate (NaGlu) and glutamine (Gln) revealed that the total amount of water molecules impeded in their dynamics around the Glu^- anion was significantly higher compared to Gln(aq). Extrapolation of the obtained hydration numbers of Glu^- to infinite dilution indicated that virtually all water molecules in the first hydration sheath are affected by the presence of the amino acid (~ 40). An increase of the solute concentration and thus increasing steric crowding leads to a rapid drop of these hydration numbers, which suggested that the hydration shell of Glu^- is rather fragile. For Gln, which was studied in a much smaller concentration range due to its solubility limit, it was found that effectively ~ 6 water dipoles were tightly bound by the hydrophilic moieties of the Gln molecule, irrespective of the concentration. No evidence for the formation of $Na^+ \cdots Glu^-$-ion pairs was found in the DR spectra of binary NaGlu(aq) solutions. The experimental effective dipole moments of Glu^- and Gln were found to be strongly governed by dipolar solute-solvent and solute-solute correlations. In particularly, the presence of the latter correlations was consistent with the literature on aqueous Gln solutions. It was pointed out that Gln zwitterions or as constituents of proteins are infamous for their tendency to form Gln$\cdots$Gln associates, which are currently linked to various degenerative human diseases. In hand with the comparably small amount of hydration water, the solvation sheath of Gln was discussed to be unable to suppress the pronounced propensity of Gln towards aggregation, although the DRS results suggested that no long-lived, but rather short-lived, Gln$\cdots$Gln aggregates are formed in solution.

The complex permittivity spectra of the NT γ-aminobutyric acid (GABA) and its isomer α-aminobutyric acid (AABA) allowed an investigation of the differing position of the onium group on their properties in solution. Significantly higher Z_{ib} values were observed for AABA(aq) and the trends of Z_s were crucially different for both amino acids, while the

total hydration numbers at infinite dilution were comparable for both zwitterions. These discrepancies were discussed to be linked to the different locations of the onium moiety and the associated effects on the hydration structure and dynamics. The obtained effective dipole moments of GABA(aq) and AABA(aq) were found to decrease with increasing solute concentration for both molecules. Consistent with the observed hydration numbers, this decline was argued to be associated with the gradual loss of hydrating water dipoles at the zwitterions with increasing concentration. It was found that the solvation structure of GABA(aq) could be fairly well modeled by considering the hydration characteristics of the individual functional groups (-COO^-, -NH_3^+), while the close location of the charged groups at AABA prohibited such a simplified approach. It was concluded that the dissimilar bioaction of GABA and AABA is not simply linked to the different spatial structures, in terms of molecular recognition, but there a also marked differences regarding their interaction with the surrounding medium, *i.e.*, water, which emphasizes the necessity to consider these interactions when discussing the biological behaviour of any biomolecule.

Inorganic Salt Solutions

The evaluation of the DR spectra of $MgCl_2$(aq), $CaCl_2$(aq) and Me_4NCl(aq) at $0.05 \leq \nu/\mathrm{GHz} \leq 89$ and 25 °C yielded hydration numbers of the individual ions and information on their tendency for association into ion-pairs (IPs).
It was established that both Mg^{2+} and Ca^{2+} are strongly hydrated, with each possessing two well-defined hydration shells. Evidence for a somewhat weaker hydration of Ca^{2+} compared to Mg^{2+} were found. The two solute-dependent modes at low frequencies in the dielectric spectra of $MgCl_2$(aq) and $CaCl_2$(aq) were assigned to the formation of IPs in these classical strong electrolyte solutions. Detailed analysis of these modes indicated that they could be assigned to double-solvent-separated and solvent-shared IPs, with no evidence for the formation of contact IPs, which was consistent with the strong hydration of the two cations. The overall IP association constants calculated from the DR spectra were in good agreement with literature data.
The analysis of the solvent related modes in the permittivity spectra of Me_4NCl(aq) revealed that effectively ~ 6 water molecules are dynamically impeded in the apolar hydration sheath of the Me_4N^+ cation. As would be expected from the low charge density of the TMA cation, practically no irrotationally bound water could be observed. The evaluation of the low-frequency solute mode showed that the degree of $Me_4N^+ \cdots Cl^-$-ion pair formation is low, but still detectable. Solvent-shared IPs were discussed to be the predominant species responsible for this IP relaxation process. The obtained association constants were in good agreement with literature values. No indications for cation-cation aggregation of Me_4N^+, which was reported for higher tetraalkylammonium homologues [22, 343, 359], could be detected in the DR spectra.

Effects of Salts on the NTs

To investigate the rather specific effect of ions on the solutions of the small biomolecules,

ternary systems involving different combinations of inorganic salts and biomolecules at varying inorganic salt : biomolecule ratios were studied with the help of DRS.

The analysis of the solvent-related relaxation modes in the dielectric spectra of AcChCl+KCl(aq) and AcChCl+KF(aq) showed that the addition of KCl as well as KF to AcChCl(aq) leads to a fast dehydration of the NT. Furthermore, changes in the overall hydration dynamics of water molecules, most likely associated with F^-, could be observed as the ratio KF : $AcCh^+$ increased. Unfortunately, the origin of this effect could not be found by DRS, which thus might be an interesting feature to take up in future studies of these systems. No separate IP relaxation mode could be resolved in the DR spectra of both sets of samples. A quantitative analysis of the $AcCh^+$ reorientation mode was hampered by the scatter of the data, but, in particularly for AcChCl+KCl(aq), some indications of possible IP formation were found.

Major differences between the addition of monovalent and divalent cations to a $\sim 0.4\,\mathrm{M}$ NaGlu(aq) solution could be observed in the corresponding DR spectra. While for NaGlu+$MgCl_2$(aq) and NaGlu+$CaCl_2$(aq) an IP relaxation mode was discernible, no separate IP process could be resolved in the complex permittivity spectra of NaGlu+LiCl(aq) and NaGlu+NaCl(aq). Nevertheless, the trends in the amplitude of the Glu^- reorientation mode were argued to be linked to the presence of Li^+/Na^+-Glu^--ion associates. A detailed analysis suggested that ion aggregates of the form $\left[M^+\cdots H_2O\cdots Cl^-\cdots Glu^-\right]^-$, where the cation *and* the chloride anion are simultaneously bound to the backbone, might be present in the solutions. In contrast, the evaluation of the IP mode in NaGlu+$MgCl_2$(aq) and NaGlu+$CaCl_2$(aq) revealed that ion-pairs with Mg^{2+} and Ca^{2+} directly bound to the sidechain carboxylate group are the most likely species to be formed and the corresponding association constants were obtained. The observed increase of Z_s with rising inorganic salt concentration in NaGlu+LiCl(aq) and NaGlu+NaCl(aq) was argued to be linked to the hydration of the quadrupolar $\left[M^+\cdots H_2O\cdots Cl^-\cdots Glu^-\right]^-$ species. Additionally, the trend of the Z_ib values of Glu^- in NaGlu+$CaCl_2$(aq) yielded slight indications for the presence of higher order aggregates.

The systems studied at last were ternary solutions involving Gln. The interpretation of the dielectric spectra indicated that the solvated Gln molecules are essentially unperturbed by the presence of NaCl. On the other hand, the addition of LiCl led to some noticeable effects on the hydration and the effective dipole moment of Gln at high c(LiCl). However, a detailed analysis of these effects was not feasible. Formation of $Li^+\cdots$Gln aggregates might be responsible for the observed effects in the Gln+LiCl(aq) system. This issue could possibly be addressed by studies at higher c(LiCl) : c(Gln) ratios. For Gln+$MgCl_2$(aq) and Gln+$CaCl_2$(aq) a different picture emerged. The observed decreasing behaviour of the effective dipole moments and hydration numbers of Gln were interpreted as strong indications for the formation of $M^{2+}\cdots$Gln ($M^{2+} = Mg^{2+}$ and Ca^{2+}) aggregates. Concentrations of these complexes were estimated under the assumption that only 1:1 species are formed. Interestingly, comparisons with quantum chemical calculations hinted that the present divalent cations most probably bind preferentially to the backbone of Gln, forming $\left[M^{2+}\cdots H_2O\cdots Cl^-\cdots Gln\right]^+$ associates, in contrast to NaGlu+MCl_2 for which a coordi-

nation to the side-chain -COO^- was proposed (see above). It seems that for Gln(aq) the M^{2+} ions coordinate to the backbone as there is no better alternative. The inclusion of a H_2O molecule and a Cl^- anion in this aggregate might diminish for the repulsive forces between the positively charged onium moiety and M^{2+}, but, all in all, the extent of this complex formation was still lower compared to the binding of the corresponding cations to the negatively charged side-chain of Glu^-.

It should be pointed out that the analysis of the solute-related relaxation modes in the DR spectra of the ternary systems was only feasible under certain assumptions. Probably the most crude assumption involves the dipolar correlations between the biomolecules and the neigbouring dipoles. Such correlations are very significant for the structure of aqueous biomolecule solutions, as indicated by the DR spectra of the binary systems. In the study of ternary solutions these were partly neglected or at least assumed to be of the same magnitude as in binary solutions, which, however, is in principal not guaranteed. This issue emphasizes the multifaceted and complex character of solvation and ion-specific phenomena, as mentioned in the introduction of this thesis. Knowing how a solute, *e.g.* biomolecule, behaves in a binary solution is certainly useful to understand some of its fundamental characteristics. However, the presence of other molecules or ions might have sever effects on its properties (and *vice versa*). This could clearly be observed in present ternary systems. Note that situation is even more complex in real biological systems, where numerous solvated ions and other solutes might interact with the biomolecule.
Nevertheless, some consistent trends and coherent pictures could be obtained for the studied systems in this work and although there is still a long way to go to fully understand how certain media affect specific solute properties, this study provides a foundation for future investigations of these putative “basic” phenomena.

Appendix A

Supplemantary Measurement & Dielectric Relaxation Data

A.1 Acetylcholine Chloride and Carbamylcholine Chloride

Table A.1: Molar concentrations, c, densities, ρ, viscosities, η, conductivities, κ, and their respective uncertainties, $\Delta\eta$ and $\Delta\kappa$, of the AcChCl(aq) solutions at 25 °C.

c / mol L^{-1}	ρ / g cm^{-3}	η / mPa s	$\Delta\eta$ / mPa s	κ / S m^{-1}	$\Delta\kappa$ / S m^{-1}
0.07496	0.998909	0.892	0.001	0.678	0.001
0.1501	1.000727	0.916	0.001	1.258	0.004
0.2005	1.002032	0.930	0.001	1.634	0.006
0.2510	1.003329	0.945	0.001	1.985	0.008
0.3013	1.004541	0.961	0.001	2.28	0.01
0.3521	1.005877	0.979	0.001	2.643	0.004
0.4027	1.007076	0.994	0.001	2.906	0.005
0.4538	1.00836	1.014	0.002	3.181	0.006
0.5334	1.010349	1.045	0.002	3.604	0.007

Table A.2: Molar concentrations, c, densities, ρ, viscosities, η, conductivities, κ, and their respective uncertainties, $\Delta\eta$ and $\Delta\kappa$, of the $b = 0.2621\,\mathrm{mol\,kg^{-1}}$ and $b = 0.3738\,\mathrm{mol\,kg^{-1}}$ AcChCl(aq) solutions as function of temperature, ϑ.

ϑ / °C	c / mol L^{-1}	ρ / g cm^{-3}	η / mPa s	$\Delta\eta$ / mPa s	κ / S m^{-1}	$\Delta\kappa$ / S m^{-1}
$b = 0.2621\,\mathrm{mol\,kg^{-1}}$						
5	0.2519	1.007031	1.619	0.003	1.209	0.005
15	0.2516	1.005712	1.2117	0.0009	1.581	0.007
25	0.2510	1.003329	0.9445	0.0008	1.985	0.008
35	0.2502	1.000074	0.7648	0.0008	2.42	0.01
45	0.2492	0.996078	0.6294	0.0006	2.87	0.01
55	0.2480	0.991433	0.532	0.003	3.33	0.01
65	0.2467	0.986216	0.454	0.004	3.80	0.02
$b = 0.3738\,\mathrm{mol\,kg^{-1}}$						
5	0.3535	1.009894	1.681	0.002	1.599	0.003
15	0.3530	1.008394	1.257	0.001	2.098	0.004
25	0.3521	1.005877	0.979	0.001	2.643	0.004
35	0.3510	1.002525	0.7918	0.0008	3.218	0.006
45	0.3495	0.998456	0.6529	0.0007	3.815	0.006
55	0.3479	0.993762	0.552	0.005	4.427	0.007
65	0.3460	0.988512	0.48	0.02	5.049	0.008

Table A.3: Molar concentrations, c, densities, ρ, viscosities, η, conductivities, κ, and their respective uncertainties, $\Delta\eta$ and $\Delta\kappa$, of the CarCl(aq) solutions at 25 °C.

c / mol L^{-1}	ρ / g cm^{-3}	η / mPa s	$\Delta\eta$ / mPa s	κ / S m^{-1}	$\Delta\kappa$ / S m^{-1}
0.07434	0.999766	0.9106	0.0005	0.661	0.001
0.1567	1.002620	0.9236	0.0004	1.277	0.003
0.2004	1.004150	0.9349	0.0006	1.573	0.005
0.2459	1.005762	0.9458	0.0005	1.927	0.003
0.3193	1.008322	0.9650	0.0007	2.394	0.004
0.3524	1.009483	0.9735	0.0008	2.774	0.006
0.4037	1.011262	0.9846	0.0009	3.090	0.007
0.4985	1.014588	1.039	0.004	3.682	0.008
0.8338	1.026270	1.131	0.002	5.36	0.01

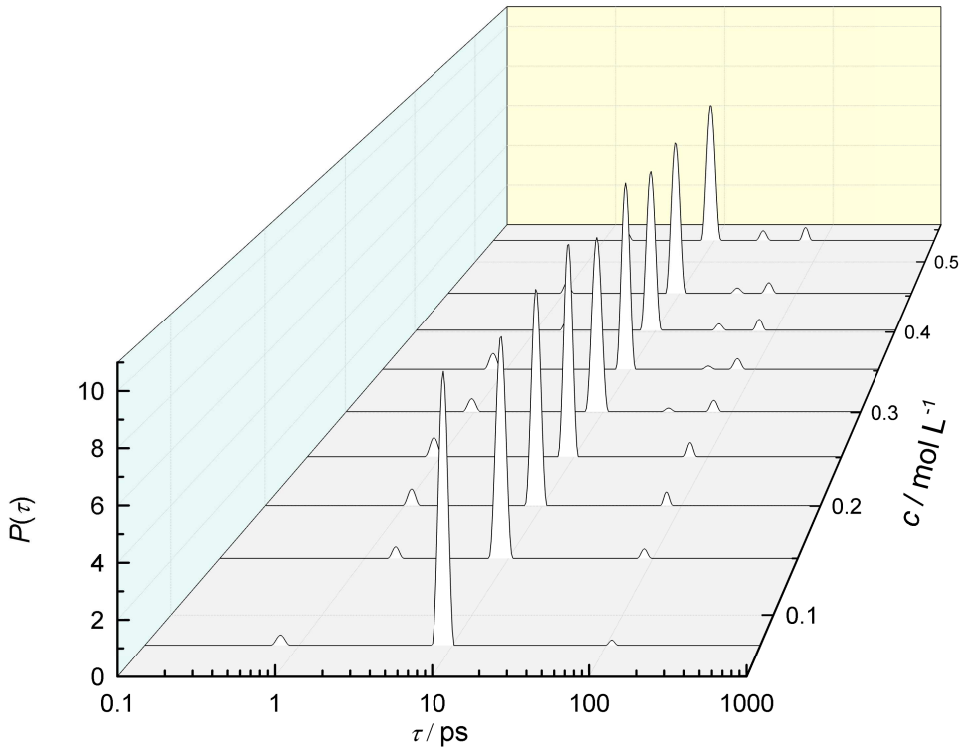

Figure A.1: Relaxation-time distribution, $P(t)$, of dielectric data of AcChCl(aq) solutions at 25 °C, obtained *via* Zasetsky's computational procedure [114].

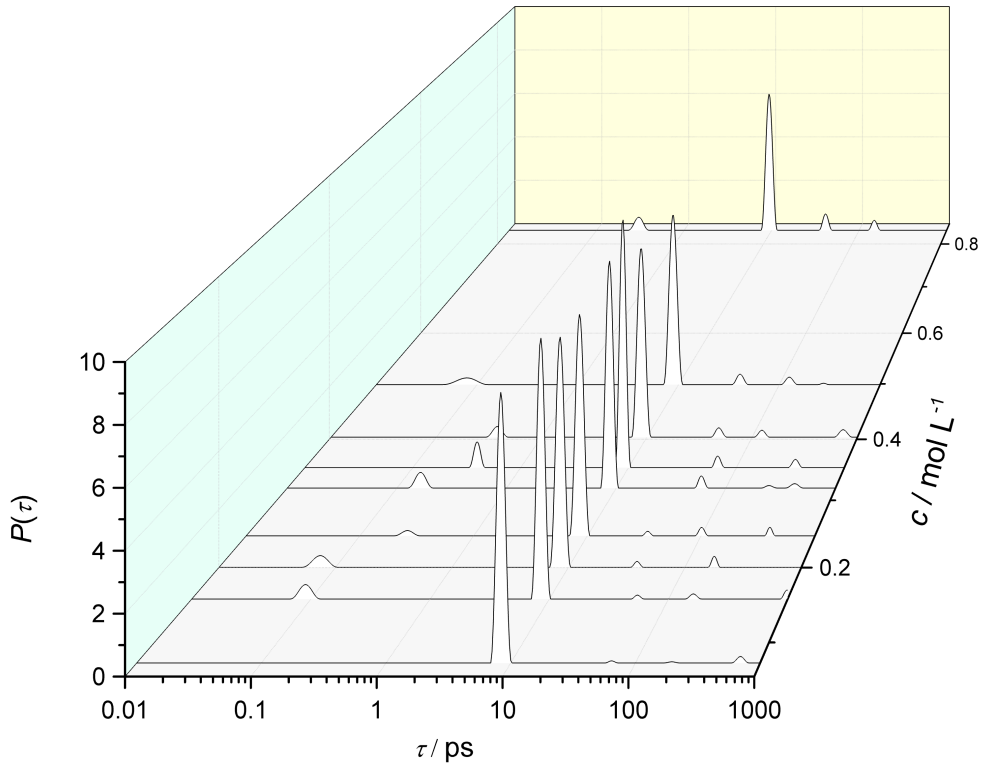

Figure A.2: Relaxation-time distribution, $P(t)$, of dielectric data of CarCl(aq) solutions at 25 °C, obtained *via* Zasetsky's computational procedure [114].

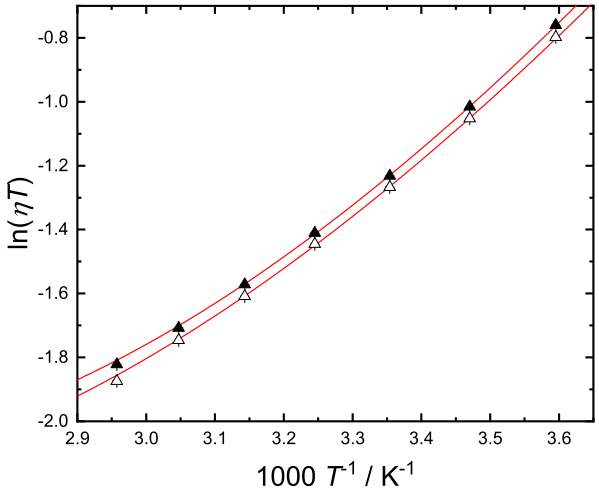

Figure A.3: Plots of $\ln(\eta T)$ *vs* $1000/T$ for $0.2621\,\mathrm{mol\,kg^{-1}}$ (△) and $0.3738\,\mathrm{mol\,kg^{-1}}$ (▲) AcChCl(aq). Lines denote the fits to the (extended) Eyring equation.

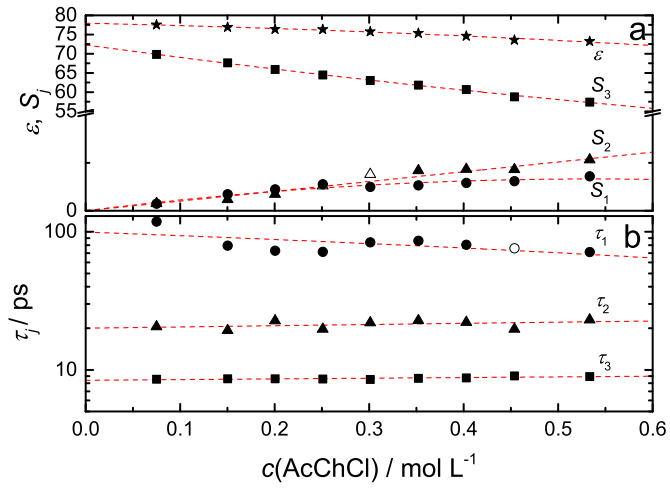

Figure A.4: (a) Static permittivities, ε(★), and relaxation amplitudes, S_1(●), S_2(▲), S_3(■), and (b) the respective relaxation times, τ_1(●), τ_2(▲), τ_3(■), of the AcChCl(aq) solutions at 25 °C as a function of solute concentration, c(AcChCl). The dashed lines are guides to the eye. Hollow symbols denote parameters which were fixed during fitting of the dielectric spectra. Parameters of fast-water mode 4 are not shown for the sake of calarity.

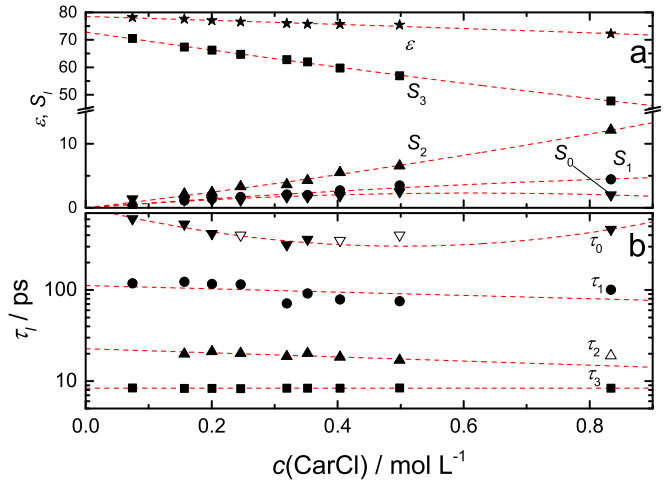

Figure A.5: (a) Static permittivities, $\varepsilon(\bigstar)$, and relaxation amplitudes, $S_0(\blacktriangledown), S_1(\bullet), S_2(\blacktriangle), S_3(\blacksquare)$, and (b) the respective relaxation times, $\tau_0(\blacktriangledown), \tau_1(\bullet), \tau_2(\blacktriangle), \tau_3(\blacksquare)$, of the CarCl(aq) solutions at 25 °C as a function of solute concentration, c(CarCl). The dashed lines are guides to the eye. Hollow symbols denote parameters which were fixed during fitting of the dielectric spectra.

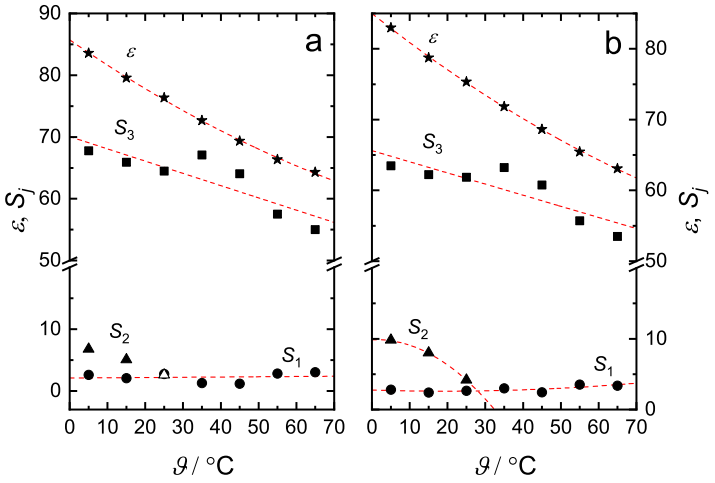

Figure A.6: Static permittivities, $\varepsilon(\bigstar)$, and relaxation amplitudes, $S_1(\bullet), S_2(\blacktriangle), S_3(\blacksquare)$, of (a) 0.2621 mol kg^{-1} and (b) 0.3738 mol kg^{-1} AcChCl(aq) as a function of ϑ. The dashed lines are guides to the eye. Hollow symbols denote fixing during fitting of the dielectric spectra. Parameters of fast-water mode 4 are not shown for the sake of calarity.

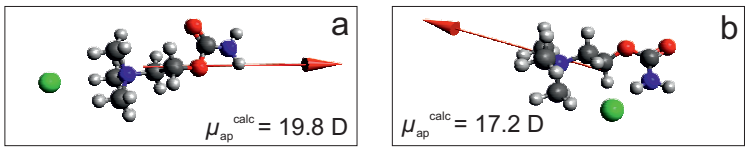

Figure A.7: Lowest-energy structures of two different kinds of contact ion pairs of carbamylcholine and chloride as obtained by Gaussian 09 at the B3LYP/6-31G(d,p) level using the PCM solvation model. Blue: nitrogen, red: oxygen, dark-gray: carbon, light-gray: hydrogen, green: chloride. The arrows indicate the dipole moments.

Table A.4: Limiting molar conductivities, Λ_0, and infinite dilution IP formation constants, K_A°, of AcChCl(aq) obtained from dilute-solution electrical conductivity measurements [149].

ϑ / °C	Λ_0 / S cm^2 mol^{-1}	K_A° / M^{-1}	lgK_A°
5	68.813	2.96	0.471
10	78.865	2.85	0.455
15	89.381	2.74	0.438
20	100.35	2.65	0.424
25	111.635	2.46	0.391
30	123.236	2.17	0.336
35	134.971	1.70	0.230
40	146.582	1.96	0.291

Table A.5: Limiting molar conductivities, Λ_0, and infinite dilution IP formation constants, K_A°, of CarCl(aq) obtained from dilute-solution electrical conductivity measurements [149].

ϑ / °C	Λ_0 / S cm^2 mol^{-1}	K_A° / M^{-1}	lgK_A°
5	68.593	3.63	0.560
10	78.587	3.49	0.542
15	89.034	3.32	0.521
20	99.963	3.26	0.513
25	111.166	2.93	0.467
30	122.745	2.67	0.427
35	134.646	2.58	0.412
40	146.673	3.51	0.545

Table A.6: Structural parameters of $AcCh^+$ (*trans, gauche* and *trans, trans* conformer) and Cl^- hydration in aqueous solution at infinite dilution (inf) and 0.53 M and under ambient conditions. The differences between the two conformations is given as $|\Delta|$. The location of the first maximum of the PDFs (in Å) is denoted as r_{M1} [148].

structural parameters	c(AcChCl) / mol L^{-1}					
	inf			0.53		
	trans, gauche	*trans, trans*	$\|\Delta\|$	*trans, gauche*	*trans, trans*	$\|\Delta\|$
-N$^+$Me$_3$						
$g_{NOw}(r_{M1})$	1.53 (0.428)	1.54 (0.430)	0.01 (0.002)	1.54 (0.428)	1.54 (0.430)	0 (0.002)
$g_{Cm2Ow}(r_{M1})$	1.51 (0.312)	1.58 (0.310)	0.07 (0.002)	1.52 (0.312)	1.60 (0.310)	0.08 (0.002)
n_{Cm2Ow}	5.88	5.94	0.06	5.42	5.47	0.05
$g_{Hm2Ow}(r_{M1})$	0.78-1.07 (0.230-0.242)	1.00-1.06 (0.233-0.235)	0.22-0.01 (0.003-0.007)	0.79-1.09 (0.230-0.240)	1.02 -1.08 (0.233-0.235)	0.23-0.01 (0.003-0.005)
CH$_2$ (Cb1 and Cb2)						
$g_{Cb1Ow}(r_{M1})$	1.24 (0.342)	1.20 (0.342)	0.04 (0)	1.25 (0.340)	1.22 (0.340)	0.03 (0)
n_{Cb1Ow}	10.43	10.42	0.01	9.6	9.59	0.01
$g_{Hb1Ow}(r_{M1})$	1.02 (0.250)	1.06 (0.250)	0.04 (0)	1.04 (0.250)	1.08 (0.250)	0.04 (0)
$g_{Cb2Ow}(r_{M1})$	1.15 (0.312)	1.12 (0.315)	0.03 (0.003)	1.17 (0.312)	1.14 (0.315)	0.03 (0.003)
n_{Cb2Ow}	4.09	3.93	0.16	3.79	3.73	0.06
$g_{Hb2Ow}(r_{M1})$	1.09 (0.233)	1.03 (0.233)	0.06 (0)	1.11 (0.233)	1.05 (0.233)	0.06 (0)
CH$_3$ (Cm1)						
$g_{Cm1Ow}(r_{M1})$	1.53 (0.340)	1.49 (0.340)	0.04 (0)	1.55 (0.338)	1.51 (0.340)	0.04 (0.002)
n_{Cm1Ow}	12.93	12.19	0.74	11.94	11.27	0.67
$g_{Hm1Ow}(r_{M1})$	1.19 (0.267)	1.19 (0.267)	0 (0)	1.21 (0.267)	1.20 (0.267)	0.01 (0)
C=O						
$g_{O2Ow}(r_{M1})$	1.74 (0.297)	1.74 (0.297)	0 (0)	1.76 (0.297)	1.75 (0.297)	0.01 (0)
n_{O2Ow}	6.46	6.36	0.1	5.99	5.99	0
$g_{O2Hw}(r_{M1})$	1.41 (0.175)	1.42 (0.175)	0.01 (0)	1.46 (0.175)	1.47 (0.175)	0.01 (0)
n_{O2Hw}	1.74	1.7	0.04	1.64	1.61	0.03
-O- (O7)						
$g_{O7Ow}(r_{M1})$	0.90 (0.305)	1.14 (0.305)	0.24 (0)	0.91 (0.305)	1.14 (0.305)	0.23 (0)
n_{O7Ow}	3.14	4.2	1.06	2.9	3.88	0.98
$g_{O7Hw}(r_{M1})$	0.25 (0.185)	0.40 (0.180)	0.15 (0.005)	0.26 (0.185)	0.41 (0.180)	0.15 (0.005)
n_{O7Hw}	0.39	0.6	0.21	0.36	0.56	0.2
n_t	**30.1**	**31.9**	**1.8**			
Cl$^-$						
$g_{ClHw}(r_{M1})$	2.40 (0.220)	2.40 (0.220)	0 (0)	2.50 (0.220)	2.49 (0.220)	0.01 (0)
n_{ClHw}	5.92	5.92	0	5.63	5.62	0.01

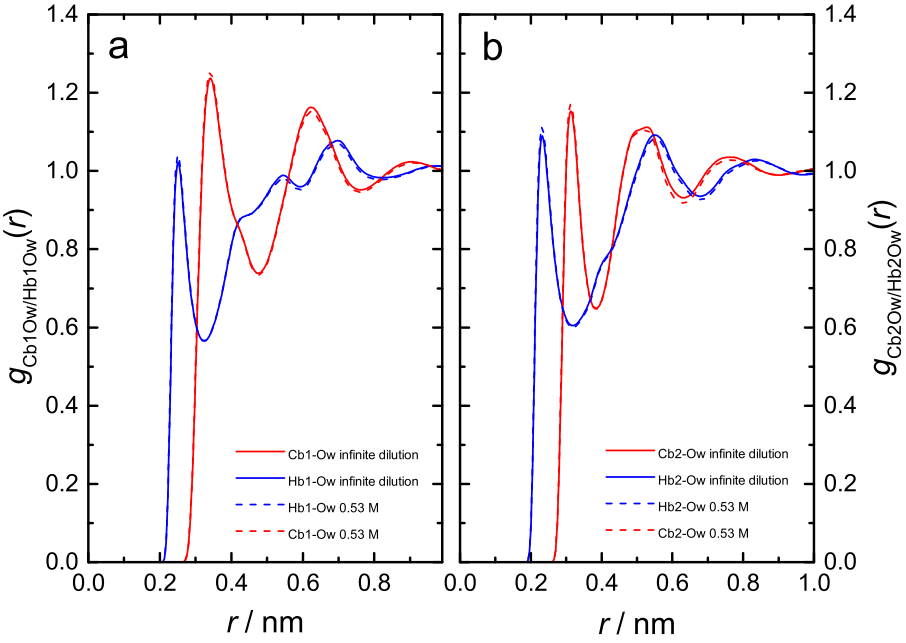

Figure A.8: PDFs (a) g_{Cb1Ow}, g_{Hb1Ow} and (b) g_{Cb2Ow}, g_{Hb2Ow} for the *trans, gauche* conformer of AcCh in aqueous solution at infinite dilution and the highest concentration of 0.53 M.

A.2 Sodium Glutamate and Glutamine

Table A.7: Molar concentrations, c, densities, ρ, viscosities, η, the respective uncertainties, $\Delta\eta$ and $\Delta\kappa$, and the pH of the NaGlu solutions at 25 °C.

c / mol L^{-1}	ρ / g cm^{-3}	η / mPa s	$\Delta\eta$ / mPa s	κ / S m^{-1}	$\Delta\kappa$ / S m^{-1}	pH
0.206	1.014738	0.9921	0.0004	1.087	0.002	6.9
0.406	1.031564	1.112	0.001	1.885	0.007	–
0.601	1.047664	1.239	0.001	2.47	0.01	–
0.783	1.062868	1.397	0.002	2.93	0.01	–
0.965	1.074612	1.556	0.002	3.29	0.01	–
1.14	1.090961	1.738	0.002	3.563	0.006	–
1.30	1.103343	1.943	0.002	3.722	0.007	–
1.44	1.115383	2.166	0.002	3.847	0.007	–
1.60	1.128067	2.454	0.003	3.898	0.007	–
1.75	1.140130	2.715	0.006	3.88	0.01	–
1.90	1.150388	3.058	0.006	3.909	0.007	6.7

Table A.8: pH, molar concentrations, c, densities, ρ, viscosities, η, and the respective uncertainties, $\Delta\eta$ and $\Delta\kappa$, of the HGlu+NaOH/HCl solutions at 25 °C.

pH	c_0(HGlu) / mol L^{-1}	c(NaOH) / mol L^{-1}	c(HCl) / mol L^{-1}	ρ / g cm^{-3}	η / mPa s	$\Delta\eta$ / mPa s	κ / S m^{-1}	$\Delta\kappa$ / S m^{-1}
1.6	0.06132	–	0.09802	1.001999	0.9120	0.0005	2.224	0.009
3.1	0.05964	–	–	1.000512	0.9081	0.0004	0.0431	0.0001
4.2	0.05928	0.03027	–	1.001498	0.9180	0.0009	0.2148	0.0007
10.9	0.05869	0.08221	–	1.003762	0.9332	0.0006	0.852	0.001
12.6	0.05848	0.1484	–	1.009615	0.9593	0.0006	3.521	0.015

Table A.9: Molar concentrations, c, densities, ρ, viscosities, η, the respective uncertainties, $\Delta\eta$, and the pH of the Gln(aq) solutions at 25 °C.

c / mol L^{-1}	ρ / g cm^{-3}	η / mPa s	$\Delta\eta$ / mPa s	pH
0.04758	0.999593	0.9044	0.0007	5.9
0.1092	1.002829	0.9222	0.0005	–
0.1716	1.006102	0.9413	0.0005	–
0.1878	1.007166	0.9487	0.0005	–
0.2166	1.008442	0.9567	0.0008	–
0.2310	1.009197	0.9598	0.0005	6.1

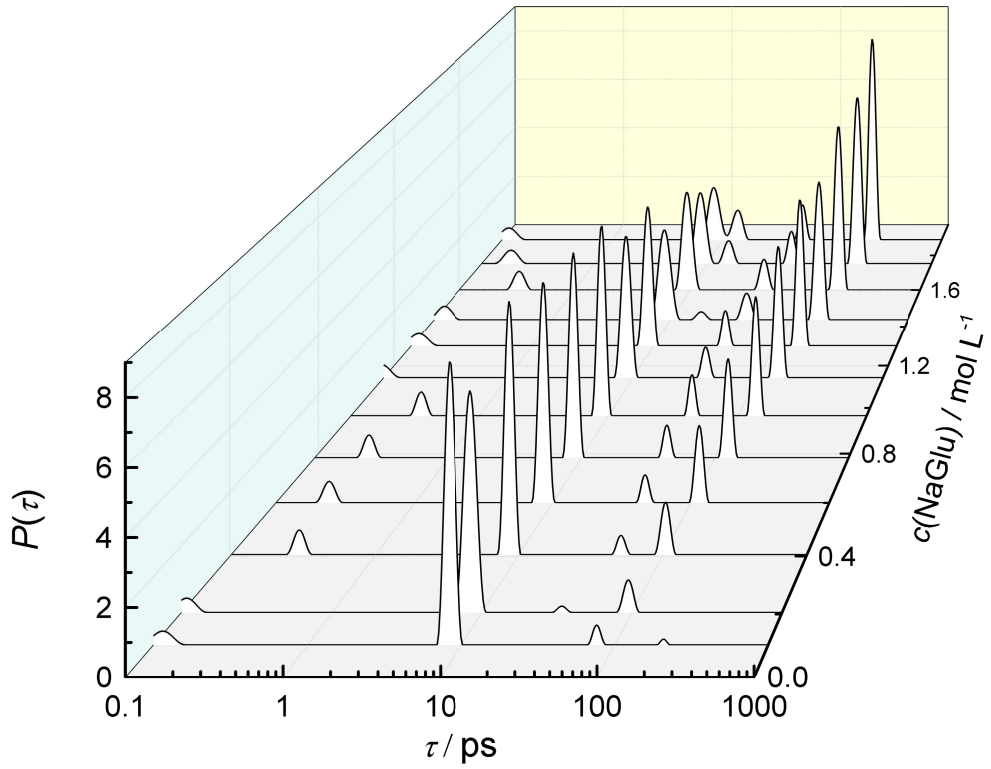

Figure A.9: Relaxation-time distribution, $P(\tau)$, of dielectric data for NaGlu(aq) at 25 °C, obtained *via* Zasetsky's computational procedure [114].

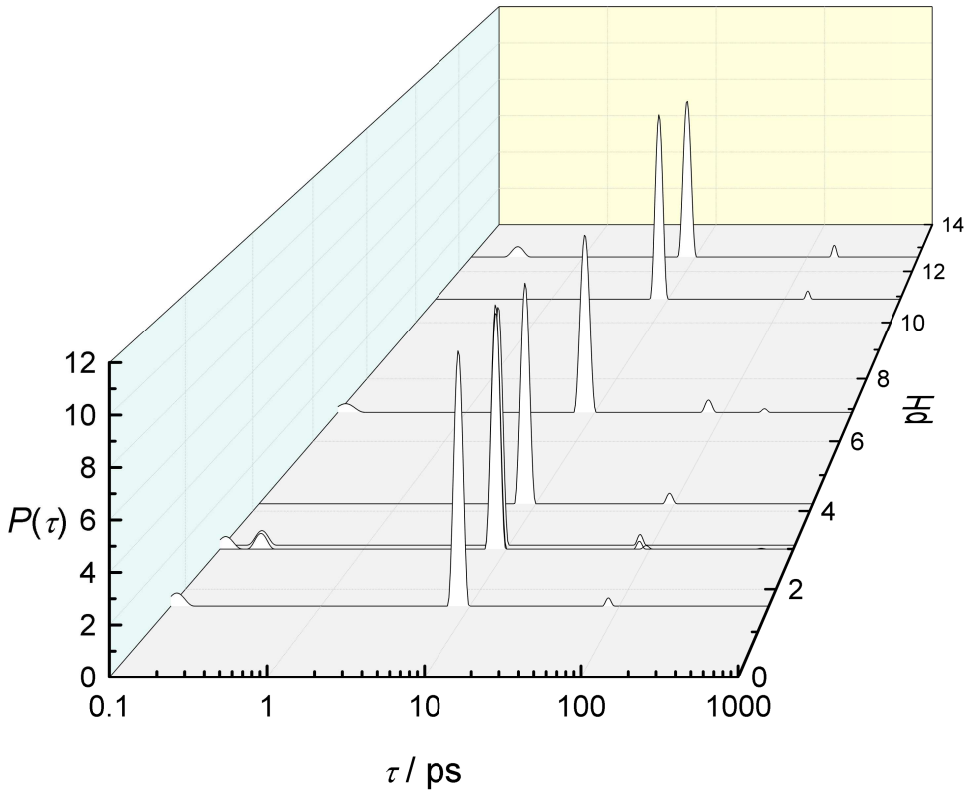

Figure A.10: Relaxation-time distribution, $P(\tau)$, of dielectric data for HGlu(aq) at 25 °C and different pH-values, obtained *via* Zasetsky's computational procedure [114].

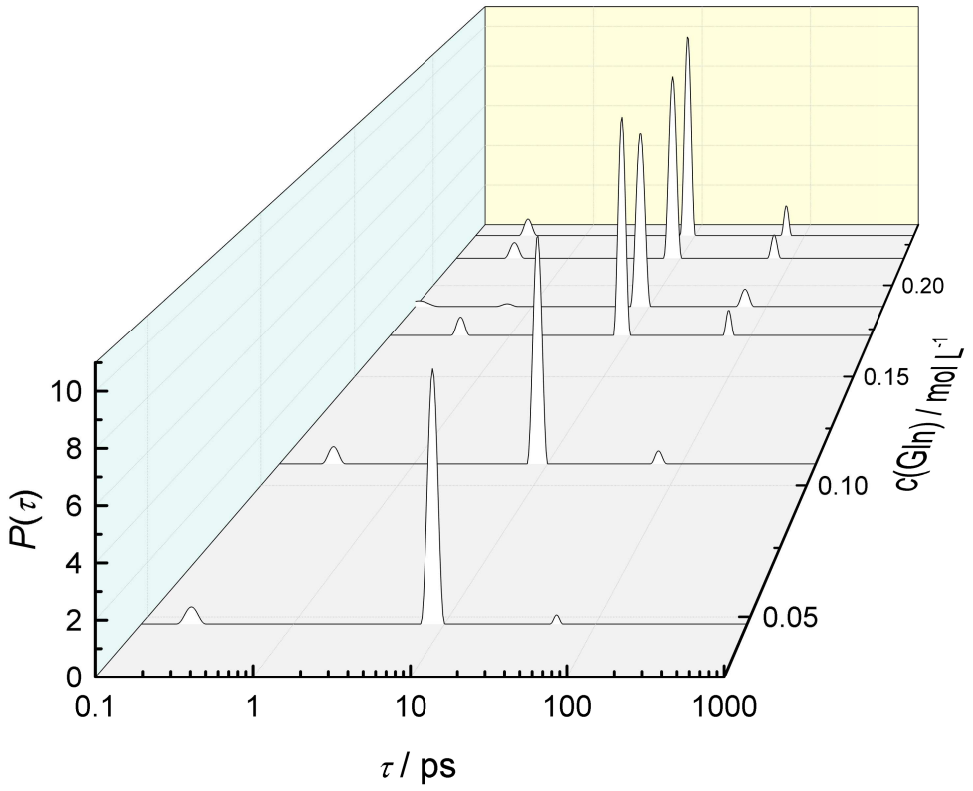

Figure A.11: Relaxation-time distribution, $P(\tau)$, of dielectric data for Gln(aq) at 25 °C, obtained *via* Zasetsky's computational procedure [114].

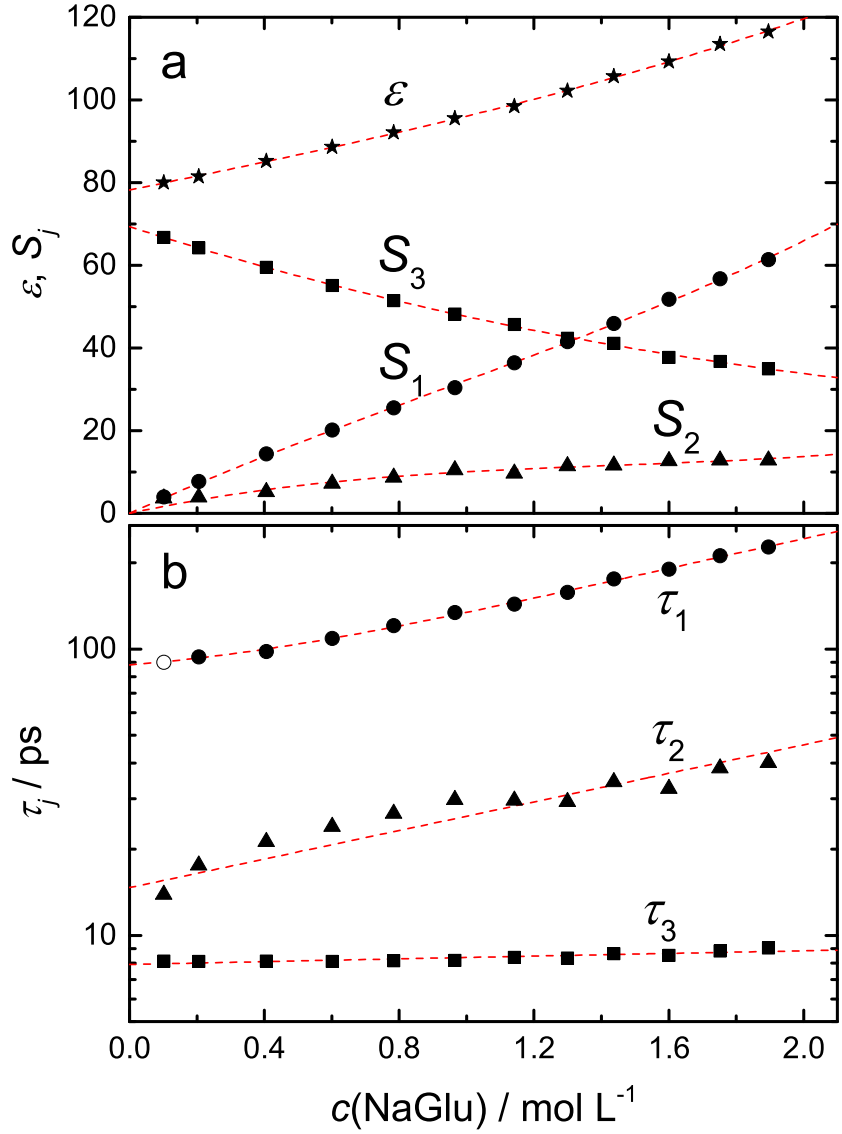

Figure A.12: (a) Static permittivities, $\varepsilon(\bigstar)$, and relaxation amplitudes, $S_1(\bullet), S_2(\blacktriangle), S_3(\blacksquare)$, and (b) the respective relaxation times, $\tau_1(\bullet), \tau_2(\blacktriangle), \tau_3(\blacksquare)$, of the NaGlu(aq) solutions at 25 °C as a function of solute concentration, c(NaGlu). The dashed lines are guides to the eye and were obtained from empirical fits. Hollow symbols denote parameters which were fixed during fitting of the dielectric spectra.

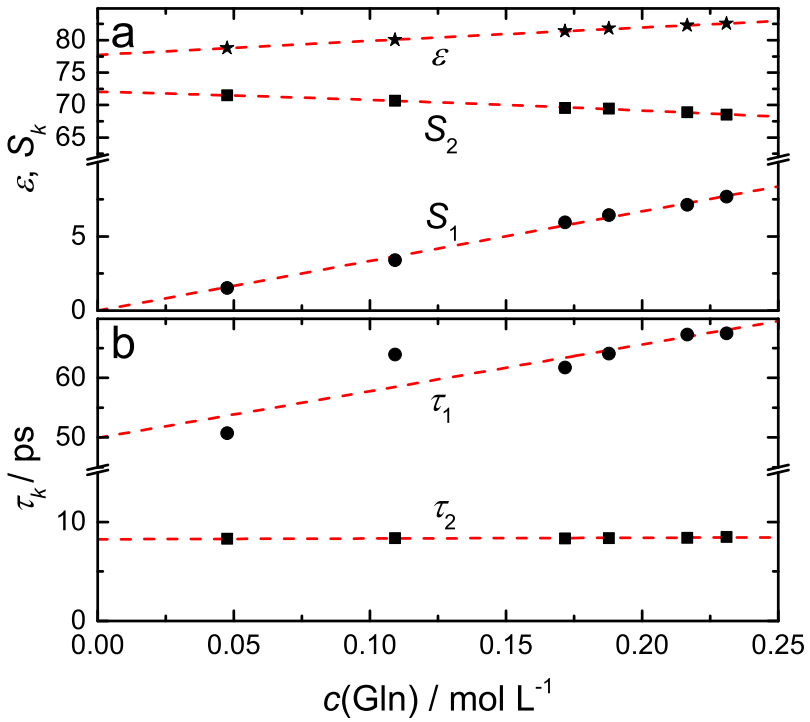

Figure A.13: (a) Static permittivities, ε(★), and relaxation amplitudes, S_1(●), S_2(■), and (b) the respective relaxation times, τ_1(●), τ_2(■), of the Gln(aq) solutions at 25 °C as a function of solute concentration, c(Gln). The dashed lines are guides to the eye and were obtained from empirical fits. Parameters of the fast-water mode $k = 3$ are not shown for clarity.

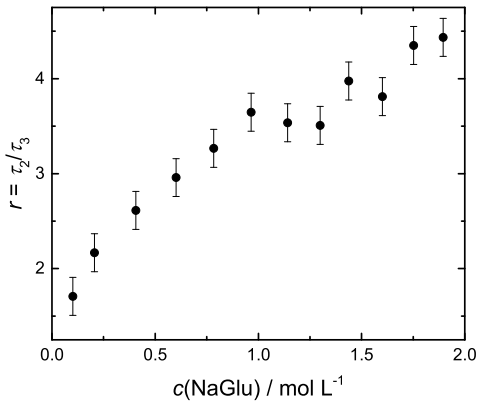

Figure A.14: Slow-water retardation factor, $r = \tau_2/\tau_3$, of aqueous NaGlu solutions at 25 °C as a function of c(NaGlu).

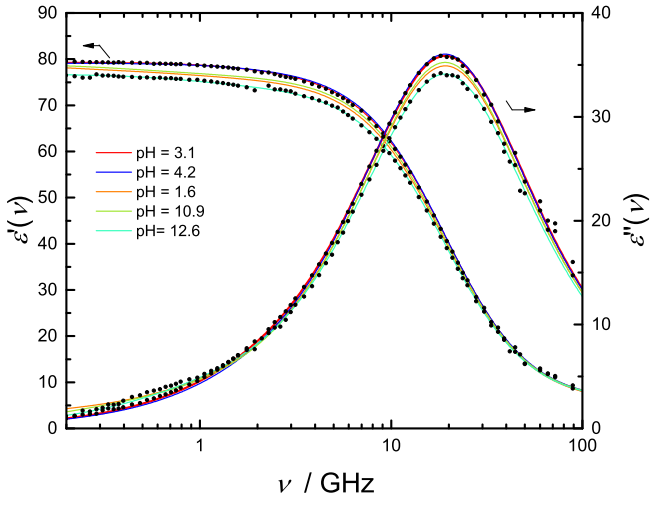

Figure A.15: Relative permittivity, $\varepsilon'(\nu)$, and dielectric loss, $\varepsilon''(\nu)$, spectra of HGlu+NaOH/HCl(aq) at different pH values and at 25 °C. Symbols denote the experimental data. For visual clarity experimental points are only shown for selected samples. Colored lines represent the respective fits at different pH.

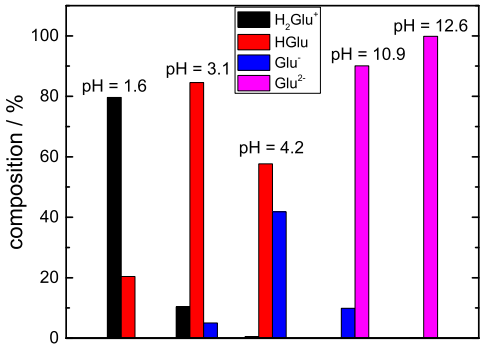

Figure A.16: Composition of the ∼0.06 M HGlu+NaOH/HCl(aq) at the different pH values of the solutions.

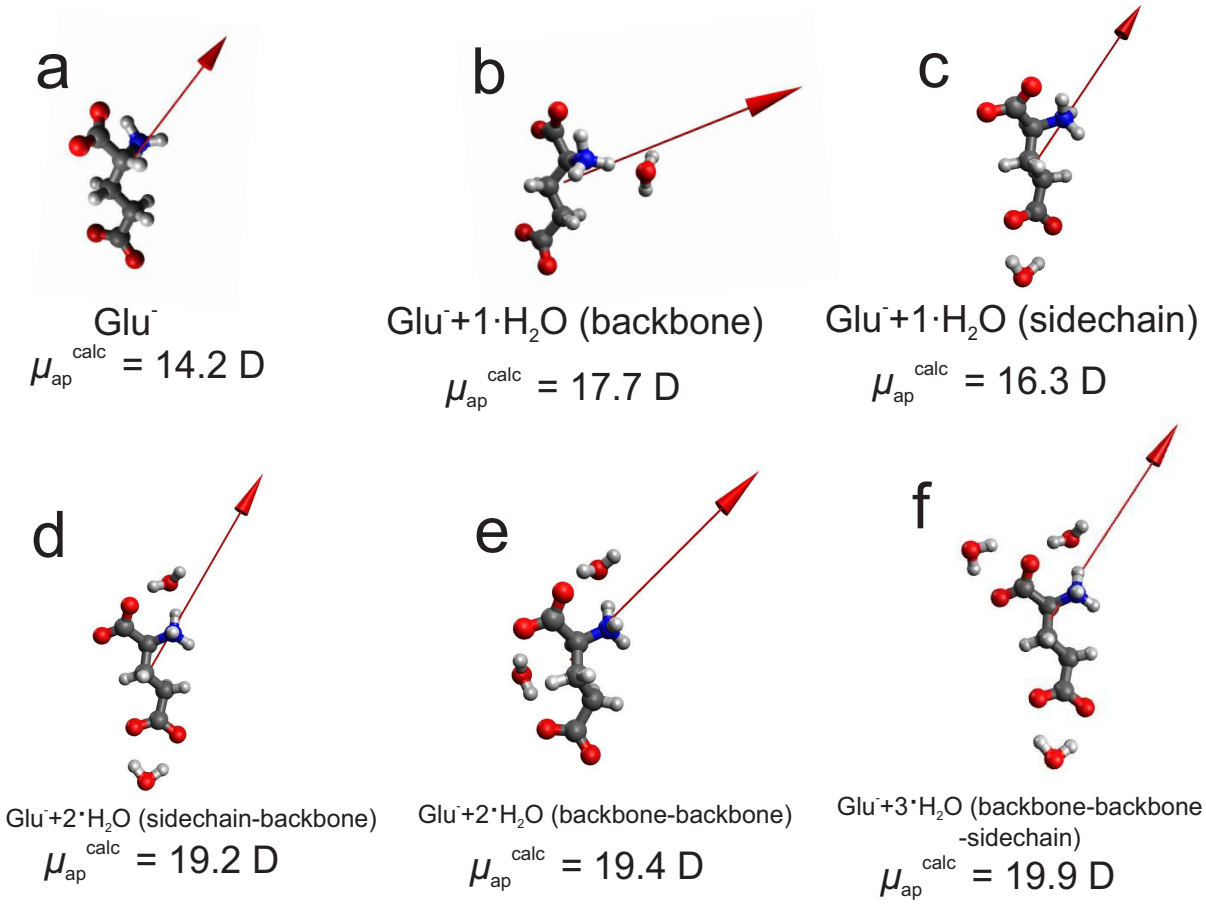

Figure A.17: Low-energy structures of (a) Glu^-, (b) Glu^-+1·H_2O(backbone), (c) Glu^-+1·H_2O(sidechain), (d) Glu^-+2·H_2O(sidechain-backbone), (e) Glu^-+2·H_2O(backbone-backbone) and (f) Glu^-+3·H_2O(backbone-backbone-sidechain) species as obtained by Gaussian 09 at the B3LYP/6-31++G(d,p) level using the PCM solvation model. Blue: nitrogen, red: oxygen, dark-gray: carbon, light-gray: hydrogen. The arrows indicate the dipole moments.

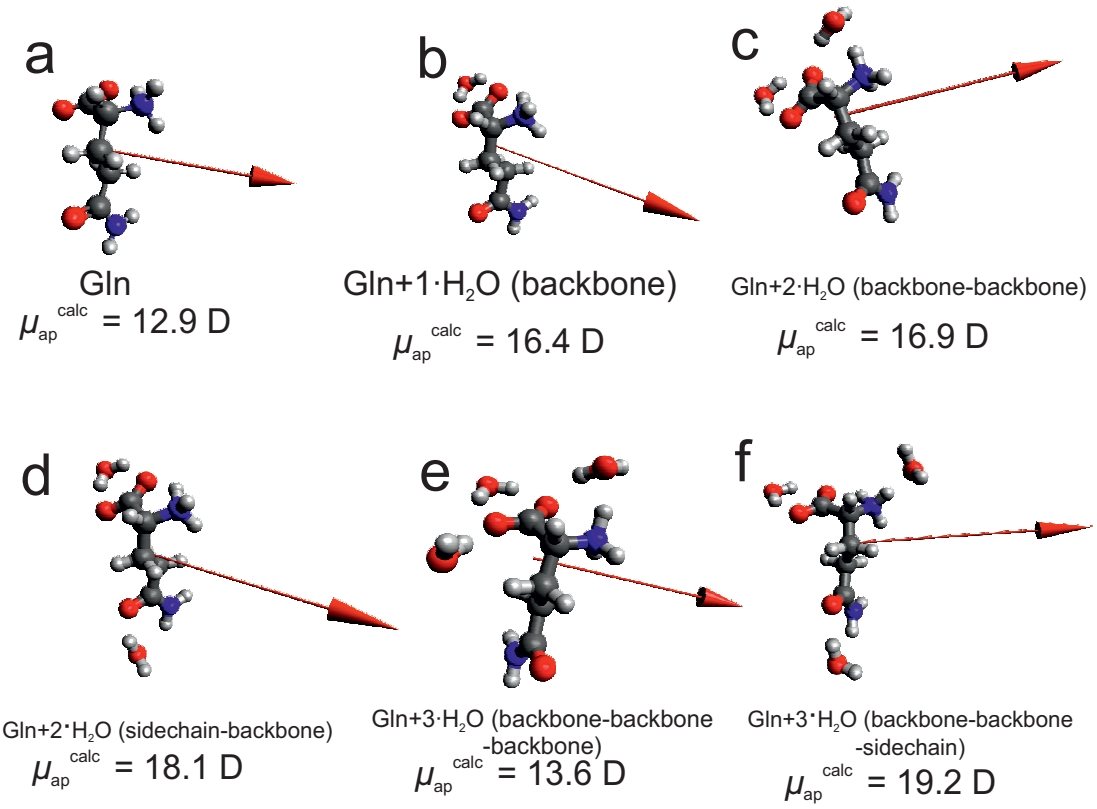

Figure A.18: Low-energy structures of (a) Gln, (b) Gln+1·H_2O(backbone), (c) Gln+2·H_2O(backbone-backbone), (d) Gln+2·H_2O(sidechain-backbone), (e) Gln+3·H_2O(backbone-backbone-backbone) and (f) Gln+3·H_2O(backbone-backbone-sidechain) species as obtained by Gaussian 09 at the B3LYP/6-31G(d,p) level using the PCM solvation model. Blue: nitrogen, red: oxygen, dark-gray: carbon, light-gray: hydrogen. The arrows indicate the dipole moments.

A.3 γ-Aminobutyric Acid, α-Aminobutyric acid & n-Butylammonium chloride

Table A.10: Molar concentrations, c, densities, ρ, viscosities, η, with its uncertainty, $\Delta\eta$, and pH-values of the GABA(aq) solutions at 25 °C.

c / mol L^{-1}	ρ / g cm^{-3}	η / mPa s	$\Delta\eta$ / mPa s	pH
0.2071	1.003291	0.950	0.002	6.2
0.3891	1.008649	1.005	0.001	6.2
0.8142	1.020972	1.162	0.001	6.4
1.250	1.033251	1.361	0.001	6.6
1.692	1.045385	1.615	0.002	6.7
2.157	1.057791	1.955	0.002	6.9
2.717	1.072337	2.70	0.07	7.1
3.280	1.086391	3.29	0.01	7.1
3.871	1.100696	4.468	0.006	7.1
4.460	1.114362	6.40	0.01	7.3
5.227	1.131253	10.75	0.02	7.4
6.241	1.152066	23.50	0.04	7.4

Table A.11: Molar concentrations, c, densities, ρ, viscosities, η, with its uncertainty, $\Delta\eta$, and pH-values of the AABA(aq) solutions at 25 °C.

c / mol L^{-1}	ρ / g cm^{-3}	η / mPa s	$\Delta\eta$ / mPa s	pH
0.09980	0.999844	0.917	0.003	6.0
0.2508	1.004006	0.977	0.002	–
0.4033	1.008189	1.016	0.002	–
0.6055	1.013704	1.095	0.002	–
0.8069	1.019202	1.189	0.004	–
1.000	1.024323	1.281	0.003	–
1.226	1.030417	1.419	0.005	–
1.441	1.036104	1.525	0.004	–
1.708	1.043146	1.737	0.007	6.5

Table A.12: Molar concentrations, c, densities, ρ, viscosities, η, conductivities, κ, and their respective uncertainties, $\Delta\eta$ and $\Delta\kappa$, of the BACl(aq) solutions at 25 °C.

c / mol L^{-1}	ρ / g cm^{-3}	η / mPa s	$\Delta\eta$ / mPa s	κ / S m^{-1}	$\Delta\kappa$ / S m^{-1}
0.03584	0.997302	0.912	0.001	0.353	0.001
0.07113	0.997500	0.912	0.001	0.637	0.002
0.1422	0.997942	0.935	0.007	1.241	0.002
0.2842	0.998813	0.972	0.002	2.304	0.003
0.3785	0.999356	0.997	0.005	3.153	0.003
0.5037	1.000103	1.037	0.002	3.665	0.007
0.6726	1.001121	1.09	0.01	4.468	0.006
0.8935	1.002532	1.184	0.001	6.158	0.005
1.190	1.004361	1.30	0.02	7.46	0.01

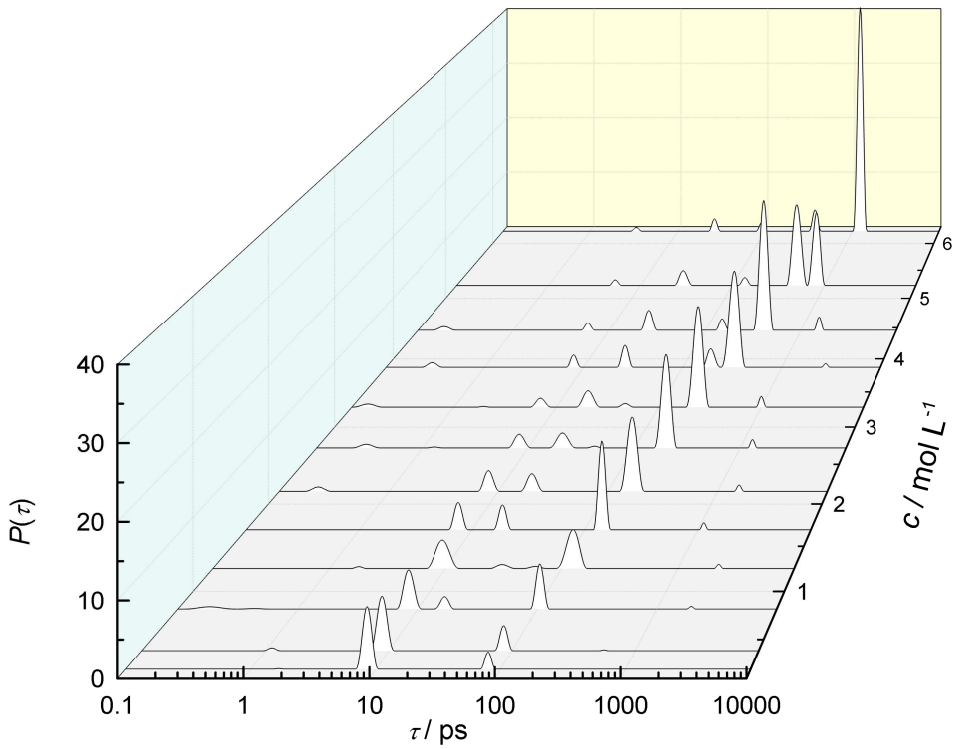

Figure A.19: Relaxation-time distribution, $P(t)$, of dielectric data of GABA(aq) solutions at 25 °C, obtained *via* Zasetsky's computational procedure [114].

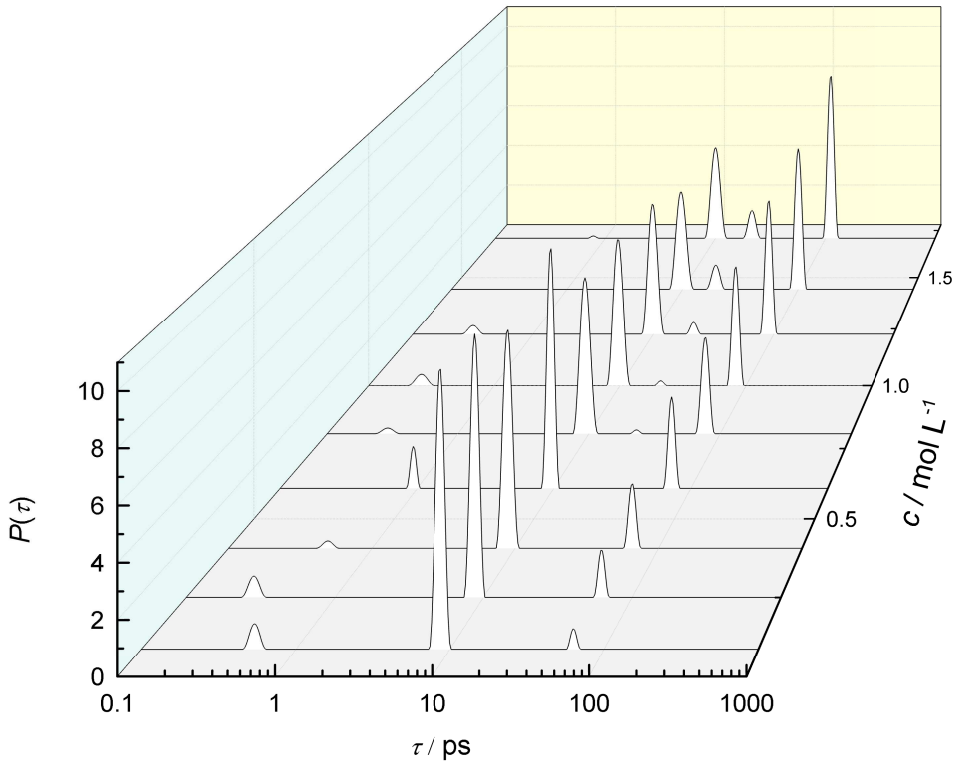

Figure A.20: Relaxation-time distribution, $P(t)$, of dielectric data of AABA(aq) solutions at 25 °C, obtained *via* Zasetsky's computational procedure [114].

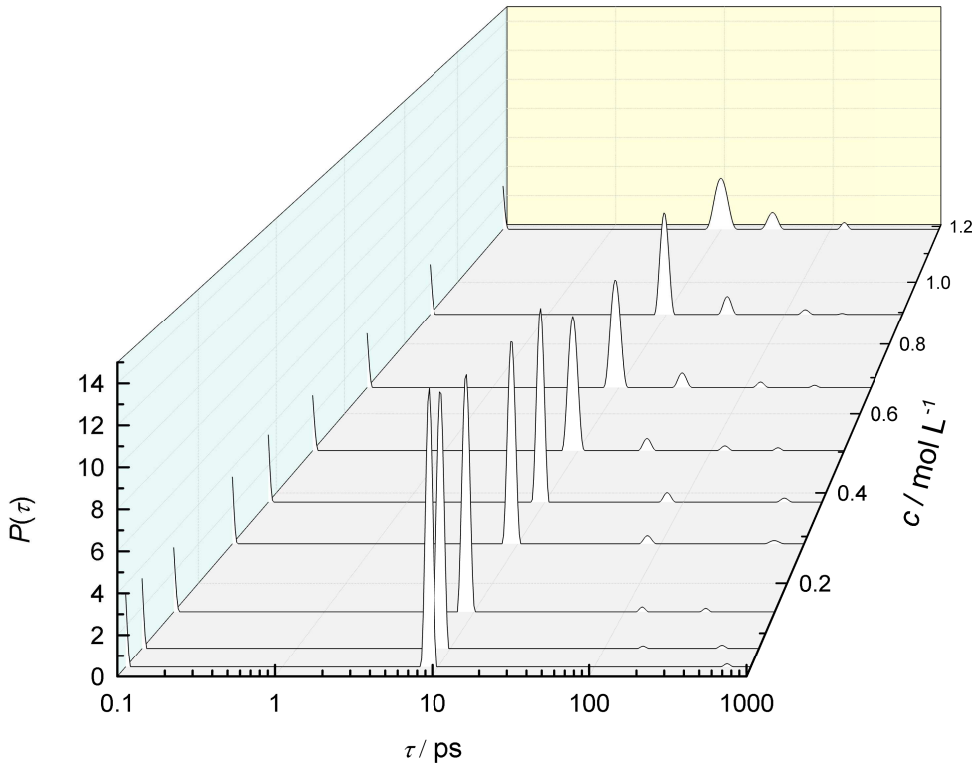

Figure A.21: Relaxation-time distribution, $P(t)$, of dielectric data of BACl(aq) solutions at 25 °C, obtained *via* Zasetsky's computational procedure [114].

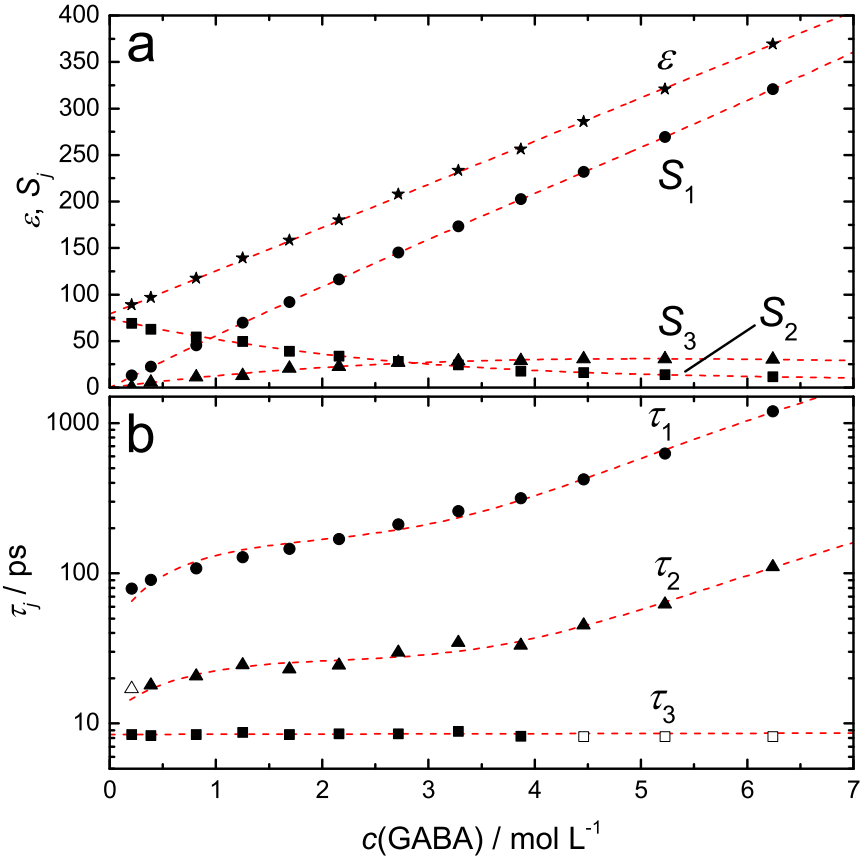

Figure A.22: (a) Static permittivities, ε(★), and relaxation amplitudes, S_1(●), S_2(▲), S_3(■), and (b) the respective relaxation times, τ_1(●), τ_2(▲), τ_3(■), of the GABA(aq) solutions at 25 °C as a function of solute concentration, c(GABA). The dashed lines are guides to the eye and were obtained from empirical fits. Hollow symbols denote parameters which were fixed during fitting of the dielectric spectra. Parameters of fast-water mode $j = 4$ are not shown.

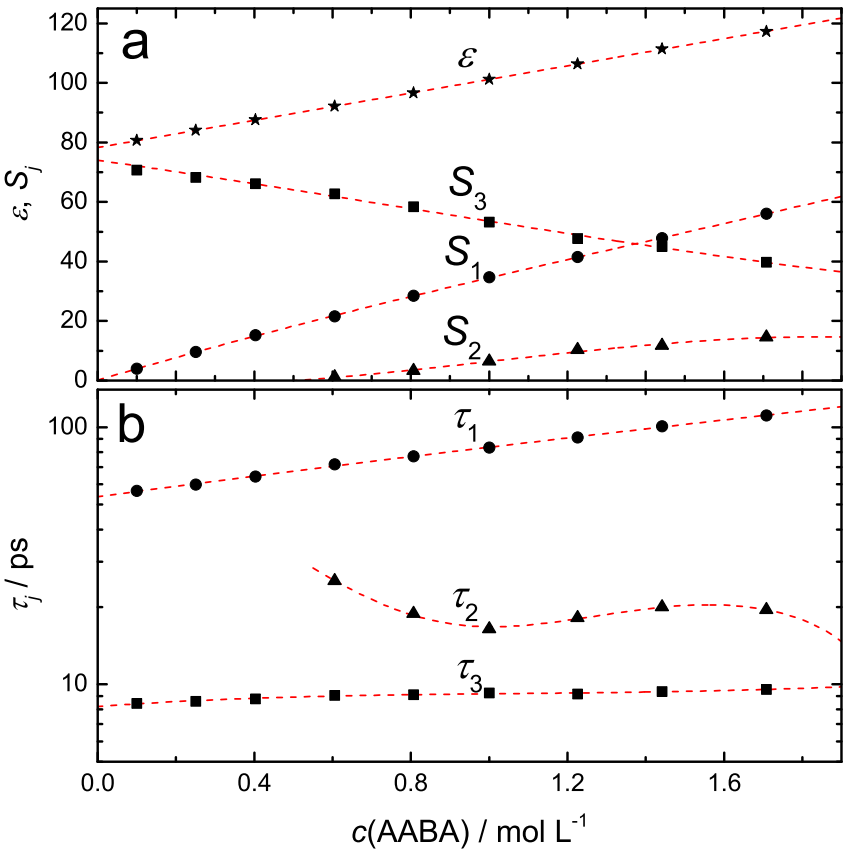

Figure A.23: (a) Static permittivities, $\varepsilon(\bigstar)$, and relaxation amplitudes, $S_1(\bullet), S_2(\blacktriangle), S_3(\blacksquare)$, and (b) the respective relaxation times, $\tau_1(\bullet), \tau_2(\blacktriangle), \tau_3(\blacksquare)$, of the AABA(aq) solutions at 25 °C as a function of solute concentration, c(AABA). The dashed lines are guides to the eye and were obtained from empirical fits. Parameters of fast-water mode $j = 4$ are not shown.

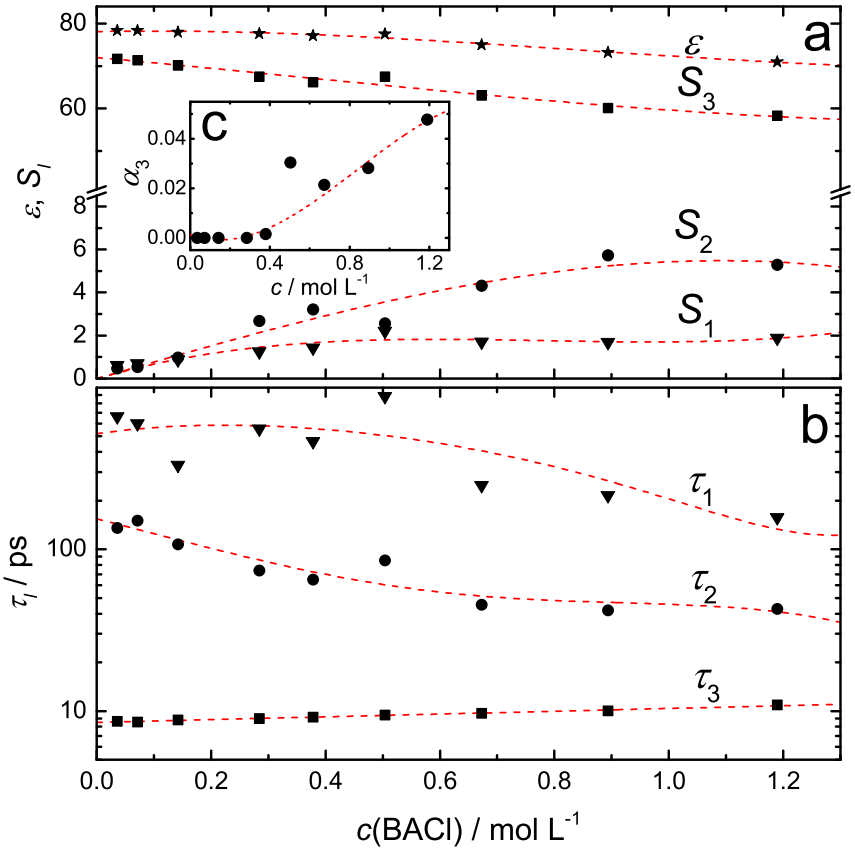

Figure A.24: (a) Static permittivities, $\varepsilon(\bigstar)$, and relaxation amplitudes, $S_1(\blacktriangledown), S_2(\bullet), S_3(\blacksquare)$, and (b) the respective relaxation times, $\tau_1(\blacktriangledown), \tau_2(\bullet), \tau_3(\blacksquare)$, of the BACl(aq) solutions at 25 °C as a function of solute concentration, c(BACl). Inset (c) shows the width parameter, α_3, as function of BACl(aq) concentration. The dashed lines are guides to the eye and were obtained from empirical fits.

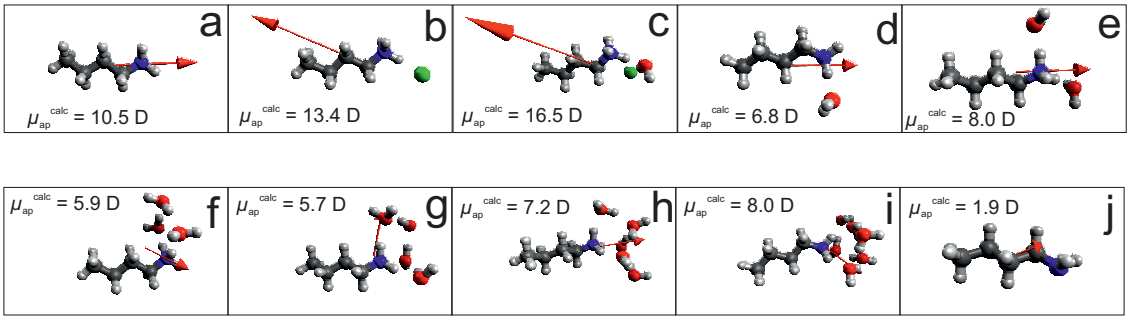

Figure A.25: Lowest-energy structures of (a) BA^+, (b) BA^+-Cl^--CIP, (c) BA^+-Cl^--SIP, (d) BA+1·H_2O, (e) BA+2·H_2O, (f) BA+3·H_2O, (g) BA+4·H_2O, (h) BA+5·H_2O, (i) BA+6·H_2O and (j) n-butylamine species as obtained by Gaussian 09 at the B3LYP/6-31G(d,p) and B3LYP/6-31++G(d,p) level using the PCM solvation model. Blue: nitrogen, red: oxygen, dark-gray: carbon, light-gray: hydrogen, green: chloride. The arrows indicate the dipole moments.

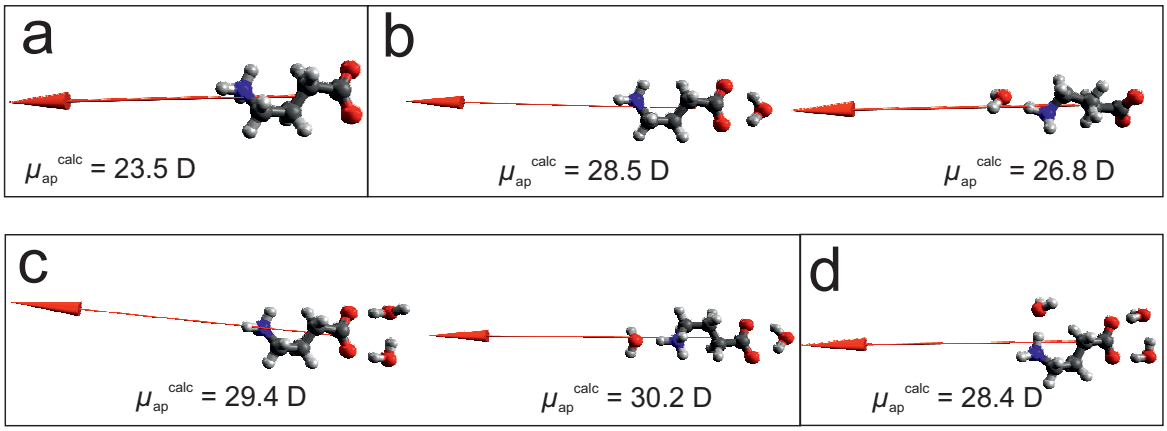

Figure A.26: Low-energy structures of (a) GABA, (b) GABA+1·H_2O, (c) GABA+2·H_2O and (d) GABA+3·H_2O species as obtained by Gaussian 09 at the B3LYP/6-31G(d,p) level using the PCM solvation model. Blue: nitrogen, red: oxygen, dark-gray: carbon, light-gray: hydrogen. The arrows indicate the dipole moments.

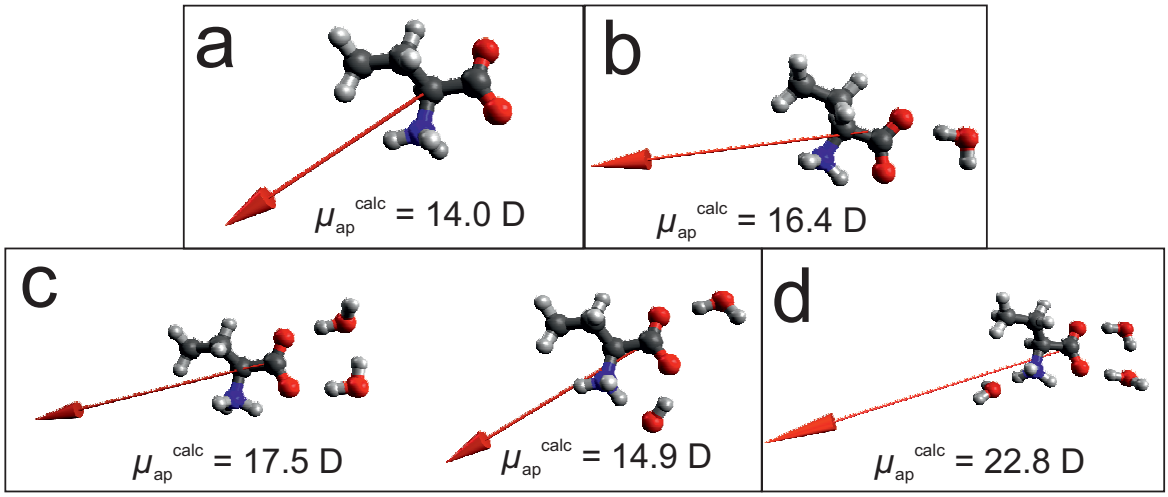

Figure A.27: Low-energy structures of (a) AABA, (b) AABA+1·H_2O, (c) AABA+2·H_2O and (d) AABA+3·H_2O species as obtained by Gaussian 09 at the B3LYP/6-31++G(d,p) level using the PCM solvation model. Blue: nitrogen, red: oxygen, dark-gray: carbon, light-gray: hydrogen. The arrows indicate the dipole moments.

A.4 Electrolyte Solutions

Table A.13: Molar concentrations, c, densities, ρ, viscosities, η, conductivities, κ, and their respective uncertainties, $\Delta\eta$ and $\Delta\kappa$, of the $MgCl_2$(aq) solutions at 25 °C.

c / mol L^{-1}	ρ / g cm^{-3}	η / mPa s	$\Delta\eta$ / mPa s	κ / S m^{-1}	$\Delta\kappa$ / S m^{-1}
0.03094	0.999576	0.899	0.002	0.623	0.001
0.07636	1.003156	0.915	0.001	1.419	0.003
0.1513	1.008510	0.949	0.002	2.550	0.004
0.3064	1.021174	1.007	0.002	4.865	0.007
0.4105	1.026234	1.038	0.002	6.08	0.01
0.5180	1.036015	1.084	0.002	7.76	0.02
0.6270	1.045995	1.134	0.002	9.11	0.02
0.8481	1.060127	1.231	0.002	11.13	0.02
1.079	1.079457	1.369	0.002	13.21	0.03
1.371	1.096575	1.510	0.002	14.64	0.04
1.642	1.117286	1.715	0.003	16.02	0.04

Table A.14: Molar concentrations, c, densities, ρ, viscosities, η, conductivities, κ, and their respective uncertainties, $\Delta\eta$ and $\Delta\kappa$, of the $CaCl_2$(aq) solutions at 25 °C.

c / mol L^{-1}	ρ / g cm^{-3}	η / mPa s	$\Delta\eta$ / mPa s	κ / S m^{-1}	$\Delta\kappa$ / S m^{-1}
0.04865	1.001551	0.9025	0.0004	1.012	0.002
0.08515	1.004869	0.9151	0.0007	1.695	0.006
0.2173	1.017112	0.9493	0.0008	3.93	0.02
0.4349	1.037585	1.016	0.001	7.20	0.01
0.6106	1.054518	1.070	0.001	9.63	0.02
0.7849	1.071914	1.136	0.001	11.70	0.04
0.8726	1.079961	1.172	0.001	12.76	0.02
1.050	1.099588	1.272	0.001	14.54	0.05
1.225	1.115283	1.346	0.001	16.11	0.06
1.786	1.149411	1.543	0.002	18.47	0.06

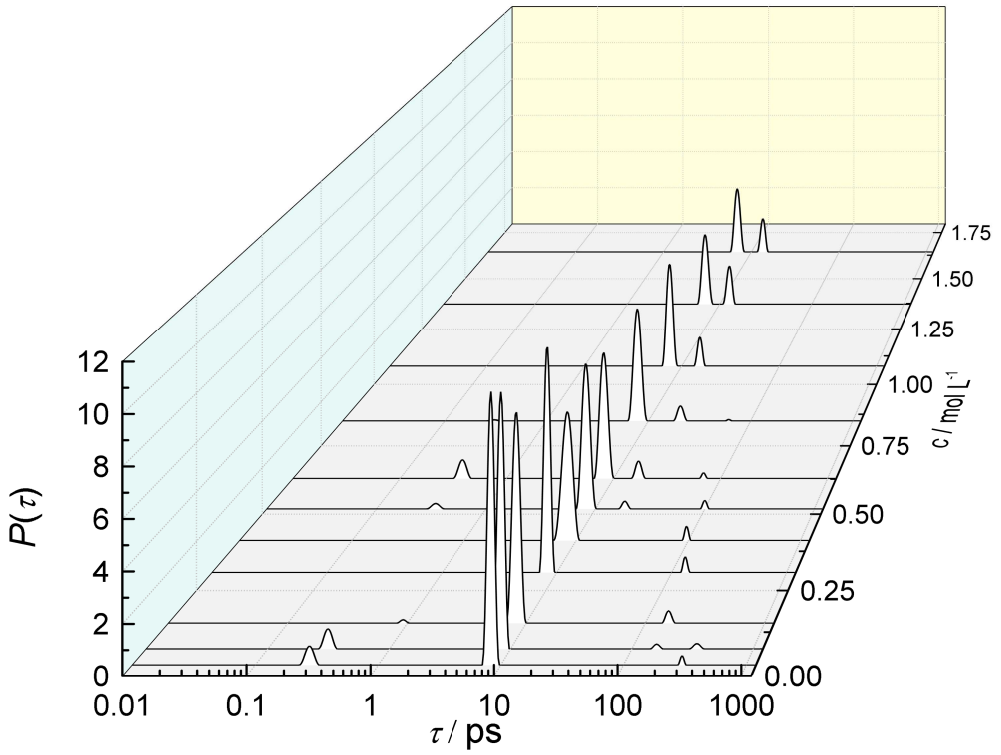

Figure A.28: Relaxation-time distribution, $P(\tau)$, of dielectric data for $MgCl_2$(aq) at 25 °C, obtained *via* Zasetsky's computational procedure [114].

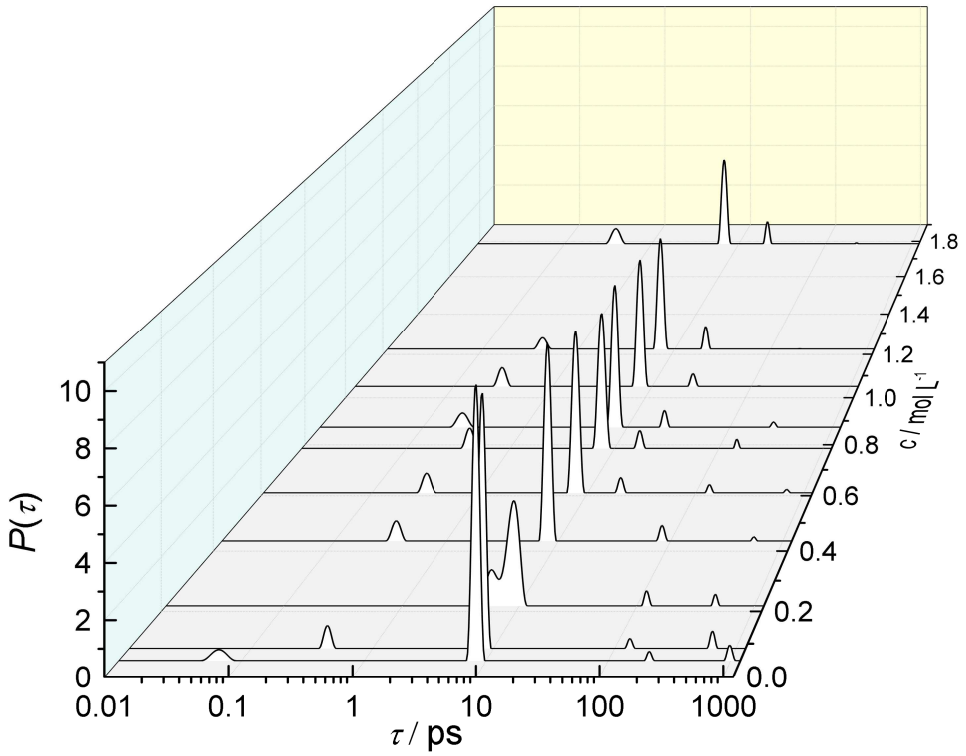

Figure A.29: Relaxation-time distribution, $P(\tau)$, of dielectric data for $CaCl_2$(aq) at 25 °C, obtained *via* Zasetsky's computational procedure [114].

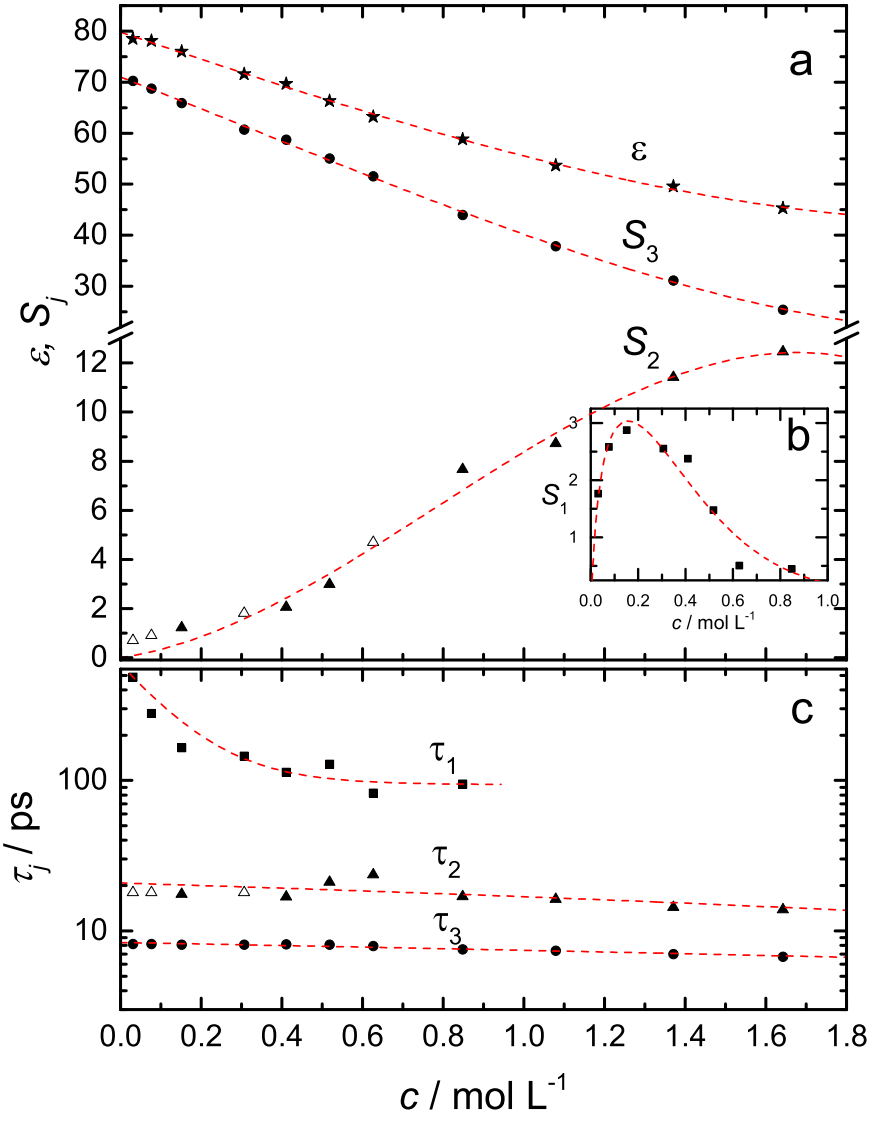

Figure A.30: (a) Static permittivities (★) and relaxation intensities, S_j ($j = 1$ ■, $j = 2$ ▲, $j = 3$ ●), and (c) relaxation times, τ_j ($j = 1$ ■, $j = 2$ ▲, $j = 3$ ●) as function of $c(MgCl_2)$. The hollow symbols indicate the parameter was fixed during fitting. Inset (b) shows S_1 at low c. Dashed lines are visual guides only.

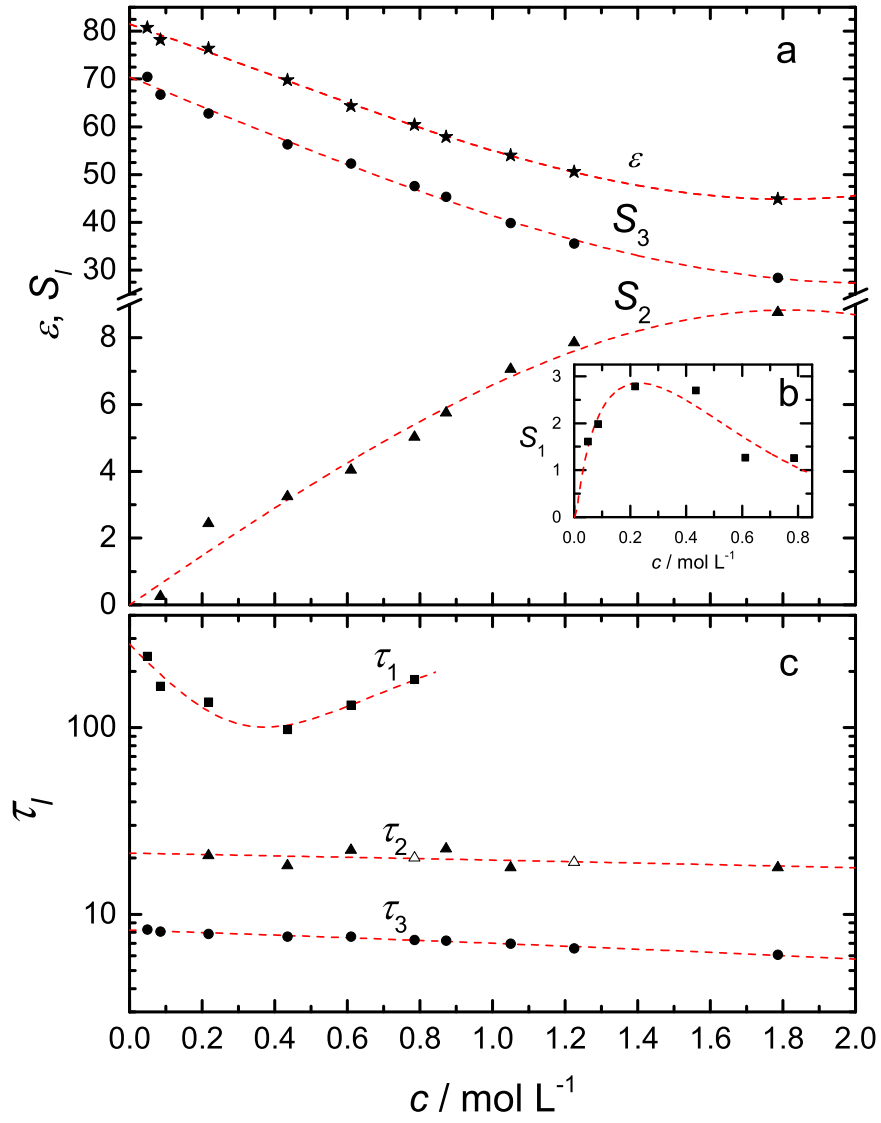

Figure A.31: (a) Static permittivities (★) and relaxation intensities, S_l ($l = 1$ ■, $l = 2$ ▲, $l = 3$ ●), and (c) relaxation times, τ_l ($k = l$ ■, $k = l$ ▲, $l = 3$ ●) as function of $c(CaCl_2)$. The hollow symbols indicate the parameter was fixed during fitting. Inset (b) shows S_1 at low c. Dashed lines are visual guides only. Parameters of mode $l = 0$ are not shown.

Table A.15: Estimated effective dipole moments of the IP species in $MgCl_2$(aq) and $CaCl_2$(aq) using the CHS as the pivot.

	$\mu_{\mathrm{eff,IP}}(MgCl^+(aq))/D$	$\mu_{\mathrm{eff,IP}}(CaCl^+(aq))/D$
CIP	20.7	23.4
SIP	44.5	46.7
2SIP	64.8	66.7

Table A.16: Molar concentrations, c, densities, ρ, viscosities, η, conductivities, κ, and their respective uncertainties, $\Delta\eta$ and $\Delta\kappa$, of the TMACl(aq) solutions at 25 °C.

c / mol L^{-1}	ρ / g cm^{-3}	η / mPa s	$\Delta\eta$ / mPa s	κ / S m^{-1}	$\Delta\kappa$ / S m^{-1}
0.09600	0.997291	0.9021	0.0008	0.928	0.002
0.1986	0.997482	0.9136	0.0006	1.814	0.003
0.4143	0.997910	0.915	0.001	3.668	0.007
0.6250	0.998323	0.946	0.001	4.814	0.007
0.8038	0.998701	0.9745	0.0009	6.30	0.01
0.9885	0.999124	1.0065	0.0007	7.38	0.02
1.197	0.999623	1.051	0.001	8.47	0.02
1.495	1.000412	1.120	0.001	9.79	0.02

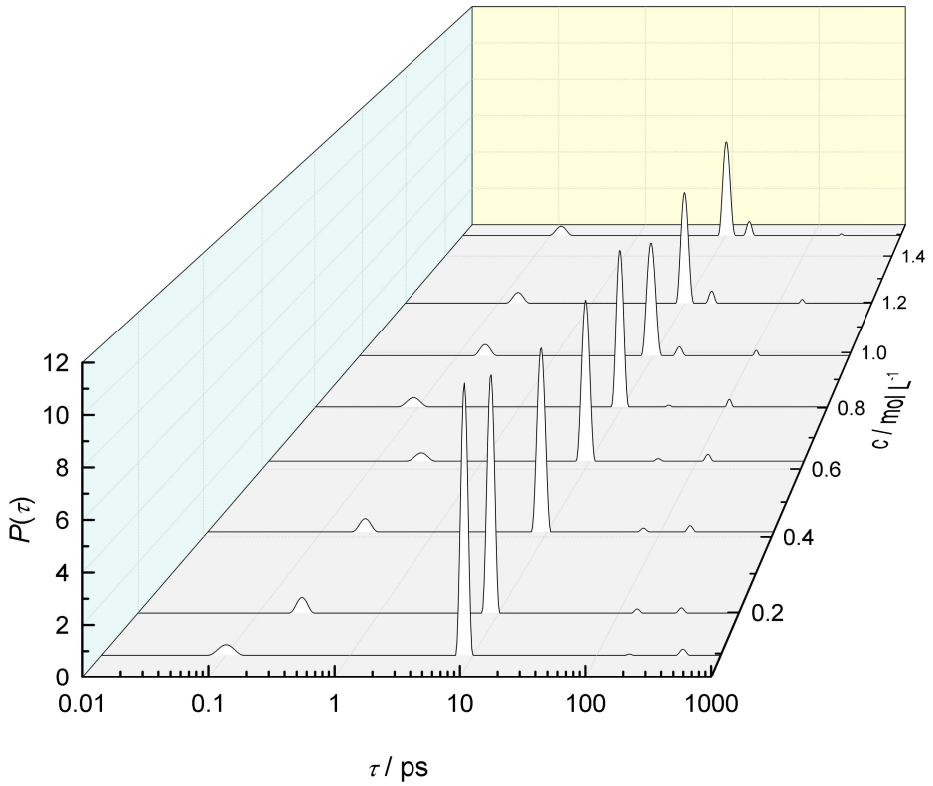

Figure A.32: Relaxation-time distribution, $P(\tau)$, of dielectric data for TMACl(aq) at 25 °C, obtained *via* Zasetsky's computational procedure [114].

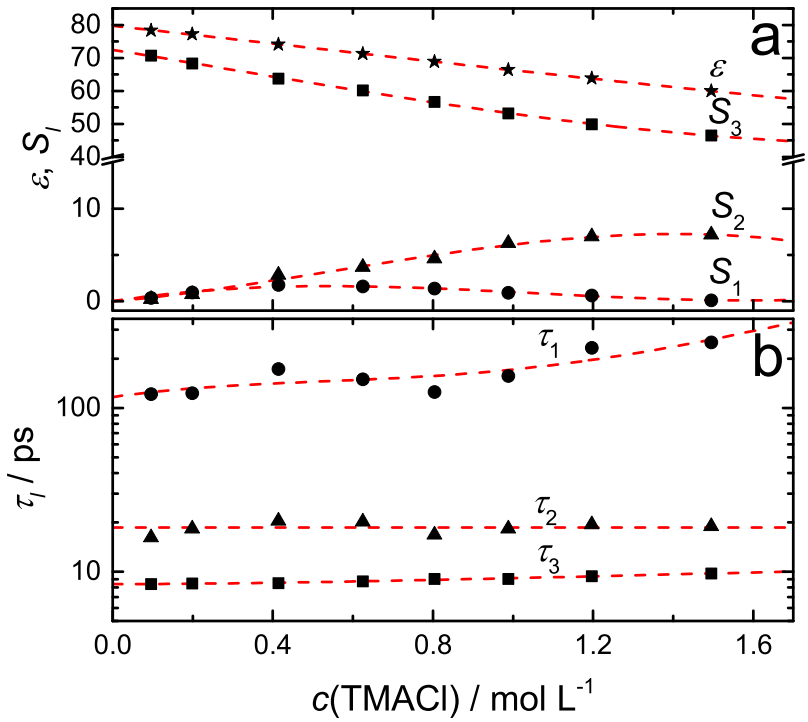

Figure A.33: (a) Static permittivities (★) and relaxation intensities, S_l ($l = 1$ ●, $j = 2$ ▲, $j = 3$ ■), and (c) relaxation times, τ_l ($l = 1$ ●, $j = 2$ ▲, $j = 3$ ■) as function of c(TMACl). Parameters of mode $l = 0$ are not shown.

A.5 Ternary Systems - Effect of Salts on the Neurotransmitter Solutions

Table A.17: Molar concentrations, c, densities, ρ, viscosities, η, conductivities, κ, and their respective uncertainties, $\Delta\eta$ and $\Delta\kappa$, of the AcChCl+KCl(aq) solutions at 25 °C.

c(KCl) / mol L^{-1}	c(AcChCl) / mol L^{-1}	ρ / g cm^{-3}	η / mPa s	$\Delta\eta$ / mPa s	κ / S m^{-1}	$\Delta\kappa$ / S m^{-1}
0	0.2507	1.003258	0.9602	0.0006	1.927	0.007
0.1521	0.2497	1.010237	0.9599	0.0003	3.55	0.01
0.3039	0.2486	1.017202	0.9608	0.0009	5.12	0.01
0.6185	0.2462	1.031394	0.9606	0.0004	8.27	0.01
0.8325	0.2447	1.041232	0.9619	0.0005	10.36	0.04
1.054	0.2429	1.050486	0.966	0.001	12.40	0.04

Table A.18: Molar concentrations, c, densities, ρ, viscosities, η, conductivities, κ, and their respective uncertainties, $\Delta\eta$ and $\Delta\kappa$, of the AcChCl+KF(aq) solutions at 25 °C.

c(KF) / mol L^{-1}	c(AcChCl) / mol L^{-1}	ρ / g cm^{-3}	η / mPa s	$\Delta\eta$ / mPa s	κ / S m^{-1}	$\Delta\kappa$ / S m^{-1}
0	0.2510	1.003303	0.966	0.005	1.949	0.003
0.1688	0.2506	1.011464	0.996	0.002	3.439	0.005
0.3281	0.2502	1.019184	1.010	0.004	4.765	0.008
0.6053	0.2494	1.032400	1.04	0.16	6.90	0.01
0.7840	0.2490	1.040804	1.109	0.002	8.13	0.03
1.015	0.2483	1.051504	1.128	0.005	9.70	0.03

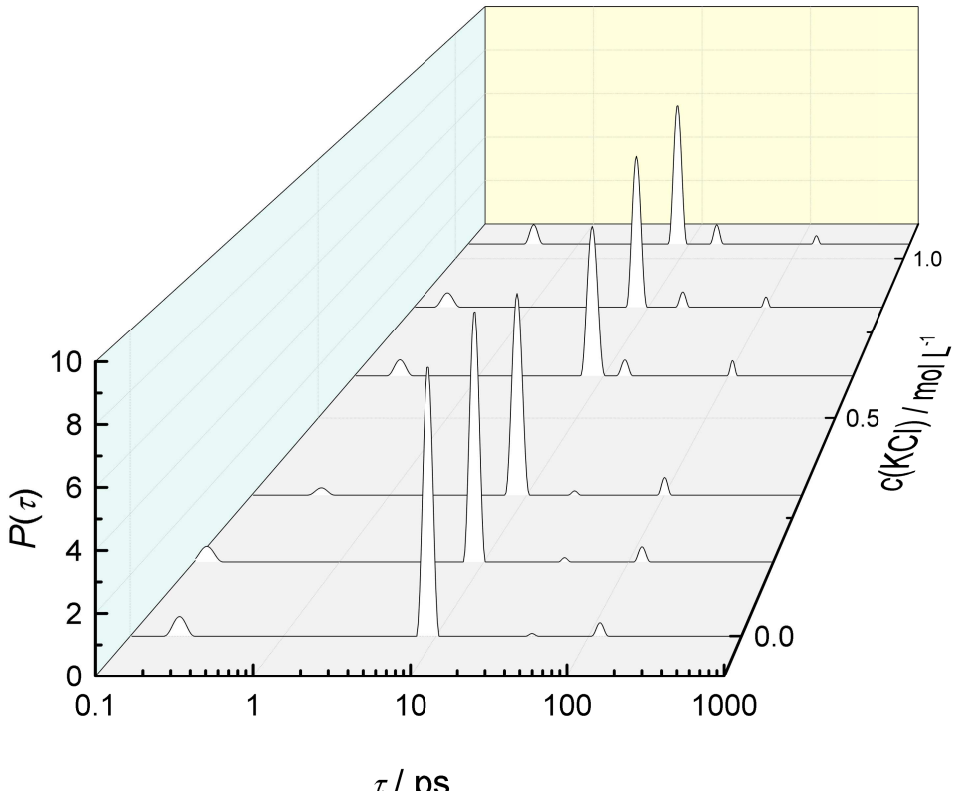

Figure A.34: Relaxation-time distribution, $P(t)$, of dielectric data of ~ 0.25 M AcChCl(aq) with added KCl (AcChCl+KCl(aq)) at 25 °C, obtained *via* Zasetsky's computational procedure [114].

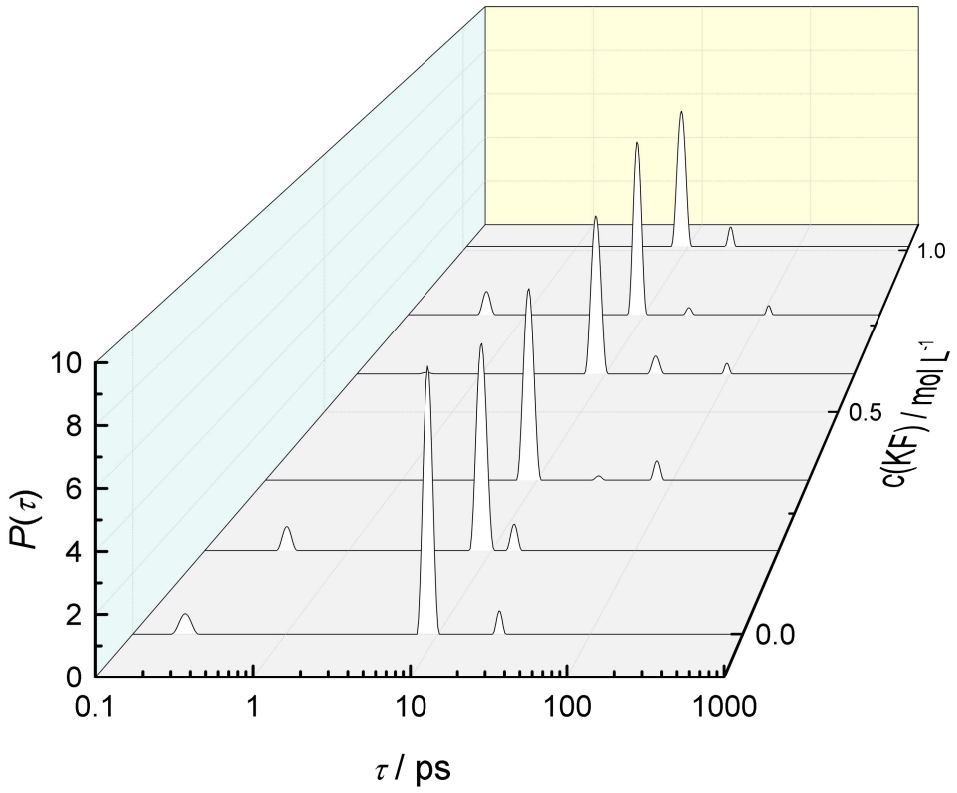

Figure A.35: Relaxation-time distribution, $P(t)$, of dielectric data of AcChCl+KF(aq) with added KF (AcChCl+KF(aq)) at 25 °C, obtained *via* Zasetsky's computational procedure [114].

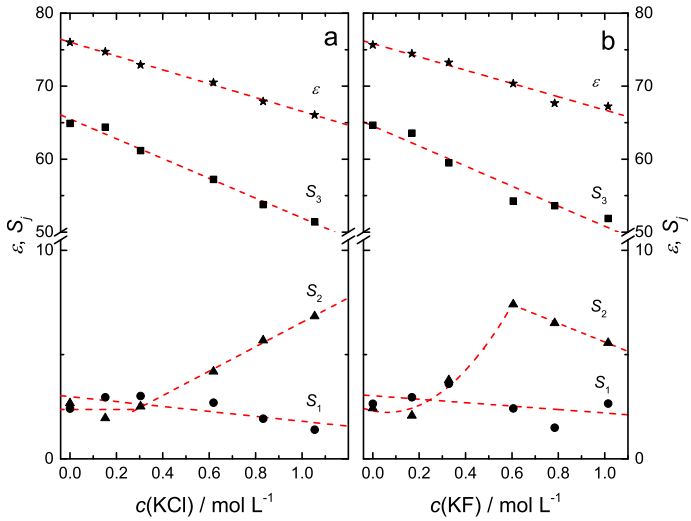

Figure A.36: Static permittivities, ε(★), and relaxation amplitudes, S_1(●), S_2(▲), S_3(■), of (a) AcChCl+KCl(aq) and (b) AcChCl+KF(aq) solutions at 25 °C as a function of the added salt concentration. Dashed lines are guides to the eye. Amplitudes S_4 are not shown for the sake of clarity.

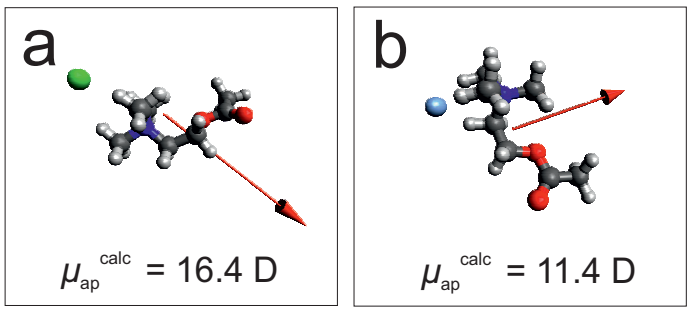

Figure A.37: Lowest-energy structures of contact ion pairs of acetylcholine and (a) chloride and (b) fluoride as obtained by Gaussian 09 at the B3LYP/6-31G(d,p) level using the PCM solvation model. Blue: nitrogen, red: oxygen, dark-gray: carbon, light-gray: hydrogen, green: chloride, light blue: fluoride. The arrows indicate the dipole moments.

Table A.19: Molar concentrations, c, densities, ρ, viscosities, η, conductivities, κ, and their respective uncertainties, $\Delta\eta$ and $\Delta\kappa$, of ternary solutions of NaGlu(aq) and different chloride salts at 25 °C.

c(salt) / mol L^{-1}	c(NaGlu) / mol L^{-1}	ρ / g cm^{-3}	η / mPa s	$\Delta\eta$ / mPa s	κ / S m^{-1}	$\Delta\kappa$ / S m^{-1}
		LiCl				
0	0.394	1.029099	1.097	0.001	1.765	0.007
0.1013	0.393	1.031882	1.106	0.002	2.518	0.004
0.2866	0.391	1.035600	1.146	0.002	3.630	0.006
0.5686	0.389	1.041962	1.206	0.003	5.302	0.008
0.9469	0.386	1.050174	1.284	0.003	7.26	0.01
1.508	0.382	1.062147	1.397	0.006	9.68	0.04
		NaCl				
0	0.424	1.033681	1.116	0.004	2.003	0.007
0.1103	0.423	1.037917	1.118	0.001	2.80	0.01
0.2518	0.422	1.043314	1.136	0.001	3.853	0.006
0.5059	0.419	1.052916	1.161	0.001	6.02	0.01
0.8046	0.417	1.064153	1.203	0.007	8.11	0.02
0.9994	0.415	1.071432	1.231	0.002	9.37	0.02
		$MgCl_2$				
0	0.424	1.033681	1.116	0.004	2.003	0.007
0.06738	0.408	1.037636	1.155	0.001	2.714	0.007
0.1594	0.402	1.044653	1.195	0.002	3.874	0.006
0.3162	0.393	1.056928	1.283	0.001	6.11	0.01
0.4865	0.381	1.070843	1.393	0.001	8.09	0.02
0.8358	0.357	1.101239	1.677	0.002	11.47	0.03
		$CaCl_2$				
0	0.424	1.033681	1.116	0.004	2.003	0.007
0.1010	0.421	1.041919	1.148	0.002	3.163	0.005
0.2007	0.418	1.050053	1.180	0.001	4.608	0.009
0.2984	0.416	1.058061	1.228	0.002	5.79	0.01
0.4948	0.410	1.074130	1.313	0.003	7.99	0.02
0.7955	0.402	1.097951	1.442	0.002	10.86	0.03

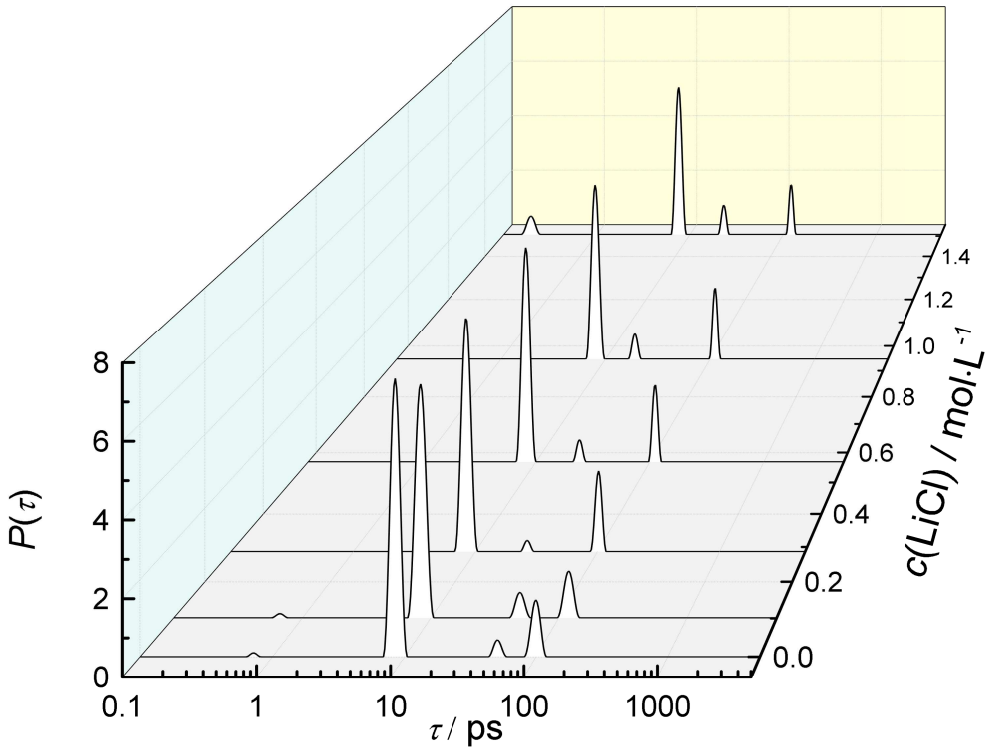

Figure A.38: Relaxation-time distribution functions, $P(\tau)$, of the dielectric data of ∼0.4 M NaGlu(aq) with added LiCl (NaGlu+LiCl(aq)) at 25 °C, obtained *via* Zasetsky's computational procedure [114].

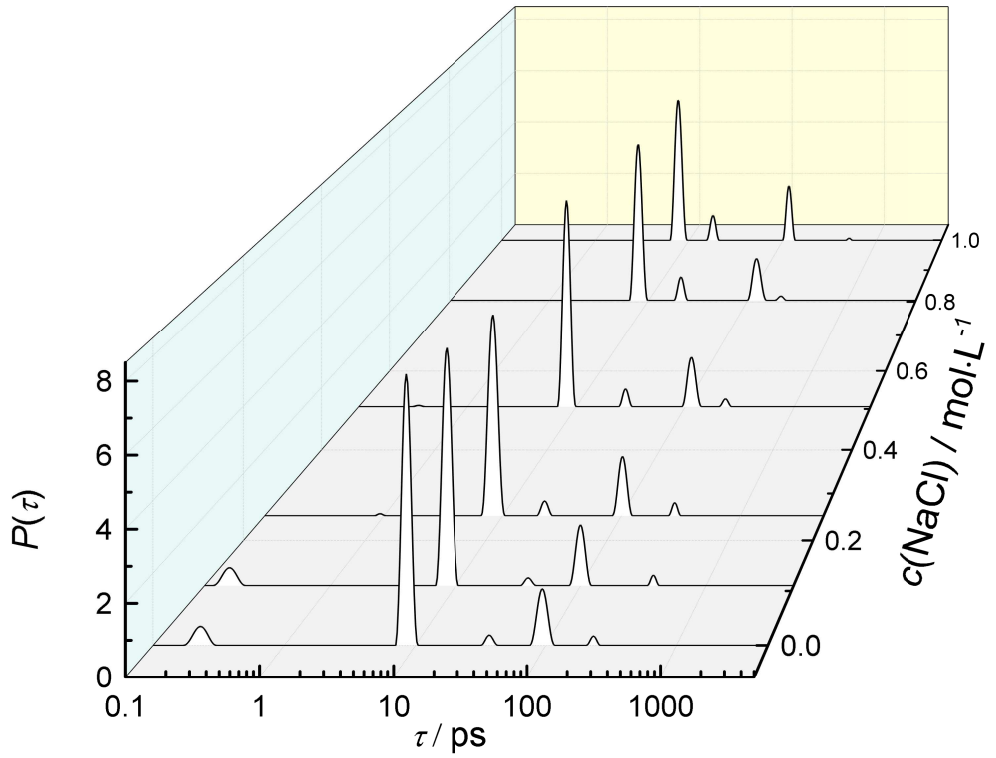

Figure A.39: Relaxation-time distribution functions, $P(\tau)$, of the dielectric data of ∼0.4 M NaGlu(aq) with added NaCl (NaGlu+NaCl(aq)) at 25 °C, obtained *via* Zasetsky's computational procedure [114].

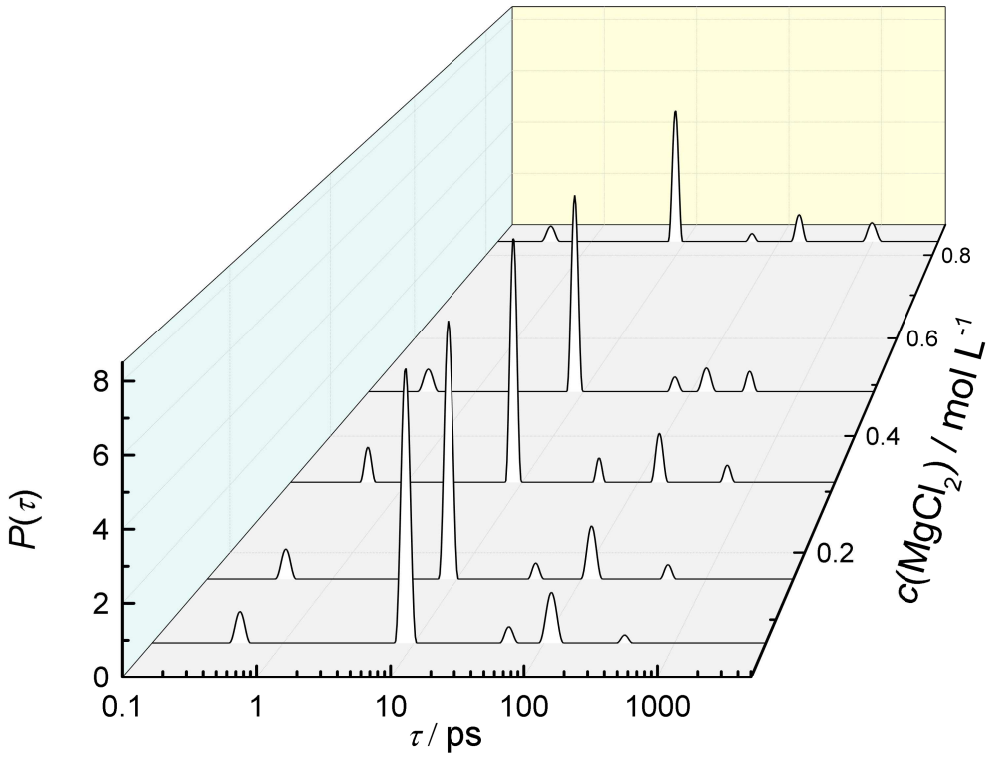

Figure A.40: Relaxation-time distribution functions, $P(\tau)$, of the dielectric data of ∼0.4 M NaGlu(aq) with added $MgCl_2$ (NaGlu+$MgCl_2$(aq)) at 25 °C, obtained *via* Zasetsky's computational procedure [114].

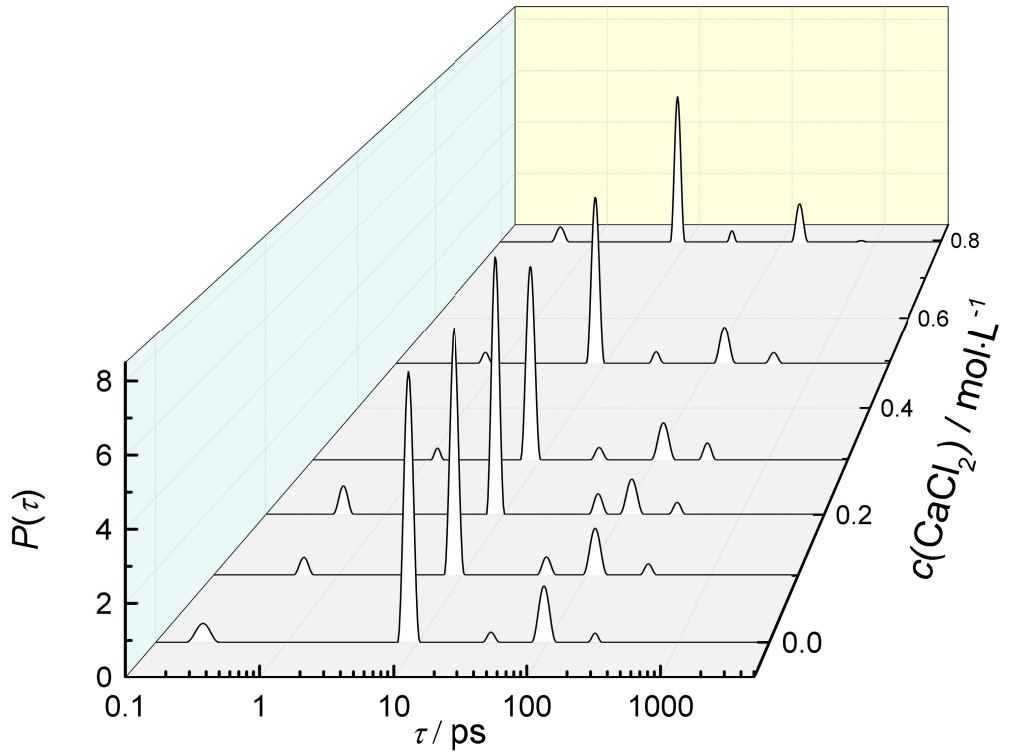

Figure A.41: Relaxation-time distribution functions, $P(\tau)$, of the dielectric data of ~0.4 M NaGlu(aq) with added $CaCl_2$ (NaGlu+$CaCl_2$(aq)) at 25 °C, obtained *via* Zasetsky's computational procedure [114].

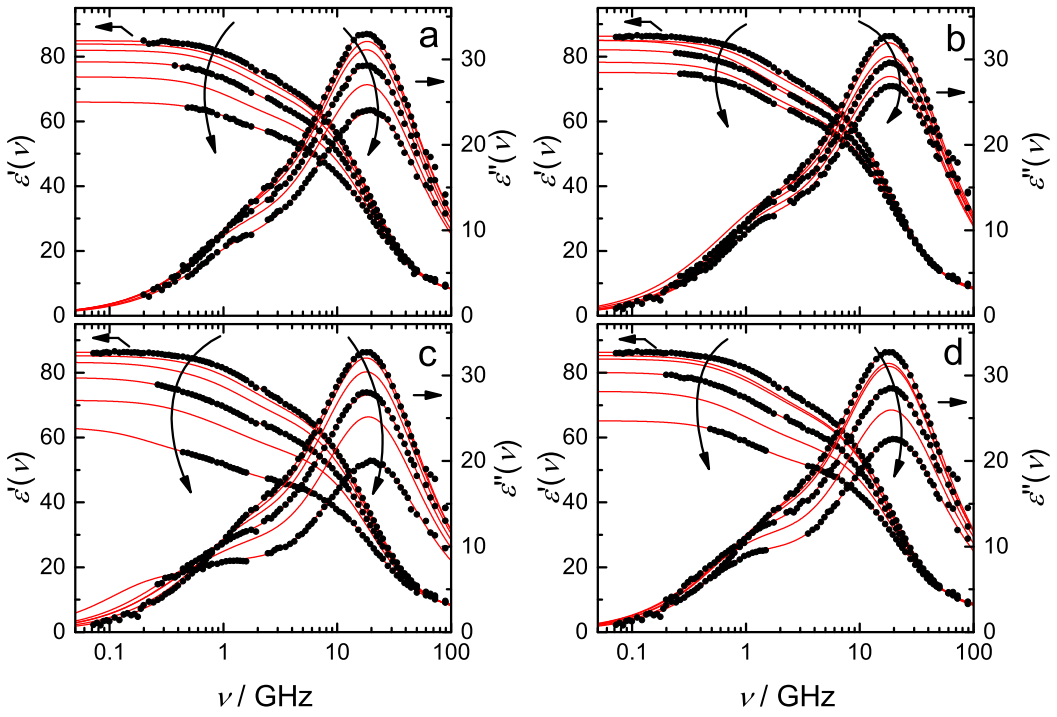

Figure A.42: Relative permittivity, $\varepsilon'(\nu)$, and dielectric loss, $\varepsilon''(\nu)$, spectra of (a) NaGlu+LiCl(aq) (c(NaGlu) $\approx 0.4\,\mathrm{M}; 0 \leq c(\mathrm{LiCl})/\mathrm{mol\,L^{-1}} \leq 1.508$), (b) NaGlu+NaCl(aq) ($c$(NaGlu) $\approx 0.4\,\mathrm{M}; 0 \leq c(\mathrm{NaCl})/\mathrm{mol\,L^{-1}} \leq 0.9994$), (c) NaGlu+$MgCl_2$(aq) ($c$(NaGlu) $\approx 0.4\,\mathrm{M}; 0 \leq c(\mathrm{MgCl_2})/\mathrm{mol\,L^{-1}} \leq 0.8358$) and (d) NaGlu+$CaCl_2$(aq) ($c$(NaGlu) $\approx 0.4\,\mathrm{M}; 0 \leq c(\mathrm{CaCl_2})/\mathrm{mol\,L^{-1}} \leq 0.7955$) at 25 °C. Symbols denote the experimental data. Solid lines represent the fits. For visual clarity data points are only shown for selected samples. Arrows indicate the trend with increasing solute concentration.

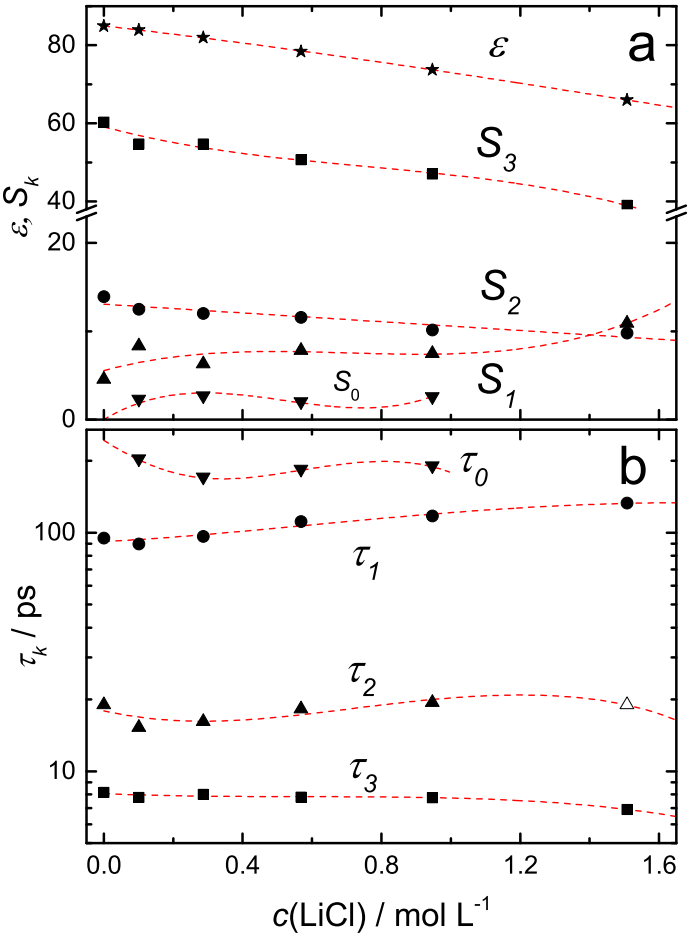

Figure A.43: (a) Static permittivities, ε(★), and relaxation amplitudes, S_0(▼), S_1(●), S_2(▲), S_3(■), and (b) the respective relaxation times, τ_0(▼), τ_1(●), τ_2(▲), τ_3(■), of the NaGlu+LiCl(aq) solutions (c(NaGlu) ≈ 0.4 M) at 25 °C as a function of LiCl concentration, c(LiCl). The dashed lines are guides to the eye. Hollow symbol denotes a parameter which was fixed during fitting of the dielectric spectra.

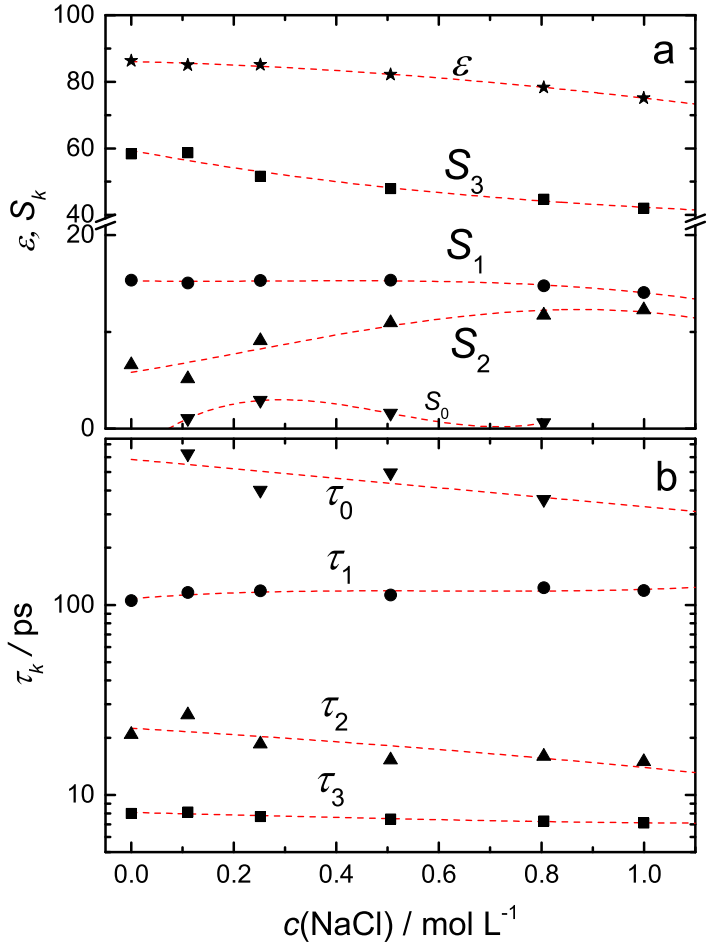

Figure A.44: (a) Static permittivities, ε(★), and relaxation amplitudes, S_0(▼), S_1(●), S_2(▲), S_3(■), and (b) the respective relaxation times, τ_0(▼), τ_1(●), τ_2(▲), τ_3(■), of the NaGlu+NaCl(aq) solutions (c(NaGlu) ≈ 0.4 M) at 25 °C as a function of LiCl concentration, c(NaCl). The dashed lines are guides to the eye.

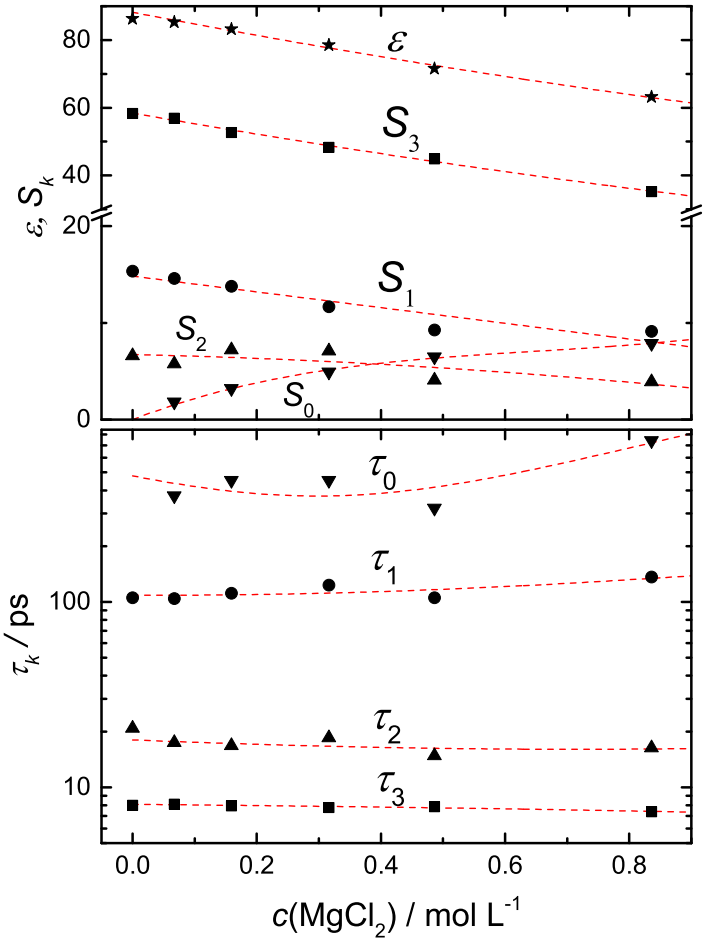

Figure A.45: (a) Static permittivities, $\varepsilon(\bigstar)$, and relaxation amplitudes, $S_0(\blacktriangledown), S_1(\bullet), S_2(\blacktriangle), S_3(\blacksquare)$, and (b) the respective relaxation times, $\tau_0(\blacktriangledown), \tau_1(\bullet), \tau_2(\blacktriangle), \tau_3(\blacksquare)$, of the NaGlu+$MgCl_2$(aq) solutions ($c$(NaGlu) $\approx$ 0.4 M) at 25 °C as a function of $MgCl_2$ concentration, $c(MgCl_2)$. The dashed lines are guides to the eye. Parameters of fast-water process $k = 4$ are not shown.

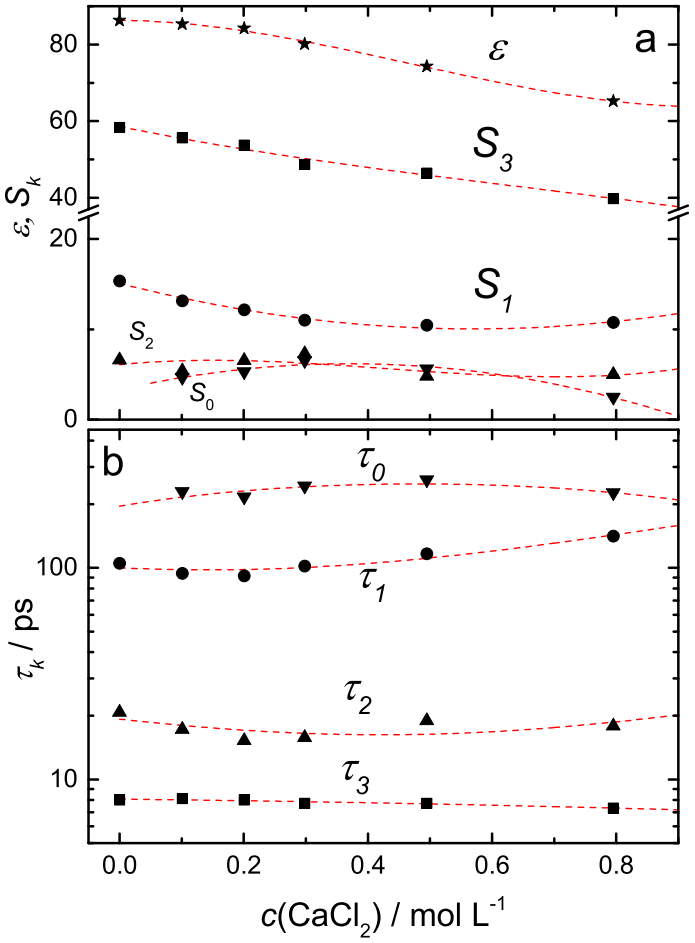

Figure A.46: (a) Static permittivities, $\varepsilon(\bigstar)$, and relaxation amplitudes, $S_0(\blacktriangledown), S_1(\bullet), S_2(\blacktriangle), S_3(\blacksquare)$, and (b) the respective relaxation times, $\tau_0(\blacktriangledown), \tau_1(\bullet), \tau_2(\blacktriangle), \tau_3(\blacksquare)$, of the NaGlu+$CaCl_2$(aq) solutions ($c$(NaGlu) $\approx$ 0.4 M) at 25 °C as a function of $CaCl_2$ concentration, $c(CaCl_2)$. The dashed lines are guides to the eye. Parameters of fast-water process $k = 4$ are not shown.

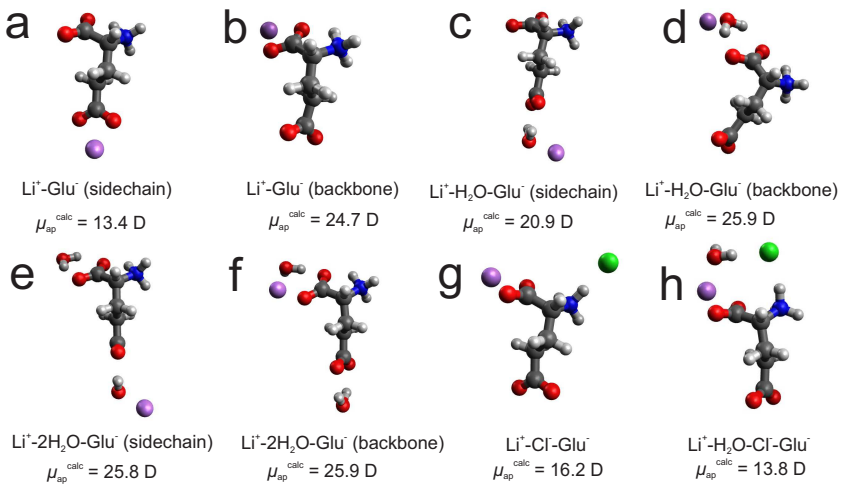

Figure A.47: Lowest-energy structures of various ion pairs of glutamate and lithium and its hydrates (a-h) as obtained by Gaussian 09 at the B3LYP/6-31G(d,p) level using the PCM solvation model. Blue: nitrogen, red: oxygen, dark-gray: carbon, light-gray: hydrogen, purple: lithium, green: chloride.

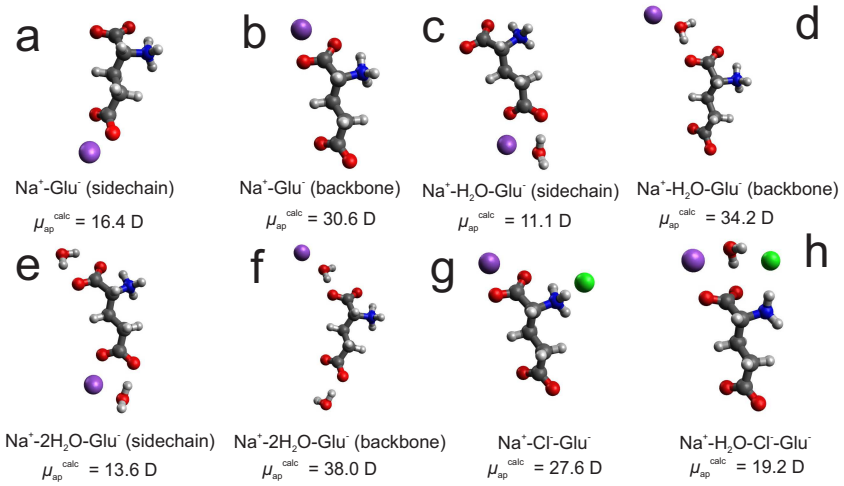

Figure A.48: Lowest-energy structures of various ion pairs of glutamate and sodium and its hydrates (a-h) as obtained by Gaussian 09 at the B3LYP/6-31G(d,p) level using the PCM solvation model. Blue: nitrogen, red: oxygen, dark-gray: carbon, light-gray: hydrogen, purple: sodium, green: chloride.

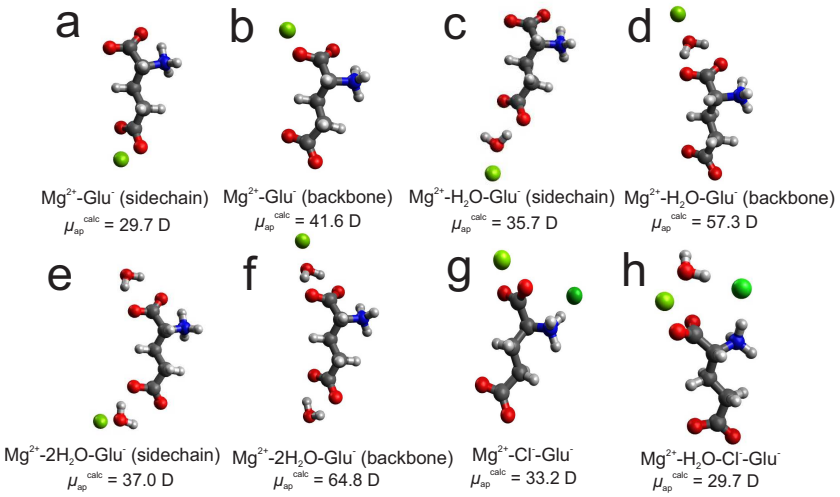

Figure A.49: Lowest-energy structures of various ion pairs of glutamate and magnesium and its hydrates (a-h) as obtained by Gaussian 09 at the B3LYP/6-31G(d,p) level using the PCM solvation model. Blue: nitrogen, red: oxygen, dark-gray: carbon, light-gray: hydrogen, mint green: magnesium, green: chloride.

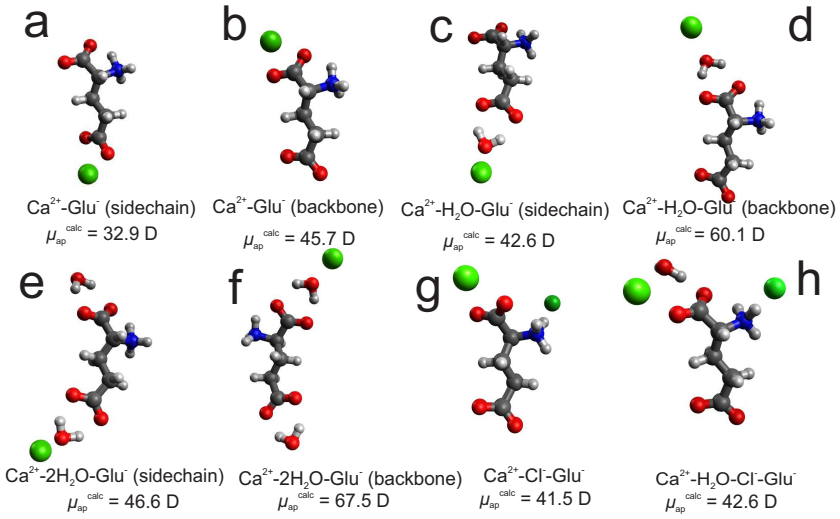

Figure A.50: Lowest-energy structures of various ion pairs of glutamate and calcium and its hydrates (a-h) as obtained by Gaussian 09 at the B3LYP/6-31G(d,p) level using the PCM solvation model. Blue: nitrogen, red: oxygen, dark-gray: carbon, light-gray: hydrogen, mint green: calcium, green: chloride.

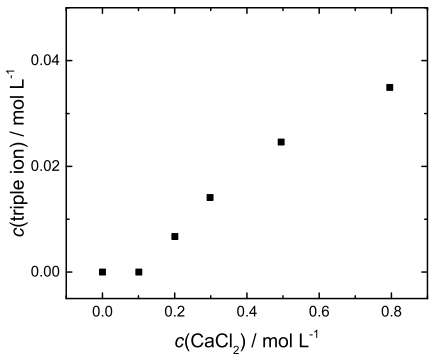

Figure A.51: Concentration of triple ions, c(triple ion), as a function of $c(CaCl_2)$, as estimated from μ_{eff} in figure 5.6(d).

Table A.20: Molar concentrations, c, densities, ρ, viscosities, η, conductivities, κ, and their respective uncertainties, $\Delta\eta$ and $\Delta\kappa$, of ternary solutions of Gln(aq) and different chloride salts at 25 °C.

c(salt) / mol L^{-1}	c(NaGlu) / mol L^{-1}	ρ / g cm^{-3}	η / mPa s	$\Delta\eta$ / mPa s	κ / S m^{-1}	$\Delta\kappa$ / S m^{-1}
			LiCl			
0	0.1991	1.007548	0.9555	0.0007	–	–
0.05155	0.1989	1.008807	0.9588	0.0005	0.503	0.001
0.1010	0.1987	1.009944	0.9647	0.0004	0.894	0.002
0.2012	0.1984	1.012396	0.9796	0.0006	1.718	0.004
0.3990	0.1976	1.017090	1.0086	0.0008	3.230	0.005
0.6335	0.1967	1.022518	1.0448	0.0006	5.91	0.01
			NaCl			
0	0.1991	1.007548	0.9555	0.0007	–	–
0.05826	0.1989	1.009924	0.9549	0.0005	0.627	0.001
0.1136	0.1987	1.012050	0.9612	0.0006	1.119	0.003
0.2078	0.1983	1.015935	0.9681	0.0006	2.032	0.003
0.4228	0.1975	1.024450	0.9879	0.0010	4.154	0.007
0.6287	0.1968	1.032523	1.008	0.002	5.88	0.01
			$MgCl_2$			
0	0.2016	1.007658	0.9427	0.0007	–	–
0.05073	0.2004	1.011551	0.990	0.003	0.925	0.002
0.08444	0.1995	1.014138	0.9838	0.0009	1.494	0.002
0.1515	0.1978	1.019158	1.0086	0.0008	2.671	0.005
0.3089	0.1937	1.030868	1.0715	0.0008	4.93	0.01
0.5640	0.1867	1.047584	1.1720	0.0008	7.67	0.02
			$CaCl_2$			
0	0.2016	1.007658	0.9427	0.0007	–	–
0.03936	0.2012	1.011197	0.959	0.001	0.770	0.002
0.0792	0.2007	1.014730	0.972	0.001	1.481	0.002
0.1748	0.1996	1.023130	1.18	0.02	3.214	0.007
0.3071	0.1980	1.034635	1.092	0.004	5.27	0.01
0.5357	0.1952	1.054279	1.123	0.002	8.36	0.02

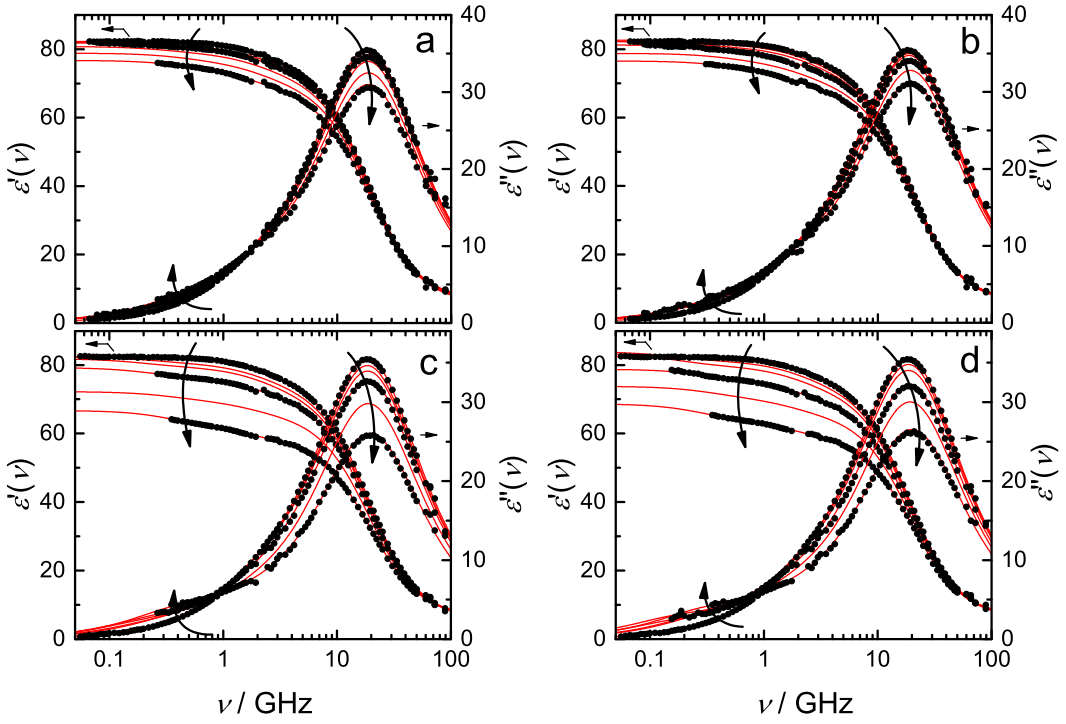

Figure A.52: Relative permittivity, $\varepsilon'(\nu)$, and dielectric loss, $\varepsilon''(\nu)$, spectra of (a) Gln+LiCl(aq) (c(Gln) $\approx$ 0.2 M; 0 $\leq$ c(LiCl)/mol L^{-1} $\leq$ 0.6335), (b) Gln+NaCl(aq) (c(Gln) $\approx$ 0.2 M; 0 $\leq$ c(NaCl)/mol L^{-1} $\leq$ 0.6287), (c) Gln+$MgCl_2$(aq) (c(Gln) $\approx$ 0.2 M; 0 $\leq$ c($MgCl_2$)/mol L^{-1} $\leq$ 0.5640) and (d) Gln+$CaCl_2$(aq) (c(Gln) $\approx$ 0.2 M; 0 $\leq$ c($CaCl_2$)/mol L^{-1} $\leq$ 0.5357) at 25 °C. Symbols denote the experimental data. Solid lines represent the fits. For visual clarity data points are only shown for selected samples. Arrows indicate the trend with increasing solute concentration.

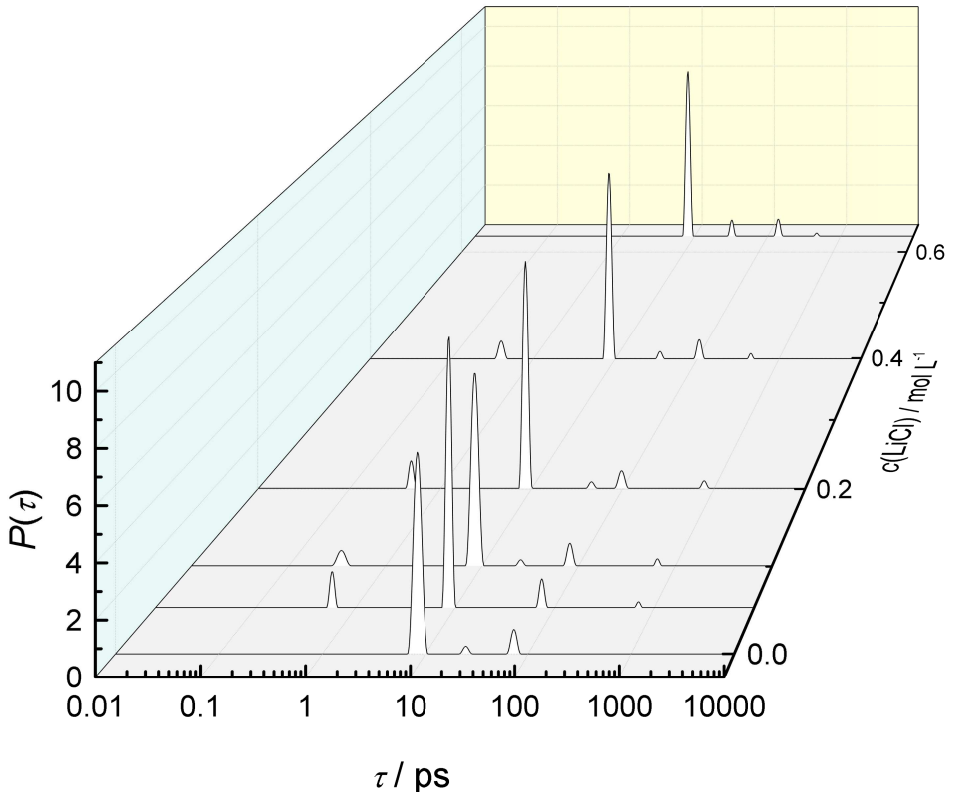

Figure A.53: Relaxation-time distribution, $P(t)$, of dielectric data of $\sim 0.2\,\mathrm{M}$ Gln(aq) with added LiCl (Gln+LiCl(aq)) at 25 °C, obtained *via* Zasetsky's computational procedure [114].

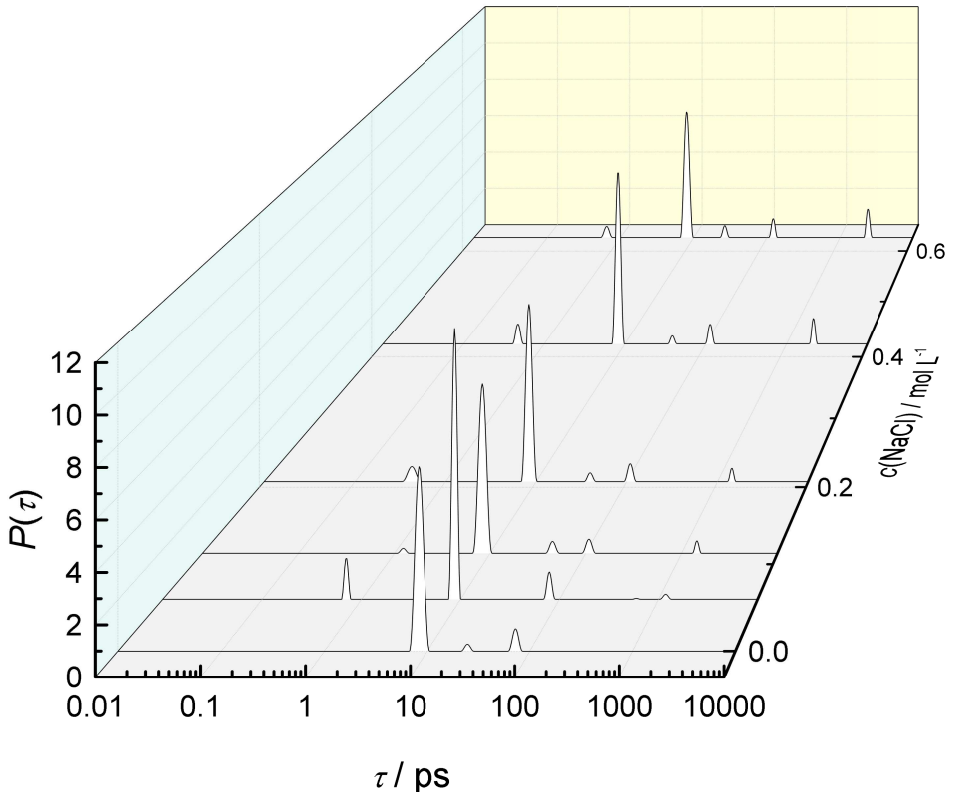

Figure A.54: Relaxation-time distribution, $P(t)$, of dielectric data of $\sim 0.2\,\mathrm{M}$ Gln(aq) with added NaCl (Gln+NaCl(aq)) at 25 °C, obtained *via* Zasetsky's computational procedure [114].

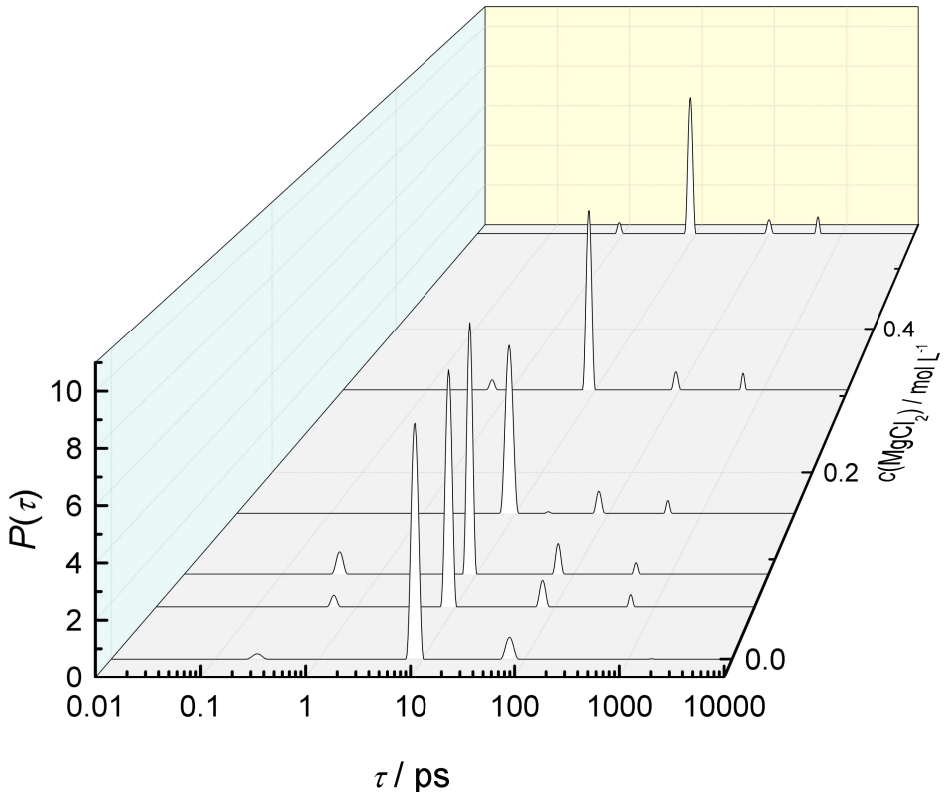

Figure A.55: Relaxation-time distribution, $P(t)$, of dielectric data of $\sim 0.2\,\mathrm{M}$ Gln(aq) with added $MgCl_2$ (Gln+$MgCl_2$(aq)) at 25 °C, obtained *via* Zasetsky's computational procedure [114].

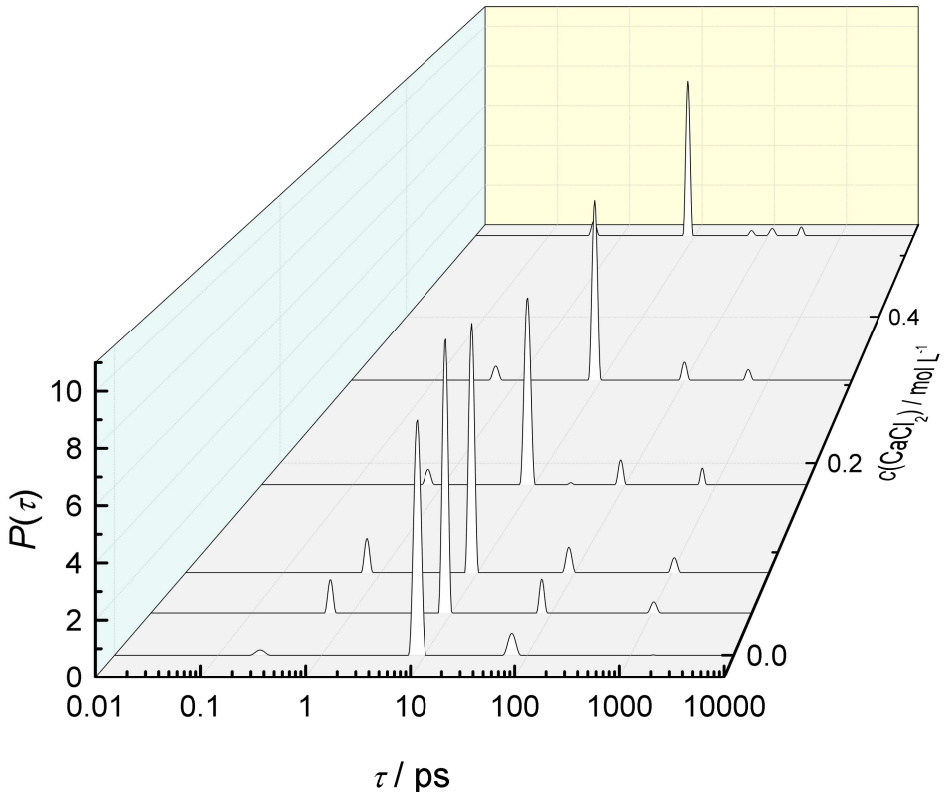

Figure A.56: Relaxation-time distribution, $P(t)$, of dielectric data of ~ 0.2 M Gln(aq) with added $CaCl_2$ (Gln+$CaCl_2$(aq)) at 25 °C, obtained *via* Zasetsky's computational procedure [114].

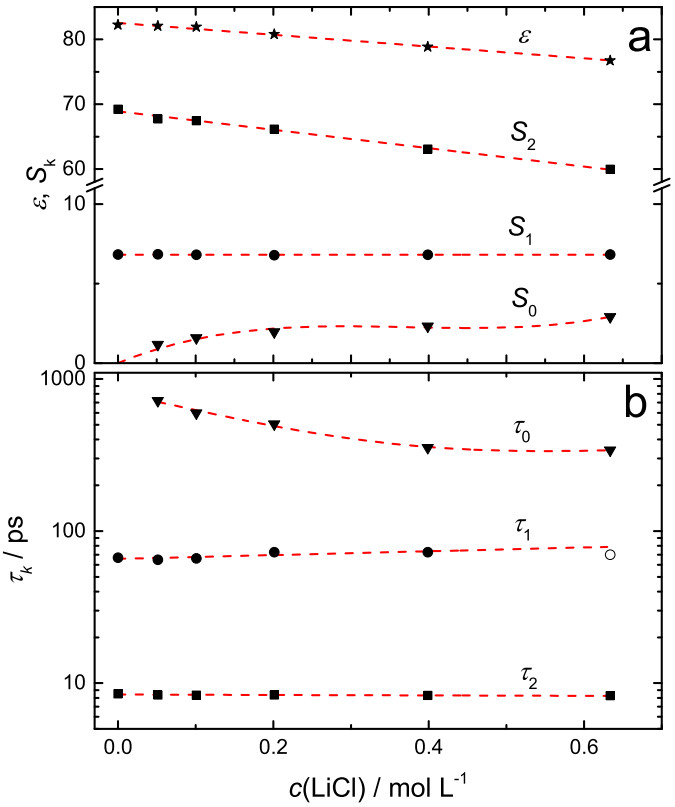

Figure A.57: (a) Static permittivities, $\varepsilon(\bigstar)$, and relaxation amplitudes, $S_0(\blacktriangledown), S_1(\bullet), S_2(\blacksquare)$, and (b) the respective relaxation times, $\tau_0(\blacktriangledown), \tau_1(\bullet), \tau_2(\blacksquare)$, of the Gln+LiCl(aq) solutions (c(Gln) $\approx 0.2\,$M) at 25 °C as a function of LiCl concentration, c(LiCl). The dashed lines are guides to the eye. Hollow symbol denotes a parameter which was fixed during fitting of the dielectric spectra. Parameters of fast-water process $k = 3$ are not shown.

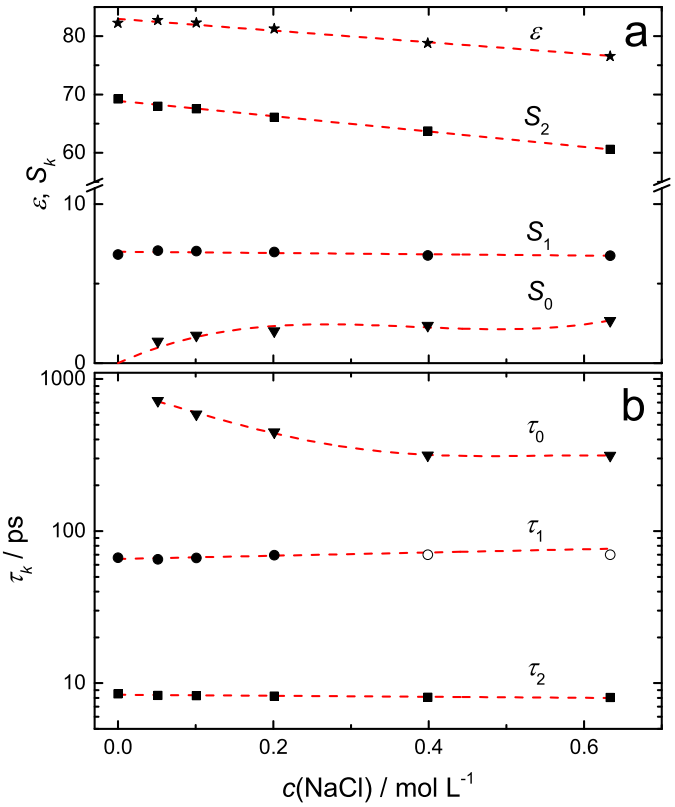

Figure A.58: (a) Static permittivities, $\varepsilon(\bigstar)$, and relaxation amplitudes, $S_0(\blacktriangledown), S_1(\bullet), S_2(\blacksquare)$, and (b) the respective relaxation times, $\tau_0(\blacktriangledown), \tau_1(\bullet), \tau_2(\blacksquare)$, of the Gln+NaCl(aq) solutions (c(Gln) $\approx 0.2\,$M) at 25 °C as a function of NaCl concentration, c(NaCl). The dashed lines are guides to the eye. Hollow symbols denote a parameters which were fixed during fitting of the dielectric spectra. Parameters of fast-water process $k = 3$ are not shown.

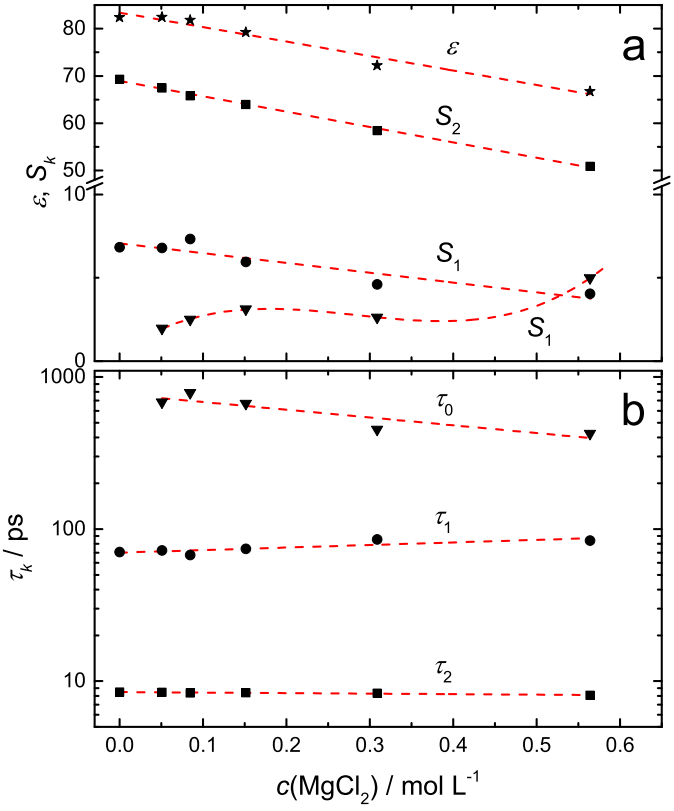

Figure A.59: (a) Static permittivities, $\varepsilon(\bigstar)$, and relaxation amplitudes, $S_0(\blacktriangledown), S_1(\bullet), S_2(\blacksquare)$, and (b) the respective relaxation times, $\tau_0(\blacktriangledown), \tau_1(\bullet), \tau_2(\blacksquare)$, of the Gln+$MgCl_2$(aq) solutions ($c$(Gln) ≈ 0.2 M) at 25 °C as a function of $MgCl_2$ concentration, $c(MgCl_2)$. The dashed lines are guides to the eye. Parameters of fast-water process $k = 3$ are not shown.

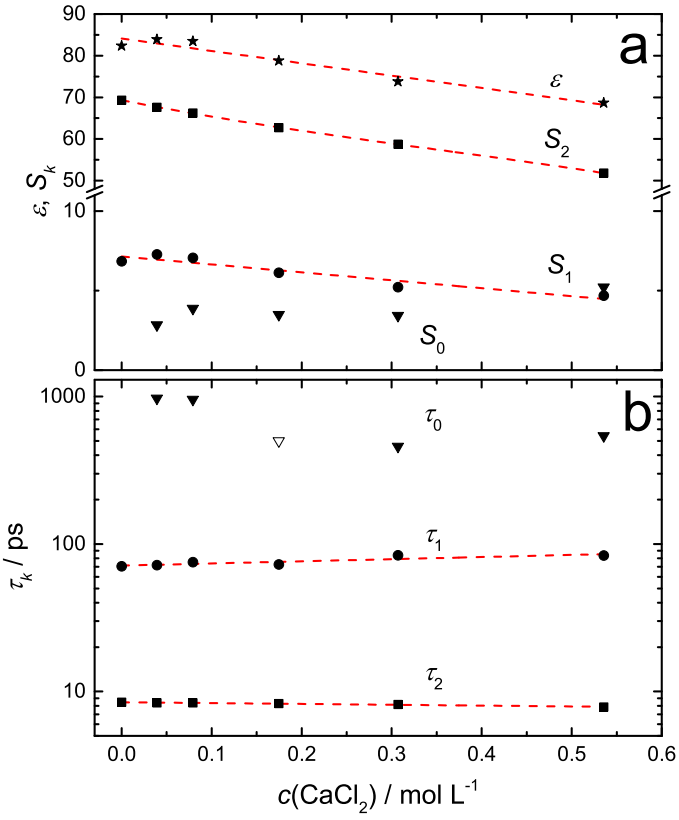

Figure A.60: (a) Static permittivities, $\varepsilon(\bigstar)$, and relaxation amplitudes, $S_0(\blacktriangledown), S_1(\bullet), S_2(\blacksquare)$, and (b) the respective relaxation times, $\tau_0(\blacktriangledown), \tau_1(\bullet), \tau_2(\blacksquare)$, of the Gln+$CaCl_2$(aq) solutions ($c$(Gln) $\approx 0.4\,$M) at 25 °C as a function of $CaCl_2$ concentration, $c(CaCl_2)$. The dashed lines are guides to the eye. Hollow symbol denotes a parameter which was fixed during fitting of the dielectric spectra. Parameters of fast-water process $k = 3$ are not shown.

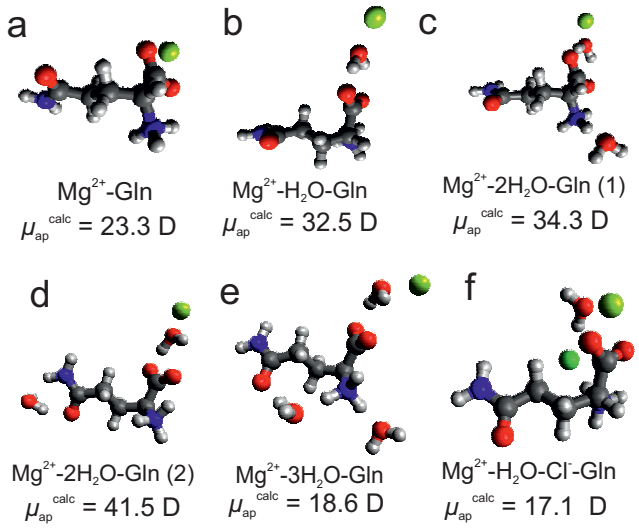

Figure A.61: Lowest-energy structures of various ion pairs of glutamine and magnesium and its hydrates (a-f) as obtained by Gaussian 09 at the B3LYP/6-31G(d,p) level using the PCM solvation model. Blue: nitrogen, red: oxygen, dark-gray: carbon, light-gray: hydrogen, mint green: magnesium, green: chloride.

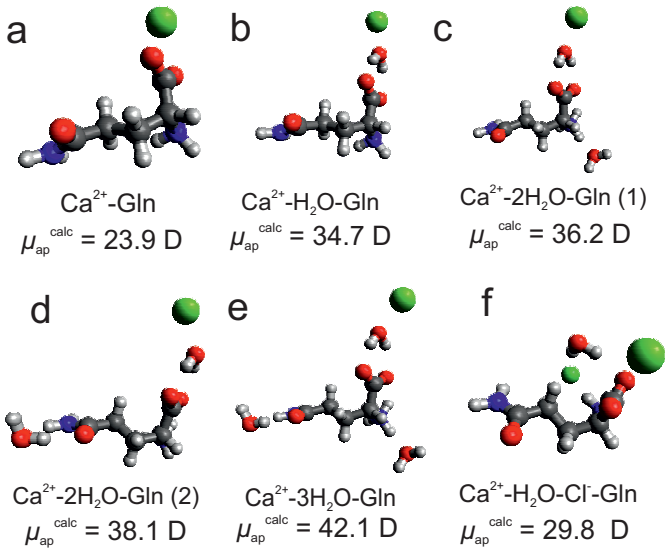

Figure A.62: Lowest-energy structures of various ion pairs of glutamine and calcium and its hydrates (a-f) as obtained by Gaussian 09 at the B3LYP/6-31G(d,p) level using the PCM solvation model. Blue: nitrogen, red: oxygen, dark-gray: carbon, light-gray: hydrogen, mint green: caclium, green: chloride.

Appendix B

Kinetic Dipolarization

About 40 years ago, Hubbard and Onsager [382–384] introduced the concept of "kinetic depolarization" in electrolyte solutions, an effect which until today has eluded direct experimental observation. Their concept can be described as follows: ions moving in an applied electric field, $\vec{E}$, exert a torque on neighboring dipolar solvent molecules. This additional force opposes the reorienting force of the applied field, resulting in a depolarization of the bulk solvent molecules. Experimentally, this depolarization is expressed as a reduction of the apparent bulk solvent amplitude, $S_{\mathrm{b}}^{\mathrm{ap}}$, by a kinetic dielectric decrement, $\Delta\varepsilon_{\mathrm{kd}}$. Thus, the corrected equilibrium solvent amplitude, $S_{\mathrm{b}}^{\mathrm{eq}}$, can be written as

$$S_{\mathrm{b}}^{\mathrm{eq}} = S_{\mathrm{b}}^{\mathrm{ap}} + \Delta\varepsilon_{\mathrm{kd}} \tag{B.1}$$

In the Hubbard-Onsager (HO) continuum model dielectric increment can be obtained by

$$\Delta\varepsilon_{\mathrm{kd}}^{\mathrm{HO}} = p \cdot \frac{\varepsilon(0) - \varepsilon_{\infty}(0)}{\varepsilon(0)} \cdot \frac{\tau(0)}{\varepsilon_0} \cdot \kappa \tag{B.2}$$

where ε_0 is the permittivity of free space, $\varepsilon(0)$ and $\varepsilon_{\infty}(0)$ are the static and infinite-frequency permittivities of the neat solvent, $\tau(0)$ is the relaxation time of the solvent dispersion step, κ is the solution electrical conductivity, and p is a hydrodynamic parameter which describes the coupling of translational ion motions to the macroscopic viscosity. For $p = 1$, so-called *stick*, and for $p = 2/3$ *slip* boundary conditions apply. Generally, *slip* conditions are considered more physically realistic [319, 385]. Consequently, *slip* conditions are frequently selected as the conditions of choice. The HO theory is valid only at infinite dilution of the electrolyte and thus its application to concentrated solutions is problematic. Recently Sega, Kantorovich and Arnold (SKA) introduced an empirical modification of the HO equation to account for finite salt concentrations [184]

$$\Delta\varepsilon_{\mathrm{kd}}^{\mathrm{SKA}} = \Delta\varepsilon_{\mathrm{kd}}^{\mathrm{HO}} \cdot \exp(\sigma R_{\mathrm{eff}}) \cdot (\sigma R_{\mathrm{eff}} + 2)/2 \tag{B.3}$$

where σ is the reciprocal Debye length and R_{eff} is the effective ion radius. Whereas σ can be calculated readily from the ionic strength [297], the determination of R_{eff} is not straightforward. For binary systems, *e.g.* a single salt dissolved in a solvent, the effective

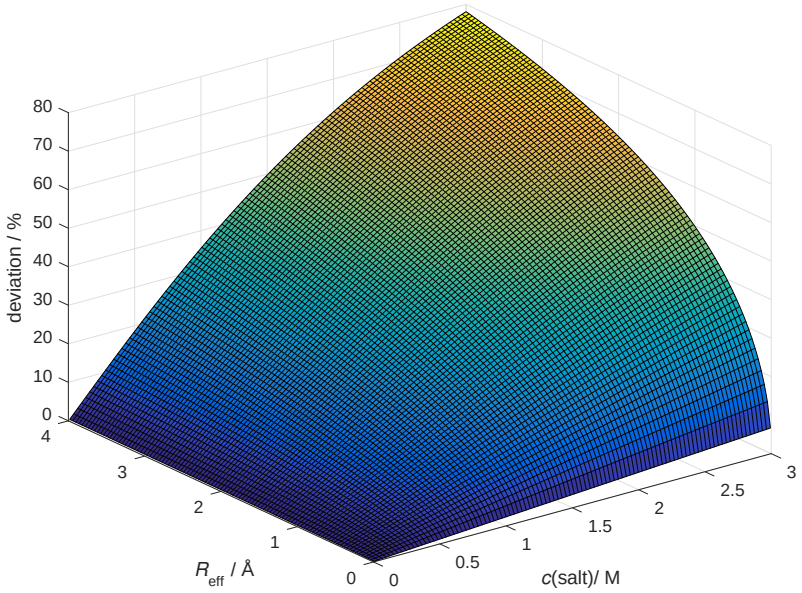

Figure B.1: Relative deviation of the SKA model from the HO continuum model as a function of the salt concentration, c(salt), and the effective ionic radius, R_{eff}, of a model salt in aqueous solution at 25 °C.

radius has to be defined in such way that the size of both, the cation and anion, are taken into account. The choice of R_{eff} is somewhat critical, as $\Delta\varepsilon_{\mathrm{kd}}^{\mathrm{Sega}}$ markedly depends on R_{eff}. Assuming a system containing of a model salt of concentration, c(salt), an effective ionic radius, R_{eff}, deviations of the SKA-approach from the classical HO-model can be calculated. As can be seen in Figure B.1, the relative deviation increases with increasing R_{eff} and increasing salt concentration, and the SKA-model reduces to the HO-model for low R_{eff} and low c(salt), respectively, as would be expected from the limitations of both theories. In the present work, the effective radii of binary solutions were calculated by taking the arithmetic mean of the respective cation and anion radius.

The situation is more complicated for ternary solutions, *i.e.*, a "solute" (*e.g.* neurotransmitter) + "background electrolyte" in water, as investigated in the present thesis. Under the assumption of additivity of the kinetic depolariazion effects of the dissolved species, while keeping the solute concentration, c(solute), constant and varying the background

electrolyte concentration, c(backgroud), the dielectric decrement could be described as

$$\begin{aligned}\Delta\varepsilon_{\mathrm{kd}}^{\mathrm{SKA}} = p \cdot \frac{\varepsilon(0) - \varepsilon_\infty(0)}{\varepsilon(0)} \cdot \frac{\tau(0)}{\varepsilon_0} \cdot \{&\kappa(\mathrm{solute}) \cdot \exp\left[\sigma R_{\mathrm{eff}}(\mathrm{solute})\right] \cdot \left[\sigma R_{\mathrm{eff}}(\mathrm{solute}) + 2\right]/2 \\ &+ \kappa(\mathrm{backgroud}) \cdot \exp\left[\sigma R_{\mathrm{eff}}(\mathrm{background})\right] \cdot \left[\sigma R_{\mathrm{eff}}(\mathrm{backgroud}) + 2\right]/2\}\end{aligned} \tag{B.4}$$

In equation B.4 R_{eff}(solute) and R_{eff}(background) denote the effective radii, while κ(solute) and κ(background) are the conductivity contributions (to the overall electrical conductivity) of the solute and the electrolyte, respectively. However, this approach is rather cumbersome and the actual separation of the conductivity in a solute and a background electrolyte-dependent part is fairly difficult to realize at higher concentrations from a theoretical standpoint. Therefore, similarly to the binary system, the approach of introducing a single effective radius was adopted for the ternary solutions. In this case, R_{eff} can be obtained as a weighted arithmetic mean of the respective ionic radii

$$R_{\mathrm{eff}} = \sum_i^n \frac{c_i}{\sum_i^n c_i} R_{\mathrm{eff},i} \tag{B.5}$$

where c_i is the concentration of ion i in the solution. Figure B.2 shows the deviation of $\Delta\varepsilon_{\mathrm{kd}}^{\mathrm{SKA}}$ using one-effective-radius approach (equation B.5) instead of the "extended" approach of equation B.4 for a model ternary system. The solute properties (c(solute) = 0.3 M; R_{eff}(solute) = 2.5 Å) as well as the ratios of the radii and the concentrations represent very well the conditions of many systems investigated in this work. The small deviations of up to only a few percent, which is the essentially the error limit of the DR measurement, justify the application of "simplified" one-effective-radius approach for the calculation of the dielectric decrement, which was consequently utilized throughout this thesis.

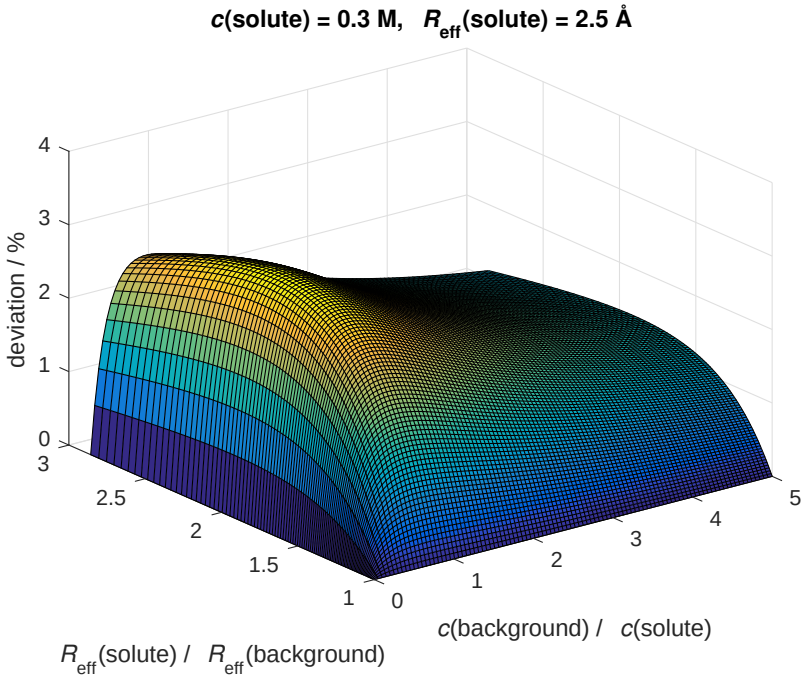

Figure B.2: Relative deviation of the one-effective-radius approach from the approach of equation B.4 as a function of the ratios of the effective radii and concentrations of the "solute" and the "background electrolyte" in a model ternary aqueous solution at 25 °C. The concentration of the solute was fixed to $c(\text{solute}) = 0.3\,\text{M}$ and the effective radius of the solute was assumed to be $R_{\text{eff}}(\text{solute}) = 2.5\,\text{Å}$.

Appendix C

Correction of Raw Spectra for the Presence of IPs

As previously shown in Section 4.1 spectra of $MgCl_2$(aq) and $CaCl_2$(aq) show clear evidence for the presence of two distinct dipolar IP species, which consequently contribute to the DR spectra. Thus, the pursued quantification of the effects of the added salt on NaGlu(aq) and Gln(aq) was superimposed by the IP relaxation of the electrolyte. In order to account for that, the contribution of the IPs was subtracted from the raw data, $\hat{\varepsilon}^{\mathrm{raw}}(\nu)$, using the parameters and association constants from Section 4.1 to predict the relaxation strength and location of the IP modes. Note that hereby ideality conditions were assumed, *i.e.,* the extent of IP formation was assumed to be only dependent on the ionic strength, I, and the relaxation times of the IP processes were supposed to be unchanged compared to "pure" $MgCl_2$(aq) and $CaCl_2$ solutions. Thus, for NaGlu(aq) and Gln(aq) solutions containing $MgCl_2$ and $CaCl_2$ the corrected dielectric spectra read

$$\hat{\varepsilon}(\nu) = \varepsilon^{\mathrm{raw}}(\nu) - \sum_{n=1}^{2} \frac{S_n^{\mathrm{IP}}(I)}{1 + \mathrm{i}2\pi\nu\tau_n^{\mathrm{IP}}} \tag{C.1}$$

with n indicating the two different IP contributions. Figures C.1 shows the effect of the correction in the NaGlu(aq)+$MgCl_2$(aq) spectra. Note this kind of IP correction was not performed for KCl, KF, NaCl and LiCl background electrolytes, as the extent of IP formation and thus their contribution to the DR spectra is rather low for these salts [55, 289–292]. Furthermore, as discussed in Ref. [55], evidence for significant contribution of ion-cloud relaxation to the alleged IP mode of NaCl(aq) was found. Although its contribution was thought to be rather small in electrolyte solutions, fairly recent results indicate that this is not necessarily the case [55, 166]. As already mentioned in the main text, currently there is no theory available to separate the IC contribution from the overall dielectric response. Reanalysis of the spectra of LiCl(aq) from Ref. [289] and KF(aq) [291], using a more recent nonlinear least-squares routine under IGOR Pro [112] of our laboratory, reveal a similar picture for the latter two salts (unpublished).

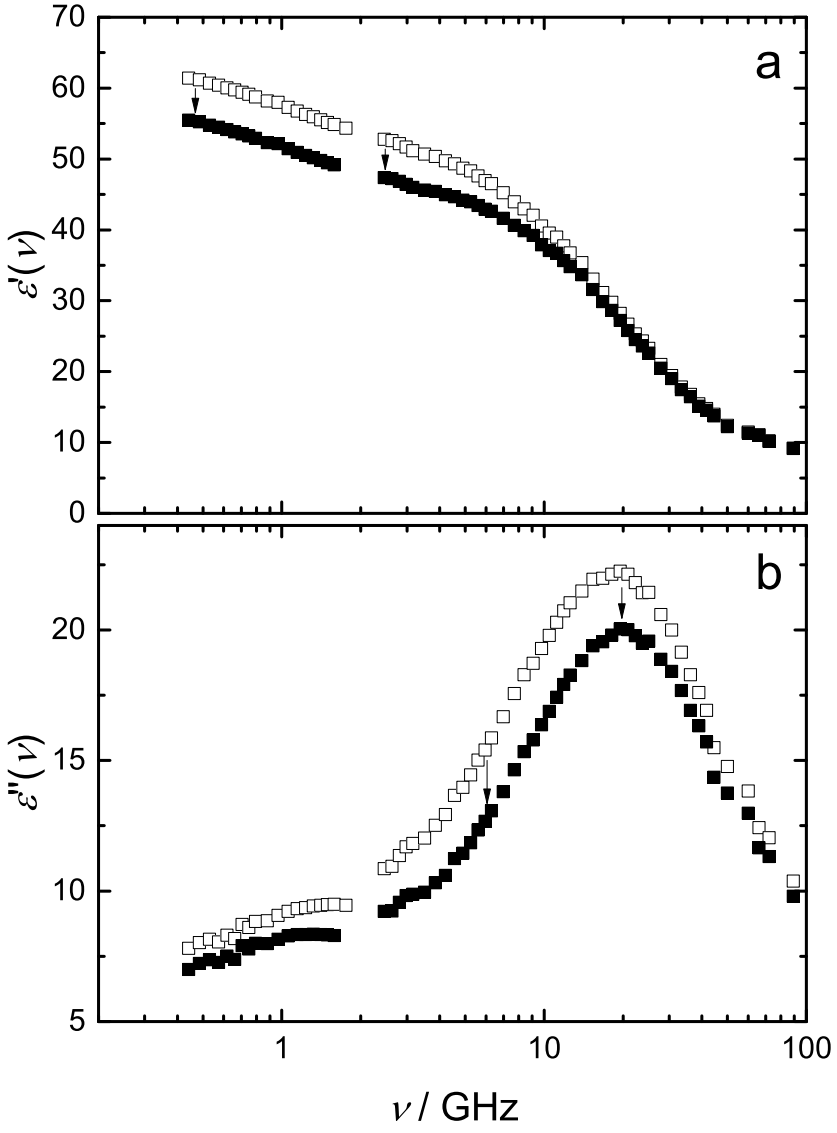

Figure C.1: (a) Relative permittivity and (b) dielectric loss spectra before (open symbols) and after (filled symbols) the correction for $MgCl^+$-IP formation in $c(\mathrm{NaGlu}) \approx 0.4\,\mathrm{M}$ with $c(\mathrm{MgCl_2}) = 0.8358\,\mathrm{M}$ at 25 °C.

Bibliography

[1] Ball, P. Water as an active constituent in cell biology. *Chem. Rev.* **2008**, *108*, 74–108.

[2] Bianco, V.; Iskrov, S.; Franzese, G. Understanding the role of hydrogen bonds in water dynamics and protein stability. *J. Biol. Phys.* **2012**, *38*, 27–48.

[3] Frauenfelder, H.; Fenimore, P. W.; Chen, G.; McMahon, B. H. Protein folding is slaved to solvent motions. *PNAS* **2006**, *103*, 15469–15472.

[4] Levy, Y.; Onuchic, J. N. Water mediation in protein folding and molecular recognition. *Annu. Rev. Biophys. Biomol. Struct.* **2006**, *35*, 389–415.

[5] Maruyama, Y.; Harano, Y. Does water drive protein folding? *Chem. Phys. Lett.* **2013**, *581*, 85–90.

[6] Papoian, G. A.; Ulander, J.; Eastwood, M. P.; Luthey-Schulten, Z.; Wolynes, P. G. Water in protein structure prediction. *Proc. Natl. Acad. Sci. U.S.A.* **2004**, *101*, 3352–3357.

[7] Levinson, N. M.; Boxer, S. G. A conserved water-mediated hydrogen bond network defines bosutinib's kinase selectivity. *Nat. Chem. Biol.* **2014**, *10*, 127–132.

[8] Breiten, B.; Lockett, M. R.; Sherman, W.; Fujita, S.; Al-Sayah, M.; Lange, H.; Bowers, C. M.; Heroux, A.; Krilov, G.; Whitesides, G. M. Water networks contribute to enthalpy/entropy compensation in protein–ligand binding. *J. Am. Chem. Soc.* **2013**, *135*, 15579–15584.

[9] Setny, P.; Baron, R.; Kekenes-Huskey, P. M.; McCammon, J. A.; Dzubiella, J. Solvent fluctuations in hydrophobic cavity–ligand binding kinetics. *PNAS* **2013**, *110*, 1197–1202.

[10] Biedermannová, L.; Schneider, B. Hydration of proteins and nucleic acids: Advances in experiment and theory. A review. *Biochim. Biophys. Acta* **2016**, *1860*, 1821–1835.

[11] Harmon, K. M.; Akin, A. C.; Avci, G. F.; Nowos, L. S.; Tierney, M. B. Hydrogen bonding: Part 33. NMR study of the hydration of choline and acetylcholine halides. *J. Mol. Struct.* **1991**, *244*, 223–236.

[12] Svergun, D. I.; Richard, S.; Koch, M. H. J.; Sayers, Z.; Kuprin, S.; Zaccai, G. Protein hydration in solution: Experimental observation by x-ray and neutron scattering. *PNAS* **1998**, *95*, 2267–2272.

[13] Soper, A. K.; Weckström, K. Ion solvation and water structure in potassium halide aqueous solutions. *Biophys. Chem.* **2006**, *124*, 180–191.

[14] Turner, J.; Soper, A.; Finney, J. A neutron-diffraction study of tetramethylammonium chloride in aqueous solution. *Mol. Phys.* **1990**, *70*, 679–700.

[15] Daub, C. D.; Leung, K.; Luzar, A. Structure of aqueous solutions of monosodium glutamate. *J. Phys. Chem. B* **2009**, *113*, 7687–7700.

[16] Fedotova, M. V.; Kruchinin, S. E. Hydration of acetic acid and acetate ion in water studied by 1D-RISM theory. *J. Mol. Liq.* **2011**, *164*, 201–206.

[17] Fedotova, M. V.; Kruchinin, S. E. Hydration of methylamine and methylammonium ion: structural and thermodynamic properties from the data of the integral equation method in the RISM approximation. *Russ. Chem. Bull.* **2012**, *61*, 240–247.

[18] Fedotova, M. V.; Kruchinin, S. E. Hydration of para-aminobenzoic acid (PABA) and its anion–The view from statistical mechanics. *J. Mol. Liq.* **2013**, *186*, 90–97.

[19] Heyden, M.; Tobias, D. J. Spatial dependence of protein-water collective hydrogen-bond dynamics. *Phys. Rev. Lett.* **2013**, *111*, 218101.

[20] Xu, J.; Plaxco, K. W.; Allen, S. J. Probing the collective vibrational dynamics of a protein in liquid water by terahertz absorption spectroscopy. *Protein Sci.* **2006**, *15*, 1175–1181.

[21] Heugen, U.; Schwaab, G.; Bründermann, E.; Heyden, M.; Yu, X.; Leitner, D. M.; Havenith, M. Solute-induced retardation of water dynamics probed directly by terahertz spectroscopy. *PNAS* **2006**, *103*, 12301–12306.

[22] Buchner, R.; Hefter, G. Interactions and dynamics in electrolyte solutions by dielectric spectroscopy. *Phys. Chem. Chem. Phys.* **2009**, *11*, 8984–8999.

[23] Kuntz, I. D.; Kauzmann, W. In *Advances in Protein Chemistry*; Anfinsen, C. B., Edsall, J. T., Richards, F. M., Eds.; Academic Press: Cambridge, 1974; Vol. 28; pp 239–345.

[24] Hofmeister, F. Zur Lehre von der Wirkung der Salze. *Arch. Exp. Pathol. Pharmakol.* **1888**, *24*, 247–260.

[25] Kunz, W.; Henle, J.; Ninham, B. W. 'Zur Lehre von der Wirkung der Salze' (about the science of the effect of salts): Franz Hofmeister's historical papers. *Curr. Opin. Colloid Interface Sci.* **2004**, *9*, 19–37.

[26] Kunz, W., Ed. *Specific Ion Effects*; World Scientific: Singapore, 2010.

[27] Schwierz, N.; Horinek, D.; Netz, R. R. Reversed anionic Hofmeister series: The interplay of surface charge and surface polarity. *Langmuir* **2010**, *26*, 7370–7379.

[28] Collins, K. D. Why continuum electrostatics theories cannot explain biological structure, polyelectrolytes or ionic strength effects in ion–protein interactions. *Biophys. Chem.* **2012**, *167*, 43–59.

[29] Salis, A.; Ninham, B. W. Models and mechanisms of Hofmeister effects in electrolyte solutions, and colloid and protein systems revisited. *Chem. Soc. Rev.* **2014**, *43*, 7358–7377.

[30] Kunz, W. Specific ion effects in colloidal and biological systems. *Curr. Opin. Colloid Interface Sci.* **2010**, *15*, 34–39.

[31] Salis, A.; Cugia, F.; Parsons, D. F.; Ninham, B. W.; Monduzzi, M. Hofmeister series reversal for lysozyme by change in pH and salt concentration: insights from electrophoretic mobility measurements. *Phys. Chem. Chem. Phys.* **2012**, *14*, 4343–4346.

[32] Gurney, R. W. *Ionic Processes In Solution*; McGraw-Hill: New York, 1953.

[33] Collins, K. D.; Washabaugh, M. W. The Hofmeister effect and the behaviour of water at interfaces. *Q. Rev. Biophys.* **1985**, *18*, 323–422.

[34] Marcus, Y. Effect of ions on the structure of water: Structure making and breaking. *Chem. Rev.* **2009**, *109*, 1346–1370.

[35] Sun, S.; Bernstein, E. R. Spectroscopy of seurotransmitters and their clusters. 1. Evidence for five molecular conformers of phenethylamine in a supersonic jet expansion. *J. Am. Chem. Soc.* **1996**, *118*, 5086–5095.

[36] Vistoli, G.; Pedretti, A.; Villa, L.; Testa, B. Solvent constraints on the property space of acetylcholine. I. Isotropic solvents. *J. Med. Chem.* **2005**, *48*, 1759–1767.

[37] Partington, P.; Feeney, J.; Burgen, A. S. V. The conformation of acetylcholine and related compounds in aqueous solution as studied by nuclear magnetic resonance spectroscopy. *Mol. Pharmacol.* **1972**, *8*, 269–277.

[38] Segall, M. D.; Payne, M. C.; Boyes, R. N. An *ab initio* study of the conformational energy map of acetylcholine. *Mol. Phys.* **1998**, *93*, 365–370.

[39] Nagy, P. I.; Alagona, G.; Ghio, C.; Takács-Novák, K. Theoretical conformational analysis for neurotransmitters in the gas phase and in aqueous solution. Norepinephrine. *J. Am. Chem. Soc.* **2003**, *125*, 2770–2785.

[40] Alagona, G.; Ghio, C.; Nagy, P. Theoretical conformational analysis for neurotransmitters in the gas phase and in aqueous solution. Serotonin. *J. Chem. Theory Comput.* **2005**, *1*, 801–816.

[41] Ottosson, N.; Pastorczak, M.; Post, S. T. v. d.; J. Bakker, H. Conformation of the neurotransmitter γ-aminobutyric acid in liquid water. *Phys. Chem. Chem. Phys.* **2014**, *16*, 10433–10437.

[42] Pálinkás, G.; Radnai, T.; Dietz, W.; Szász, G. I.; Heinzinger, K. Hydration shell structures in an $MgCl_2$ solution from X-ray and MD studies. *Z. Naturforsch. A.* **1982**, *37*, 1049–1060.

[43] Dai, Q.; Xu, J.-J.; Li, H.-J.; Yi, H.-B. Ion association characteristics in $MgCl_2$ and $CaCl_2$ aqueous solutions: a density functional theory and molecular dynamics investigation. *Mol. Phys.* **2015**, *113*, 3545–3558.

[44] Barthel, J.; Hetzenauer, H.; Buchner, R. Dielectric relaxation of aqueous electrolyte solutions. I. Solvent relaxation of 1:2, 2:1, and 2:2 electrolyte solutions. *Ber. Bunsen Ges.* **1992**, *96*, 988–997.

[45] Fulton, J. L.; Heald, S. M.; Badyal, Y. S.; Simonson, J. M. Understanding the effects of concentration on the solvation structure of Ca^{2+} in aqueous solution. I: The perspective on local structure from EXAFS and XANES. *J. Phys. Chem. A* **2003**, *107*, 4688–4696.

[46] Megyes, T.; Bakó, I.; Bálint, S.; Grósz, T.; Radnai, T. Ion pairing in aqueous calcium chloride solution: Molecular dynamics simulation and diffraction studies. *J. Mol. Liq.* **2006**, *129*, 63–74.

[47] Phutela, R. C.; Pitzer, K. S. Thermodynamics of aqueous calcium chloride. *J. Solution Chem.* **1983**, *12*, 201–207.

[48] Slusher, J. T.; Cummings, P. T. Molecular simulation study of tetraalkylammonium halides. 1. Solvation structure and hydrogen bonding in aqueous solutions. *J. Phys. Chem. B* **1997**, *101*, 3818–3826.

[49] Hawlicka, E.; Dlugoborski, T. Molecular dynamics simulations of the aqueous solution of tetramethylammonium chloride. *Chem. Phys. Lett.* **1997**, *268*, 325–330.

[50] Raicu, V., Feldman, Y., Eds. *Dielectric Relaxation in Biological Systems: Physical Principles, Methods, and Applications*, first edition ed.; Oxford University Press: Oxford, United Kingdom, 2015.

[51] Böttcher, C. F. J.; Bordewijk, P. *Theory of Electric Polarisation*; Elsevier: Amsterdam, 1978; Vol. 1 and 2.

[52] Barthel, J.; Buchner, R.; Eberspächer, P. N.; Münsterer, M.; Stauber, J.; Wurm, B. Dielectric relaxation spectroscopy of electrolyte solutions. Recent developments and prospects. *J. Mol. Liq.* **1998**, *78*, 83–109.

[53] Buchner, R.; Barthel, J. In *Encyclopedia of Science and Technology*; Meyer, R. A., Ed.; Academic Press: Orlando, 1990; Chapter Permittivity of Liquids, High Frequency, pp 471–478.

[54] Falkenhagen, H.; Ebeling, W.; Hertz, H. G. *Theorie der Elektrolyte*; Hirzel: Stuttgart, 1971.

[55] Eiberweiser, A.; Buchner, R. Ion-pair or ion-cloud relaxation? On the origin of small-amplitude low-frequency relaxations of weakly associating aqueous electrolytes. *J. Mol. Liq.* **2012**, *176*, 52–59.

[56] Cole, R. H. Time Domain Reflectometry. *Annu. Rev. Phys. Chem.* **1977**, *28*, 283–300.

[57] Bertolini, D.; Cassettari, M.; Salvetti, G.; Tombari, E.; Veronesi, S. Time domain reflectometry to study the dielectric properties of liquids: Some problems and solutions. *Rev. Sci. Instrum.* **1991**, *62*, 450–456.

[58] Barthel, J.; Buchner, R. Dielectric permittivity and relaxation of electrolyte solutions and their solvents. *Chem. Soc. Rev.* **1992**, *21*, 263–270.

[59] Debye, P. *Polar Molecules*; Chemical Catalog Company, 1929.

[60] Pellat, H. *Annales de Chimie et de Physique* **1899**, *18*, 150–181.

[61] Wagner, K. W. *Ann. Physik.* **1913**, *40*, 817–855.

[62] Cole, K. S.; Cole, R. H. Dispersion and absorption in dielectrics I. Alternating current characteristics. *J. Chem. Phys* **1941**, *9*, 341–351.

[63] Cole, K. S.; Cole, R. H. Dispersion and absorption in dielectrics II. Direct current characteristics. *J. Chem. Phys* **1942**, *10*, 98–105.

[64] Davidson, D. W.; Cole, R. H. Dielectric relaxation in glycerine. *J. Chem. Phys* **1950**, *18*, 1417–1417.

[65] Davidson, D. W.; Cole, R. H. Dielectric relaxation in glycerol, propylene glycol, and n-propanol. *J. Chem. Phys* **1951**, *19*, 1484–1490.

[66] Havriliak, S.; Negami, S. A complex plane analysis of -dispersions in some polymer systems. *J. Polym. Sci., Part C* **1966**, *14*, 99–117.

[67] Turton, D. A.; Wynne, K. Structural relaxation in the hydrogen-bonding liquids N-methylacetamide and water studied by optical Kerr effect spectroscopy. *J. Chem. Phys* **2008**, *128*, 154516.

[68] Onsager, L. Electric moments of molecules in liquids. *J. Am. Chem. Soc.* **1936**, *58*, 1486–1493.

[69] Kirkwood, J. G. The dielectric polarization of polar liquids. *J. Chem. Phys* **1939**, *7*, 911–919.

[70] Frohlich, H. *Theory of dielectrics: dielectric constant and dielectric loss*, 2nd ed.; Clarendon Press: Oxford, 1987.

[71] Cavell, E. A. S.; Knight, P. C.; Sheikh, M. A. Dielectric relaxation in non aqueous solutions. Part 2. Solutions of tri(n-butyl)ammonium picrate and iodide in polar solvents. *Trans. Faraday Soc.* **1971**, *67*, 2225–2233.

[72] Barthel, J.; Hetzenauer, H.; Buchner, R. Dielectric relaxation of aqueous electrolyte solutions II. Ion-pair relaxation of 1:2, 2:1, and 2:2 electrolytes. *Ber. Bunsen Ges.* **1992**, *96*, 1424–1432.

[73] Scholte, T. G. A contribution to the theory of the dielectric constant of polar liquids. *Physica* **1949**, *15*, 437–449.

[74] Dote, J. L.; Kivelson, D.; Schwartz, R. N. A molecular quasi-hydrodynamic free-space model for molecular rotational relaxation in liquids. *J. Phys. Chem.* **1981**, *85*, 2169–2180.

[75] Dote, J. L.; Kivelson, D. Hydrodynamic rotational friction coefficients for non-spheroidal particles. *J. Phys. Chem.* **1983**, *87*, 3889–3893.

[76] Philips, L. A.; Webb, S. P.; Clark, J. H. High-pressure studies of rotational reorientation dynamics: The role of dielectric friction. *J. Chem. Phys* **1985**, *83*, 5810–5821.

[77] Kauzmann, W. Dielectric relaxation as a chemical rate process. *Rev. Mod. Phys.* **1942**, *14*, 12–44.

[78] Buchner, R.; Barthel, J.; Stauber, J. The dielectric relaxation of water between 0 °C and 35 °C. *Chem. Phys. Lett.* **1999**, *306*, 57–63.

[79] Rønne, C.; Åstrand, P.-O.; Keiding, S. R. THz spectroscopy of liquid H_2O and D_2O. *Phys. Rev. Lett.* **1999**, *82*, 2888–2891.

[80] Kaatze, U.; Behrends, R.; Pottel, R. Hydrogen network fluctuations and dielectric spectrometry of liquids. *J. Non-Cryst. Solids* **2002**, *305*, 19–28.

[81] Popov, I.; Ishai, P. B.; Khamzin, A.; Feldman, Y. The mechanism of the dielectric relaxation in water. *Phys. Chem. Chem. Phys.* **2016**, *18*, 13941–13953.

[82] Laage, D.; Stirnemann, G.; Sterpone, F.; Rey, R.; Hynes, J. T. Reorientation and allied dynamics in water and aqueous solutions. *Annu. Rev. Phys. Chem.* **2011**, *62*, 395–416.

[83] Powles, J. G. Dielectric relaxation and the internal field. *J. Chem. Phys.* **1953**, *21*, 633–637.

[84] Glarum, S. H. Dielectric relaxation of polar liquids. *J. Chem. Phys.* **1960**, *33*, 1371–1375.

[85] Madden, P.; Kivelson, D. A consistent molecular treatment of dielectric phenomena. *Adv. Chem. Phys.* **1984**, *56*, 467–566.

[86] Moor, W. J.; Hummel, D. O. *Physikalische Chemie*; de Gruyter: Berlin, 1986.

[87] Glasstone, S.; Laidler, K. J.; Eyring, H. *The Theory of Rate Processes*; McGraw Hill: New York, 1977.

[88] Barthel, J.; Bachhuber, K.; Buchner, R.; Hetzenauer, H.; Kleebauer, M. A computer-controlled system of transmission lines for the determination of the complex permittivity of lossy liquids between 8.5 and 90 GHz. *Ber. Bunsen-Ges. Phys. Chem.* **1991**, *95*, 853–859.

[89] Systat Software GmbH, Website (07.05.2019), `http://www.systat.de/TC2D_Produktseite.html`.

[90] Pehl, E. *Mikrowellentechnik*; Dr. Alfred Hüthig Verlag: Heidelberg, 1984; Vol. 2.

[91] Wachter, W. Cooperative Dynamics of Didodecyldimethylammonium Bromide / Water / n-Dodecane Microemulsions. Ph.D. thesis, Universität Regensburg, 2007.

[92] Keysight Technologies, Website (08.05.2019), `http://www.keysight.com`.

[93] *Understanding the Fundamental Princioples of Vector Network Analyzers*; Agilent Technologies, 2012.

[94] Blackham, D.; Pollard, R. D. An improved technique for permittivity measurements using a coaxial probe. *IEEE Trans. Instrum. Meas.* **1997**, *46a*, 1093–1099.

[95] *Reference Guide Agilent Technologies Electronic Calibration Modules*; Agilent Technologies, 2013.

[96] Misra, D. K. A quasi-static analysis of open-ended coaxial lines. *IEEE Trans. Micrwave Theory Tech* **1987**, *35*, 925–928.

[97] Eiberweiser, A. Hydration and Ion Pairing of Aqueous Phosphate Solutions as Observed by Dielectric Spectroscopy. Ph.D. thesis, Universität Regensburg, 2013.

[98] Friesen, S.; Krickl, S.; Luger, M.; Nazet, A.; Hefter, G.; Buchner, R. Hydration and ion association of La^{3+} and Eu^{3+} salts in aqueous solution. *Phys. Chem. Chem. Phys.* **2018**, *20*, 8812–8821.

[99] Friesen, S.; Hefter, G.; Buchner, R. Cation hydration and ion pairing in aqueous solutions of $MgCl_2$ and $CaCl_2$. *J. Phys. Chem. B* **2019**, *123*, 891–900.

[100] Buchner, R.; Barthel, J. A Time Domain Reflectometer for dielectric relaxation spectroscopy of electrolyte solutions. *Ber. Bunsen-Ges. Phys. Chem.* **1997**, *101*, 1509–1516.

[101] Hölzl, C. Optimierung einer TDR-Apparatur zur Untersuchung der dielektrischen Relaxation von H_2O, D_2O und wässrigen Tetra-alkylammoniumbromidlösungen. Ph.D. thesis, Universität Regensburg, 1998.

[102] Göttmann, O.; Kaatze, U.; Petong, P. Measurement science and technology coaxial to circular waveguide transition as high-precision easy-to-handle measuring cell for the broad band dielectric spectrometry of liquids. *Meas. Sci. Technol.* **1996**, *7*, 525–534.

[103] Hunger, J. Effects of Polar Compounds on the Dynamics and Dielectric Properties of Room-Temperature Ionic Liquids. Ph.D. thesis, University of Regensbrug, 2009.

[104] Maplesoft, Website (10.05.2019), `https://www.maplesoft.com/products/maple/`.

[105] Schrödle, S.; Hefter, G.; Kunz, W.; Buchner, R. Effects of nonionic surfactant C12E5 on the cooperative dynamics of water. *Langmuir* **2006**, *22*, 924–932.

[106] Barthel, J.; Bachhuber, K.; Buchner, R.; Gill, J. B.; Kleebauer, M. Dielectric spectra of some common solvents in the microwave region. Dipolar aprotic solvents and amides. *Chem. Phys. Lett.* **1990**, *167*, 62–66.

[107] Barthel, J.; Buchner, R.; Hölzl, C.; Münsterer, M. Dynamics of benzonitrile, propylene carbonate and butylene carbonate: the Influence of molecular shape and flexibility on the dielectric relaxation behaviour of dipolar aprotic liquids. *Z. Phys. Chem.* **2000**, *214*, 1213–1231.

[108] Barthel, J.; Buchner, R.; Wurm, B. The dynamics of liquid formamide, N-methylformamide, N,N-dimethylformamide, and N,N-dimethylacetamide. A dielectric relaxation study. *Journal of Molecular Liquids* **2002**, *98–99*, 51–69.

[109] The MathWorks, Inc., Website (10.05.2019), `https://de.mathworks.com/products/matlab.html`.

[110] Gregory, A. P.; Clarke, R. N. Dielectric metrology with coaxial sensors. *Meas. Sci. Technol.* **2007**, *18*, 1372–1386.

[111] Sonnleitner, T. DRSFit Manual. 2012.

[112] WaveMetrics, Website (14.05.2019), `https://www.wavemetrics.com/products/igorpro`.

[113] Bevington, P.; Robinson, D. K. *Data Reduction and Error Analysis for the Physical Sciences*, revised. ed.; Mcgraw Hill Book Co: Boston, 2002.

[114] Zasetsky, A. Y.; Buchner, R. Quasi-linear least squares and computer code for numerical evaluation of relaxation time distribution from broadband dielectric spectra. *J. Phys.: Condens. Matter* **2011**, *23*, 025903.

[115] Pratt, K. W.; Koch, W. F.; Wu, Y. C.; Berezansky, P. A. Molality-based primary standards of electrolytic conductivity (IUPAC Technical Report). *Pure Appl. Chem.* **2001**, *73*, 1783–1793.

[116] Płaczek, A.; Hefter, G.; Rahman, H. M. A.; Buchner, R. Dielectric relaxation study of the ion solvation and association of $NaCF_3SO_3$, $Mg(CF_3SO_3)_2$, and $Ba(ClO_4)_2$ in *N, N* -dimethylformamide. *J. Phys. Chem. B* **2011**, *115*, 2234–2242.

[117] Frisch, M. J. et al. Gaussian 09 Revision E.01. 2010; Gaussian Inc. Wallingford CT 2009.

[118] Bondi, A. van der Waals volumes and radii. *J. Phys. Chem.* **1964**, *68*, 441–451.

[119] Miertuš, S.; Scrocco, E.; Tomasi, J. Electrostatic interaction of a solute with a continuum. A direct utilizaion of Ab initio molecular potentials for the prevision of solvent effects. *Chem. Phys.* **1981**, *55*, 117–129.

[120] Miertuš, S.; Tomasi, J. Approximate evaluations of the electrostatic free energy and internal energy changes in solution processes. *Chem. Phys.* **1982**, *65*, 239–245.

[121] Tomasi, J.; Mennucci, B.; Cammi, R. Quantum mechanical continuum solvation models. *Chem. Rev.* **2005**, *105*, 2999–3094.

[122] Hirata, F. In *Molecular Theory of Solvation*; Hirata, F., Ed.; Springer Netherlands: Dordrecht, 2004.

[123] Chandler, D.; Andersen, H. C. Optimized cluster expansions for classical fluids. II. Theory of molecular liquids. *J. Chem. Phys.* **1972**, *57*, 1930–1937.

[124] Kovalenko, A.; Hirata, F. Hydration free energy of hydrophobic solutes studied by a reference interaction site model with a repulsive bridge correction and a thermodynamic perturbation method. *J. Chem. Phys* **2000**, *113*, 2793–2805.

[125] Kovalenko, A.; Hirata, F. Self-consistent description of a metal–water interface by the Kohn–Sham density functional theory and the three-dimensional reference interaction site model. *J. Chem. Phys.* **1999**, *110*, 10095–10112.

[126] Case, D. A. et al. AMBER 14. 2014; University of California, San Francisco.

[127] Kovalenko, A.; Ten-no, S.; Hirata, F. Solution of three-dimensional reference interaction site model and hypernetted chain equations for simple point charge water by modified method of direct inversion in iterative subspace. *J. Comput. Chem.* **1999**, *20*, 928–936.

[128] Lue, L.; Blankschtein, D. Liquid-state theory of hydrocarbon-water systems: application to methane, ethane, and propane. *J. Phys. Chem.* **1992**, *96*, 8582–8594.

[129] Rang, H.; Dale, M.; Ritter, J.; Flower, R.; Henderson, G. *Pharmacology*, 8th ed.; Elsevier: Amsterdam, 2012.

[130] Marieb, E. N.; Hoehn, K. *Human Anatomy & Physiology*, 9th ed.; Pearson Education: Boston, 2012.

[131] Berg, J. M.; Tymoczko, J. L.; Gatto jr., G. J.; Stryer, L. *Stryer Biochemie*, 8th ed.; Springer: Berlin, 2017.

[132] Dale, H. H.; Feldberg, W.; Vogt, M. Release of acetylcholine at voluntary motor nerve endings. *J. Physiol.* **1936**, *86*, 353–380.

[133] Berthier, G.; Savinelli, R.; Pullman, A. Cation π interaction between acetylcholine and the benzene ring. *Theor. Chem. Acc.* **2000**, *104*, 78–81.

[134] Celie, P. H. N.; van Rossum-Fikkert, S. E.; van Dijk, W. J.; Brejc, K.; Smit, A. B.; Sixma, T. K. Nicotine and carbamylcholine binding to nicotinic acetylcholine receptors as studied in AChBP crystal structures. *Neuron* **2004**, *41*, 907–914.

[135] Hulme, E. C.; Lu, Z. L.; Bee, M. S. Scanning mutagenesis studies of the M1 muscarinic acetylcholine receptor. *Recept. Channels* **2003**, *9*, 215–228.

[136] Zacharias, N.; Dougherty, D. A. Cation-π interactions in ligand recognition and catalysis. *Trends Pharmacol. Sci.* **2002**, *23*, 281–287.

[137] Marino, T.; Russo, N.; Tocci, E.; Toscano, M. Molecular dynamics, density functional and second-order Møller–Plesset theory study of the structure and conformation of acetylcholine in vacuo and in solution. *Theor. Chem. Acc.* **2001**, *107*, 8–14.

[138] Ju Kim, Y.; Choon Kim, S.; Kee Kang, Y. Conformation and hydration of acetylcholine. *J. Mol. Struct.* **1992**, *269*, 231–241.

[139] Williamson, P. T. F.; Watts, J. A.; Addona, G. H.; Miller, K. W.; Watts, A. Dynamics and orientation of $N^+(CD_3)_3$-bromoacetylcholine bound to its binding site on the nicotinic acetylcholine receptor. *Proc. Natl. Acad. Sci. U.S.A.* **2001**, *98*, 2346–2351.

[140] Chothia, C.; Pauling, P. Conformation of cholinergic molecules relevant to acetylcholinesterase. *Nature* **1969**, *223*, 919.

[141] Behling, R. W.; Yamane, T.; Navon, G.; Jelinski, L. W. Conformation of acetylcholine bound to the nicotinic acetylcholine receptor. *Proc. Natl. Acad. Sci. U.S.A.* **1988**, *85*, 6721–6725.

[142] Rodin, L.; Stevens, L. *Psychiatry-An Illustrated Colour Text*, 2nd ed.; Churchill Livingstone: London, 2010.

[143] Stamper, R. L.; Lieberman, M. F.; Drake, M. V. *Becker-Shaffer's Diagnosis and Therapy of the Glaucomas*, 8th ed.; Mosby Elsevier, 2009.

[144] Shiroma, L. O.; Costa, V. P. In *Glaucoma*, 2nd ed.; Shaarawy, T. M., Sherwood, M. B., Hitchings, R. A., Crowston, J. G., Eds.; W.B. Saunders, 2015; pp 577–582.

[145] Hulme, E.; Soper, A.; McLain, S.; Finney, J. The hydration of the neurotransmitter acetylcholine in aqueous solution. *Biophys. J.* **2006**, *91*, 2371–2380.

[146] Hernández, B.; Houzé, P.; Pflüger, F.; Kruglik, S. G.; Ghomi, M. Raman scattering-based multiconformational analysis for probing the structural differences between acetylcholine and acetylthiocholine. *J. Pharm. Biomed. Anal.* **2017**, *138*, 54–62.

[147] Margheritis, C.; Corongiu, G. Acetylcholine in water: Ab-initio potential and Monte Carlo simulation. *J. Comput. Chem.* **1988**, *9*, 1–10.

[148] Fedotova, M. V. and Kruchinin, S. E., personal communication, 2018.

[149] Bešter-Rogač, M., personal communication, 2019.

[150] Fukasawa, T.; Sato, T.; Watanabe, J.; Hama, Y.; Kunz, W.; Buchner, R. Relation between dielectric and low-frequency Raman spectra of hydrogen-bond liquids. *Phys. Rev. Lett.* **2005**, *95*.

[151] Wachter, W.; Kunz, W.; Buchner, R.; Hefter, G. Is there an anionic hofmeister effect on water dynamics? Dielectric spectroscopy of aqueous solutions of NaBr, NaI, $NaNO_3$, $NaClO_4$, and NaSCN. *J. Phys. Chem. A* **2005**, *109*, 8675–8683.

[152] Eiberweiser, A.; Nazet, A.; Kruchinin, S. E.; Fedotova, M. V.; Buchner, R. Hydration and ion binding of the osmolyte ectoine. *J. Phys. Chem. B* **2015**, *119*, 15203–15211.

[153] Agieienko, V.; Buchner, R. Urea hydration from dielectric relaxation spectroscopy: old findings confirmed, new insights gained. *Phys. Chem. Chem. Phys.* **2016**, *18*, 2597–2607.

[154] Eiberweiser, A.; Nazet, A.; Hefter, G.; Buchner, R. Ion hydration and association in aqueous potassium phosphate solutions. *J. Phys. Chem. B* **2015**, *119*, 5270–5281.

[155] Vinh, N. Q.; Sherwin, M. S.; Allen, S. J.; George, D. K.; Rahmani, A. J.; Plaxco, K. W. High-precision gigahertz-to-terahertz spectroscopy of aqueous salt solutions as a probe of the femtosecond-to-picosecond dynamics of liquid water. *J. Chem. Phys.* **2015**, *142*, 164502.

[156] Buchner, R.; Hölzl, C.; Stauber, J.; Barthel, J. Dielectric spectroscopy of ion-pairing and hydration in aqueous tetra-n-alkylammonium halide. *Phys. Chem. Chem. Phys.* **2002**, *4*, 2169–2179.

[157] Kaatze, U.; Rupprecht, A. Hydrophobic hydration and concentration fluctuations in aqueous solutions of urea derivatives. Evidence from dielectric and ultrasonic spectrometry. *J. Chem. Phys.* **2002**, *117*, 4936–4939.

[158] Rezus, Y. L. A.; Bakker, H. J. Observation of immobilized water molecules around hydrophobic groups. *Phys. Rev. Lett.* **2007**, *99*, 148301.

[159] Bakulin, A. A.; Pshenichnikov, M. S.; Bakker, H. J.; Petersen, C. Hydrophobic molecules slow down the hydrogen-bond dynamics of water. *J. Phys. Chem. A* **2011**, *115*, 1821–1829.

[160] Rahman, H. M. A.; Hefter, G.; Buchner, R. Hydration of formate and acetate ions by dielectric relaxation spectroscopy. *J. Phys. Chem. B* **2012**, *116*, 314–323.

[161] Laage, D.; Stirnemann, G.; Hynes, J. T. Why water reorientation slows without iceberg formation around hydrophobic solutes. *J. Phys. Chem. B* **2009**, *113*, 2428–2435.

[162] Dmitrieva, O. A.; Fedotova, M. V.; Buchner, R. Evidence for cooperative Na^+ and Cl^- binding by strongly hydrated L-proline. *Phys. Chem. Chem. Phys.* **2017**, *19*, 20474–20483.

[163] Oleinikova, A.; Sasisanker, P.; Weingärtner, H. What can really be learned from dielectric spectroscopy of protein solutions? A case study of ribonuclease A. *J. Phys. Chem. B* **2004**, *108*, 8467–8474.

[164] Laage, D.; Elsaesser, T.; Hynes, J. T. Water dynamics in the hydration shells of biomolecules. *Chem. Rev.* **2017**, *117*, 10694–10725.

[165] Debye, P.; Falkenhagen, H. The dispersion of conductivity and dielectric constant of strong electrolytes. *Phys. Z.* **1928**, *29*, 121–132.

[166] Yamaguchi, T.; Matsuoka, T.; Koda, S. A theoretical study on the frequency-dependent electric conductivity of electrolyte solutions. II. Effect of hydrodynamic interaction. *J. Chem. Phys.* **2009**, *130*, 094506.

[167] Rø/nne, C.; Thrane, L.; Åstrand, P.-O.; Wallqvist, A.; Mikkelsen, K. V.; Keiding, S. R. Investigation of the temperature dependence of dielectric relaxation in liquid water by THz reflection spectroscopy and molecular dynamics simulation. *J. Chem. Phys.* **1997**, *107*, 5319–5331.

[168] Duboué-Dijon, E.; Fogarty, A. C.; Laage, D. Temperature dependence of hydrophobic hydration dynamics: from retardation to acceleration. *J. Phys. Chem. B* **2014**, *118*, 1574–1583.

[169] Turton, D. A.; Hunger, J.; Hefter, G.; Buchner, R.; Wynne, K. Glasslike behavior in aqueous electrolyte solutions. *J. Chem. Phys* **2008**, *128*, 161102.

[170] Ohtaki, H.; Radnai, T. Structure and dynamics of hydrated ions. *Chem. Rev.* **1993**, *93*, 1157–1204.

[171] Zemaitis, J. F.; Cark, D.; Rafal, M.; Scrivner, N. C. *Handbook of Aqueous Electrolyte Thermodynamics: Theory & Application*; Wiley: Hoboken, New Jersey, 1986.

[172] Bešter-Rogač, M.; Habe, D. Modern advances in electrical conductivity measurements of solutions. *Acta Chim. Slov.* **2006**, *53*, 391–395.

[173] Shaukat, S.; Fedotova, M. V.; Kruchinin, S. E.; Bešter-Rogač, M.; Podlipnik, r.; Buchner, R. Hydration and ion association of aqueous choline chloride and chlorocholine chloride. *Phys. Chem. Chem. Phys.* **2019**, *21*, 10970–10980.

[174] Bešter-Rogač, M.; Fedotova, M. V.; Kruchinin, S. E.; Klähn, M. Mobility and association of ions in aqueous solutions: the case of imidazolium based ionic liquids. *Phys. Chem. Chem. Phys.* **2016**, *18*, 28594–28605.

[175] Barthel, J. M. G.; Krienke, H.; Kunz, W. *Physical Chemistry of Electrolyte Solutions. Modern Aspects*; Springer: New York, 1998; Vol. 5.

[176] Bešter-Rogač, M.; Klofutar, C.; Rudan-Tasic, D. Association of hydrophobic ions in aqueous solution: A conductometric study of symmetrical tetraalkylammonium cyclohexylsulfamates. *J. Mol. Liq.* **2010**, *156*, 82–88.

[177] Accascina, F.; Goffredi, M.; Triolo, R. Ion-pair formation of quaternary ammonium salts in hydrogen-bonded solvents. *Zeitschrift für Physikalische Chemie* **2011**, *81*, 148–157.

[178] Tissier, M.; Douhéret, G. The conductance of tetraethylammonium salts in water-methanol mixtures. *J. Solution Chem.* **1978**, *7*, 87–98.

[179] Greenwood, N. N.; Earnshaw, A. *Chemistry of the Elements*, 2nd ed.; Butterworth-Heinemann: Oxford ; Boston, 1997.

[180] Cassidei, L.; Sciacovelli, O. Conformational analysis of the C(6)-O(1)-C(5)-C(4) fragment in acetylcholine by carbon-13 NMR spectroscopy. *J. Am. Chem. Soc.* **1981**, *103*, 933–934.

[181] Edvardsen, .; Dahl, S. G. Molecular structure and dynamics of acetylcholine. *J. Neural Transm.* **1991**, *83*, 157–170.

[182] Vistoli, G.; Pedretti, A.; Villa, L.; Testa, B. The solutesolvent system: Solvent constraints on the conformational dynamics of acetylcholine. *J. Am. Chem. Soc.* **2002**, *124*, 7472–7480.

[183] Conti, F.; Damiani, A.; Pietronero, C.; Russo, N. Conformational flexibility of choline derivatives. *Nature New Biol.* **1971**, *233*, 232–234.

[184] Sega, M.; Kantorovich, S.; Arnold, A. Kinetic dielectric decrement revisited: phenomenology of finite ion concentrations. *Phys. Chem. Chem. Phys.* **2015**, *17*, 130–133.

[185] Rinne, K. F.; Gekle, S.; Netz, R. R. Ion-specific solvation water dynamics: single water versus collective water effects. *J. Phys. Chem. A* **2014**, *118*, 11667–11677.

[186] Buchner, R.; Hefter, G. T.; May, P. M. Dielectric relaxation of aqueous NaCl solutions. *J. Phys. Chem. A* **1999**, *103*, 1–9.

[187] Tielrooij, K.-J.; Hunger, J.; Buchner, R.; Bonn, M.; Bakker, H. J. Influence of Concentration and temperature on the dynamics of water in the hydrophobic hydration shell of tetramethylurea. *J. Am. Chem. Soc.* **2010**, *132*, 15671–15678.

[188] Rezus, Y. L. A.; Bakker, H. J. Strong slowing down of water reorientation in mixtures of water and tetramethylurea. *J. Phys. Chem. A* **2008**, *112*, 2355–2361.

[189] Agieienko, V.; Horinek, D.; Buchner, R. Hydration and self-aggregation of a neutral cosolute from dielectric relaxation spectroscopy and MD simulations: the case of 1,3-dimethylurea. *Phys. Chem. Chem. Phys.* **2016**, *19*, 219–230.

[190] Chang, G.; Guida, W. C.; Still, W. C. An internal-coordinate Monte Carlo method for searching conformational space. *J. Am. Chem. Soc.* **1989**, *111*, 4379–4386.

[191] Bochevarov, A. D.; Harder, E.; Hughes, T. F.; Greenwood, J. R.; Braden, D. A.; Philipp, D. M.; Rinaldo, D.; Halls, M. D.; Zhang, J.; Friesner, R. A. Jaguar: A high-performance quantum chemistry software program with strengths in life and materials sciences. *Int. J. Quantum Chem.* **2013**, *113*, 2110–2142.

[192] Tannor, D. J.; Marten, B.; Murphy, R.; Friesner, R. A.; Sitkoff, D.; Nicholls, A.; Honig, B.; Ringnalda, M.; Goddard, W. A. Accurate first principles calculation of molecular charge distributions and solvation energies from ab initio quantum mechanics and continuum dielectric theory. *J. Am. Chem. Soc.* **1994**, *116*, 11875–11882.

[193] Marten, B.; Kim, K.; Cortis, C.; Friesner, R. A.; Murphy, R. B.; Ringnalda, M. N.; Sitkoff, D.; Honig, B. New model for calculation of solvation free energies: Correction of self-consistent reaction field continuum dielectric theory for short-range hydrogen-bonding effects. *J. Phys. Chem.* **1996**, *100*, 11775–11788.

[194] Schrödinger, LLC, New York, NY, USA, Jaguar, Release 2017-3, 2017.

[195] Cox, S. R.; Williams, D. E. Representation of the molecular electrostatic potential by a net atomic charge model. *J. Comput. Chem.* **1981**, *2*, 304–323.

[196] Foglia, F.; Lawrence, M. J.; Lorenz, C. D.; Mclain, S. E. On the hydration of the phosphocholine headgroup in aqueous solution. *J. Chem. Phys* **2010**, *133*, 14510.

[197] Fedotova, M. V.; Kruchinin, S. E.; Chuev, G. N. Hydration structure of osmolyte TMAO: concentration/pressure-induced response. *New J. Chem.* **2017**, *41*, 1219–1228.

[198] Fedotova, M.; E. Kruchinin, S. Hydration and ion-binding of glycine betaine: How they may be involved into protection of proteins under abiotic stresses. *J. Mol. Liq.* **2017**, *244*, 100–108.

[199] Krienke, H.; Vlachy, V.; Ahn-Ercan, G.; Bakó, I. Modeling tetraalkylammonium halide salts in water: How hydrophobic and electrostatic interactions shape the thermodynamic properties. *J. Phys. Chem. B* **2009**, *113*, 4360–4371.

[200] García-Tarrés, L.; Guàrdia, E. Hydration and dynamics of a tetramethylammonium ion in water: A Computer simulation study. *J. Phys. Chem. B* **1998**, *102*, 7448–7454.

[201] Zhou, Y.; Danbolt, N. C. Glutamate as a neurotransmitter in the healthy brain. *J. Neural Transm.* **2014**, *121*, 799–817.

[202] Sano, C. History of glutamate production. *Am. J. Clin. Nutr.* **2009**, *90*, 728S–732S.

[203] Michael, N.; Erfurth, A.; Ohrmann, P.; Gössling, M.; Arolt, V.; Heindel, W.; Pfleiderer, B. Acute mania is accompanied by elevated glutamate/glutamine levels within the left dorsolateral prefrontal cortex. *Psychopharmacology (Berl.)* **2003**, *168*, 344–346.

[204] Niswender, C. M.; Conn, P. J. Metabotropic glutamate receptors: physiology, pharmacology, and disease. *Annu. Rev. Pharmacol. Toxicol.* **2010**, *50*, 295–322.

[205] Bennett, K. A.; Doré, A. S.; Christopher, J. A.; Weiss, D. R.; Marshall, F. H. Structures of mGluRs shed light on the challenges of drug development of allosteric modulators. *Curr. Opin. Pharmacol.* **2015**, *20*, 1–7.

[206] Pin, J.-P.; Bettler, B. Organization and functions of mGlu and $GABA_B$ receptor complexes. *Nature* **2016**, *540*, 60–68.

[207] Bridges, R. J.; Stanley, M. S.; Anderson, M. W.; Cotman, C. W.; Chamberlin, A. R. Conformationally defined neurotransmitter analogues. Selective inhibition of glutamate uptake by one pyrrolidine-2,4-dicarboxylate diastereomer. *J. Med. Chem.* **1991**, *34*, 717–725.

[208] McLain, S. E.; Soper, A. K.; Watts, A. Structural studies on the hydration of l-glutamic acid in solution. *J. Phys. Chem. B* **2006**, *110*, 21251–21258.

[209] Collis, A. B.; Tulip, P. R.; Bates, S. P. Structure and bonding of aqueous glutamic acid from classical molecular dynamics simulations. *Phys. Chem. Chem. Phys.* **2010**, *12*, 5341–5352.

[210] Eid, T.; Thomas, M. J.; Spencer, D. D.; Rundén-Pran, E.; Lai, J. C. K.; Malthankar, G. V.; Kim, J. H.; Danbolt, N. C.; Ottersen, O. P.; de Lanerolle, N. C. Loss of glutamine synthetase in the human epileptogenic hippocampus: possible mechanism for raised extracellular glutamate in mesial temporal lobe epilepsy. *Lancet.* **2004**, *363*, 28–37.

[211] Curi, R.; Lagranha, C. J.; Doi, S. Q.; Sellitti, D. F.; Procopio, J.; Pithon-Curi, T. C.; Corless, M.; Newsholme, P. Molecular mechanisms of glutamine action. *J. Cell. Physiol.* **2005**, *204*, 392–401.

[212] Faux, N. G.; Bottomley, S. P.; Lesk, A. M.; Irving, J. A.; Morrison, J. R.; de la Banda, M. G.; Whisstock, J. C. Functional insights from the distribution and role of homopeptide repeat-containing proteins. *Genome Res.* **2005**, *15*, 537–551.

[213] Landles, C.; Bates, G. P. Huntingtin and the molecular pathogenesis of Huntington's disease. *EMBO Rep.* **2004**, *5*, 958–963.

[214] Perevozchikova, T.; Stanley, C.; McWilliams-Koeppen, H.; Rowe, E.; Berthelier, V. Investigating the structural impact of the glutamine repeat in Huntingtin assembly. *Biophys. J.* **2014**, *107*, 411–421.

[215] Kaye, J. A.; Finkbeiner, S. Modeling Huntington's disease with induced pluripotent stem cells. *Mol. Cell. Neurosci.* **2013**, *0*, 50–64.

[216] Burgunder, J.-M. Orphan drugs in development for Huntington's disease: challenges and progress. *ODRR* **2015**, *5*, 1–9.

[217] Bocharova, N.; Chave-Cox, R.; Sokolov, S.; Knorre, D.; Severin, F. Protein aggregation and neurodegeneration: clues from a yeast model of Huntington's disease. *Biochemistry Mosc.* **2009**, *74*, 231–234.

[218] Sánchez, I.; Mahlke, C.; Yuan, J. Pivotal role of oligomerization in expanded polyglutamine neurodegenerative disorders. *Nature* **2003**, *421*, 373–379.

[219] Crick, S. L.; Jayaraman, M.; Frieden, C.; Wetzel, R.; Pappu, R. V. Fluorescence correlation spectroscopy shows that monomeric polyglutamine molecules form collapsed structures in aqueous solutions. *PNAS* **2006**, *103*, 16764–16769.

[220] Dougan, L.; Li, J.; Badilla, C. L.; Berne, B. J.; Fernandez, J. M. Single homopolypeptide chains collapse into mechanically rigid conformations. *PNAS* **2009**, *106*, 12605–12610.

[221] Rhys, N. H.; Soper, A. K.; Dougan, L. The hydrogen-bonding ability of the amino acid glutamine revealed by neutron diffraction experiments. *J. Phys. Chem. B* **2012**, *116*, 13308–13319.

[222] Rhys, N. H.; Soper, A. K.; Dougan, L. Hydrophilic association in a dilute glutamine solution persists independent of increasing temperature. *J. Phys. Chem. B* **2015**, *119*, 15644–15651.

[223] Liu, F.; Wang, F.; Jia, G.; Huang, K. Molecular dynamics simulation of the cooperative effect by different force fields in monosodium glutamate aqueous solution. *RSC Adv.* **2015**, *5*, 35572–35578.

[224] Shikata, T.; Hashimoto, K. Dielectric features of neurotransmitters, γ-aminobutyric acid and l-Glutamate, for molecular recognition by receptors. *J. Phys. Chem. B* **2003**, *107*, 8701–8705.

[225] Lide, D. R., Ed. *CRC Handbook of Chemistry and Physics*, 84th ed.; CRC Press: Boca Raton, USA, 2003.

[226] Sato, T.; Buchner, R.; Fernandez, a.; Chiba, A.; Kunz, W. Dielectric relaxation spectroscopy of aqueous amino acid solutions: dynamics and interactions in aqueous glycine. *J. Mol. Liq.* **2005**, *117*, 93–98.

[227] Samanta, N.; Das Mahanta, D.; Choudhury, S.; Barman, A.; Kumar Mitra, R. Collective hydration dynamics in some amino acid solutions: A combined GHz-THz spectroscopic study. *J. Chem. Phys.* **2017**, *146*, 125101.

[228] Rodríguez-Arteche, I.; Cerveny, S.; Alegría, n.; Colmenero, J. Dielectric spectroscopy in the GHz region on fully hydrated zwitterionic amino acids. *Phys. Chem. Chem. Phys.* **2012**, *14*, 11352–11362.

[229] Leenders, E. J. M.; Bolhuis, P. G.; Meijer, E. J. Microscopic picture of the aqueous solvation of glutamic acid. *J. Chem. Theory Comput.* **2008**, *4*, 898–907.

[230] Spickermann, C.; Thar, J.; Lehmann, S. B. C.; Zahn, S.; Hunger, J.; Buchner, R.; Hunt, P. A.; Welton, T.; Kirchner, B. Why are ionic liquid ions mainly associated in water? A Car-Parrinello study of 1-ethyl-3-methyl-imidazolium chloride water mixture. *J. Chem. Phys.* **2008**, *129*, 104505.

[231] Pálinkás, G.; Radnai, T.; Szász, G. I.; Heinzinger, K. The structure of an aqueous ammonium chloride solution. *J. Chem. Phys.* **1981**, *74*, 3522–3526.

[232] Intharathep, P.; Tongraar, A.; Sagarik, K. Structure and dynamics of hydrated NH_4^+: An ab initio QM/MM molecular dynamics simulation. *J. Comput. Chem.* **2005**, *26*, 1329–1338.

[233] Ekimova, M.; Quevedo, W.; Szyc, u.; Iannuzzi, M.; Wernet, P.; Odelius, M.; Nibbering, E. T. J. Aqueous solvation of ammonia and ammonium: Probing hydrogen bond motifs with FT-IR and Soft X-ray Spectroscopy. *J. Am. Chem. Soc.* **2017**, *139*, 12773–12783.

[234] Alagona, G.; Ghio, C.; Kollman, P. Monte Carlo simulation studies of the solvation of ions. 1. Acetate anion and methylammonium cation. *J. Am. Chem. Soc.* **1986**, *108*, 185–191.

[235] Brugé, F.; Bernasconi, M.; Parrinello, M. Ab initio simulation of rotational dynamics of solvated ammonium ion in water. *J. Am. Chem. Soc.* **1999**, *121*, 10883–10888.

[236] Hesske, H.; Gloe, K. Hydration behavior of alkyl amines and their corresponding protonated forms. 1. Ammonia and methylamine. *J. Phys. Chem. A* **2007**, *111*, 9848–9853.

[237] Rahman, H. M. A.; Hefter, G.; Buchner, R. Hydrophilic and hydrophobic hydration of sodium propanoate and sodium butanoate in aqueous solution. *J. Phys. Chem. B* **2013**, *117*, 2142–2152.

[238] Zavitsas, A. A. The nature of aqueous solutions: Insights into multiple facets of chemistry and biochemistry from freezing-point depressions. *Chem. Eur. J* **2010**, *16*, 5942–5960.

[239] Hollenberg, J. L.; Ifft, J. B. Hydration numbers by near-infrared spectrophotometry. 1. Amino acids. *J. Phys. Chem.* **1982**, *86*, 1938–1941.

[240] Vorob'ev, M. M.; Baranov, A. A.; Belikov, V. M.; Khurgin, Y. I. Investigation of hydration of α-amino acids by means of absorption millimeter spectroscopy. *Russ. Chem. Bull.* **1996**, *45*, 577–581.

[241] Malomouzh, A. I.; Petrov, K. A.; Nurullin, L. F.; Nikolsky, E. E. Metabotropic $GABA_B$ receptors mediate GABA inhibition of acetylcholine release in the rat neuromuscular junction. *J. Neurochem.* **2015**, *135*, 1149–1160.

[242] Ramachandran, P. V.; Shekhar, A. Welcome to 'GABAergic drugs'. *Future Med. Chem.* **2011**, *3*, 139–140.

[243] O'Hagan, D. 3-fluoro-GABA enantiomers: exploring the conformation of GABA binding to $GABA_A$ receptors and GABA aminotransferase. *Future Med. Chem.* **2011**, *3*, 189–195.

[244] Pearl, P. L.; Gibson, K. M. Clinical aspects of the disorders of GABA metabolism in children. *Curr. Opin. Neurol.* **2004**, *17*, 107–113.

[245] Geng, Y.; Bush, M.; Mosyak, L.; Wang, F.; Fan, Q. R. Structural mechanism of ligand activation in human $GABA_B$ receptor. *Nature* **2013**, *504*, 254–259.

[246] Clift, M. D.; Ji, H.; Deniau, G. P.; O'Hagan, D.; Silverman, R. B. Enantiomers of 4-amino-3-fluorobutanoic acid as substrates for γ-aminobutyric acid aminotransferase. Conformational probes for GABA binding. *Biochemistry* **2007**, *46*, 13819–13828.

[247] Deniau, G.; Slawin, A. M. Z.; Lebl, T.; Chorki, F.; Issberner, J. P.; van Mourik, T.; Heygate, J. M.; Lambert, J. J.; Etherington, L.-A.; Sillar, K. T.; O'Hagan, D. Synthesis, conformation and biological evaluation of the enantiomers of 3-fluoro-gamma-aminobutyric acid ((R)- and (S)-3F-GABA): an analogue of the neurotransmitter GABA. *Chem. Bio. Chem* **2007**, *8*, 2265–2274.

[248] Shelp, B. Metabolism and functions of gamma-aminobutyric acid. *Trends Plant Sci.* **1999**, *4*, 446–452.

[249] *The Human Metabolome Database (HMDB)*; HMDB No.: HMDB0000452; http://www.hmdb.ca/metabolites/HMDB0000452 (8.08.2019).

[250] unpublished data from the Regensburg laboratory, 2013.

[251] Halász, A.; Baráth, g.; Simon-Sarkadi, L.; Holzapfel, W. Biogenic amines and their production by microorganisms in food. *Trends Food Sci. Technol.* **1994**, *5*, 42–49.

[252] Rudnick, G.; Clark, J. From synapse to vesicle: The reuptake and storage of biogenic amine neurotransmitters. *Biochimica et Biophysica Acta* **1993**, *1144*, 249–263.

[253] Mahoney, J. M.; Davis, J. P.; Beatty, A. M.; Smith, B. D. Molecular recognition of alkylammonium contact ion-pairs using a ditopic receptor. *J. Org. Chem.* **2003**, *68*, 9819–9820.

[254] Li, D.-H.; Smith, B. D. Shape-selective recognition of quaternary ammonium chloride ion pairs. *J. Org. Chem.* **2019**, *84*, 2808–2816.

[255] Kaatze, U.; Bieler, H.; Pottel, R. Dielectric spectroscopy on aqueous solutions of some zwitterionic amino acids. *J. Mol. Liq.* **1985**, *30*, 101–113.

[256] Pottel, R.; Adolph, D.; Kaatze, U. Dielectric relaxation in aqueous solutions of some dipolar organic molecules. *Ber. Bunsen-Ges. Phys. Chem.* **1975**, *79*, 278–285.

[257] Suzuki, M.; Shigematsu, J.; Fukunishi, Y.; Kodama, T. Hydrophobic hydration analysis on amino acid solutions by the microwave dielectric method. *J. Phys. Chem. B* **1997**, *101*, 3839–3845.

[258] Kaatze, U.; Limberg, C. H.; Pottel, R. Dielectric relaxation of water in aqueous solutions of n-alkylamine hydrochlorides part 1: Solute concentrations smaller than the critical micelle concentrations. *Ber. Bunsenges. Phys. Chem.* **1974**, *78*, 555–560.

[259] Dawson, R. M. C. *Data for Biochemical Research*; Clarendon Press: Oxford, 1959.

[260] Vallet, V.; Masella, M. Benchmark binding energies of ammonium and alkylammonium ions interacting with water. Are ammonium–water hydrogen bonds strong? *Chem. Phys. Lett.* **2015**, *618*, 168–173.

[261] Chaiyasit, P.; Tongraar, A.; Kerdcharoen, T. Characteristics of methylammonium ion (CH_3NH^{3+}) in aqueous electrolyte solution: An ONIOM-XS MD simulation study. *Chem. Phys.* **2017**, *493*, 91–101.

[262] Marlow, G. E.; Pettitt, B. M. Simulation of the bis-(penicillamine) enkephalin in ammonium chloride solution: A comparison with sodium chloride. *Biopolymers* **2003**, *68*, 192–209.

[263] Lee, H.; Wilmshurst, J. K. Observation of ion-pairs in aqueous solutions by vibrational spectroscopy. *Aust. J. Chem.* **1964**, *17*, 943–945.

[264] Sharygin, A. V.; Wood, R. H. Volumes and heat capacities of aqueous solutions of ammonium chloride from the temperatures 298.15 K to 623 K and pressures to 28 MPa. *J. Chem. Thermodynamics* **1996**, *28*, 851–872.

[265] Shaukat, S. Hydration, ion binding and self-aggregation of choline and choline-based surfactants. Ph.D. thesis, Universität Regensburg, 2013.

[266] Kaatze, U. Kinetics of micelle formation and concentration fluctuations in solutions of short-chain surfactants. *J. Phys. Chem. B* **2011**, *115*, 10470–10477.

[267] Sahara, H.; Harada, S. Calorimetric study of micelle formation of alkylammonium chlorides in water. *J. Oleo Sci.* **2018**, *67*, 1417–1424.

[268] Kusalik, P. G.; Bergman, D.; Laaksonen, A. The local structure in liquid methylamine and methylamine–water mixtures. *J. Chem. Phys.* **2000**, *113*, 8036–8046.

[269] Tanaka, K.; Akutsu, H.; Ozaki, Y.; Kyogoko, Y.; Tomita, K.-i. Molecular conformations of γ-aminobutyric acid and γ-aminohydroxybutyric acid in aqueous solution. *Bull. Chem. Soc. Jpn.* **1978**, *51*, 2654–2658.

[270] Crittenden, D. L.; Chebib, M.; Jordan, M. J. T. Stabilization of zwitterions in solution: γ-aminobutyric acid (GABA). *J. Phys. Chem. A* **2004**, *108*, 203–211.

[271] Blanco, S.; López, J. C.; Mata, S.; Alonso, J. L. Conformations of γ-aminobutyric acid (GABA): the role of the n$\rightarrow\pi*$ interaction. *Angew. Chem. Int. Ed.* **2010**, *49*, 9187–9192.

[272] Sharma, B.; Chandra, A. On the issue of closed versus open forms of gamma-aminobutyric acid (GABA) in water: Ab initio molecular dynamics and metadynamics studies. *J. Chem. Phys.* **2018**, *148*, 194503.

[273] Odai, K.; Sugimoto, T.; Kubo, M.; Ito, E. Theoretical research on structures of γ-aminobutyric acid and glutamic acid in aqueous conditions. *J. Biochem.* **2003**, *133*, 335–342.

[274] Song, I. K.; Kang, Y. K. Conformational preferences of γ-aminobutyric acid in the gas phase and in water. *J. Mol. Struct.* **2012**, *1024*, 163–169.

[275] Rodrigo, M.; Esteso, M.; Verissimo, L.; Romero, C.; Ramos, M.; Justino, L.; Burrows, H.; Ribeiro, A. Diffusion and structural behaviour of the DL-2-aminobutyric acid. *J. Chem. Thermodyn.* **2019**, *135*.

[276] Dunn, W. J.; Nagy, P. I. Monte Carlo studies on aqueous solutions of methylamine and acetonitrile: hydration of sp3 and sp nitrogen. *J. Phys. Chem.* **1990**, *94*, 2099–2105.

[277] Wee, S. S.; Kim, S.; Jhon, M. S. Analytical intermolecular potential functions from ab initio self-consistent-field calculations for hydration of methylamlne and methylammonlum ion. *J. Phys. Chem.* **1990**, *94*, 1656–1660.

[278] Jorgensen, W. L.; Gao, J. Monte Carlo simulations of the hydration of ammonium and carboxylate ions. *J. Phys. Chem.* **1986**, *90*, 2174–2182.

[279] Meng, E. C.; Kollman, P. A. Molecular dynamics studies of the properties of water around simple organic solutes. *J. Phys. Chem.* **1996**, *100*, 11460–11470.

[280] Kuntz, I. D. Hydration of macromolecules. III. Hydration of polypeptides. *J. Am. Chem. Soc.* **1971**, *93*, 514–516.

[281] Burakowski, A.; Gliński, J. Hydration numbers of nonelectrolytes from acoustic methods. *Chem. Rev.* **2012**, *112*, 2059–2081.

[282] Marcus, Y. *Ions in solution and their solvation*; John Wiley & Sons, Inc: Hoboken, New Jersey, 2015.

[283] James Port, G. N.; Pullman, A. An ab initio study of the hydration of alkylammonium groups. *Theoret. Chim. Acta* **1973**, *31*, 231–237.

[284] Davis, J. G.; Zukowski, S. R.; Rankin, B. M.; Ben-Amotz, D. Influence of a neighboring charged group on hydrophobic hydration shell structure. *J. Phys. Chem. B* **2015**, *119*, 9417–9422.

[285] Banipal, T. S.; Singh, G. Thermodynamic study of solvation of some amino acids, diglycine and lysozyme in aqueous and mixed aqueous solutions. *Thermochim. Acta* **2004**, *412*, 63–83.

[286] Shiraga, K.; Suzuki, T.; Kondo, N.; Ogawa, Y. Hydration and hydrogen bond network of water around hydrophobic surface investigated by terahertz spectroscopy. *J. Chem. Phys.* **2014**, *141*, 235103.

[287] Ramek, M.; Nagy, P. I. Theoretical investigation of the neutral/zwitterionic equilibrium of γ-aminobutyric acid (GABA) conformers in aqueous solution. *J. Phys. Chem. A* **2000**, *104*, 6844–6854.

[288] Silva, J. J. R. F. D.; Williams, R. J. P. *The Biological Chemistry of the Elements: The Inorganic Chemistry Of Life*, 2nd ed.; Oxford University Press: Oxford, 2001.

[289] Wachter, W.; Fernandez, a.; Buchner, R.; Hefter, G. Ion association and hydration in aqueous solutions of LiCl and Li_2SO_4 by dielectric spectroscopy. *J. Phys. Chem. B* **2007**, *111*, 9010–9017.

[290] Buchner, R.; Hefter, G. T.; Barthel, J. Dielectric relaxation of aqueous NaF and KF solutions. *J. Chem. Soc., Faraday Trans.* **1994**, *90*, 2475–2479.

[291] unpublished data from the Regensburg laboratory, 2007.

[292] Chen, T.; Hefter, G.; Buchner, R. Dielectric spectroscopy of aqueous solutions of KCl and CsCl. *J. Phys. Chem. A* **2003**, *107*, 4025–4031.

[293] Millero, F. J. *Chemical Oceanography*, 4th ed.; CRC Press: Boca Raton, 2013.

[294] Wetzel, R. G. *Limnology: Lake and River Ecosystems*, 3rd ed.; Academic Press: San Diego, 2001.

[295] Burgess, J.; Raven, E. In *Advances in Inorganic Chemistry*; van Eldik, R., Hubbard, C. D., Eds.; Academic Press, 2009; Vol. 61; pp 251–366.

[296] Butler, J. N.; Roy, R. N. In *Activity Coefficients in Electrolyte Solutions*, 2nd ed.; Pitzer, K. S., Ed.; CRC Press: Boca Raton, USA, 2017; Chapter 4, pp 155–208.

[297] Robinson, R. A.; Stokes, R. H. *Electrolyte Solutions*, 2nd ed.; Dover Publications: Mineola, NY, 2002.

[298] Yamaguchi, T.; Hayashi, S.; Ohtaki, H. X-ray diffraction study of calcium(II) chloride hydrate melts: $CaCl_2 \cdot RH_2O$ (R = 4.0, 5.6, 6.0, and 8.6). *Inorg. Chem.* **1989**, *28*, 2434–2439.

[299] Caminiti, R.; Licheri, G.; Pinna, G. P. G. X-ray diffraction study of $MgCI_2$ aqueous solutions. *J. Appl. Cryst.* **1979**, *12*, 34–38.

[300] Duboué-Dijon, E.; Mason, P. E.; Fischer, H. E.; Jungwirth, P. Hydration and ion pairing in aqueous Mg^{2+} and Zn^{2+} solutions: Force-field description aided by neutron scattering experiments and ab initio molecular dynamics simulations. *J. Phys. Chem. B* **2017**, *122*, 3296–3306.

[301] Martinek, T.; Duboué-Dijon, E.; Timr, Š.; Mason, P. E.; Baxová, K.; Fischer, H. E.; Schmidt, B.; Pluhařová, E.; Jungwirth, P. Calcium ions in aqueous solutions: Accurate force field description aided by ab initio molecular dynamics and neutron scattering. *J. Chem. Phys.* **2018**, *148*, 222813.

[302] Pham, V.-T.; Fulton, J. L. Ion-pairing in aqueous $CaCl_2$ and RbBr solutions: Simultaneous structural refinement of XAFS and XRD data. *J. Chem. Phys.* **2013**, *138*, 044201.

[303] Jalilehvand, F.; Spångberg, D.; Lindqvist-Reis, P.; Hermansson, K.; Persson, I.; Sandström, M. Hydration of the calcium ion. An EXAFS, large-angle X-ray scattering, and molecular dynamics simulation study. *J. Am. Chem. Soc.* **2001**, *123*, 431–441.

[304] Jiao, D.; King, C.; Grossfield, A.; Darden, T. A.; Ren, P. Simulation of Ca^{2+} and Mg^{2+} solvation using polarizable atomic multipole potential. *J. Phys. Chem. B* **2006**, *110*, 18553–18559.

[305] Li, M.; Duan, Z.; Zhang, Z.; Zhang, C.; Weare, J. The structure, dynamics and solvation mechanisms of ions in water from long time molecular dynamics simulations: a case study of $CaCl_2$ (aq) aqueous solutions. *Mol. Phys.* **2008**, *106*, 2685–2697.

[306] Kohagen, M.; Mason, P. E.; Jungwirth, P. Accurate description of calcium solvation in concentrated aqueous solutions. *J. Phys. Chem. B* **2014**, *118*, 7902–7909.

[307] Callahan, K. M.; Casillas-Ituarte, N. N.; Roeselová, M.; Allen, H. C.; Tobias, D. J. Solvation of magnesium dication: Molecular dynamics simulation and vibrational spectroscopic study of magnesium chloride in aqueous solutions. *J. Phys. Chem. A* **2010**, *114*, 5141–5148.

[308] Hofer, T. S.; Tran, H. T.; Schwenk, C. F.; Rode, B. M. Characterization of dynamics and reactivities of solvated ions by ab initio simulations. *J. Comput. Chem.* **2003**, *25*, 211–217.

[309] Ikeda, T.; Boero, M.; Terakura, K. Hydration properties of magnesium and calcium ions from constrained first principles molecular dynamics. *J. Chem. Phys.* **2007**, *127*, 074503.

[310] Lightstone, F. C.; Schwegler, E.; Allesch, M.; Gygi, F.; Galli, G. A first-principles molecular dynamics study of calcium in water. *ChemPhysChem* **2005**, *6*, 1745–1749.

[311] Martell, A. E., Smith, R. M., Eds. *Critical Stability Constants: First Supplement*; Springer US: New York, 1982; Vol. 5.

[312] Hefter, G. When spectroscopy fails: The measurement of ion pairing. *Pure Appl. Chem.* **2006**, *78*, 1571–1586.

[313] Kaatze, U.; Loennecke, V.; Pottel, R. Dielectric spectroscopy on aqueous solutions of zinc(II) chloride. Evidence of ion complexes. *J. Phys. Chem.* **1987**, *91*, 2206–2211.

[314] Eigen, M.; Tamm, K. Schallabsorption in Elektrolytlösungen als Folge chemischer Relaxation I. Relaxationstheorie der mehrstufigen Dissoziation. *Z. Elektrochem.* **1962**, *66*, 93–107.

[315] Eigen, M.; Tamm, K. Schallabsorption in Elektrolytlösungen als Folge chemischer Relaxation II. Meßergebnisse und Relaxationsmechanismen für 2-2- wertige Elektrolyte. *Z. Elektrochem.* **1962**, *66*, 107–121.

[316] Pyper, N. C.; Pike, C. G.; Edwards, P. P. The polarizabilities of species present in ionic solutions. *Mol. Phys.* **1992**, *76*, 353–372.

[317] Marcus, Y. *Ion Properties*; CRC Press: Boca Raton, 1997.

[318] Hasted, J. In *Water - A Comprehensive Treatise*; Franks, F., Ed.; Plenum: New York, 1973; Vol. 1.

[319] Buchner, R.; Chen, T.; Hefter, G. Complexity in "simple" electrolyte solutions: Ion pairing in $MgSO_4$(aq). *J. Phys. Chem. B* **2004**, *108*, 2365–2375.

[320] Larentzos, J. P.; Criscenti, L. J. A molecular dynamics study of alkaline earth metal chloride complexation in aqueous solution. *J. Phys. Chem. B* **2008**, *112*, 14243–14250.

[321] Majer, V.; Štulík, K. A study of the stability of alkaline-earth metal complexes with fluoride and chloride ions at various temperatures by potentiometry with ion-selective electrodes. *Talanta* **1982**, *29*, 145–148.

[322] Johnson, K. S.; Pytkowicz, R. M. Ion association of Cl^- with H^+ , Na^+ ,K^+ , Ca^{2+} , and Mg^{2+} in aqueous solutions at 25 °C. *Am. J. Sci.* **1978**, *278*, 1428–1447.

[323] De Robertis, A.; Rigano, C.; Sammartano, S.; Zerbinati, O. Ion association of Cl^- with Na^+, K^+, Mg^{2+} and Ca^{2+} in aqueous solution at $10 \leq T \leq 45\,°C$ and $0 \leq I \leq 1\,mol\,l^{-1}$: A literature data analysis. *Thermochim. Acta* **1987**, *115*, 241–248.

[324] Zhu, C.; Lu, P. Alkali feldspar dissolution and secondary mineral precipitation in batch systems: 3. Saturation states of product minerals and reaction paths. *Geochim. Cosmochim. Acta* **2009**, *73*, 3171–3200.

[325] Marcus, Y.; Hefter, G. Ion pairing. *Chem. Rev.* **2006**, *106*, 4585–4621.

[326] De Robertis, A.; Di Giacomo, P.; Foti, C. Ion-selective electrode measurements for the determination of formation constants of alkali and alkaline earth metals with low-molecular-weight ligands. *Anal. Chim. Acta* **1995**, *300*, 45–51.

[327] Waizumi, K.; Masuda, H.; Fukushima, N. A molecular approach to the formation of KCl and $MgCl^+$ ion-pairs in aqueous solution by density functional calculations. *Chem. Phys. Lett.* **1993**, *205*, 317–323.

[328] Badyal, Y. S.; Barnes, A. C.; Cuello, G. J.; Simonson, J. M. Understanding the effects of concentration on the solvation structure of Ca^{2+} in aqueous solution. II: Insights into longer range order from neutron diffraction isotope substitution. *J. Phys. Chem. A* **2004**, *108*, 11819–11827.

[329] Gibbs, J. H.; Cohen, C.; Fleming III, P. D.; Porosoff, H. In *The Physical Chemistry of Aqueous Systems*; Kay, R. L., Ed.; Plenum: New York, 1973; pp 179–201.

[330] Helm, L.; Merbach, A. E. Water exchange on metal ions: experiments and simulations. *Coord. Chem. Rev.* **1999**, *187*, 151–181.

[331] Schwenk, C. F.; Loeffler, H. H.; Rode, B. M. Dynamics of the solvation process of Ca^{2+} in water. *Chem. Phys. Lett.* **2001**, *349*, 99–103.

[332] Naor, M. M.; Nostrand, K. V.; Dellago, C. Car–Parrinello molecular dynamics simulation of the calcium ion in liquid water. *Chem. Phys. Lett.* **2003**, *369*, 159–164.

[333] Neely, J.; Connick, R. Rate of water exchange from hydrated magnesium ion. *J. Am. Chem. Soc.* **1970**, *92*, 3476–3478.

[334] Lyashchenko, A.; Lileev, A. Dielectric relaxation of water in hydration shells of ions. *J. Chem. Eng. Data* **2010**, *55*, 2008–2016.

[335] Kaatze, U. Aspects of ion hydration. Adiabatic compressibility compared to the dielectric properties of aqueous electrolyte solutions. *J. Phys. Chem. B* **2013**, *117*, 12252–12260.

[336] Brandes, E.; Stage, C.; Motschmann, H.; Rieder, J.; Buchner, R. Is surface layering of aqueous alkali halides determined by ion pairing in the bulk solution? *J. Chem. Phys.* **2014**, *141*, 18C509.

[337] Eriksson, P.-O.; Lindblom, G.; Burnell, E. E.; Tiddy, G. J. T. Influence of organic solutes on the self-diffusion of water as studied by nuclear magnetic resonance spectroscopy. *J. Chem. Soc., Faraday Trans. 1* **1988**, *84*, 3129–3139.

[338] Buckner, J. K.; Jorgensen, W. L. Energetics and hydration of the constituent ion pairs of tetramethylammonium chloride. *J. Am. Chem. Soc.* **1989**, *111*, 2507–2516.

[339] Dong, D.; Hooper, J. B.; Bedrov, D. Structural and dynamical properties of tetraalkylammonium bromide aqueous solutions: A molecular dynamics simulation study using a polarizable force field. *J. Phys. Chem. B* **2017**, *121*, 4853–4863.

[340] Green, J. L.; Sceats, M. G.; Lacey, A. R. Hydrophobic effects in the water network structure of aqueous solutions of a semiclathrate molecule. *J. Chem. Phys.* **1987**, *87*, 3603–3610.

[341] Heyda, J.; Lund, M.; Ončák, M.; Slavíček, P.; Jungwirth, P. Reversal of Hofmeister prdering for Pairing of NH_4^+ vs alkylated ammonium cations with halide anions in water. *J. Phys. Chem. B* **2010**, *114*, 10843–10852.

[342] Huang, N.; Schlesinger, D.; Nordlund, D.; Huang, C.; Tyliszczak, T.; Weiss, T. M.; Acremann, Y.; Pettersson, L. G. M.; Nilsson, A. Microscopic probing of the size dependence in hydrophobic solvation. *J. Chem. Phys.* **2012**, *136*, 074507.

[343] Kühnel, V.; Kaatze, U. Uncommon ultrasonic absorption spectra of tetraalkylammonium bromides in aqueous solution. *J. Phys. Chem.* **1996**, *100*, 19747–19757.

[344] Lindenbaum, S.; Boyd, G. E. Osmotic and activity coefficients for the symmetrical tetraalkyl ammonium halides in aqueous solution at 25 °C. *J. Phys. Chem.* **1964**, *68*, 911–917.

[345] Marcus, Y. Tetraalkylammonium ions in aqueous and non-aqueous solutions. *J. Solution Chem.* **2008**, *37*, 1071.

[346] Turner, J.; Soper, A. K. The effect of apolar solutes on water structure: Alcohols and tetraalkylammonium ions. *J. Chem. Phys.* **1994**, *101*, 6116–6125.

[347] Bhowmik, D.; Malikova, N.; Mériguet, G.; Bernard, O.; Teixeira, J.; Turq, P. Aqueous solutions of tetraalkylammonium halides: ion hydration, dynamics and ion-ion interactions in light of steric effects. *Phys. Chem. Chem. Phys.* **2014**, *16*, 13447–13457.

[348] Jerie, K.; Baranowski, A.; Jákli, G.; Gliński, J. Structure of aqueous solutions of tetraethylammonium chloride investigated by positron annihilation and ultrasonic methods. *J. Radioanal. Nucl. Chem.* **1999**, *240*, 223–229.

[349] Koga, Y.; Sebe, F.; Nishikawa, K. Effects of tetramethyl- and tetraethylammonium chloride on H_2O: Calorimetric and near-infrared spectroscopic study. *J. Phys. Chem. B* **2013**, *117*, 877–883.

[350] Kustov, A. V.; Korolev, V. P. Temperature and length scale dependence of tetraalkylammonium ionamide interaction. *J. Phys. Chem. B* **2008**, *112*, 2040–2044.

[351] Frank, H. S.; Evans, M. W. Free volume and entropy in condensed systems III. Entropy in binary liquid mixtures; partial molal entropy in dilute solutions; structure and thermodynamics in aqueous electrolytes. *J. Chem. Phys.* **1945**, *13*, 507–532.

[352] van der Post, S. T.; Scheidelaar, S.; Bakker, H. J. Water dynamics in aqueous solutions of tetra-n-alkylammonium salts: Hydrophobic and coulomb Interactions disentangled. *J. Phys. Chem. B* **2013**, *117*, 15101–15110.

[353] Geng, Y.; Romsted, L. S. Ion pair formation in water. Association constants of bolaform, bisquaternary ammonium, electrolytes by chemical trapping. *J. Phys. Chem. B* **2005**, *109*, 23629–23637.

[354] Robinson, G.; Singh, S.; Zhu, S. B.; ; Evans, M. *Water in Biology, Chemistry and Physics*; World Scientific: Singapore, 1996.

[355] Tanford, C. *The Hydrophobic Effect: Formation of Micelles and Biological Membranes*, 2nd ed.; John Wiley & Sons Inc: New York, 1980.

[356] Martell, A. E.; Hancock, R. D. *Metal Complexes in Aqueous Solutions*; Modern Inorganic Chemistry; Springer US: New York, 1996.

[357] Kaatze, U. Kinetic depolarization in aqueous solutions of alkylammonium bromides. *Ber. Bunsenges. Phys. Chem.* **1980**, *84*, 1195–1197.

[358] Finney, J. L.; Turner, J. Direct measurement by neutron diffraction of the solvation of molecules with apolar surface: The hydration of the tetramethylammonium ion. *Physica B* **1989**, *156-157*, 148–150.

[359] Polydorou, N. G.; Wicks, J. D.; Turner, J. Z. Hydrophobic interaction of tetrapropylammonium ions in water: A neutron diffraction and reverse Monte Carlo study. *J. Chem. Phys.* **1997**, *107*, 197–204.

[360] Collins, K. D. Charge density-dependent strength of hydration and biological structure. *Biophys. J.* **1997**, *72*, 65–76.

[361] Ohtomo, N.; Arakawa, K. Neutron diffraction study of aqueous ionic solutions. II. Aqueous solutions of sodium chloride and potassium chloride. *Bull. Chem. Soc. Jpn.* **1980**, *53*, 1789–1794.

[362] Sripa, P.; Tongraar, A.; Kerdcharoen, T. Characteristics of K^+ and Rb^+ as "structure-breaking" ions in dilute aqueous solution: Insights from ONIOM-XS MD simulations. *Chem. Phys.* **2016**, *C*, 72–80.

[363] Ikeda, T.; Boero, M.; Terakura, K. Hydration of alkali ions from first principles molecular dynamics revisited. *J. Chem. Phys.* **2007**, *126*, 034501.

[364] Liu, Y.; Lu, H.; Wu, Y.; Hu, T.; Li, Q. Hydration and coordination of K^+ solvation in water from ab initio molecular-dynamics simulation. *J. Chem. Phys.* **2010**, *132*, 124503.

[365] Ojha, D.; Chandra, A. Vibrational echo spectral observables and frequency fluctuations of hydration shell water around a fluoride ion from first principles simulations. *J. Chem. Sci.* **2017**, *129*, 1069–1080.

[366] Boisson, J.; Stirnemann, G.; Laage, D.; Hynes, J. T. Water reorientation dynamics in the first hydration shells of F^- and I^-. *Phys. Chem. Chem. Phys.* **2011**, *13*, 19895–19901.

[367] Migliorati, V.; Sessa, F.; Aquilanti, G.; D'Angelo, P. Unraveling halide hydration: A high dilution approach. *J. Chem. Phys.* **2014**, *141*, 044509.

[368] Trumm, M.; Martínez, Y. O. G.; Réal, F.; Masella, M.; Vallet, V.; Schimmelpfennig, B. Modeling the hydration of mono-atomic anions from the gas phase to the bulk phase: The case of the halide ions F^-, Cl^-, and Br^-. *J. Chem. Phys.* **2012**, *136*, 044509.

[369] Mancinelli, R.; Botti, A.; Bruni, F.; Ricci, M. A.; Soper, A. K. Hydration of sodium, potassium, and chloride ions in solution and the concept of structure maker/breaker. *J. Phys. Chem. B* **2007**, *111*, 13570–13577.

[370] Davies, A.; O. George, W.; T. Howard, S. Ab initio and DFT computer studies of complexes of quaternary nitrogen cations: trimethylammonium, tetramethylammonium, trimethylethylammonium, choline and acetylcholine with hydroxide, fluoride and chloride anions. *Phys. Chem. Chem. Phys.* **2003**, *5*, 4533–4540.

[371] Buchner, R.; Barthel, J. Kinetic processes in the liquid phase studied by high-frequency permittivity measurements. *J. Mol. Liq.* **1995**, *63*, 55–75.

[372] Bartoli, S.; Roelens, S. Binding of acetylcholine and tetramethylammonium to a cyclophane receptor: anion's contribution to the Cation-π interaction. *J. Am. Chem. Soc.* **2002**, *124*, 8307–8315.

[373] Sajadi, S. A. A. Metal ion-binding properties of L-glutamic acid and L-aspartic acid, a comparative investigation. *Nat. Sci.* **2010**, *2*, 85–90.

[374] Smith, R. M.; Motekaitis, R. J.; Martell, A. E. Prediction of stability constants. II. Metal chelates of natural alkyl amino acids and their synthetic analogs. *Inorg. Chim. Acta* **1985**, *103*, 73–82.

[375] Tang, N.; Skibsted, L. H. Calcium binding to amino acids and small glycine peptides in aqueous solution: Toward peptide design for better calcium bioavailability. *J. Agric. Food Chem.* **2016**, *64*, 4376–4389.

[376] Stevens, M. J.; Rempe, S. L. B. Ion-specific effects in carboxylate binding sites. *J. Phys. Chem. B* **2016**, *120*, 12519–12530.

[377] Campo, M. G. Molecular dynamics simulation of glycine zwitterion in aqueous solution. *J. Chem. Phys.* **2006**, *125*, 114511.

[378] Heyda, J.; Hrobárik, T.; Jungwirth, P. Ion-specific interactions between halides and basic amino acids in water. *J. Phys. Chem. A* **2009**, *113*, 1969–1975.

[379] Fedotova, M. V.; Kruchinin, S. E. Ion-binding of glycine zwitterion with inorganic ions in biologically relevant aqueous electrolyte solutions. *Biophys. Chem.* **2014**, *190–191*, 25–31.

[380] Andersen, U. N.; Bojesen, G. The order of lithium ion affinities for the 20 common α-amino acids. Calculation of energy-well depth of ion-bound dimers. *J. Chem. Soc., Perkin Trans.* **1997**, *2*, 323–327.

[381] Feng, W. Y.; Gronert, S.; Lebrilla, C. B. Lithium and sodium ion binding energies of N-Acetyl and N-Glycyl Amino Acids. *J. Am. Chem. Soc.* **1999**, *121*, 1365–1371.

[382] Hubbard, J.; Onsager, L. Dielectric dispersion and dielectric friction in electrolyte solutions. I. *J. Chem. Phys* **1977**, *67*, 4850–4857.

[383] Hubbard, J. B. Dielectric dispersion and dielectric friction in electrolyte solutions. II. *J. Chem. Phys* **1978**, *68*, 1649–1664.

[384] Hubbard, J. B.; Colonomos, P.; Wolynes, P. G. Molecular theory of solvated ion dynamics. III. The kinetic dielectric decrement. *J. Chem. Phys* **1979**, *71*, 2652–2661.

[385] Schrödle, S.; Rudolph, W. W.; Hefter, G.; Buchner, R. Ion association and hydration in 3:2 electrolyte solutions by dielectric spectroscopy: Aluminum sulfate. *Geochim. Cosmochim. Acta* **2007**, *71*, 5287–5300.

Eidesstattliche Erklärung

(1) Ich erkläre hiermit an Eides statt, dass ich die vorliegende Arbeit ohne unzulässige Hilfe Dritter und ohne Benutzung anderer als der angegebenen Hilfsmittel angefertigt habe; die aus anderen Quellen direkt oder indirekt übernommenen Daten und Konzepte sind unter Angabe des Literaturzitats gekennzeichnet.

(2) Bei der Auswahl und Auswertung folgenden Materials haben mir die nachstehend aufgeführten Personen in der jeweils beschriebenen Weise entgeltlich/unentgeltlich geholfen:

1. Dominik Feucht: Führte im Rahmen seiner Bacherlorarbeit Messungen von wässrigen Natriumglutamat Messungen durch

2. Matthias Kawalek: Führte im Rahmen seiner Bacherlorarbeit Messungen von wässrigen n-Butylammnoniumchlorid Messungen durch

(3) Weitere Personen waren an der inhaltlich-materiellen Herstellung der vorliegenden Arbeit nicht beteiligt. Insbesondere habe ich hierfür nicht die entgeltliche Hilfe eines Promotionsberaters oder anderer Personen in Anspruch genommen. Niemand hat von mir weder unmittelbar noch mittelbar geldwerte Leistungen für Arbeiten erhalten, die im Zusammenhang mit dem Inhalt der vorgelegten Dissertation stehen.

(4) Die Arbeit wurde bisher weder im In- noch im Ausland in gleicher oder ähnlicher Form einer anderen Prüfungsbehörde vorgelegt.

Regensburg, den 21. Oktober 2019

Sergej Friesen